

**DESIGNING PARTICLE SHAPES TO PASSIVELY TUNE  
SUSPENSION RHEOLOGY**

A Dissertation

Presented to the Faculty of the Graduate School

of Cornell University

In Partial Fulfillment of the Requirements for the Degree of

Doctor of Philosophy

by

NEERAJ NITIN SINAI BORKER

[December 2019]

© 2019 Neeraj Nitin Sinai Borker

ALL RIGHTS RESERVED

DESIGNING PARTICLE SHAPES TO PASSIVELY TUNE SUSPENSION  
RHEOLOGY

Neeraj Nitin Sinai Borker, Ph. D.

Cornell University 2019

This thesis concerns with the ability to change the properties of particle suspensions in a low Reynolds number simple shear flow over two orders of magnitude by designing shapes of the individual particles. The motion of particles such as rings with sharper outer edges, fibers with non-circular cross-sections or ramified particles can display unusual dynamics by small changes in their respective particle geometries. This work specifically focuses on particles that attain an equilibrium orientation without application of external forces or torques. Rheological properties of a suspension of such self-aligning particles (SAPs), such as intrinsic viscosity, hydrodynamic diffusivity and orientational dispersion, as a function of the particle aspect ratio display a phase transition-like behavior where the value of each of the rheological property drops by an order of magnitude near a critical aspect ratio  $A^*$ . Using suspension of SAPs, rheological properties such as viscosity can be controlled by small changes in the particle aspect ratio; by adding a small number of tumbling particles to the suspension; or by varying the absolute particle, shear rate and/or the underlying fluid viscosity. This tunability of macroscopic properties of particle suspensions via passive control of the motion of its individual constituent particles opens new opportunities to fabricate functional materials with tunable properties using current processing flow technology such as injection molding or spin casting.

A computationally inexpensive boundary element method for axisymmetric particles and a slender body theory accounting for cross-sectional effects on the force distribution of slender filaments, both in any linear flow fields, were developed as part of this thesis. These tools were used to obtain the motion of individual particles with exotic shapes. The suspension rheology was obtained through Brownian dynamics

simulations and numerical calculations accounting for pairwise far-field hydrodynamic interactions and along with collisions. The shear rheology of rotating rings was also investigated to demonstrate its differences from the rheology of rotating fibers and discs. With the advancement in manufacturing techniques, self-aligning particle geometries can be accessed using fabrication methods such as 3D printing or lithography thereby allowing for experimental verification of our results and fabrication of functional materials.

## BIOGRAPHICAL SKETCH

Neeraj was born in Margao located on the western coast of India. He joined Cornell in 2014 after obtaining his Bachelor of Technology degree in Mechanical Engineering from Indian Institute of Technology Madras. He enjoys sketching, cycling and hiking.

Dedicated to my parents Sneha & Nitin Sinai Borker

## ACKNOWLEDGMENTS

I would like to thank my committee members Prof. Koch, Prof. Stroock and Prof. Kirby for their guidance during my PhD. I would like to thank Prof. Donald Koch for his mentorship and support during my time at Cornell. I would like to thank Prof. Stroock for always motivating me to think about the broader impact of my work.

Moreover, I want to thank Mohammed Alhashimi, Johnson Dhanasekaran, Mukul Tikekar, Udayshankar Menon, Gaojin Li, Jay Gandhi, Michael Santiago and Hanwen Lu for engaging in discussions on my research work. I would also like to acknowledge Luke McCarney and Ryan Branch for the fruitful research together. I would also like to thank Prof. Michel Louge for a productive teaching assistantship in the undergraduate heat transfer course. Special thanks to Frank and Sue for fun get togethers on Thanksgiving and Christmas. I would also like to thank the people of Ithaca for maintaining a cheerful atmosphere in the town that made me ignore the ever gloomy winters of upstate New York.

Finally, I want to thank my family who have always been supportive and encouraging throughout my life.

## TABLE OF CONTENTS

### Chapter 1 Introduction

Chapter 2 Controlling rotation and migration of rings in a simple shear flow through geometric modifications.

- 1 Introduction
- 2 Particle dynamics in linear flows
- 3 Computational approach
- 4 Results and discussion
  - 4.1 Fore-aft symmetric particles that do not drift
  - 4.2 Fore-aft asymmetric particles that align and drift
- 5 Conclusion
- 6 Acknowledgements
- 7 References

Chapter 3 Slender body theory for particles with non-circular cross-sections with application to particle dynamics in shear flows

- 1 Introduction
- 2 SBT solution for circular cross-section
- 3 SBT solution for non-circular cross-sections
  - 3.1 Regular perturbation of inner solution
  - 3.2 Matching the inner and outer velocity field for a slightly non-circular cross-section
  - 3.3 Extending the analysis to a general cross-sectional shape
- 4 Resistance to motion of a triaxial ellipsoid
- 5 Translation of a straight slender body in a simple shear flow
- 6 Motion of rings in a simple shear flow

## 7 Conclusion

Chapter 4 Rheology of dilute suspension of thin rings

1 Introduction

2 Rheology of pairwise interacting non-Brownian rings

    2.1 Simulation strategy for pairwise particle interactions

    2.2  $O(n^2)$  rheology of hydrodynamically interacting rings

3 Simulation strategy

    3.1 Rheology of isolated Brownian particles

    3.2 Structure and rheology of isolated Brownian rings

4 Conclusion

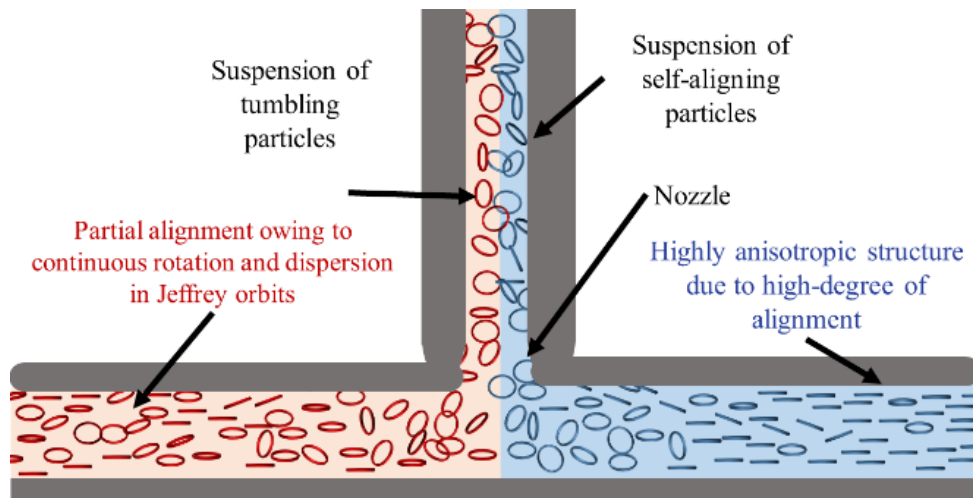
Chapter 5 Shear Rheology of Self-Aligning Particles

Chapter 6 Future work

## CHAPTER 1

### Introduction

Self-aligning particles (SAPs) are rigid bodies that can attain an equilibrium orientation without application of any external forces or torques in a simple shear flow, which is a linear approximation to a pressure driven flow found in many natural and industrial processes. Self-alignment of particles could be a technologically revolutionary behavior because it allows for creation of materials with *perfect anisotropy* using current processing flow techniques like injection molding, spin-casting or extrusion as shown in figure 1 (a). The orientational order of SAPs allows for the fabrication of functional materials with great control over the mechanical, optical, electrical, or thermal properties of the final product. For instance, SAPs embedded during the curing process can be used to fabricate lightweight high strength materials with a layered microstructure, mimicking that of an abalone shell, which can also withstand crack propagation (Lin, et al., 2006) thereby making them useful for making bulletproof armor. Conducting self-aligning rings can also be used instead of fibers to fabricate optical films with the uniform planar conductivity desirable in electronic devices (De, et al., 2009).



(a)

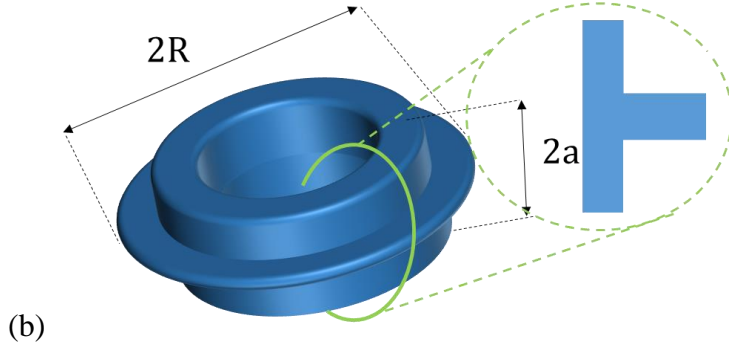


Figure 1 (a) Schematic of an injection molding system with self-aligning particles on the right, and tumbling particles on the left, demonstrates the difference in the micro-structure. (b) Ring-shaped particles that can self-align in a simple shear flow without application of external torques and forces. Family of rings with this inverted T-shaped cross-section can self-align at aspect ratios as small as 26 and provide accessibility to fabrication using multi-step photolithography (Foulds & Parameswaran., 2006).

Most particles rotate continuously in a Newtonian fluid subject to a simple shear flow at low Reynolds number because they respond more strongly to the vorticity than to the extensional component of the flow (Bretherton 1962 a). The shear stresses acting on most particles, whether globular (sphere-like) or thin (rod-like or disc-like), force the particles to rotate in the vorticity direction. Thin particles like fibers or discs tend to spend a long time with their longitudinal direction perpendicular to the gradient direction ( $\hat{\Gamma}_\infty$ ). However, high-aspect ratio rings with sharp outer and blunt inner edges can attain an equilibrium orientation without application of external forces (Singh, Koch and Stroock 2013). This thesis explores the origin of this self-aligning behavior, gives design principles to construct self-aligning particles and derives the rheology of a suspension of self-aligning particles. New theoretical tools and numerical techniques are also developed in this thesis which have broad applicability beyond self-aligning particles.

The origin of self-aligning behavior is explored in chapter 2 by carefully examining the stresses acting on the surface of rings with distinct cross-sectional shapes. The typical intuition of a fluid dynamicist suggests that shear stresses acting on a rigid body should force the particle to rotate continuously in a simple shear flow. However, pressure, which always acts normal to a surface, can be manipulated to generate counter-vorticity rotation by careful choice of the particle

geometry. This counter vorticity rotation balances the rotation induced by the shear stresses leading to flow-alignment of rings. Rings with sharp outer and blunt inner edges, such as the one shown in figure 1 (b), can most effectively utilize the fluid pressure for the purpose of flow alignment. The aspect ratio of such rings ( $A$ ) needs to be greater than a critical value of  $A^*$  for the particle to self-align. The aspect ratio  $A$  of the ring is defined as the ratio of the extent of the particle in the plane of the ring ( $2R$ ) and the extent normal to the plane ( $2a$ ) (i.e.  $A = R/a$ ). In chapter 2, ring cross-sectional shapes that have  $A^*$  as small as 10 are identified using boundary element method calculations. A lower value of  $A^*$  would mean that the ring would be less prone to bending and buckling, thus improving the structural integrity of the particle. Furthermore, self-aligning rings that lack mirror symmetry about a plane normal to the particle's axis of symmetry can also migrate relative to the fluid velocity at its center of mass. Such migrating rings have potential application in controlling surface texture of materials via systematic particle deposition. In chapter 2, geometries with large cross-stream migration velocities are also explored using boundary element method (BEM) computations. An intuitive explanation about the features of ring cross-sectional shapes that lead to self-alignment at low  $A^*$  is also elucidated through a two-dimensional Stokes flow calculation involving a simple shear flow past a stationary cross-section.

In Chapter 2, a novel boundary element method is developed to solve Stokes flow problems involving axisymmetric bodies in a linear flow field which involves analytical integration along the azimuthal direction and only requires a one-dimensional mesh along the cross-sectional contour. Linearity of Stokes flow and the boundary conditions along with the axisymmetry of the particle requires the force per unit area to be linear in the translational velocity of the particle relative to the fluid, the relative rotation rate of the particle and fluid, and the rate of strain of the imposed linear field. This condition can be used to derive the functional dependence of the force-per-unit area on the azimuthal angle. The boundary integral is then analytically obtained along the azimuthal coordinate leaving behind a term that is just a path integral along the cross-sectional contour of the axisymmetric particle. This greatly reduces the computational cost because the path integral requires a much smaller number of one-dimensional discretization segments than the number of two-dimensional surface mesh elements required in the traditional boundary element method approach. This simplification allowed us to solve Stokes flow problems to explore a large range of high-aspect ratio ring shapes that can self-align in a simple shear flow. This task would

be quite daunting with a traditional boundary element method solver, particularly for particles with sharper features which were found to self-align at small values of  $A^*$ .

In Chapter 3, a slender body theory is developed to account for the influence of the cross-sectional shape on the force per unit length acting on a slender filament in a fluid at low Reynolds number. Using a regular perturbation of the inner solution, we show that the force per unit length has  $O(1/\ln(2A))$  and  $O(\alpha/\ln^2(2A))$  contributions driven by the relative motion of the particle and the local fluid velocity and an  $O(\alpha/(\ln(2A)A))$  contribution driven by the gradient in the imposed fluid velocity. Here, the aspect ratio ( $A = l/a_0$ ) is defined as the ratio of the particle size ( $l$ ) to the cross-sectional dimension ( $a_0$ ); and  $\alpha$  is the amplitude of the non-circular perturbation. Using thought experiments, we show that two-lobed and three-lobed cross-sections affect the response to relative motion and velocity gradients, respectively. A two-dimensional Stokes flow calculation is used to extend the perturbation analysis to cross-sections that deviate significantly from a circle (i.e.,  $\alpha \sim O(1)$ ). We demonstrate the ability of our method to accurately compute the resistance to translation and rotation of a slender triaxial ellipsoid. Furthermore, we illustrate novel dynamics of straight rods in a simple shear flow that translate and rotate quasi-periodically if they have two-lobed cross-sections; and rotate chaotically and translate diffusively if they have a combination of two- and three-lobed cross-sections. Finally, we show the remarkable ability of our theory to accurately predict the motion of rings, retaining great accuracy for moderate aspect ratios ( $\sim 10$ ) and cross-sections that deviate significantly from a circle, thereby making our theory a computationally inexpensive alternative to other Stokes flow solvers. Through the slender body theory formulation, we also derive a computationally efficient method to search for ring geometries that can self-align at the least aspect ratio. This method only requires the solution of certain 2D Stokes flow problems around the particles' cross-section, discussed in section (3.3) of chapter 3. Additionally, this slender body theory formulation was used to obtain the influence of pairwise interactions on the dynamics of individual particles in chapters 4 and 5.

In Chapter 4, the rheology of a dilute suspension of tori rotating in an unbounded low Reynolds number simple shear flow is established. High aspect ratio tori rotate in Jeffery orbits similar to thin discs but produce weak velocity disturbance similar to thin fibers and thereby a suspension of rings has a rheology with characteristics of both fiber and disc rheology. The

suspension rheology of non-Brownian rings at dilute particle number densities ( $Pe\phi_T^{-2} \ll n \ll 1$ ) is computed by simulating pairwise interactions in which hydrodynamic interactions are modeled using slender body theory and collisions are modeled using a short-range repulsive force. Here, the Peclet number  $Pe$  is the ratio of the shear rate to the rotary diffusivity of the particle,  $\phi_T$  is the effective particle aspect ratio which is equal to  $2\pi$  times the inverse of its Jeffery time period, and  $n$  is the non-dimensional number density equal to the dimensional number density times the cube of the ring radius. Rotary Brownian dynamics simulations of isolated Brownian rings were also performed to understand the shear rate dependence of suspension rheology for  $n \ll Pe\phi_T^{-2}$ . Furthermore, the Jeffery orbit distribution set by weak Brownian motion ( $Pe \ll \phi_T^{-3}$ ) is similar to the one set by pairwise interactions implying the pairwise simulation should accurately predict the rheology for  $n \ll 1$  and  $Pe \ll \phi_T^{-3}$ .

In chapter 5, the shear rheology of self-aligning rings is calculated. A suspension of aligned particles has unconventional rheological properties including sharp drops in the intrinsic viscosity, hydrodynamic diffusivity and orientational dispersion compared to a suspension of rotating particles of the same aspect ratio. These suspension properties as a function of the aspect ratio at dilute particle concentrations display a phase transition like behavior near a critical aspect ratio  $A^*$  which is the minimum aspect ratio at which a ring can self-align. The sharp difference in the magnitude of these suspension properties allows one to passively tune the rheology by changing the particle geometry, the shear rate or adding a small number of tumblers in a suspension of self-aligning particles. Here, we establish the shear rate dependence on the rheology of ring suspensions using Brownian Dynamics simulations wherein we compute a critical shear rate that is required to self-align colloidal scale rings. The influence of pairwise interactions is also simulated using a dynamic calculation which includes hydrodynamic interactions modeled using the slender body theory developed in chapter 3 and collisions modeled through a short-range repulsive force. The pairwise calculation suggests that hydrodynamic interactions are the dominant interactions in setting the suspension rheology. This is starkly different from a suspension of tumbling rings whose rheology is strongly influence by both collisions and hydrodynamic interactions leading to a large difference in the magnitude of hydrodynamic diffusivities, orientational dispersion and the viscosity exerted by particles on the fluid.

## CHAPTER 2

# Controlling rotation and migration of rings in a simple shear flow through geometric modifications

### 1. Introduction

Most particles tumble continuously in a Newtonian fluid subject to a simple shear flow at low Reynolds number because they respond more strongly to the vorticity than to the extensional component of the flow (Bretherton 1962 a). However, rings with certain cross-sectional shapes, as shown in figure 1 (a), were shown to exhibit permanent alignment at finite particle aspect ratios (Singh, Koch and Stroock 2013). The aspect ratio ( $A = R/a$ ) is defined as the ratio of the maximum extent of the particle in the plane of the ring ( $2R$ ) and the maximum extent of the particle along the axis of symmetry ( $2a$ ) as shown in figure 1 (a). This finding is fascinating as dynamics of the particle is not only affected by its shape on the larger length scale, but is significantly influenced by the geometry of the smaller dimension to the point that it can lead to a bifurcation in dynamics. In this paper, we describe the mechanism leading to alignment of rings with certain cross-sections. Using this mechanism, we obtain cross-sectional geometries that allow rings to align at much smaller aspect ratios (<10) than the previously reported minimum of 30 (Singh et al. 2013). This is important from the standpoint of fabrication as a higher aspect-ratio ring will be more prone to bending, buckling and breakage and thus, might not align. We also elucidate the mechanism that leads to cross-stream migration of particles that lack fore-aft or mirror symmetry. We show ways to control the magnitude of this migration or drift velocity by appropriate choice of the cross-sectional geometry. We point out that this ability to control dynamics of individual particles could allow for precise control over the macroscopic properties of the suspension.

A simple shear flow is a good local approximation to a pressure driven flow, if the channel size is much larger than the length scale of interest, which is the particle dimension in our case. Thus, a simple shear flow could approximate processing flows such as injection molding, extrusion and spin-casting in certain regions of the flow field. Particles aligning in a simple shear flow

provide unique opportunities in the material processing industry to impart enhanced properties using current processing technologies. Particles that align in a simple shear flow could be embedded in composites during curing to impart anisotropic properties to the final product. For instance, a composite material with aligned, rigid rings would have enhanced specific stiffness. Aligned particles are also more effective at reinforcing composites prone to plastic deformation (Bao, Hutchinson and McMeeking 1991). Aligned particles with cross-stream migration have possible application as surface modifying agents in polymer composite materials processed in mold filling flows. These particles could be systematically deposited by the flow onto a surface to improve its scratch resistance (Isla et al. 2003).

The motion of particles in a simple shear flow has been studied for over a century. Einstein (1906) in his study of the effective viscosity of sheared suspensions showed that a rigid sphere rotates steadily along the fluid vorticity in an unbounded simple shear flow. Later, Jeffery (1922) demonstrated that spheroids rotate in periodic orbits in a simple shear flow slowing down but not stopping when the large dimension of the particle is nearly perpendicular to the velocity gradient direction. Four decades later, Bretherton (1962-a) proved that this periodic tumbling was not restricted to spheroids but spanned almost all axisymmetric particles, except for a few shapes of extreme aspect ratio. This prediction of Bretherton about the tumbling behavior of axisymmetric particles has been tested by both theory and experiments for discs and fibers (Anczurowski and Mason 1962; Trevelyan and Mason 1951; Stover and Cohen 1990). The particle tumbles in one of the infinitely many orbits depending on its initial orientation. At dilute particle concentrations, there is a distribution of particle orientations across various orbits due to secondary effects such as particle interactions or Brownian motion (Rahnama, Koch and Shaqfeh 1994; Leal and Hinch 1971). This distribution across orbits along with particle tumbling ensures a dispersion of orientations in the suspension. An aligning particle on the other hand, should always move towards a stable orientation irrespective of the initial orientation of the particle. Hence a sheared suspension of aligned particles should possess a micro-structure with a high degree of anisotropy.

Bretherton (1962a) was the first to propose a geometry that aligned in a simple shear flow. The body was a thin rod with slightly non-spherical lobes attached at each end, such that the lobe size was much smaller than the rod length. However, he showed that the aspect ratio of the rod

would need to be much larger than the exponential of the ratio of the length of the rod and the diameter of the lobes for the particle to align, leading to impractically low rigidity of the rod. Over half a century later Singh et al. (2013), predicted the existence of rings with certain cross-sections that align at finite particle aspect ratios. However, the cross-sectional shapes studied in Singh et al. (2013) were limited to a very specific perturbation of a circular cross-section. In this paper, we elucidate the mechanism of alignment by giving insight into the forces that lead to particle alignment in a simple shear flow. In particular, we identify ways to control rotation of a ring, by changing the cross-sectional shape.

An axisymmetric particle can also migrate in a simple shear flow if it lacks fore-aft or mirror symmetry about a plane normal to the axis of symmetry. Brenner (1964) and Nir and Avrivos (1973), showed that particles that lack fore-aft symmetry can possess a cross-stream drift velocity. However, particles that tumble periodically undergo no net migration. Curved fibers can break this periodicity and lead to a constant cross-stream migration (Wang et al. 2012). However, such particles do not migrate for all initial orientations and the drift velocity depends on the initial orientation of the particle. Kim and Rae (1991) showed that screw-shaped particles migrate along or opposite to the vorticity direction depending on the handedness of the particle. However, the magnitude of the drift velocity of a screw shaped particle was shown to depend on its initial orientation. In all the above studies, the translational motion is either periodic with no net migration or the migration velocity depends on the initial particle orientation. A ring that attains an equilibrium orientation in a simple shear flow can possess a constant cross-stream velocity if it lacks fore-aft symmetry about a plane normal to the axis of symmetry of the particle. The particle obtains this constant drift velocity as it approaches the stable orientation in a time that scales with the inverse of the strain rate. We describe the mechanism leading to this drift and ways to control its magnitude by changing the cross-sectional geometry. We also elucidate the effect of the equilibrium orientation of the particle on this drift velocity.

The rotation and migration of particles in an external flow field depends on the stresses acting on the particle surface. We numerically obtain the stresses on the particle surface using the boundary element method (BEM). BEM is usually used if the primary goal is to obtain the value of the variable on the boundary. However, BEM can only be used if the fundamental solution of

the governing differential equations is known (Abramowitz and Stegun, 1964). The flow field generated by a point force is a fundamental solution to the governing equations at low Reynolds number and thus we can use BEM to obtain the force per unit area exerted by the fluid on the particle surface. In our case BEM not only reduces the dimensionality of the problem, but also allows us to solve the problem in an unbounded domain.

In the following section, we solve the dynamical equations that describe the rotation of the particle and obtain the necessary conditions for alignment in a simple shear flow. In section 3 we formulate the problem and set up the equations necessary to obtain parameters governing the motion of particles in a linear flow field. The equations are numerically solved using the boundary element method. Section 4 describes the mechanisms for alignment and cross-stream drift by visualizing the flow field and stresses acting on the particle. We suggest shapes that align at low values of aspect ratios using BEM calculations. We also elucidate the importance of particle orientation on the particle drift. Section 5 presents the conclusion and implications of the ability to control particle dynamics for manipulating macroscopic properties of particle suspensions.

## 2. Particle dynamics in linear flows.

The linearity of Stokes flow is used to obtain the functional form of the rate of change of orientation ( $\dot{\mathbf{p}}$ ) as well as the drift velocity ( $\mathbf{U}_p$ ) of an axisymmetric particle in an unbounded linear flow field.  $\dot{\mathbf{p}}$  and  $\mathbf{U}_p$  can be described fully by three scalar parameters,  $\lambda$ ,  $\eta_1$  and  $\eta_2$ , that depend on the particle geometry (Singh, et al. 2013). The rotation parameter,  $\lambda$ , determines the rate of change of orientation of an axisymmetric particle and depends purely on its geometry. The rate of change of orientation ( $\dot{\mathbf{p}}$ ) of the particle is given by

$$\dot{\mathbf{p}} = \mathbf{p} \cdot \mathbf{R}^\infty + \lambda(\mathbf{E}^\infty \cdot \mathbf{p} - \mathbf{p} \mathbf{p} : \mathbf{E}^\infty \mathbf{p}) \quad (1)$$

as shown by Bretherton (1962) and Jeffery (1922). Here  $\mathbf{p}$  is the particle orientation.  $\mathbf{R}^\infty$  and  $\mathbf{E}^\infty$  are the vorticity and straining tensor of a linear flow field respectively and are given by

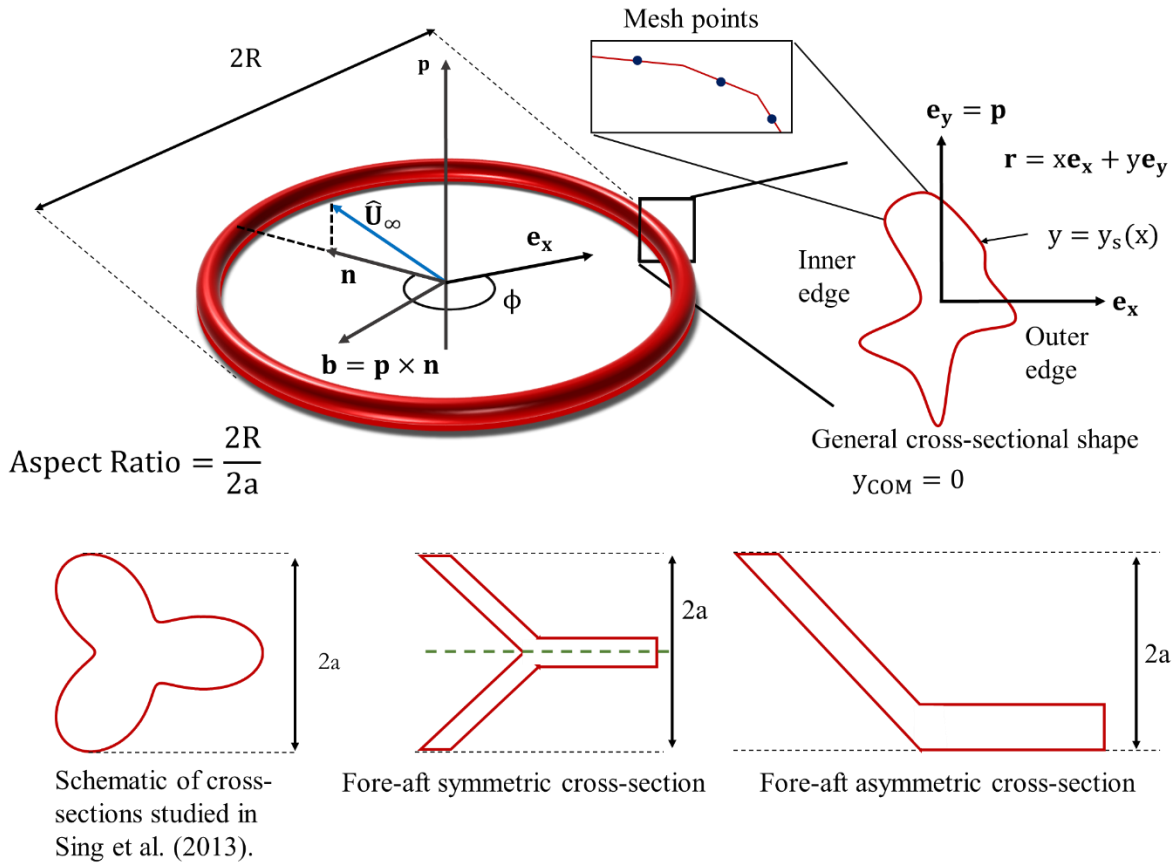
$$\mathbf{R}^\infty = \frac{1}{2}(\nabla \mathbf{u}^\infty - (\nabla \mathbf{u}^\infty)^T), \quad (2 a)$$

$$\mathbf{E}^\infty = \frac{1}{2}(\nabla \mathbf{u}^\infty + (\nabla \mathbf{u}^\infty)^T), \quad (2 b)$$

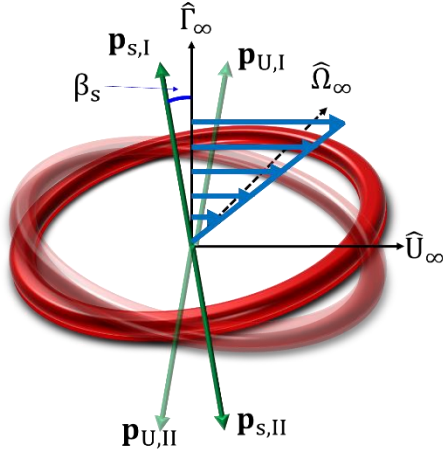
where  $\mathbf{u}^\infty$  is the fluid velocity in the absence of the particle. The migration parameters  $\eta_1$  and  $\eta_2$  determine the drift velocity of the particle relative to the fluid velocity at its centre-of-mass (COM) which takes the form given by

$$\mathbf{U}_p = \mathbf{u}^\infty(r_{\text{COM}}) + \eta_1 \mathbf{E}^\infty \cdot \mathbf{p} + \eta_2 (\mathbf{p} \cdot \mathbf{p} : \mathbf{E}^\infty). \quad (3)$$

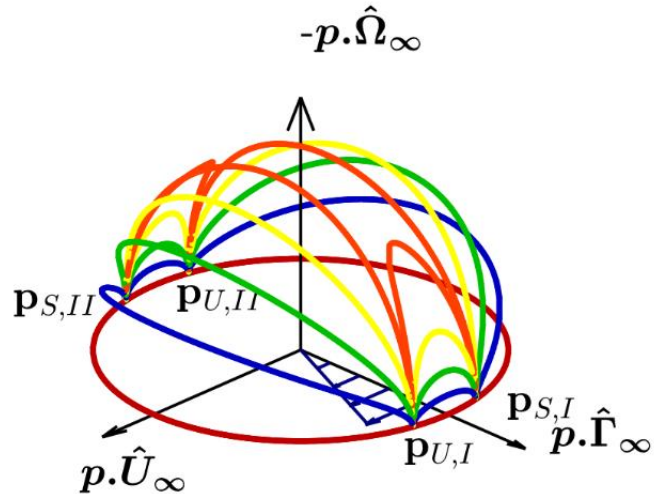
Equation (3) indicates that a particle with mirror or fore-aft symmetry about a plane normal to  $\mathbf{p}$ , as shown in figure 1 (a), will not drift as orientation  $\mathbf{p}$  and  $-\mathbf{p}$  are equivalent. As per equation (3), this is true only when  $\eta_1 = \eta_2 = 0$ . Absence of fore-aft symmetry is the necessary condition for having a finite cross-stream drift. In this section, we obtain the necessary conditions for particle alignment and obtain this orientation in terms of the rotation parameter,  $\lambda$ .



(a)



(b)



(c)

Figure. 1. Ring shaped particles that align in a simple shear flow. (a) Schematic of a ring with a non-circular cross-section that is representative of the geometry studied here. The cross-sections on the left and in the center have mirror or fore-aft symmetry about a plane normal to  $\mathbf{p}$ . An orthogonal coordinate system defined by the axis of symmetry ( $\mathbf{p}$ ), the projection of the flow direction ( $\hat{\mathbf{U}}_\infty$ ) in the plane of the ring ( $\mathbf{n}$ ) and a vector  $\mathbf{b} = \mathbf{p} \times \mathbf{n}$ . The center of this coordinate

system is chosen such that the center of mass of the particle lies at the origin  $\mathbf{r}_{\text{COM}} \cdot \mathbf{p} = 0$ . The azimuthal angle ( $\phi$ ) is defined relative to  $\mathbf{n}$ . The inset also shows the 1-D mesh and a 2-D coordinate system (x,y) with the origin at the COM of the particle.  $\mathbf{e}_x$  is a unit radial vector in the plane perpendicular to  $\mathbf{p}$  while  $\mathbf{e}_y$  is a unit vector along  $\mathbf{p}$ . (b) The stable fixed orientation  $\mathbf{p}_s$  (solid) and the unstable orientation  $\mathbf{p}_u$  (transparent), relative to the flow field. Both  $\mathbf{p}_s$  and  $\mathbf{p}_u$  lie in the flow gradient plane and make an angle of  $\beta_s$  with the gradient direction ( $\hat{\Gamma}_\infty$ ). (c) Orientation trajectories for  $\lambda = -1.1$ . The trajectories move towards the stable nodes and away from the unstable nodes.

We use the orthogonal coordinate system, as shown in figure 1 (b), defined by the flow ( $\hat{\mathbf{U}}_\infty$ ), the gradient ( $\hat{\Gamma}_\infty$ ) and the negative of the vorticity ( $-\hat{\Omega}_\infty$ ) direction of a simple shear flow. Equation (1) can have six nodes for a general axisymmetric shape in a simple shear flow. There are two saddle nodes, independent of geometry, that correspond to rotation of the particle about its axis of symmetry, wherein  $\mathbf{p} \cdot \hat{\Omega}_\infty = \pm 1$ . Four other nodes, two stable ( $\mathbf{p}_s$ ) and two unstable ( $\mathbf{p}_u$ ), can exist in the system for geometries that have  $|\lambda| > 1$ . These nodes are shown in figure 1 (b) for a ring-shaped particle with  $\lambda < -1$ . All four nodes lie in the flow gradient plane and subtend an angle of  $\beta_s = 0.5 \arccos(-1/\lambda)$  with the gradient direction as shown in figure 1 (b). These nodes are mathematically given by  $\mathbf{p} \cdot \hat{\mathbf{U}}_\infty = \pm \sin\left(\frac{-1}{2} \arccos\left(-\frac{1}{\lambda}\right)\right)$ ,  $\mathbf{p} \cdot \hat{\Gamma}_\infty = \pm \cos\left(\frac{1}{2} \arccos\left(-\frac{1}{\lambda}\right)\right)$  and  $\mathbf{p} \cdot \hat{\Omega}_\infty = 0$  with  $\mathbf{p}\mathbf{p} : \mathbf{E}^\infty < 0$  corresponding to the stable nodes, and  $\mathbf{p}\mathbf{p} : \mathbf{E}^\infty > 0$  corresponding to the unstable nodes. When the particle is aligned in the gradient direction ( $\mathbf{p} = \hat{\Gamma}_\infty$ ) the rate of rotation due to the straining component ( $\lambda \mathbf{p} \cdot \mathbf{E}^\infty$ ) is higher than the rate of rotation due to the rotational component ( $\mathbf{p} \cdot \mathbf{R}^\infty$ ) for  $|\lambda| > 1$  as per equation 1. When the plane of the ring lies in the extensional quadrant these two rotation rates can be equal since the magnitude of rotation due to the straining flow is reduced. The plane of the ring being in this orientation corresponds to the stable nodes and is mathematically given by  $\mathbf{p}\mathbf{p} : \mathbf{E}^\infty < 0$ .

Thus,  $|\lambda| > 1$  is the only requirement for an axisymmetric particle to attain an equilibrium orientation in a simple shear flow. However, the dependence of  $\lambda$  on the geometry of the particle is non-trivial (Bretherton 1962 a). Most axisymmetric particles, such as spheres, spheroids, and cylinders, have  $|\lambda| < 1$  and thus constantly tumble in a low Reynolds number simple shear flow

(Bretherton 1962 a). The rod-shaped particle with non-spherical lobes envisioned by Bretherton (1962 a) had  $\lambda > 1$ , but the aspect ratio of the rod was impractically large. A ring-shaped particle with a specified non-circular cross-section was shown to have  $\lambda < -1$  at finite aspect ratios (Singh et al. 2013). The trajectories obtained from equation (1) for  $\lambda < -1$ , as shown in figure 1 (c), have some resemblance to periodic orbits far from the nodes (Jeffery 1922). The four nodes in the system are an additional feature for aligning particles that emerge for shapes with  $|\lambda| > 1$ . The particle orientation diverges away from the unstable nodes ( $\mathbf{p}_U$ ) and converges towards the stable nodes ( $\mathbf{p}_S$ ). The particle approaches a stable node in a time that scales with the inverse of the shear rate for any initial orientation. In the following section, we formulate an approach for obtaining the three dynamical parameters, namely,  $\lambda$ ,  $\eta_1$  and  $\eta_2$ , for any general axisymmetric particle.

### 3. Computational approach

We use the solution to the governing equations of fluid flow around a particle in an unbounded domain along with the appropriate boundary conditions to derive the dynamical parameters  $(\lambda, \eta_1, \eta_2)$  of the particle. The boundary element method provides an elegant way of obtaining the stresses acting on the particle surface in an unbounded domain by reducing the dimensionality of the problem. A two-dimensional integral version of the creeping-flow equation is solved instead of a three-dimensional spatial partial differential equation (Youngren and Acrivos (1974); Kim & Karilla (1991)). The integral representation of the flow around a rigid body used in this study is given by

$$\mathbf{u}(\mathbf{r}) = \mathbf{u}^\infty(\mathbf{r}) + \frac{1}{8\pi\mu} \int \mathbf{J}(\mathbf{r} - \mathbf{r}') \cdot \mathbf{f}(\mathbf{r}') dA', \quad (4 \text{ a})$$

where  $\mathbf{r}$  is the position vector,  $\mathbf{u}$  is the velocity of the fluid at the location  $\mathbf{r}$ ,  $\mathbf{u}^\infty$  is the velocity of the imposed flow field at  $\mathbf{r}$ ,  $\mu$  is the fluid viscosity,  $\mathbf{f}$  is the unknown force per unit area the particle exerts on the fluid and  $\mathbf{J}$  is the Green's function for the creeping flow equations. The Green's function  $\mathbf{J}$  is given by

$$\mathbf{J} = \frac{\mathbf{I}}{r} + \frac{\mathbf{r}\mathbf{r}}{r^3}. \quad (4 \text{ b})$$

The axisymmetry of the particle accompanied by linearity of the governing equations allows a further reduction in dimensionality of the problem if the imposed flow is linear. The linear imposed fluid velocity ( $\mathbf{u}^\infty$ ) can be defined as

$$\mathbf{u}^\infty = \mathbf{u}_0 + \mathbf{r} \cdot (\mathbf{E}^\infty + \mathbf{R}^\infty), \quad (5)$$

where  $\mathbf{u}_0$  is the velocity of the imposed flow at the center of mass of the particle ( $\mathbf{r} = 0$ ).  $\mathbf{E}^\infty$  and  $\mathbf{R}^\infty$  represent the straining and vorticity tensor, respectively, defined in equation 2. The force per unit area ( $\mathbf{f}$ ) at position  $\mathbf{r}$  can depend on  $\mathbf{r}$ ,  $\mathbf{u}_0$ ,  $\mathbf{E}^\infty$ ,  $\mathbf{R}^\infty$  and the boundary conditions of the particle surface. The boundary conditions are given in terms of the linear velocity of the particle at its center of mass ( $\mathbf{U}_p$ ) and the angular velocity ( $\boldsymbol{\omega}_p$ ) of the particle. Solid body translation ( $\mathbf{u}^\infty = \mathbf{u}_0$ ) and rotation ( $\mathbf{u}^\infty = \boldsymbol{\epsilon} : \mathbf{R}^\infty$ ) of the particle and the fluid, where  $\boldsymbol{\epsilon}$  is the permutation tensor, do not lead to any stress on the particle and thus the choice of origin does not affect  $\mathbf{f}$ . The origin is chosen as the center of mass of the particle without loss of generality. The position on the particle surface ( $\mathbf{r} = \mathbf{r}_s$ ) can be decomposed into a component along the axis of symmetry and a component in the plane of the ring, which is given by

$$\mathbf{r} = (\mathbf{r} \cdot \mathbf{p})\mathbf{p} + \mathbf{r} \cdot (\mathbf{I} - \mathbf{p}\mathbf{p}). \quad (6)$$

The azimuthal dependence comes only from the second term in equation (6). The vector  $\mathbf{e}_x$  is defined normal to  $\mathbf{p}$  at each azimuthal location. The projection of  $\mathbf{r}$  along  $\mathbf{e}_x$  is represented as  $\mathbf{r}_x = \mathbf{r} \cdot \mathbf{e}_x \mathbf{e}_x = \mathbf{r} \cdot (\mathbf{I} - \mathbf{p}\mathbf{p})$ . Using these observations and the constraint that the force per unit area ( $\mathbf{f}$ ) must be a real vector, one can deduce that  $\mathbf{f}$  must be linear in the relative translational velocity  $\mathbf{U} = \mathbf{U}_p - \mathbf{u}^\infty(\mathbf{r}_{COM})$  of the particle and the fluid, the relative rotation rate  $\boldsymbol{\omega} = \boldsymbol{\omega}_p - \boldsymbol{\epsilon} : \mathbf{R}^\infty$  of the particle and fluid and the rate of strain  $\mathbf{E}^\infty$  of the fluid. The azimuthal variation of force per unit area ( $\mathbf{f}$ ) is thus given by

$$\begin{aligned} \mathbf{f} = & C_1 \mathbf{U} + C_2 \mathbf{p} \mathbf{p} \cdot \mathbf{U} + C_3 \mathbf{r}_x \mathbf{r}_x \cdot \mathbf{U} + C_4 \mathbf{r}_x \mathbf{p} \cdot \mathbf{U} + C_5 \mathbf{p} \mathbf{r}_x \cdot \mathbf{U} + C_6 (\mathbf{r}_x \times \mathbf{p})(\mathbf{r}_x \times \mathbf{p}) \cdot \mathbf{U} + C_7 \boldsymbol{\omega} \times \mathbf{p} + \\ & C_8 \boldsymbol{\omega} \times \mathbf{r}_x + C_9 \mathbf{r}_x \times \mathbf{p} \mathbf{r}_x \cdot \boldsymbol{\omega} + C_{10} \mathbf{r}_x \times \mathbf{p} \mathbf{p} \cdot \boldsymbol{\omega} + (C_{11} (\boldsymbol{\omega} \times \mathbf{p}) + C_{12} (\boldsymbol{\omega} \times \mathbf{r}_x)) \times (\mathbf{r}_x \times \mathbf{p}) + C_{13} (\boldsymbol{\omega} \times \\ & \mathbf{p}) \cdot \mathbf{p} \mathbf{p} + C_{14} (\boldsymbol{\omega} \times \mathbf{p}) \cdot \mathbf{r}_x \mathbf{p} + C_{15} (\boldsymbol{\omega} \times \mathbf{p}) \cdot \mathbf{p} \mathbf{r}_x + C_{16} (\boldsymbol{\omega} \times \mathbf{p}) \cdot \mathbf{r}_x \mathbf{r}_x + C_{17} \mathbf{p} \mathbf{p} \mathbf{p} : \mathbf{E}^\infty + \\ & C_{18} \mathbf{p} \mathbf{r}_x \mathbf{p} : \mathbf{E}^\infty + C_{19} \mathbf{p} \mathbf{r}_x \mathbf{r}_x : \mathbf{E}^\infty + C_{20} \mathbf{p} \cdot \mathbf{E}^\infty + C_{21} \mathbf{r}_x \mathbf{p} \mathbf{p} : \mathbf{E}^\infty + C_{22} \mathbf{r}_x \mathbf{r}_x \mathbf{p} : \mathbf{E}^\infty + C_{23} \mathbf{r}_x \mathbf{r}_x \mathbf{r}_x : \mathbf{E}^\infty + \end{aligned}$$

$$C_{24} \mathbf{r}_x \cdot \mathbf{E}^\infty + C_{25} \mathbf{p}(\mathbf{r}_x \times \mathbf{p}) : \mathbf{E}^\infty (\mathbf{r}_x \times \mathbf{p}) + C_{26} \mathbf{r}_x(\mathbf{r}_x \times \mathbf{p}) : \mathbf{E}^\infty (\mathbf{r}_x \times \mathbf{p}) + C_{27} (\mathbf{r}_x \times \mathbf{p})(\mathbf{r}_x \times \mathbf{p}) : \mathbf{E}^\infty \mathbf{p} + C_{28} (\mathbf{r}_x \times \mathbf{p})(\mathbf{r}_x \times \mathbf{p}) : \mathbf{E}^\infty \mathbf{r}_x, \quad (7)$$

where  $C_1, C_2 \dots, C_{28}$  are independent of the azimuthal position and thus only depend on the cross-sectional shape of the axisymmetric body and the position on the cross-sectional contour. The reference for the azimuthal angle ( $\phi$ ) can be chosen relative to the line of intersection of a plane normal to  $\mathbf{p}$  and the plane of the imposed linear flow. This line of intersection is along  $\mathbf{n}$  as shown in figure 1 (a) for a simple shear flow. Equation (7), which is applicable to a general linear flow field, can be used to obtain the variation of  $\mathbf{f}$  with  $\phi$  in the case of a simple shear flow. Using equation (7), equation (4 a) can be integrated along  $\phi$ , using elliptic integrals (Appendix), thus reducing the dimensionality of the problem. A 1-D curved mesh, as shown in figure 1 (a), is enough to obtain the force per unit area acting on the surface, instead of a 2-D surface mesh traditionally employed in a BEM formulation. For the purpose of obtaining  $\lambda, \eta_1, \eta_2$ , it is sufficient to solve the governing equations when the imposed flow is a simple shear flow and when  $\mathbf{p}$  lies in the flow-gradient plane where  $\mathbf{p} \neq \hat{\mathbf{U}}^\infty$  and  $\mathbf{p} \neq \hat{\mathbf{F}}^\infty$ . The reference for the azimuthal angle is chosen along the projection of the flow direction in the plane of the ring ( $\mathbf{n}$ ) as shown in figure 1 (a). Along with  $\mathbf{n}$ , the orientation of the particle ( $\mathbf{p}$ ) and a vector  $\mathbf{b} = \mathbf{p} \times \mathbf{n}$  define a coordinate system relative to the particle. In this case, the dependence of  $\mathbf{f}$  on the azimuthal angle ( $\phi$ ) given by

$$\mathbf{f} \cdot \mathbf{n} = f_0 + f_1 \cos(\phi) + f_2 \cos(2\phi) + f_3 \cos(3\phi), \quad (8 \text{ a})$$

$$\mathbf{f} \cdot \mathbf{p} = f_4 + f_5 \cos(\phi) + f_6 \cos(2\phi), \quad (8 \text{ b})$$

$$\mathbf{f} \cdot \mathbf{b} = f_7 \sin(\phi) + f_8 \sin(2\phi) + f_9 \sin(3\phi), \quad (8 \text{ c})$$

where the coefficients,  $[f_0, f_1, \dots, f_9]$ , depend on the contour of the ring cross-section, size of the ring ( $R$ ) and the position on the ring cross-sectional contour. The integral in equation (4 a) in the azimuthal direction can be performed analytically using  $\mathbf{f}$  as given in equation (8). The remainder of the integral is evaluated numerically by discretizing the cross-sectional contour into a mesh of  $N$  elements as shown in figure 1 (a). The left-hand side of equation (4 a), which is the fluid velocity on the ring surface, is known in terms of the linear and angular velocity of the particle at each of

the N mesh points. Thus, we obtain 3 equations at each mesh point on the cross-section for a given  $\phi$  giving a total of 3N equations for each value of  $\phi$ . We can obtain more equations by choosing a different value of  $\phi$ . For this study, we need to evaluate equation (4 a) at four different values of  $\phi$  so we have 10N equations to obtain  $[f_0, f_1, \dots, f_9]$  at each of the N mesh points. If the linear and angular velocities of the particles are also unknown, then an appropriate condition specifying the total force and torque on the body can be applied to obtain 6 additional equations. This procedure along with the detailed expression can be found in the appendix. The cross-sectional contour is given by  $y_s = y(x)$ , where x is the normal distance from axis of symmetry, y is the distance along the axis of symmetry and the subscript s represents the respective values on the cross-sectional boundary. In this analysis, the reference for the position along the axis of symmetry is chosen such that the plane of the ring,  $y = 0$ , passes through the centre-of-mass of the particle. This choice does not affect the value for the cross-stream drift velocity ( $U_d$ ). The following problems are solved using the boundary element method.

### *Mobility problem*

The particle velocities ( $\mathbf{U}_p$  and  $\boldsymbol{\omega}_p$ ), and thus the dynamical parameters ( $\lambda$ ,  $\eta_1$  and  $\eta_2$ ), are obtained by applying the force- and torque-free conditions about the COM of the particle (equations (9) and (10)), when the particle is oriented in the flow gradient plane such that  $\mathbf{p} \neq \hat{\mathbf{U}}^\infty$  and  $\mathbf{p} \neq \hat{\mathbf{r}}^\infty$ .

$$\int \mathbf{f}(\mathbf{r}') dA' = \mathbf{0}, \quad (9)$$

$$\int \mathbf{r}' \times \mathbf{f}(\mathbf{r}') dA' = \mathbf{0}, \quad (10)$$

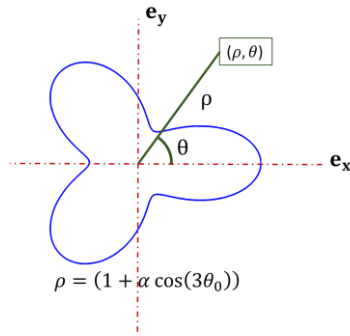
### *Resistivity problem for alignment mechanism*

The direction of the torque exerted by the fluid on the particle when it is kept stationary ( $\mathbf{U}_p = 0, \boldsymbol{\omega}_p = 0$ ) with  $\mathbf{p} = \hat{\mathbf{r}}^\infty$  distinguishes between tumbling and aligning behavior. If the fluid applies a torque against the vorticity direction, then the particle is trying to rotate in the counter-vorticity direction towards the stable node as shown in figure 1 (b). A fluid torque along the

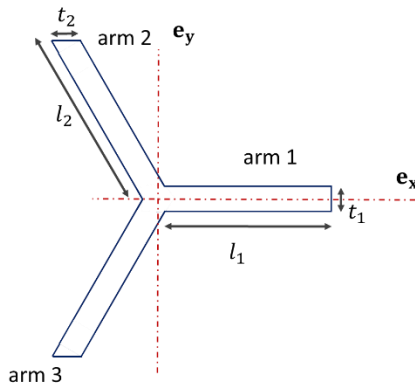
vorticity direction implies a tumbling behavior. This resistivity problem is used to understand the alignment mechanism through visualization of stresses on the particle surface. It also gives insight into the cross-sectional geometry necessary for alignment.

### *Resistivity problem for drifting mechanism*

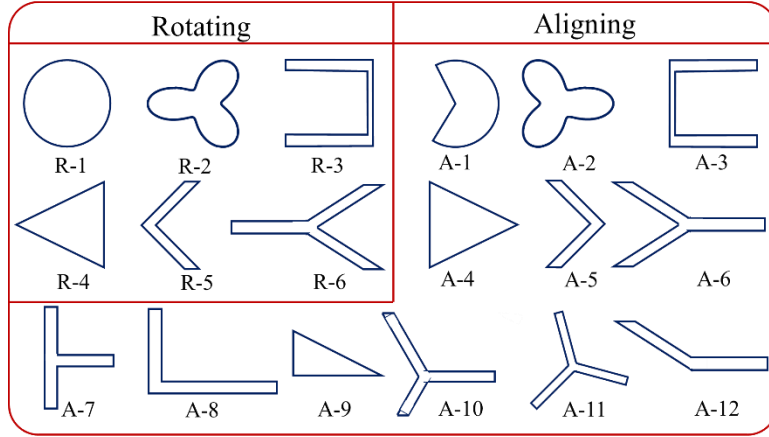
The scaling for cross-stream drift of the particle ( $U_d$ ) can be obtained when the particle is oriented along the stable orientation ( $\mathbf{p} = \mathbf{p}_s$ ) and held stationary ( $\mathbf{U}_p = 0, \boldsymbol{\omega}_p = 0$ ). At this orientation, the force acting on the particle drives its drifting motion. This problem will only be solved as a thought experiment to predict the scaling for the drift velocity, which can be obtained by equating this force to the force required for translating the particle in a quiescent fluid.



(a)



(b)



(c)

Figure 2. Ring cross-sectional shapes studied here. (a) Shape given by  $\rho = 1 + \alpha \cos(3\theta)$  that was shown to lead to flow aligning rings by Singh et al. (2013). (b) Y-shaped fore-aft symmetric shape inspired by figure 2 (a). (c) Some of the ring cross-sections studied using BEM calculations. Rings with cross sections R-i, for  $i = 1, 2, \dots, 6$ , rotate in a simple shear flow, while rings with cross-sections A-i, for  $i = 1, 2, \dots, 12$ , align in a simple shear flow at finite aspect ratios.

In this study, we try to understand the mechanism leading to alignment of particles at much lower aspect ratios than the previously reported minimum of 30 (Singh et al. 2013). A family of 2D contours is chosen based on previous insight into aligning shapes. The family of shapes given by  $\rho = (1 + \alpha \cos(3\theta))$  was shown to achieve permanent alignment at finite aspect ratios (Singh et al. 2013). Here  $\rho$  and  $\theta$  represent the polar coordinates in the plane of the cross-section (x-y plane) and  $\theta$  is measured relative to  $\mathbf{e}_x$ , as shown in figure 2 (a).  $\alpha$  changes the shape of the cross-section. Based on this insight a 3-lobed shape shown in figure 2 (b) is used for studying fore-aft symmetric shapes. This fore-aft symmetric shape can be described by 5 parameters: “ $l_1$ ”, length of arm 1; “ $t_1$ ”, thickness of arm 1; “ $l_2$ ”, length of arm 2 and arm 3; “ $t_2$ ”, thickness of arm 2 and arm 3; and  $\psi$ , angle made by arm 2 and arm 3 with arm 1. Although this family of “Y-shaped” cross-sections does not cover all shapes, it gives insight into particle geometries that will lead to alignment. The choice of a Y-shaped cross-section will be motivated in the next section, where results obtained from BEM are used to describe the mechanism of alignment. Cross-sections shown in figure 2 (c) were also studied, but were found to align at higher aspect ratios. Cross-

sections A-8 to A-12 lack fore-aft symmetry and thus can possess cross-stream drift. We shall also discuss the mechanism leading to cross-stream drift and show ways to control the magnitude of drift by proper choice of cross-sectional shape. All cross-sections shown in the remainder of the paper are in figure 1 (a), where the left side of the cross-section is the inner edge closer to the ring center while the right side is the outer edge of the ring.

We also solved for flow past a two-dimensional obstacle with the same shape as the ring cross-section in a two-dimensional domain using a finite element method (FEM) solver in COMSOL. This flow field qualitatively resembles the flow field around a slender ring in the cross-sectional plane near the surface of the particle. This gives a qualitative visualization of fluid velocity and stresses near the particle surface with lower computational effort. This problem also removes the effect of the size (aspect ratio) of the particle, and isolates the effect of the cross-sectional shape on the stresses acting on the particle surface. The domain size  $L \gg a$ , ensures that the fluid velocity near the particle is not influenced by the shape of the box. The fluid velocity varies logarithmically with radial distance,  $\rho$ , for  $a \ll \rho \ll L$ , similar to the variation for  $a \ll \rho \ll R$  near a ring with high aspect ratio ( $A \gg 1$ ). The no-slip boundary condition was applied at the particle surface, while the velocity at the domain boundary far from the particle was a simple shear flow.

#### 4. Results and discussion

In this section, we present the results of BEM calculations for the mobility and resistivity problems described earlier for cross-sectional shapes shown in figure 2 (c). We also look at the flow field around the cross-section via the solution of the 2-D Stokes flow problem by FEM. For characterizing the shape, a critical aspect ratio ( $A^*$ ) was defined as the minimum aspect ratio at which a particle aligns. The objective, in addition to understanding the alignment mechanism, is to obtain shapes that align at low values of  $A^*$ . This is important from the standpoint of fabrication as a higher aspect-ratio ring will be susceptible to damage thereby losing the aligning characteristics. For fore-aft asymmetric cross-sections, the focus is to understand the mechanism of cross-stream drift ( $U_d = |(\mathbf{U}_p - \mathbf{u}^\infty(r_{COM})) \cdot \hat{\mathbf{r}}_\infty|$ ) and thus control its magnitude. It will be

shown that the cross-stream drift also depends strongly on the stable orientation of these particle, which in turn depends on aspects of the particle geometry that influence rotation.

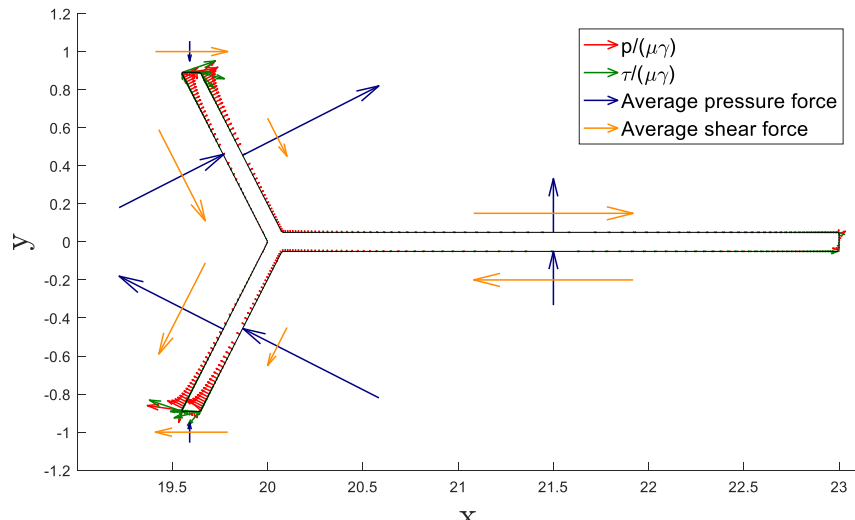
#### *4.1 Fore-aft symmetric that align but do not drift*

To gain insight into the mechanism that prevents tumbling, the resistivity problem was solved for fore-aft symmetric cross-sections shown in figure 2 (b) using BEM for  $\mathbf{p} = \hat{\Gamma}_\infty$ . The geometric parameters, as shown in figure 2 (b) were chosen as  $t_1/l_2 = 0.1$ ,  $t_2/l_2 = 0.1$ ,  $l_1/l_2 = 3$  and  $\psi = 0.65\pi$ . These parameters were chosen because the value of  $l_1/l_2$  and  $\psi$  lie near their optima for these arm thicknesses. The fluid exerts a force per unit area of  $-\mathbf{f}$  on the particle surface. The force per unit area,  $-f_0$ , in the flow direction contributes to the torque in the vorticity direction, while  $-f_5$  is the force per unit area along the axis of symmetry ( $\mathbf{p} = \hat{\Gamma}_\infty$ ) contributing to the torque in vorticity direction. The torque exerted by the fluid forces in the vorticity direction ( $\hat{\Omega}_\infty$ ),  $G$ , is given by

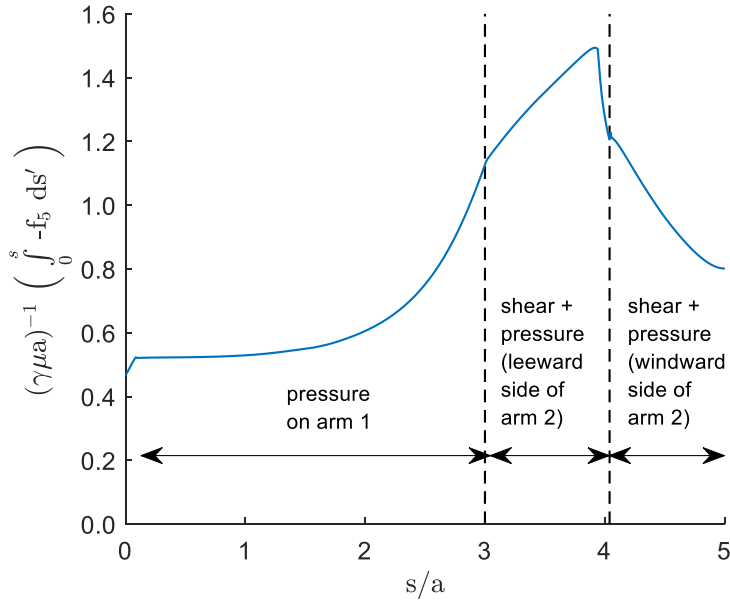
$$G = \int_{y=y_s} ds' (-2\pi y f_0 + \pi x f_5), \quad (11)$$

where  $ds'$  represents the elemental length along the tangent to the cross-sectional contour and  $s'$  represents the position along the contour such that  $s = 0$  corresponds to the point on the outer edge for which  $y_s = 0$ . A negative value of this torque, which is the torque opposite to the vorticity direction, implies alignment. The moment arm for forces along  $\mathbf{e}_y$ , i.e.,  $x$ , scales with the particle size ( $x \sim R$ ), while the moment arm for the forces acting along  $\mathbf{e}_x$ , i.e.,  $y$ , scales with the cross-sectional dimension ( $y \sim a$ ). Thus, at a sufficiently high aspect ratio,  $A$ , the torque due to the force along  $\mathbf{e}_y$  ( $-f_5$ ) alone is important. Figure 3 (a) shows the part of the force per unit area ( $\mathbf{f}'$ ) acting on the cross-section that contributes to the torque, at  $\phi = 0$ , such that  $\mathbf{f}' \cdot \mathbf{e}_x = -f_0$  and  $\mathbf{f}' \cdot \mathbf{e}_y = -f_5$ .  $\mathbf{f}'$  is decomposed into a normal force which is due to pressure ( $p$ ) and a tangential force which is due to the shear or viscous stress ( $\tau$ ). Figure 3 (a) shows the variation of pressure along with the total pressure force and total viscous force per unit circumference on each linear element of the cross-section ( $\int ds' p / (\mu \gamma)$  and  $\int ds' \tau / (\mu \gamma)$  respectively, where  $\gamma$  is the shear rate of the simple shear flow and  $\mu$  is the viscosity of the fluid). This allows for the visualization of forces that lead to a force along the positive  $\mathbf{e}_y$ . From figure 3 (a), the pressure on average generates a force in the

positive  $\hat{\Gamma}_\infty$ , which tries to rotate the particle towards the stable orientation. On the other hand, the viscous stress generates a force along negative  $\hat{\Gamma}_\infty$  which tries to tumble the particle in the vorticity direction. The viscous stress is localized near the stagnation points, which are at the tip of each arm, and thus acts on a smaller area. The pressure decays slowly along the arms due to small velocity gradients (except for a small region near the stagnation point) and so it acts on a larger area. The obtuse angle of arm 2 with the flow direction ensures the pressure generates a force in the positive  $\hat{\Gamma}_\infty$  direction. Pressure on arm 1 also generates a force in the positive  $\hat{\Gamma}_\infty$  direction. Figure 3 (b) shows the variation of  $\int_0^s ds'(-f_5)$  along the cross-section from the tip of arm 1 ( $s=0$ ) to the point of intersection of arms 2 and 3. The pressure on each arm makes a positive contribution to  $(-f_5)$ , while the viscous stress mainly near the tip of arm 2 and most of arm 3 makes a negative contribution to  $(-f_5)$ . While the viscous stresses try to tumble the particle irrespective of the cross-sectional shape, the pressure force for certain cross-sections leads to alignment.



(a)



(b)

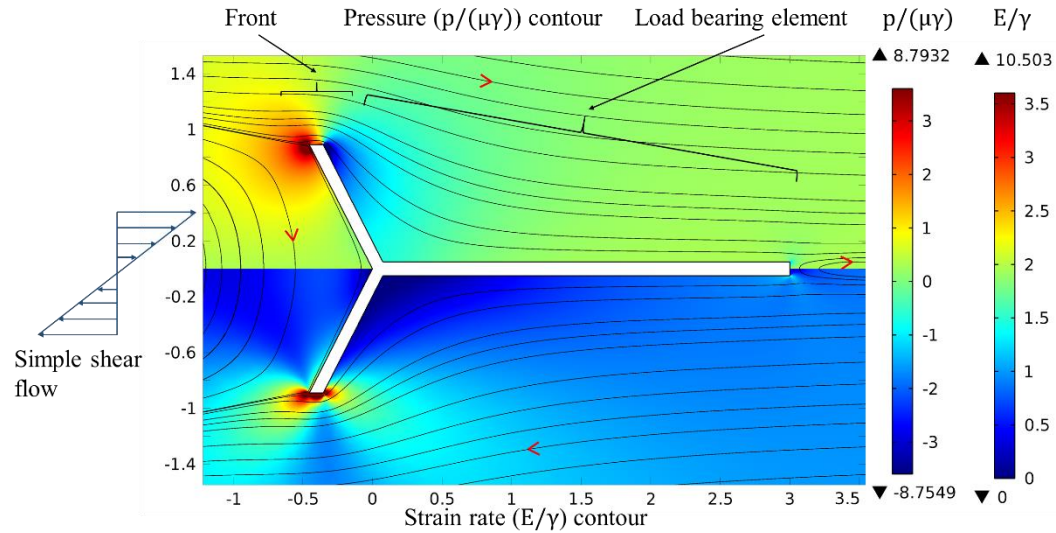
Figure 3. Stresses on ring cross-section contributing to particle rotation rate. (a) Plotting forces on the cross-section such that  $\mathbf{f}' \cdot \mathbf{e}_x = -f_0$  and  $\mathbf{f}' \cdot \mathbf{e}_y = -f_5$  for a particle with aspect ratio of 25.8. These forces are decomposed into the pressure ( $\rightarrow$ ) and the viscous stress ( $\rightarrow$ ). The pressure ( $\rightarrow$ ) and viscous stress ( $\rightarrow$ ) variation along the cross-section; total pressure force ( $\int_{s_1}^{s_2} ds' p / (\mu\gamma)$ ) ( $\rightarrow$ ) and total viscous force ( $\int_{s_1}^{s_2} ds' \tau / (\mu\gamma)$ ) ( $\rightarrow$ ) per unit circumference on each face of each arm is plotted. (b) Cumulative value of  $-f_5$  along the cross-section from tip of arm 1 ( $s=0$ ) to a point  $s$  along arm 1. Here,  $\gamma$  is the shear rate of the simple shear flow and  $\mu$  is the viscosity of the fluid.

Figure 4 (a) shows the pressure, strain rate and streamlines obtained from the solution of the 2-D Stokes flow problem near a Y-shaped cross-section. The strain rate is defined as  $E = \left( 0.5(\nabla \mathbf{u} + (\nabla \mathbf{u})^T) : (\nabla \mathbf{u} + (\nabla \mathbf{u})^T) \right)^{0.5}$ , and gives a measure of the viscous stress in the fluid. From symmetry of the particle and the simple shear flow, it can be shown that  $\mathbf{f} \cdot \hat{\mathbf{U}}_\infty(x, -y) = -\mathbf{f} \cdot \hat{\mathbf{U}}_\infty(x, y)$  and  $\mathbf{f} \cdot \hat{\mathbf{F}}_\infty(x, -y) = \mathbf{f} \cdot \hat{\mathbf{F}}_\infty(x, y)$ ,  $\mathbf{f}$  being the force per unit area acting on the particle surface. The strain rate, as shown in the bottom half of figure 4 (a), is localized near the end of each arm and thus, acts on a small area generating a small force. The low-pressure, relative to the

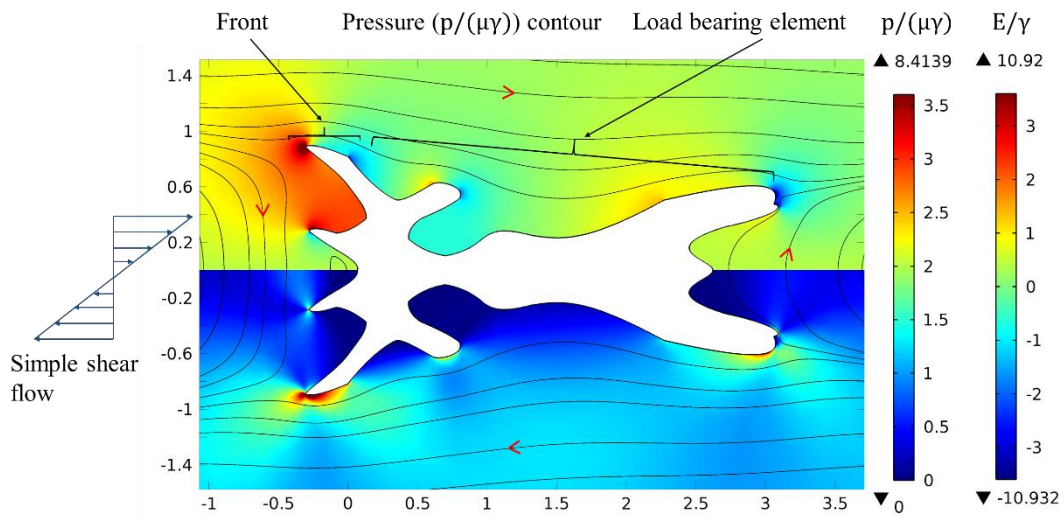
pressure far away from the particle, on the right of arm 2 and top of arm 1 is created by the presence of the stagnation point on the tip of arm 2. This low-pressure due to the obtuse angle made by arm 2 about the flow direction and the presence of arm 1 is utilized to generate a force on the particle along  $\mathbf{e}_y$ . The obtuse angle made by arm 2 ensures that the pressure force generates a positive force in the y-direction. It can be easily envisioned that pressure generates a force in the negative y-direction if arm 2 makes an acute angle with the flow direction. The presence of arm 1 helps to further utilize this low pressure generated on the leeward (left) side of arm 2 by providing more surface area on which the low pressure acts. It should be noted that a cross-section which is the mirror image of this Y-shape (R-6 in figure 2 (c)) would not be able to align, because the sign of the forces would reverse. The pressure on top of arm 1 would generate a force in the negative y-direction while the acute angle made by arm 2 with the flow direction would also make the pressure on it generate a force in the negative y-direction.

The above information can be used to understand the requirements on the shape of the cross-section of aligning rings. The cross-section should be asymmetric about any plane normal to  $\mathbf{e}_x$  such that it has a blunt inner edge and a sharp outer edge. This generates a load-bearing element (arms 1,2 and 3) that thins out as one approaches the outer edge utilizing the pressure to generate a counter rotating torque. Figure 4 (b) and (c) show the contours for pressure and strain rate ( $E$ ), along with the streamlines obtained from the solution of the 2-D Stokes problem using FEM. As illustrated by these figures, the viscous stress mainly acts in small regions around the stagnation points on the tips of the arms, generating a smaller force in comparison to the pressure force that acts on a larger projected area of the load-bearing element. The viscous force on the front will be smaller if the flow is streamlined, and thus shapes with branched load bearing elements, as shown in figure 4 (b), will tend to perform poorly. Branching not only increases the area available for the viscous stress to act, but also increases the moment arm of forces in the x-direction, thus increasing  $A^*$ . An unbranched load bearing element, shown in figure 4 (c), thus is ideal for alignment at low  $A^*$ . A Y-shaped cross-section, being the simplest shape with linear arms, was thus chosen for further analysis. A streamlined shape, as shown in figure 4 (c), ensures that the viscous stress is localized near the tip of the inner edge of the cross-section and thus acts on a small area. Although optimization of the cross-section to minimize  $A^*$  is beyond the scope of this study, our results can be the starting point for this search.

We can use these insights to rationalize the aligning or rotating nature of rings with cross-sections shown in figure 2 (c). A circular cross-section does not align due to its symmetry. A pie shaped cross-section (A-1) breaks the symmetry about a plane normal to  $\mathbf{e}_x$ , thus allowing pressure to generate a counter rotating torque. A V-shaped particle (A-5) aligns at a higher  $A^*$  as the length of the load bearing element is smaller than for a Y-shaped particle. Thus, we have seen that the 2D Stokes flow problem solved using FEM can give the qualitative nature of the forces acting on rings with the given cross-section.



(a)



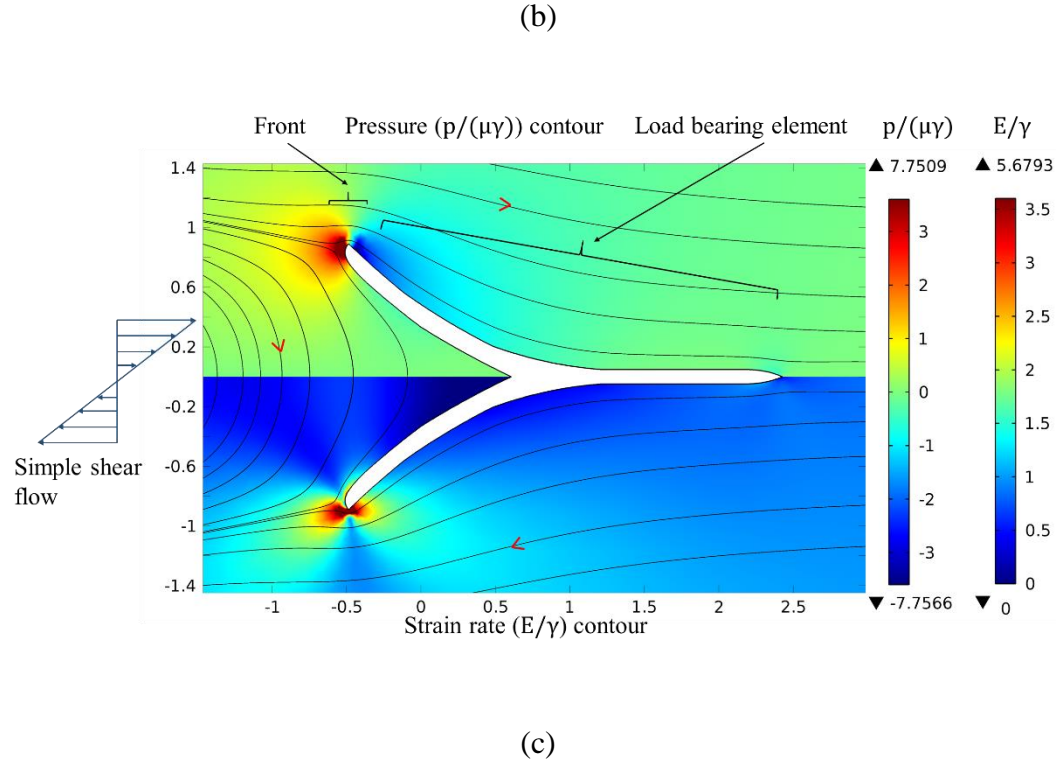


Figure 4. Pressure, strain rate contours and streamlines for different cross-sections: (a) Y-shaped cross-section, (b) cross-section with a branched load-bearing element, and (c) cross-section with streamlined load bearing element. The top half shows the pressure ( $p/(\gamma\mu)$ ) contour, while the bottom half shows the strain rate ( $E/\gamma$ ) contour.

The solution to the mobility problem gives the dynamical parameters of the particle and thus  $A^*$ . The dynamic parameters  $\eta_1$  and  $\eta_2$  are identically equal to zero for fore-aft symmetric shapes, as orientations  $\mathbf{p}$  and  $-\mathbf{p}$  are equivalent. The rotation parameter,  $\lambda$ , obtained from BEM simulation of this mobility problem for  $\mathbf{p}$  lying in the flow-gradient plan is given by

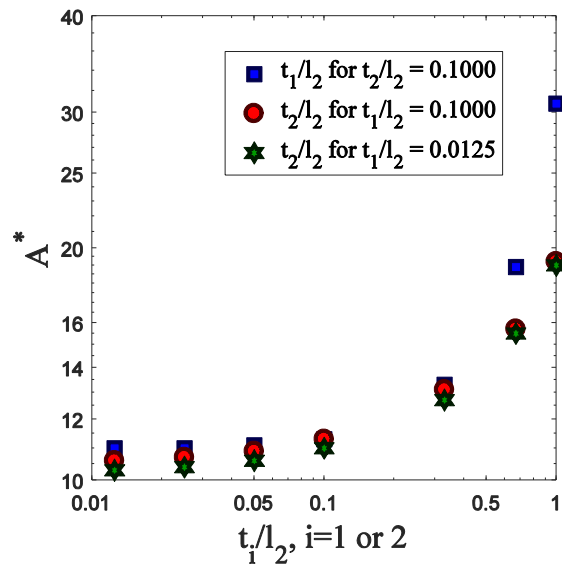
$$\lambda = \frac{\gamma^{-1}(\omega_p) \cdot \hat{\Omega}^\infty - 0.5}{(\mathbf{p} \cdot \hat{\mathbf{r}}^\infty)^2 - 0.5}, \quad (12)$$

where  $\gamma$  is the shear rate of the simple shear flow. Figure 5 (a) presents predictions for Y-shaped particles with  $\psi = \pi/2$ , also referred to as T-shaped particles. Such shapes are of practical interest due to ease of fabrication using multi-step lithography (Foulds and Parameswaram (2006)). The

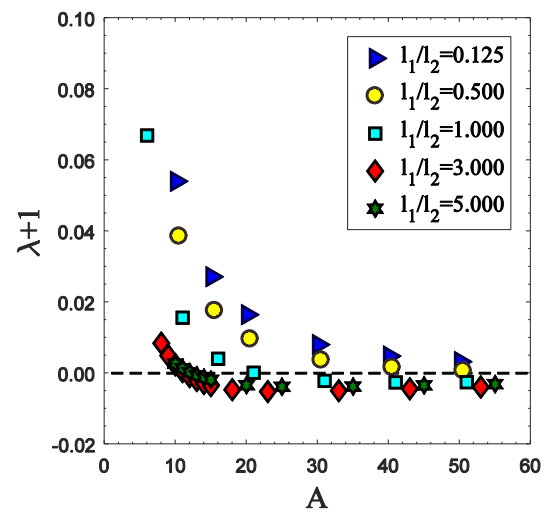
critical aspect ratio decreases with decreasing arm thickness ( $t_1/l_2$  and  $t_2/l_2$ ) as seen in figure 5 (a) for a fixed value of  $l_1/l_2 = 3$ . This is mainly due to reduction in the viscous stress acting on the particle, confirming that viscous stress increases  $A^*$ . Thus, arms of zero thickness can be assumed to be better for all values of  $l_1/l_2$  and  $\psi$ . Figure 5 (b), shows the variation of the rotation parameter,  $\lambda$ , with aspect ratio,  $A$ . ( $\lambda + 1$ ) rapidly decreases with increasing  $A$ , attains a minimum value that is less than zero and then slowly returns to zero. When  $(\lambda + 1) \geq 0$ , the time period of rotation, which equals  $4\pi/(\gamma\sqrt{1 - \lambda^2})$ , increases as  $\lambda$  approaches -1. This period becomes infinite at  $\lambda = -1$  and the particle aligns for the first time. Thus even though  $A < A^*$ , due to the rapid increase in time period, the particle will remain aligned for long time durations. Once  $\lambda$  crosses -1, the particle attains an equilibrium orientation. As shown in section 2, the angle made by  $\mathbf{p}$  with gradient direction is given by  $0.5 \arccos(-1/\lambda)$ . This angle attains a maximum value when  $\lambda + 1$  attains a minimum value. However, since the change in  $\lambda$  is small after attaining this minimum value the angle also changes slowly. Figure 5 (c) shows the variation of  $A^*$  with  $\psi$  and  $l_1/l_2$  for  $t_1/l_2 = t_2/l_2 = 0.0125$ , which approximates the zero-thickness limit. The contour is obtained by linear interpolation between data points using a Delaunay triangulation. The optimal value is found to be  $A^* \approx 9$  for  $\psi = 0.65\pi$  and  $l_1/l_2 = 2$ . There is a shallow valley near this optimum in which  $A^*$  varies slowly. Thus, any imperfections in particle fabrication will not change the aligning behavior of the particle to a great extent. This also means that the particle dynamics is not strongly affected by small changes at the small length scale, as long as the general shape necessary for alignment is maintained.

Rings with Y-shaped cross-sections have suppressed rotation at all aspect ratios in comparison to rings with circular cross-sections as evident in figure 5 (d). This primarily comes due to the strong counter-rotating pressure force, absent in rings with a circular cross-section. It should be noted that rings with cross-sectional shapes studied in Singh et al. (2013), as shown in figure 2 (a), do not have suppressed rotation at small aspect ratios. This is primarily because the magnitude of the pressure force acting at the stagnation point is lower in comparison to a Y-shaped cross-section with thin arms. The rings with Y-shaped cross-sections of aspect ratio,  $A$ , somewhat smaller than  $A^*$  could have a similar practical utility as aligning rings because of the large increase in the time period of rotation of the ring at all aspect ratios. Apart from alignment, the particle rotation rate can be significantly increased, as shown in figure 5 (d), by using a shape that is a

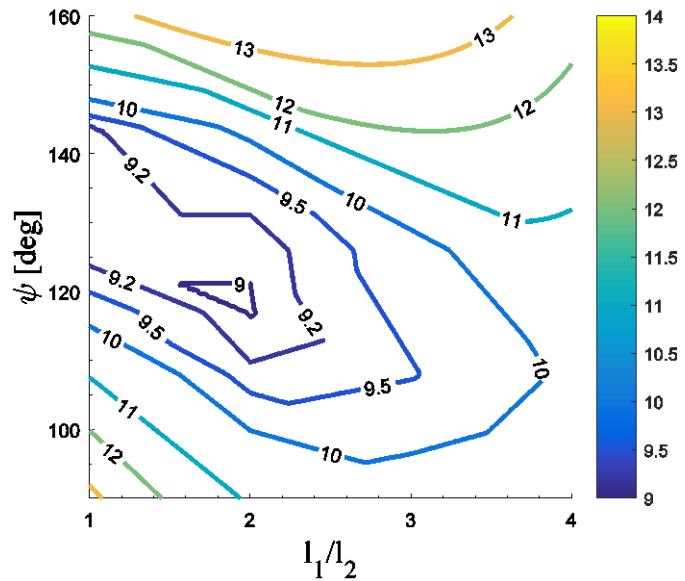
mirror image of the Y-shaped cross-section (R-6). This is because the pressure that was originally inducing a counter-rotating torque is now generating a torque in the vorticity direction leading to enhanced tumbling. Enhanced rotation of particles could increase the viscosity of the suspension for the same volume fraction of the particles. At high enough particle concentrations, enhanced rotation could lead to more frequent contacts between particles leading to a larger increase in stress in the suspension. High aspect ratio conducting particles with enhanced rotation could be embedded in composites during curing to increase the thermal conductivity of the final material.



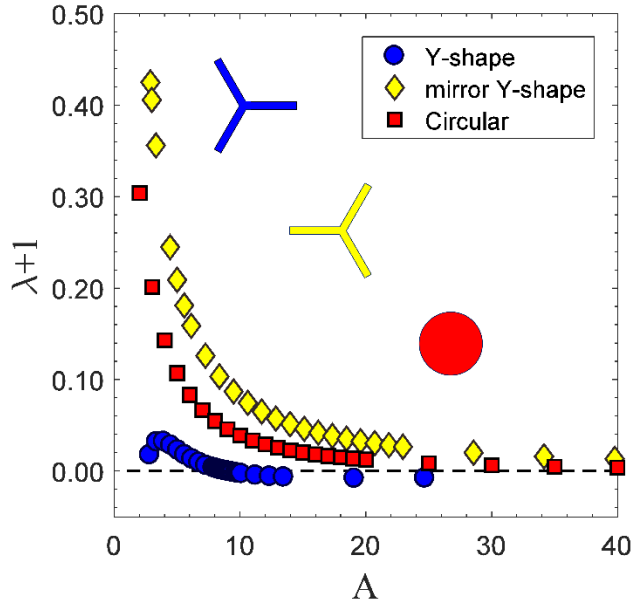
(a)



(b)



(c)



(d)

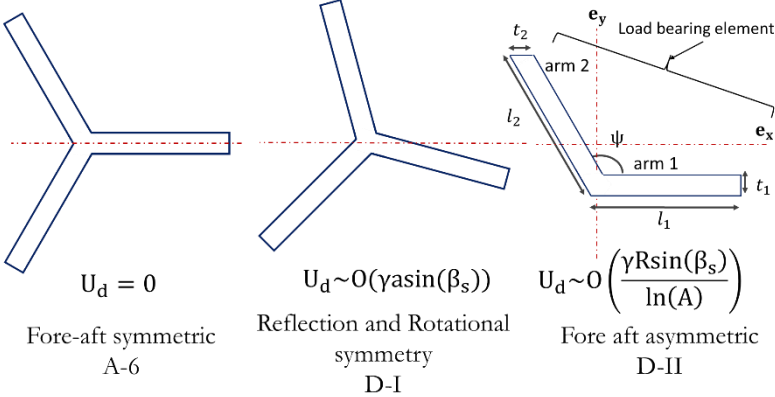
Figure 5.  $\lambda$  and  $A^*$  variation for different shapes. (a) Variation of  $A^*$  with thickness of one arm at a time for a Y-shaped cross-section shown in figure 2 (b).  $A^*$  variation with  $t_1/l_2$  for  $t_2/l_2 = 0.1$  (■); with  $t_2/l_2$  for  $t_1/l_2 = 0.1$  (●); and with  $t_2/l_2$  for  $t_1/l_2 = 0.0125$  (★).  $l_1/l_2 = 3$  and  $\psi = 0.5\pi$  for all three curves. (b)  $\lambda+1$  variation with aspect ratio of the particle ( $A$ ) for a Y-shaped cross-section with  $\psi = 0.5 \pi$  and  $t_1/l_1 = t_2/l_1 = 0.1$ . (c) Contour map of  $A^*$  with  $\psi$  and  $l_1/l_2$  for a Y-shaped cross-section with  $t_1/l_2 = t_2/l_2 = 0.0125$  (d) Variation of  $\lambda + 1$  with  $A$  for a Y-shaped cross-section ( $\psi = 0.65\pi, l_1 = 2l_2, t_1 = t_2 = 0.0125l_2$ ), mirror image of the Y-shaped cross-section (figure 3 (c) R-6) with ( $\psi = 0.65\pi, l_1 = 2l_2, t_1 = t_2 = 0.0125l_2$ ) and a circular cross-section (figure 3 (c) R-1).

#### 4.2 Fore-aft asymmetric particles that align and drift

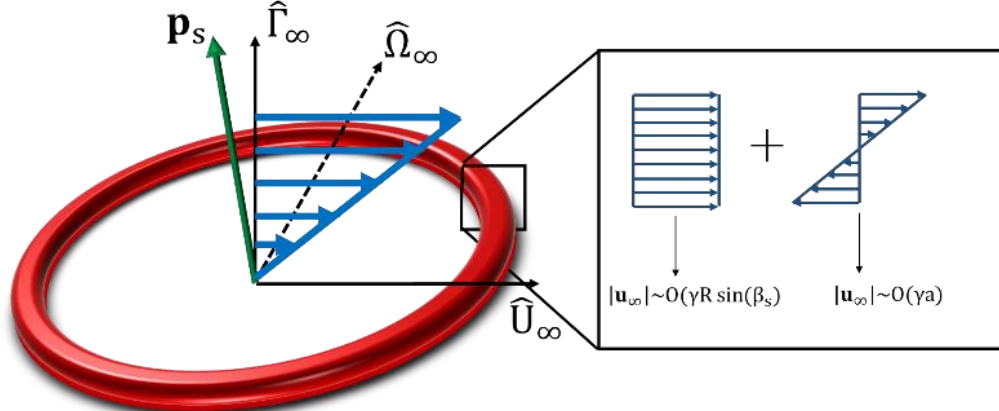
Fore-aft asymmetric particles, in addition to aligning, also migrate in the cross-stream direction. Alignment of the particle can be understood by observing the local flow field around the particle when  $\mathbf{p} = \hat{\mathbf{f}}_\infty$ , as described earlier. Here, we describe the mechanism leading to the cross-stream drift velocity of the particle ( $U_d$ ) once it is aligned and ways of controlling it by

manipulating the cross-sectional shape. Different symmetries of cross-sectional shapes lead to different orders of magnitude of the drift velocity ( $U_d = |(\mathbf{U}_p - \mathbf{u}^\infty(\mathbf{r}_{COM})) \cdot \hat{\mathbf{f}}_\infty|$ ) as shown in figure 6 (a). The direction of the cross-stream drift velocity depends on  $\mathbf{p}$  and the cross-sectional shape of the particle. The stable orientation of the particle,  $\mathbf{p}_s$ , is chosen such that  $\mathbf{p}_s \cdot \mathbf{U}_p > 0$ . This choice is made after obtaining the direction of  $\mathbf{U}_p$  from BEM calculation without loss of generality. A particle that is aligned along  $-\mathbf{p}_s$  would have a cross-stream migration in the opposite direction. A general cross-sectional shape will have a drift velocity that scales as  $\gamma R \sin(\beta_s) / \ln(A)$  (figure 6 (a) D-II). However, a cross-section with rotational and reflectional symmetry, as shown in figure 6 (a) D-I, generates  $U_d$  that scales as  $\gamma a \sin(\beta_s)$ . On the other hand, fore-aft symmetry of the cross-section leads to no cross-stream drift. The mechanism leading to cross-stream drift can be understood by obtaining the lift force on the particle when it is held stationary and oriented along its stable orientation ( $\mathbf{p} = \mathbf{p}_s$ ). At this orientation, the local flow field can be decomposed into a uniform flow field and a simple shear flow as shown in figure 6 (b). The local uniform flow field due to the small angle  $\beta_s$  of the particle with respect to the gradient axis scales as  $\gamma R \sin(\beta_s)$  over most of the ring. The scaling for the lift force due to the local uniform flow can be understood from slender body theory (Batchelor (1970)). Batchelor (1970) explains that the leading order force per unit length acting on a slender filament of high aspect ratio ( $A \gg 1$ ) is independent of the shape of the slender body and scales as  $\mu U_0 / \ln(A)$ ,  $U_0$  being the measure of the undisturbed fluid velocity. Since the only direction in the problem is the flow direction, the slender filament only experiences a drag force per unit length that scales as  $\mu \gamma R \sin(\beta_s) / \ln(A)$  for  $\ln(A) \gg 1$ . The details of the cross-section affect the force at a higher order in  $\ln(A)$  and thus the lift force per unit length, if any, scales as  $\mu |U_0| / [\ln(A)]^2$ . Thus, the local uniform flow field generates a lift force per unit length at each azimuthal location that scales as  $\mu \gamma R \sin(\beta_s) / [\ln(A)]^2$ . The local simple shear flow generates a lift force per unit length that primarily arises due to the tilt about the gradient direction ( $\beta_s$ ). This lift force per unit length scales as  $\mu a \sin(\beta_s) / \ln(A)$ . The net lift force for a general fore-aft asymmetric particle scales as  $\mu \gamma R^2 \sin(\beta_s) / [\ln(A)]^2$  and thus the cross-stream drift velocity scales as  $\gamma R \sin(\beta_s) / \ln(A)$  at large aspect ratios ( $A \gg 1$ ). The contribution to drift from the local uniform flow becomes identically zero if the cross-section has both reflectional and rotational symmetry. Shapes with reflectional and rotational symmetry, shown in figure 6 (a) (D-II), cannot generate a lift force in a 2-D uniform flow along two-different cross-sectional

orientations, and thus should have zero lift for all cross-sectional orientations by linear superposition. For such cross-sections, the drift comes from the local simple shear flow alone and scales as  $\gamma a \sin(\beta_s)$ . Thus, depending on the symmetry properties of the cross-sectional shape the cross-stream drift scales differently. However, contributions from both the mechanisms are important for particles with low aspect ratios. The angle made by the particle with the gradient direction,  $\beta_s = 0.5 \arccos(-1/\lambda) \approx (0.5(\lambda + 1))^{0.5}$ , also depends on the particle geometry. The maximum value of  $\beta_s$  depends on the capability of the shape to generate the highest counterrotating torque. To understand this variation, consider a shape shown in figure 6 (a) (D-II) and a fore-aft symmetric cross-section obtained by adding a reflection of this cross-section in a manner that keeps the particle aligned, as shown in figure 6 (a) (A-6). The forces acting on the particle when  $\mathbf{p} = \hat{\Gamma}_\infty$ , will be nearly the same for the asymmetric cross-section and the top half of the fore-aft symmetric cross-section. Therefore, a fore-aft symmetric shape, A-6, can generate approximately twice the counterrotating torque of the corresponding fore-aft asymmetric shape, D-II, at half the aspect ratio. The aspect ratio for a A-6 shape halves because the cross-sectional dimension “2a” is twice that of the D-II shape. Consequently, the maximum  $\beta_s$  is not only higher for the A-6 than the D-II shape but also occurs at a smaller aspect ratio. Fore-aft symmetry does not allow for migration, but rotating the cross-section breaks the fore-aft symmetry and allows for a finite drift. Shapes with rotational and reflectional symmetry, as shown in figure 6 (a) (D-I), have some resemblance to an equivalent fore-aft symmetric shape (A-6) and some resemblance to a fore-aft asymmetric shape (D-II). The D-I shape can align at a lower aspect ratio and have a higher  $\beta_s$  than a D-II shape and it could have a maximum value of cross-stream drift that is larger than that for a D-II shape. However, since the scaling of  $U_d$  with aspect ratio is a factor of  $1/A$  smaller than that for a D-II shape, the drift velocity of the D-II shape becomes larger as  $A \rightarrow \infty$ . This will be shown towards the end of this section by using specific examples. Consequently, particle migration is intertwined with the orientational dynamics of the particle and this intertwining is stronger for particles that align at low aspect ratios. We now elucidate the dependence on geometry for certain cross-sectional shapes from the solution of the mobility problem.



(a)



(b)

Figure 6. (a) Three types of cross-sectional shapes that can generate different scaling of cross-stream drift. (b) Flow field near the cross-section decomposed into a local uniform flow and a local simple shear flow that are  $O(yR \sin(\beta_s))$  and  $O(ya)$  respectively.

The alignment for rings with cross-section D-II can be understood from the previous discussion. The load bearing element as marked in figure 6 (a), allows one to envision the pressure forces that lead to alignment. For a general fore-aft asymmetric cross-section, where a similar picture is non-trivial, observing the lift force through the solution of a two-dimensional Stokes flow problem, as shown in figure 4, is a good method of comparing geometries.

Aligning particles that lack fore-aft symmetry have non-zero values of the dynamic parameters,  $\eta_1$  and  $\eta_2$  and thus have a constant cross-stream drift ( $U_d$ ). This cross-stream drift velocity as well as the dynamic parameters are obtained from the solution of the mobility problem. The rotation parameter,  $\lambda$ , is obtained by equation (5) while  $\eta_1$  and  $\eta_2$  are given by

$$\eta_1 = \frac{U_p \cdot n}{\gamma((p \cdot \hat{F}^\infty)^2 - 0.5)} \quad (13)$$

$$\eta_2 = -\eta_1 + \frac{U_p \cdot p}{\gamma(pp:E^\infty)}. \quad (14)$$

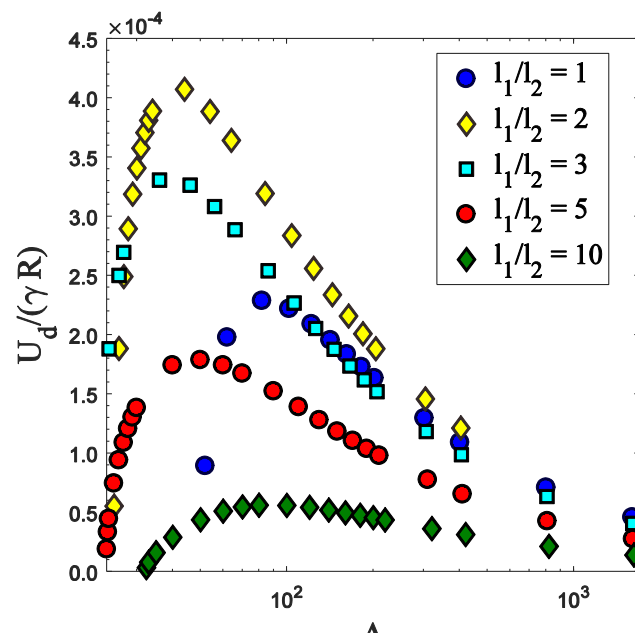
Equations (13) and (14) can be obtained from equation (1) and (3) when the imposed flow is a simple shear flow. The drift velocity in the gradient direction for rings that align in a simple shear flow, i.e.,  $\lambda < -1$ , is given by

$$U_d = \mathbf{U} \cdot \hat{\mathbf{F}}^\infty = \left| \frac{\gamma}{2} \left( \eta_1 + \eta_2 - \frac{\eta_2}{\lambda} \right) \sqrt{\frac{\lambda+1}{2\lambda}} \right|. \quad (15)$$

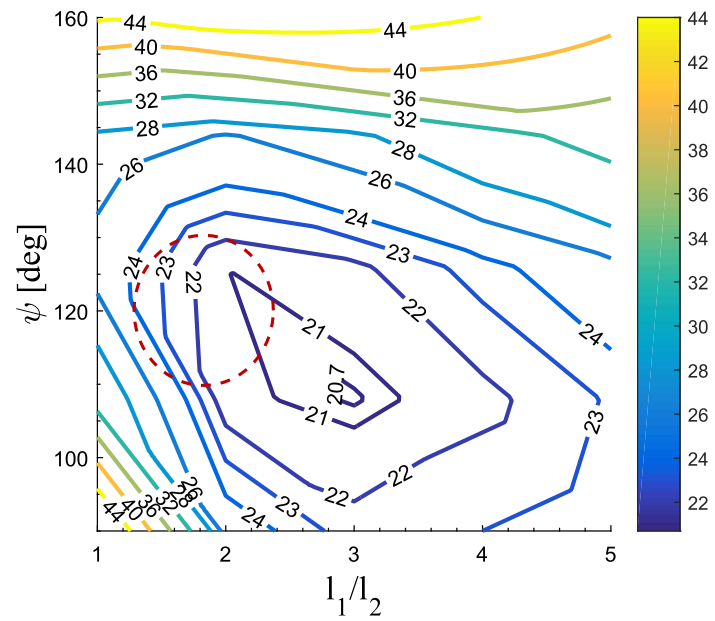
The proportionality with  $\sin(\beta_s) \approx \beta_s \approx \sqrt{-0.5(1+\lambda)}$  can be seen from this equation.

The cross-section shown in figure 6 (a) (D-II) was studied due to its resemblance with the Y-shaped cross-section and because of ease of fabrication afforded by its flat base. Figure 7 (a) shows the variation of the non-dimensional drift velocity of the particle ( $\bar{U}_d = U_d / (\gamma R)$ ) with aspect ratio for  $\psi = 0.5\pi$  and nearly zero arm thickness ( $t_1/l_2 = t_2/l_2 = 0.0125$ ). Reducing arm thickness reduces the area available for the viscous stresses to act as seen earlier. The variation of  $\bar{U}_d$  with respect to aspect ratio shown in figure 7 (a) is qualitatively similar across all shapes that can migrate across streamlines.  $\bar{U}_d$  is small near the critical aspect ratio due to the vanishingly small value of  $\beta_s$ .  $\bar{U}_d$  rapidly increases to a maximum value and then decays slowly thereafter. The maximum value occurs at an aspect ratio which is close to that yielding the minimum value of  $\lambda$  or the maximum value of  $\beta_s$ .  $\bar{U}_d$  slowly decays to zero with further increase in aspect ratio. Figure 7 (b) shows the contour map for the critical aspect ratio for alignment,  $A^*$ , for varying values of  $\psi$  and  $l_1/l_2$  for  $t_1/l_2 = t_2/l_2 = 0.0125$ . The optimal value of  $A^*$  is 20.6 and occurs approximately

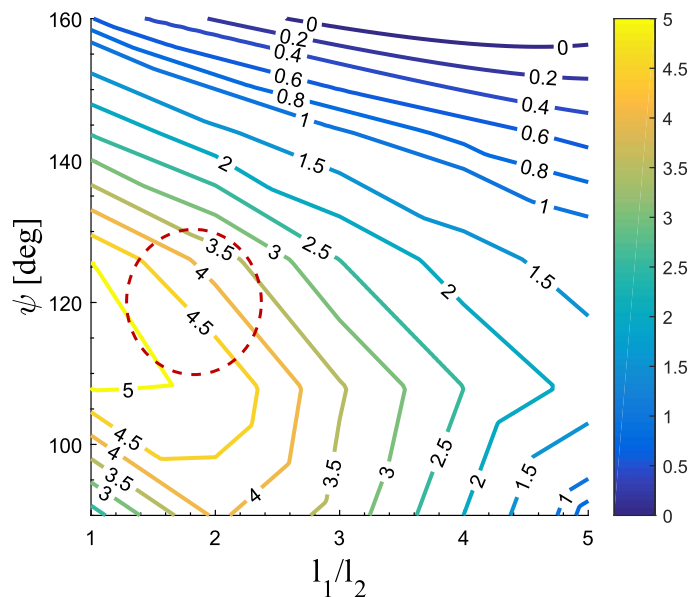
at  $\psi = 0.65\pi$  and  $l_1/l_2 = 3$ . This minimum value of  $A^*$  is more than double the value obtained for a Y shaped cross-section. This cross-section represents the top-half of the Y-shape cross-section with nearly the same forces acting on it. Thus, the cross-sectional dimension “2a” is half that of a Y-shaped cross-section, which leads to the near doubling of  $A^*$ . Additional viscous stresses acting on the bottom part of arm 1 make  $A^*$  more than double the value for an equivalent Y-shaped cross-section. As shown in figure 7 (b),  $A^*$  varies slowly in a large region near the optimum, which suggests that the particle dynamics varies slowly for slight changes in the cross-sectional shape. Figure 7 (c) shows the contour for the maximum value attained by  $\bar{U}_d$  with  $\psi$  and  $l_1/l_2$ .  $\bar{U}_d$  attains a maximum value when  $\psi \approx 0.6\pi$  and  $l_1/l_2 \approx 1$ . However, this maximum does not coincide with parameters that give the lowest  $A^*$ . Thus, an appropriate shape should be chosen based on the relative importance of attaining a high drift velocity and maintaining particle rigidity by restricting to a low aspect ratio. Parameters highlighted by the dotted region in figure 7 (b) and (c) suggest a region that has a balance between alignment at low aspect ratio and attainment of a high drift velocity.



(a)

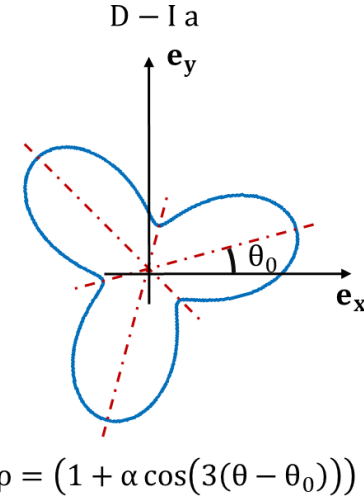


(b)

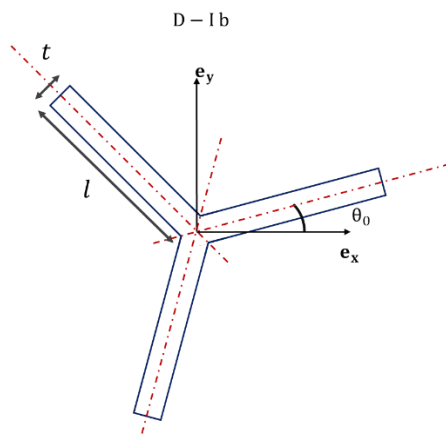


(c)

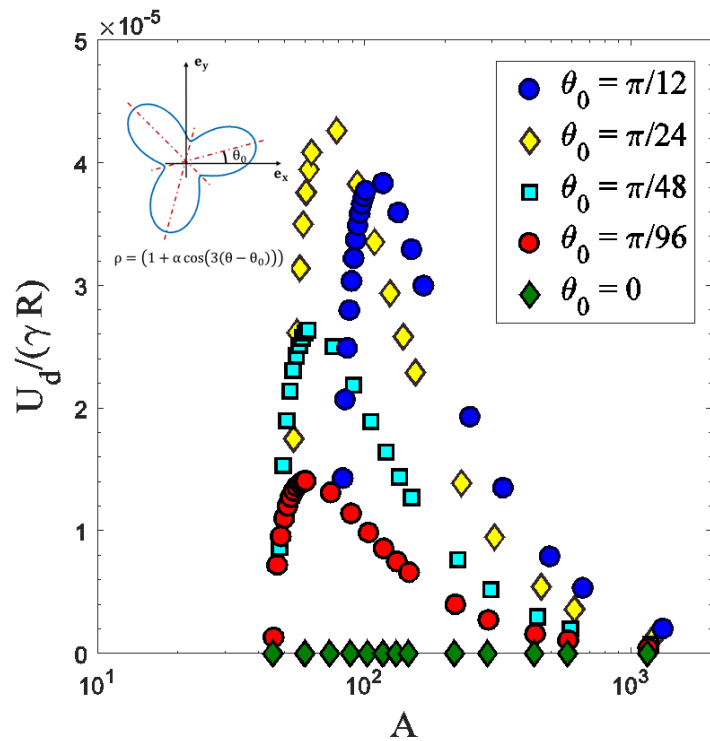
Figure 7. Variation of cross-stream drift velocity ( $U_d$ ) for shapes shown in figure 6 (a) (D-II). (a) Variation of non-dimensional drift velocity,  $\bar{U}_d = U_d/(\gamma R)$ , with the ring aspect ratio and ratio of arm lengths ( $l_1/l_2$ ) with  $t_1/l_2 = t_2/l_2 = 0.0125$  and  $\psi = 0.5\pi$ . (b) Contour of  $A^*$  with  $\psi$  and  $l_1/l_2$  for D-II shape with  $t_1/l_2 = t_2/l_2 = 0.0125$ . (c) Contour of  $(U_d/(\gamma R)) \times 10^4$  with  $\psi$  and  $l_1/l_2$  for D-II shape with  $t_1/l_2 = t_2/l_2 = 0.0125$ .



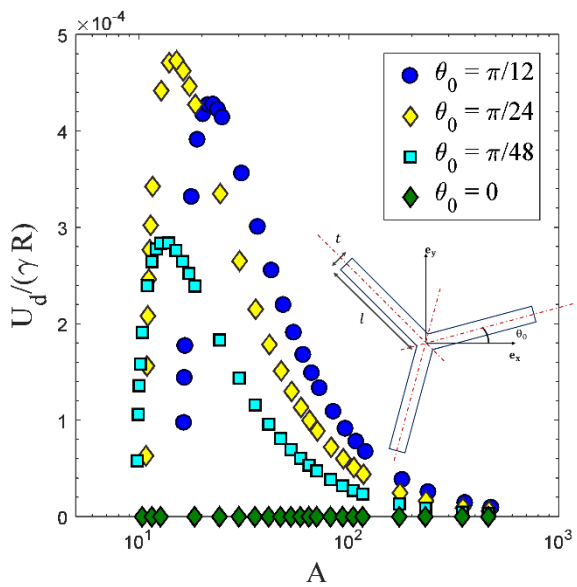
(a)



(b)



(c)



(d)

Figure 8. Variation of cross-stream drift velocity ( $U_d$ ) for shapes with reflectional and rotational symmetry (D-I shapes). (a) A cross-section given by  $\rho = (1 + \alpha \cos(3(\theta - \theta_0)))$ , which is the cross-section studied in Singh et al. (2013) rotated by an angle  $\theta_0$  relative to  $\mathbf{e}_x$ . (b) D-I shape with rotational and reflectional symmetry. The angle  $\theta_0$  of one of the arms with  $\mathbf{e}_x$  controls the degree of fore-aft asymmetry. (c) Non-dimensional drift velocity ( $U_d/(\gamma R)$ ) for shape in figure 8 (a) for  $\alpha = 0.55$ . (d)  $U_d/(\gamma R)$  for shape shown in figure 8 (b) with  $l=1$  and  $t=0.0125$ .

We considered two cross-sections with reflectional and rotational symmetry as shown in figures 8 (a) and (b), where  $\theta_0$  is the angle of rotation about  $\mathbf{e}_x$ . The parameters that gave the least value of  $A^*$  for  $\theta_0 = 0$  were chosen for each of the shapes. The parameters are  $\alpha = 0.55$  for the shape in figure 8 (a) and  $l_1/l_2 = 1$  and  $\psi = 0.6\pi$  for the shape in figure 8 (b). If  $\theta_0 = \pm \pi/6$ , these cross-section becomes symmetric about a plane normal to  $\mathbf{e}_x$  and thus cannot generate a force in the gradient direction when  $\mathbf{p} = \hat{\Gamma}_\infty$  because of the equivalence of the problem in flow reversal ( $\mathbf{u}_\infty = -\mathbf{u}_\infty$ ). As seen in figure 8 (c),  $\bar{U}_d = U_d/(\gamma R)$  is an order of magnitude lower for the 3-lobed cross-section in figure 8 (a) in comparison to an equivalent D-II shape.  $\bar{U}_d$  follows a similar trend of rapidly increasing to a maximum and slowly decaying to zero at large aspect ratios. The drift velocity for the rotated Y-shape cross-section, i.e., D-I b shape, has values comparable with the D-II shape because rings with D-I b shaped cross-sections align at a smaller aspect ratio. Thus, rings with D-I b cross-sections generate a higher counter-rotating torque leading to a higher value of  $\beta_s$  than the corresponding D-II shape. This increases the drift velocity of rings with D-I b shapes at lower aspect ratios. However, at higher aspect ratios rings with D-II shapes will increase  $\bar{U}_d$  due to a stronger scaling of  $\bar{U}_d$  with the particle aspect ratio,  $A$ . The 3-lobed cross-section, i.e., D-I a shape, in figure 8 (a) aligns around the same aspect ratio as an equivalent D-II shape leading to similar values of  $\beta_s$ . Thus, the drift velocity is a factor of  $1/A$  smaller than an equivalent D-II shape as per the scaling argument. The aligning angle of the particle,  $\beta_s$ , is a crucial factor, and the drift velocity can be augmented by increasing  $\beta_s$ . Thus, as observed above, to control particle migration, it is pertinent to consider particle alignment as well.

We considered a cross-sectional shape, shown in figure 9 (a), whose degree of asymmetry could be controlled systematically. This family of shapes allows another way of analyzing the importance of particle symmetry in controlling the magnitude of  $\bar{U}_d$ . This shape is fore-aft

symmetric for  $l_3/l_2 = 1$  and the degree of fore-aft asymmetry increases as  $l_3/l_2$  changes from 1 to 0. Figure 9 (b) and (c) show the variation of  $\beta_s$  and  $\bar{U}_d$  with particle aspect ratio (A) for varying lengths of arm 3 ( $l_3/l_2$ ) for  $l_1/l_2 = 1$ ,  $\psi_2 = \psi_3 = 0.65\pi$  and  $t_1 = t_2 = t_3 = 0.0125l_2$ .  $\beta_s$  increases as  $(l_3/l_2) \rightarrow 1$ , but the particle approaches a fore-aft symmetric shape (i.e.,  $\eta_1 \rightarrow 0$  and  $\eta_2 \rightarrow 0$ ) which has no drift. The highest drift is obtained for a particle that has a balance between aligning at a low aspect ratio while still deviating sufficiently from fore-aft symmetry (i.e.,  $0 < l_3/l_2 < 1$ ) as seen in figure 9 (b) for  $l_3/l_2 = 0.25$  and  $A = 25.14$ . Such a shape could be used as a starting point to obtain the shapes that generate the highest drift ( $U_d/(\gamma R)$ ). It should be noted that at high aspect ratios,  $A > 100$ ,  $\beta_s$  is nearly the same for all cross-sectional shapes at a given A. Thus, at sufficiently high aspect ratios the drift is higher for the shape that possesses the highest degree of fore-aft asymmetry, as seen in figure 9 (c).

The drift velocity obtained by scaling arguments earlier are verified by BEM results at large aspect ratios of the particle (A). The variation of drift velocity ( $U_d$ ) non-dimensionalized with the appropriate scaling velocity ( $U_s$ ), depending on the mechanism of drift, is used to verify the scaling arguments presented earlier. Figure 10 shows the variation of  $U_d/U_s$  for various shapes studied here.  $U_s = \gamma a \sin(\beta_s)$  for shapes that posses reflectional and rotational symmetry (D-I shape), and  $U_s = \gamma R \sin(\beta_s)/\ln(A)$  for fore-aft asymmetric cross-sections that lack reflectional and/or rotational symmetry (D-II shape). Figure 10 shows that at moderately high aspect ratios,  $U_d/U_s$  attains a constant value, thus verifying the scaling and the mechanism for cross-stream migration mentioned earlier.

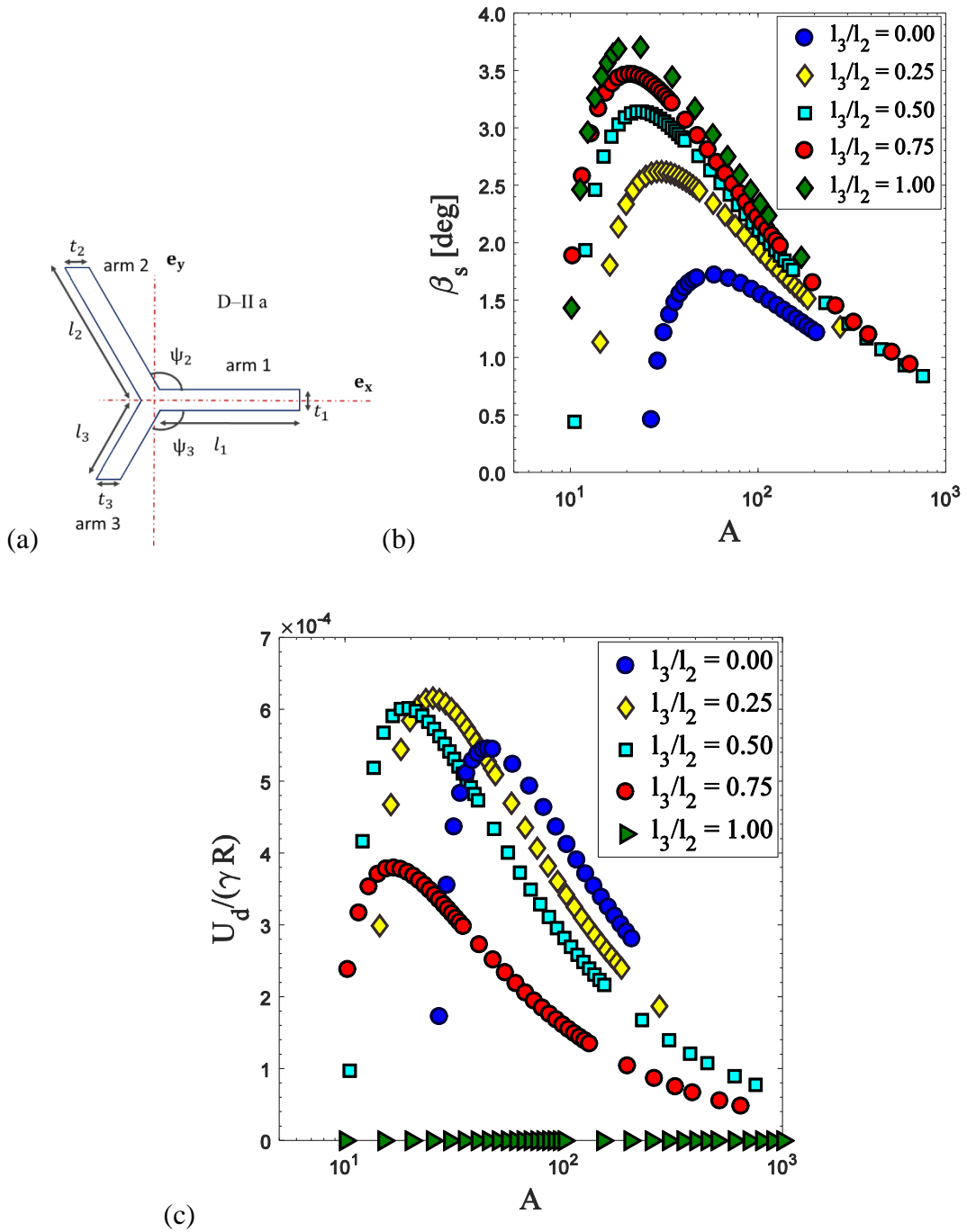


Figure 9. Drift velocity variation with varying degree of fore-aft asymmetry of a cross-section D-II a. (a) D-II a shape that generates varying cross-stream drift as the deviation from fore-aft symmetry is adjusted by changing length of arm 3 relative to arm 2 (i.e.,  $l_3/l_2$ ). (b) Parametric variation of  $\beta_s$  with particle aspect ratio ( $A$ ) and relative length of arm 3 ( $l_3/l_2$ ) for (D-II a) shape. (c) Parametric variation of  $\bar{U}_d = U_d / (\gamma R)$  with  $A$  and ( $l_3/l_2$ ) for (D-II a) shape. In both these plots,  $l_1/l_2 = 1$ ,  $\psi_2 = \psi_3 = 0.65\pi$  and  $t_1/l_2 = t_2/l_2 = t_3/l_2 = 0.0125$ .

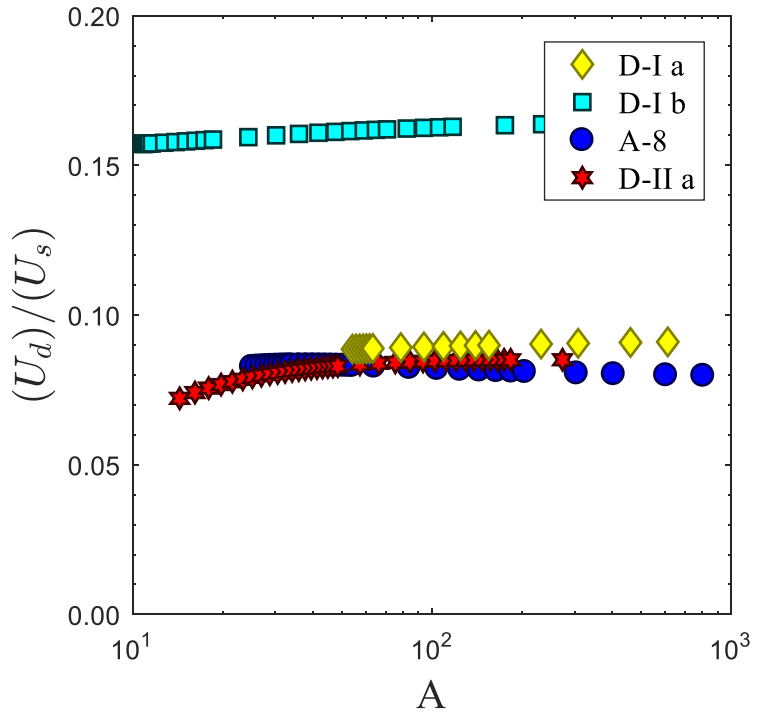


Figure 10. Drift velocity non-dimensionalized with the velocity obtained by scaling arguments ( $U_s$ ). D-I a shape (figure 8 (a)) with  $\alpha = 0.55$  and  $\theta_0 = \pi/24$ ; D-I b shape (figure 8 (b)) with  $\theta_0 = \pi/24$  and  $t/l = 0.0125$ ; A-8 shape (L-shape) with  $l_1/l_2 = 2$  and  $t_1/l_2 = t_2/l_2 = 0.0125$ ; and D-II a shape with  $l_1/l_2 = 1$ ,  $l_3/l_2 = 0.25$ ,  $\psi_2 = \psi_3 = 0.65\pi$  and  $t_1/l_2 = t_2/l_2 = t_3/l_2 = 0.0125$ . The scaling for velocity for D-I a and D-I b shapes is  $U_s = \gamma(a)\sin(\beta_s)$ , while the scaling for the remaining two-shapes is  $U_s = \gamma(R)\sin(\beta_s)/\ln(A)$ .

## 5. Conclusion

In conclusion, our calculations show that the rotational and translational dynamics of rings can be controlled by appropriately manipulating the cross-sectional shape. We elucidated the mechanism that leads to permanent alignment of particles in a simple shear flow: it is the pressure acting on the particle surface that leads to alignment. Rings with cross-sections that possess a blunt inner edge and a sharp outer edge, as shown in figure (4), acquire an equilibrium orientation in a simple shear flow. Rings with a streamlined cross-sectional shape, such as a Y-shaped cross-section shown in figure 2 (b), align at lower aspect ratios than blunter shapes due to localization of the viscous stress at any extending elements of the cross-section. The optimal shape in the family of Y-shaped particles was shown to be  $\psi = 0.65 \pi$ ,  $t_2/l_2 \rightarrow 0$ ,  $t_1/l_2 \rightarrow 0$  and  $l_1/l_2 = 2$ . This might not be the globally optimal shape, but provides a starting point to search for shapes that align at lower aspect ratios. Rings with certain geometries, such as Y-shaped cross-sections shown in figure 2 (b), have suppressed rotation in comparison to rings with circular cross-sections (torus) at similar aspect ratios. This is an important finding as these rings remain aligned for longer periods of time than an equivalent torus and thus from a practical standpoint could mimic aligning particle dynamics.

For fore-aft asymmetric cross-sections, we elucidated the mechanism leading to cross-stream drift which could be controlled by altering the symmetry of the cross-section. Particles with fore-aft symmetric cross-sections have no drift. Particles with cross-sections that possess rotational and reflectional symmetry have drift that scales as  $\gamma a \sin(\beta_s)$  while those that lack this symmetry have a drift that scales as  $\gamma R \sin(\beta_s) / \ln(A)$ . We explained the important role that the aligning angle ( $\beta_s$ ) plays in determining the magnitude of the drift. In particular, certain shapes can possess a higher drift due to a higher aligning angle. Both alignment and migration of rings depends on the lift force generated by pressure and thus engineering the geometry to effectively utilize pressure and localizing the viscous stresses should be a starting point to tune motion of particles in shear flows.

A T-shaped (A-7) and an L-shaped (A-8) cross-section, studied in this work, are of practical interest due to ease of fabrication. These particles could be fabricated using multi-step

photolithography (Foulds & Parameswaran 2006). Techniques such as direct-ink writing (Raney and Lewis 2015) or optofluidic fabrication (Paulson, Di Carlo and Chung 2015) could be used to fabricate more complicated geometries studied in this work. Fabrication of these particles, would not only allow for the verification of our results, but also pave the way for practical utility of these particles. The macroscopic properties of a particle suspension differ depending on tumbling or aligning behavior of individual particles. Usually anisotropic tumbling particles cannot fully impart their anisotropy to the suspension due to orientational dispersion. On the other hand, aligning rings would lead to a high degree of anisotropy due to particle alignment near the flow-vorticity plane. Materials processed with aligning particle suspension should have a high degree of anisotropy in properties such as elastic modulus; specific stiffness; and thermal, electric and magnetic conductivity. Migrating particles could be used to impart surface properties such as scratch resistance by systematically depositing particles near the surface (Isla et al. 2003). The viscosity of these suspensions should also be lower due to alignment along the lamellae improving the ease of processing. These materials could be manufactured on a large scale using existing material processing technologies such as injection molding, spin-casting and extrusion. Consequently, these aligning particles provide a unique opportunity to design particle suspensions with tunable structure using existing manufacturing techniques.

## **6. Appendix: Analytical integration of fluid disturbance due to particle along the azimuthal direction**

The boundary integral equation given in equation (3.1a) can be solved to obtain the force per unit area acting on the particle surface using a 2-D surface mesh. As mentioned in section 3, the azimuthal variation of the force per unit area for our problem, given by equation (3.5), can be used to reduce the dimensionality of the problem. Here, we give a detailed methodology of achieving this for a ring in a simple shear flow, such that  $\mathbf{p}$  lies in the flow gradient plane. This could be easily extended for an axisymmetric particle with arbitrary orientation in a general linear flow field. The boundary integral equation (3.1a) can be written as:

$$\mathbf{u} \cdot \mathbf{n} = \mathbf{u}^\infty \cdot \mathbf{n} + \frac{1}{8\pi\mu} \int ds' \int_\phi^{\phi+2\pi} d\phi' x' \left[ f_n(\mathbf{r}') \left( \frac{1}{|\mathbf{r}-\mathbf{r}'|} + \frac{(x \cos(\phi) - x' \cos(\phi'))^2}{|\mathbf{r}-\mathbf{r}'|^3} \right) + f_b(\mathbf{r}') \left( \frac{(x \cos(\phi) - x' \cos(\phi'))(x \sin(\phi) - x' \sin(\phi'))}{|\mathbf{r}-\mathbf{r}'|^3} \right) + f_p(\mathbf{r}') \left( \frac{(x \cos(\phi) - x' \cos(\phi'))(y - y')}{|\mathbf{r}-\mathbf{r}'|^3} \right) \right], \quad (\text{A } 1)$$

$$\mathbf{u} \cdot \mathbf{b} = \mathbf{u}^\infty \cdot \mathbf{b} + \frac{1}{8\pi\mu} \int ds' \int_\phi^{\phi+2\pi} d\phi' x' \left[ f_n(\mathbf{r}') \left( \frac{(x \cos(\phi) - x' \cos(\phi'))(x \sin(\phi) - x' \sin(\phi'))}{|\mathbf{r}-\mathbf{r}'|^3} \right) + f_b(\mathbf{r}') \left( \frac{1}{|\mathbf{r}-\mathbf{r}'|} + \frac{(x \sin(\phi) - x' \sin(\phi'))^2}{|\mathbf{r}-\mathbf{r}'|^3} \right) + f_p(\mathbf{r}') \left( \frac{(x \sin(\phi) - x' \sin(\phi'))(y - y')}{|\mathbf{r}-\mathbf{r}'|^3} \right) \right], \quad (\text{A } 2)$$

$$\mathbf{u} \cdot \mathbf{p} = \mathbf{u}^\infty \cdot \mathbf{p} + \frac{1}{8\pi\mu} \int ds' \int_\phi^{\phi+2\pi} d\phi' x' \left[ f_n(\mathbf{r}') \left( \frac{(x \cos(\phi) - x' \cos(\phi'))(y - y')}{|\mathbf{r}-\mathbf{r}'|^3} \right) + f_b(\mathbf{r}') \left( \frac{(x \sin(\phi) - x' \sin(\phi'))(y - y')}{|\mathbf{r}-\mathbf{r}'|^3} \right) + f_p(\mathbf{r}') \left( \frac{1}{|\mathbf{r}-\mathbf{r}'|} + \frac{(y - y')^2}{|\mathbf{r}-\mathbf{r}'|^3} \right) \right], \quad (\text{A } 3)$$

where the subscripts n, b, p represent the components of a vector along **n**, **b** and **p** respectively. x and y are the position along  $\mathbf{e}_x$  and  $\mathbf{e}_y$  respectively and  $\phi$  is the angular position. The primed variables ( $ds'$ ,  $x'$  and  $\mathbf{r}'$ ) are dummy variables. The integrals in (A 1) – (A 3) can be analytically integrated along the azimuthal direction by substituting  $\phi'' = \phi' - \phi$  in equations to (A 1) – (A 3). Upon this substitution  $|\mathbf{r} - \mathbf{r}'|$  is given by

$$r'' = |\mathbf{r} - \mathbf{r}'| = [A^2 - B^2 \cos(\phi'')]^{0.5}, \quad (\text{A } 4)$$

where  $A^2 = x^2 + x'^2 + y^2$ ,  $B^2 = 2xx'$ . On changing the dummy variable to  $\phi''$  and substituting (A 4) and equation (3.5) into (A 1) – (A 3), the numerators of the integrands in (A 1) – (A 3) will be either a constant, powers of  $\cos(\phi'')$  or powers of  $\sin(\phi'')$ , while the denominator will be either  $r''$  or  $r''^3$ . Terms with odd powers of  $\sin(\phi'')$  will integrate to zero, while any even powers of  $\sin(\phi'')$  can be transformed into an equivalent term in  $\cos(\phi'')$ . A constant term and any power of  $\cos(\phi'')$  can be transformed into an elliptic integral using elementary calculus as shown in Singh et al. (2013). This procedure can be understood from the transformation given by

$$\int_0^{2\pi} d\phi'' \frac{\cos^a(\phi'')}{(A^2 - B^2 \cos(\phi''))^{\frac{m}{2}}} = \frac{4(-1)^a}{(C^2)^{m/2}} \int_0^{2\pi} d\phi'' \frac{\cos^a(2\phi'')}{(1 - D^2 \sin^2(\phi''))^{\frac{m}{2}}}, \quad (\text{A } 5)$$

where  $C^2 = A^2 + B^2$ ,  $D^2 = 2B^2/C^2 < 1$ ,  $a$  and  $m$  are integers. The left-hand side of (A 5) represents a general term expected in (A 1) – (A 3). The right-hand side of (A 5) can be given in terms of complete elliptic integrals of the first (K) and second (E) kind which are given by

$$K(D) = \int_0^{2\pi} \frac{d\phi''}{(1-D^2 \sin^2(\phi''))^{0.5}}, \quad (A 6)$$

$$E(D) = \int_0^{2\pi} d\phi'' (1 - D^2 \sin^2(\phi''))^{0.5}. \quad (A 7)$$

The integrals in (A5) are obtained from Singh et al. (2013) for  $a = \{0, 1, 2\}$  and  $m = \{1, 3\}$  and are denoted as  $S_1, S_2, \dots, S_8$  following the same notation used in their paper. Two additional integrals are required for  $a = 3$  and  $m = \{1, 3\}$  for our case which are given by  $S_9$  and  $S_{10}$ . All the integrals involved in (A 1) – (A 3) are given by

$$S_1 = \int_0^{2\pi} d\phi'' \frac{1}{(A^2 - B^2 \cos(\phi''))^{0.5}} = \frac{4}{C} K, \quad (A 8 a)$$

$$S_2 = \int_0^{2\pi} d\phi'' \frac{\cos(\phi'')}{(A^2 - B^2 \cos(\phi''))^{0.5}} = -\frac{4}{C} \left( \frac{D^2 - 2}{D^2} K + \frac{2}{D^2} E \right), \quad (A 8 b)$$

$$S_3 = \int_0^{2\pi} d\phi'' \frac{1}{(A^2 - B^2 \cos(\phi''))^{1.5}} = \frac{4}{C^3} \frac{E}{1 - D^2}, \quad (A 8 c)$$

$$S_4 = \int_0^{2\pi} d\phi'' \frac{\cos(\phi'')}{(A^2 - B^2 \cos(\phi''))^{1.5}} = \frac{4}{C^3 D^2} \left( -2K + \frac{D^2 - 2}{(D^2 - 1)} E \right), \quad (A 8 d)$$

$$S_5 = \int_0^{2\pi} d\phi'' \frac{\cos^2(\phi'')}{(A^2 - B^2 \cos(\phi''))^{0.5}} = \frac{4}{C^3 D^4} \left( 4(D^2 - 2)K + \frac{D^4 - 8D^2 + 8}{1 - D^2} E \right), \quad (A 8 e)$$

$$S_6 = \int_0^{2\pi} d\phi'' \frac{\cos^2(\phi'')}{(A^2 - B^2 \cos(\phi''))^{0.5}} = \frac{4}{3CD^4} \left( (3D^4 - 8D^2 + 8)K + 4(D^2 - 2)E \right), \quad (A 8 f)$$

$$S_7 = \int_0^{2\pi} d\phi'' \frac{\cos^3(\phi'')}{(A^2 - B^2 \cos(\phi''))^{0.5}} = \frac{-4}{3C^3 D^6} \left( 2(9D^4 - 32D^2 + 32)K + \frac{(3D^6 - 38D^4 + 96D^2 - 64)E}{1 - D^2} \right), \quad (A 8 g)$$

$$S_8 = \int_0^{2\pi} d\phi'' \frac{\cos^4(\phi'')}{(A^2 - B^2 \cos(\phi''))^{0.5}} = \frac{4}{10C^3 D^8} \left( 16(D^2 - 2)(5D^4 - 16D^2 + 16)K + \frac{2(5D^8 - 96D^6 + 352D^4 - 512D^2 + 256)}{1 - D^2} E \right), \quad (\text{A } 8 \text{ h})$$

$$S_9 = \int_0^{2\pi} d\phi'' \frac{\cos^3(\phi'')}{(A^2 - B^2 \cos(\phi''))^{0.5}} = -\frac{4}{15C D^6} ((15D^6 - 62D^4 + 96D^2 - 64)K + 2(17D^4 - 32D^2 + 32)E), \quad (\text{A } 8 \text{ i})$$

$$S_{10} = \int_0^{2\pi} d\phi'' \frac{\cos^5(\phi'')}{(A^2 - B^2 \cos(\phi''))^{0.5}} = -\frac{4}{105C D^{10}} \left( (1050D^8 - 7072D^6 + 19360D^4 - 24576D^2 + 12288)K + \frac{(-105D^{10} + 2594D^8 - 13296D^6 + 29344D^4 - 30720D^2 + 12288)}{D^2 - 1} E \right). \quad (\text{A } 8 \text{ j})$$

Applying the no slip boundary condition on the particle surface equations (A 1) – (A 3) are simplified to obtain a set of linear equations, which can be rewritten in the form:

$$-\mathbf{u}^\infty \cdot \mathbf{n} = -(\mathbf{U} + \boldsymbol{\omega}_p \times \mathbf{r}) \cdot \mathbf{n} + \sum_{j=1}^N \sum_{k=1}^{N_s} ds'_k x'_k [(f_0^j I_{nn0} + f_1^j I_{nn1} + f_2^j I_{nn2} + f_3^j I_{nn3}) + (f_4^j I_{nb1} + f_5^j I_{nb2} + f_6^j I_{nb3}) + (f_7^j I_{np0} + f_8^j I_{np1} + f_9^j I_{np2})], \quad (\text{A } 9\text{a})$$

$$-\mathbf{u}^\infty \cdot \mathbf{b} = -(\mathbf{U} + \boldsymbol{\omega}_p \times \mathbf{r}) \cdot \mathbf{b} + \sum_{j=1}^N \sum_{k=1}^{N_s} ds' x' [(f_0^j I_{bn0} + f_1^j I_{bn1} + f_2^j I_{bn2} + f_3^j I_{bn3}) + (f_4^j I_{bb1} + f_5^j I_{bb2} + f_6^j I_{bb3}) + (f_7^j I_{bp0} + f_8^j I_{bp1} + f_9^j I_{bp2})], \quad (\text{A } 9\text{b})$$

$$-\mathbf{u}^\infty \cdot \mathbf{p} = -(\mathbf{U} + \boldsymbol{\omega}_p \times \mathbf{r}) \cdot \mathbf{p} + \sum_{j=1}^N \sum_{k=1}^{N_s} ds' x' [(f_0^j I_{pn0} + f_1^j I_{pn1} + f_2^j I_{pn2} + f_3^j I_{pn3}) + (f_4^j I_{pb1} + f_5^j I_{pb2} + f_6^j I_{pb3}) + (f_7^j I_{pp0} + f_8^j I_{pp1} + f_9^j I_{pp2})]. \quad (\text{A } 9\text{c})$$

Here  $N$  is the number of elements in the primary mesh,  $N_s$  is the number of elements in the secondary mesh and  $ds'_k$  is the size of the secondary mesh, as shown in figure A.1 (c). The summation in equation (A 9) is performed using the secondary mesh points, which are subdivisions to the primary mesh, to get an accurate estimate of the Green's function. This secondary mesh is used to for the numerical integral in equation (A 9). Expressions to obtain  $x'$ ,  $y'$  and  $ds'_k$  are also shown in figure A. 1 (c). Furthermore, we assume that the values of  $[f_0, f_1, \dots, f_9]$  remain constant

over secondary mesh as shown in figure A.1 (c) which works well as long as sufficient number of primary mesh points exist. The additional terms on the right-hand side of (A 9), denoted by  $I$ , can be obtained by simple but lengthy algebra from (A 1) – (A 3) after appropriate substitution. These additional terms are obtained by performing analytical integration over  $\phi''$  and are given by

$$I_{nn0} = S_1 + x^2 \cos^2(\phi) S_3 - 2xx' \cos^2(\phi) S_4 + x'^2 (\cos(2\phi) S_5 + \sin^2(\phi) S_3), \quad (A 10 a)$$

$$I_{nn1} = \cos(\phi) S_2 + \cos(\phi) (x^2 \cos^2(\phi) S_4 - 2xx' \cos^2(\phi) S_5 + x'^2 (\cos(2\phi) S_7 + \sin^2(\phi) S_4) - \sin(\phi) \sin(2\phi) (xx'(S_3 - S_5) - x'^2 (S_4 - S_7))), \quad (A 10 b)$$

$$I_{nn2} = \cos(2\phi) (2S_6 - S_1) + \cos(2\phi) \left( x^2 \cos^2(\phi) (2S_5 - S_3) - 2xx' \cos^2(\phi) (2S_7 - S_4) + x'^2 (\cos(2\phi) (2S_8 - S_5) + \sin^2(\phi) (2S_5 - S_3)) \right) - 2 \sin^2(2\phi) (xx'(S_4 - S_7) - x'^2 (S_5 - S_8)), \quad (A 10 c)$$

$$I_{nn3} = \cos(3\phi) (4S_9 - 3S_2) + \cos(3\phi) \left( x^2 \cos^2(\phi) (4S_7 - 3S_4) - 2xx' \cos^2(\phi) (4S_8 - 3S_5) + x'^2 (\cos(2\phi) (4S_{10} - 3S_7) + \sin^2(\phi) (4S_7 - 3S_4)) \right) - \sin(3\phi) \sin(2\phi) (xx' \sin(2\phi) (5S_5 - S_3 - 4S_8) - x'^2 (5S_7 - S_4 - 4S_{10})), \quad (A 10 d)$$

$$I_{nb1} = 0.5 \sin(\phi) \sin(2\phi) (x^2 S_4 - 2xx' S_5 + x'^2 (2S_7 - S_4)) + \cos(\phi) \cos(2\phi) (-xx'(S_3 - S_5) + x'^2 (S_4 - S_7)), \quad (A 10 e)$$

$$I_{nb2} = 0.5 \sin^2(2\phi) (x^2 (2S_5 - S_3) - 2xx' (2S_7 - S_4) + x'^2 (4S_8 - 4S_5 + S_3)) + 2 \cos^2(2\phi) (-xx'(S_4 - S_7) + x'^2 (S_5 - S_8)), \quad (A 10 f)$$

$$I_{nb3} = 0.5 \sin(3\phi) \sin(2\phi) (x^2 (4S_7 - 3S_4) - 2xx' (4S_8 - 3S_5) + x'^2 (8S_{10} - 10S_7 + 3S_4)) + \cos(3\phi) \cos(2\phi) (-xx' (-4S_8 + 5S_5 - S_3) + x'^2 (-4S_{10} + 5S_7 - S_4)), \quad (A 10 g)$$

$$I_{np0} = (y - y') \cos(\phi) (x S_3 - x' S_4), \quad (A 10 h)$$

$$I_{np1} = (y - y') (\cos^2(\phi) (xS_4 - x'S_5) - \sin^2(\phi) x'(S_3 - S_5)), \quad (A 10 i)$$

$$I_{np2} = (y - y') \left( \cos(2\phi) \cos(\phi) (x(2S_5 - S_3) - x'(2S_7 - S_4)) - 2 \sin(2\phi) \sin(\phi) x'(S_4 - S_7) \right), \quad (A 10 j)$$

$$I_{bn0} = 0.5 \sin(2\phi) (x^2 S_3 - 2xx' S_4 + x'^2 (2S_5 - S_3)), \quad (A 11 a)$$

$$I_{bn1} = 0.5 \sin(2\phi) \cos(\phi) (x^2 S_4 - 2xx' S_5 + x'^2 (2S_7 - S_4)) - \cos(2\phi) \sin(\phi) (x'^2 (-S_7 + S_4) - xx' (-S_5 + S_3)), \quad (A 11 b)$$

$$I_{bn2} = 0.5 \sin(2\phi) \cos(2\phi) (x^2 (2S_5 - S_3) - 2xx' (2S_7 - S_4) + x'^2 (4S_8 - 4S_5 + S_3)) - 2 \cos(2\phi) \sin(2\phi) (x'^2 (-S_8 + S_5) - xx' (-S_7 + S_4)), \quad (A 11 c)$$

$$I_{bn3} = 0.5 \sin(2\phi) \cos(3\phi) (x^2 (4S_7 - 3S_4) - 2xx' (4S_8 - 3S_5) + x'^2 (8S_{10} - 10S_7 + 3S_4)) - 2 \cos(2\phi) \sin(3\phi) (x'^2 (-4S_{10} + 5S_7 - S_4) - xx' (-4S_8 + 5S_5 - S_3)), \quad (A 11 d)$$

$$I_{bb1} = \sin(\phi) S_2 + \sin(\phi) (x^2 \sin^2(\phi) S_4 - 2xx' \sin^2(\phi) S_5 + x'^2 (\cos^2(\phi) S_4 - \cos(2\phi) S_7)) + \sin(2\phi) \cos(\phi) (-xx' (S_3 - S_5) + x'^2 (S_4 - S_7)), \quad (A 11 e)$$

$$I_{bb2} = \sin(2\phi) (2S_6 - S_1) + \sin(2\phi) \left( x^2 \sin^2(\phi) (2S_5 - S_3) - 2xx' \sin^2(\phi) (2S_7 - S_4) + x'^2 (-\cos(2\phi) (2S_8 - S_5) + \cos^2(\phi) (2S_5 - S_4)) \right) + 2 \sin(2\phi) \cos(2\phi) (-xx' (S_4 - S_7) + x'^2 (S_5 - S_8)), \quad (A 11 f)$$

$$I_{bb3} = \sin(3\phi) (4S_9 - 3S_2) + \sin(3\phi) \left( x^2 \sin^2(\phi) (4S_7 - 3S_5) - 2xx' \sin^2(\phi) (4S_8 - 3S_5) + x'^2 (\sin^2(\phi) (4S_{10} - 3S_7) + \cos^2(\phi) (-4S_{10} + 7S_7 - 3S_4)) \right) + \sin(2\phi) \cos(3\phi) (-xx' (-4S_8 + 5S_5 - S_3) + x'^2 (-4S_{10} + 5S_7 - S_4)), \quad (A 11 g)$$

$$I_{bp0} = (y - y') \sin(\phi) (xS_3 - x'S_4), \quad (A 11 h)$$

$$I_{bp1} = (y - y') (\cos(\phi) \sin(\phi) (xS_4 - x'S_5) + \sin(\phi) \cos(\phi) x'(S_3 - S_5)), \quad (A 11 i)$$

$$I_{bp2} = (y - y') \left( \cos(2\phi) \sin(\phi) (x(2S_5 - S_3) - x'(2S_7 - S_4)) + 2 \sin(2\phi) \cos(\phi) (S_4 - S_7) \right), \quad (A 11 j)$$

$$I_{pn0} = (y - y') \cos(\phi) (xS_3 - x'S_4), \quad (A 12 a)$$

$$I_{pn1} = (y - y') (\cos^2(\phi) (xS_4 - x'S_5) - \sin^2(\phi) x'(S_3 - S_5)), \quad (A 12 b)$$

$$I_{pn2} = (y - y') \left( \cos(2\phi) (x \cos(\phi) (2S_5 - S_3) - x' \cos(\phi) (2S_7 - S_4)) - 2 \sin(2\phi) \sin(\phi) x'(S_4 - S_7) \right), \quad (A 12 c)$$

$$I_{pn3} = (y - y') \left( \cos(3\phi) (x \cos(\phi) (4S_7 - 3S_4) - x' \cos(\phi) (4S_8 - 3S_5)) - \sin(3\phi) \sin(\phi) x' (-4S_8 + 5S_5 - S_3) \right), \quad (A 12 d)$$

$$I_{pb1} = (y - y') (\sin^2(\phi) (xS_4 - x'S_5) - \cos^2(\phi) (S_3 - S_5)), \quad (A 12 e)$$

$$I_{pb2} = (y - y') (\sin(2\phi) \sin(\phi) (x(2S_5 - S_3) - x'(2S_7 - S_4)) - 2 \cos(2\phi) \cos(\phi) x'(S_4 - S_7)), \quad (A 12 f)$$

$$I_{pb3} = (y - y') \left( \sin(3\phi) \sin(\phi) (x(4S_7 - 3S_4) - x'(4S_8 - 3S_5)) - \cos(3\phi) \cos(\phi) x' (-4S_8 + 5S_5 - S_3) \right), \quad (A 12 g)$$

$$I_{pp0} = S_1 + (y - y')^2 S_3, \quad (A 12 h)$$

$$I_{pp1} = S_2 \cos(\phi) + (y - y')^2 S_4 \cos(\phi), \quad (A 12 i)$$

$$I_{pp2} = (2S_6 - S_1) \cos(2\phi) + (y - y')^2 (2S_5 - S_3) \cos(2\phi). \quad (A 12 j)$$

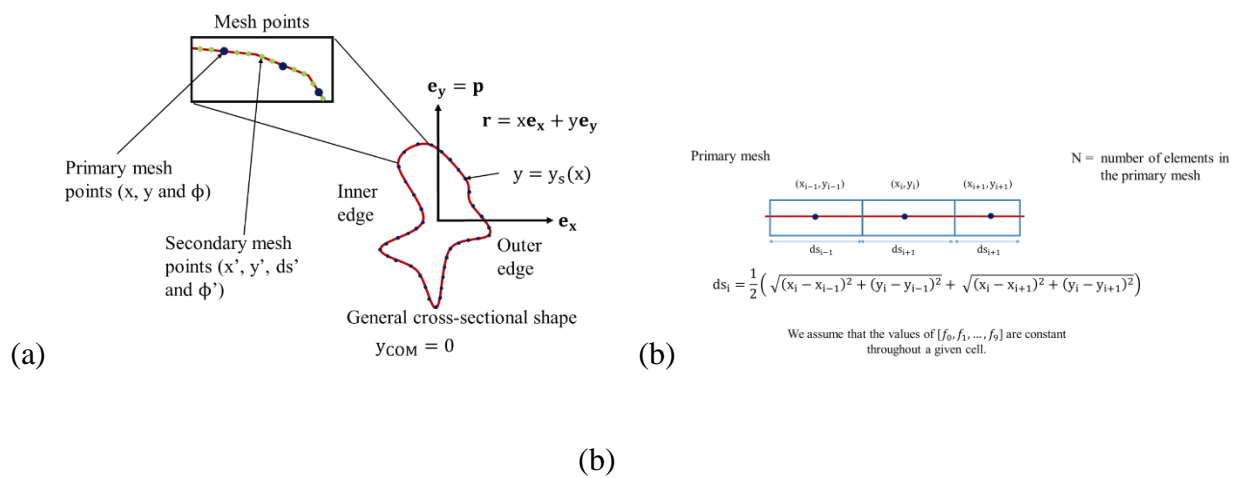
Using expressions in equations (A 10) – (A 12), the inner summation in equation (A 9) can be evaluated to give linear equations for  $[f_0, f_1, \dots, f_9]$  at each mesh point. One gets 3 linear equations for each mesh point using equation (A 9), giving a total of  $3N$  equations for a given value of  $\phi$ .  $10N$  equations can be obtained by evaluating equation (A 9) at four different values of  $\phi$ . We also need to enforce force and torque free condition on the particle using equations (3.6) and (3.7) to obtain the linear and angular velocities of the particle for the mobility problem.

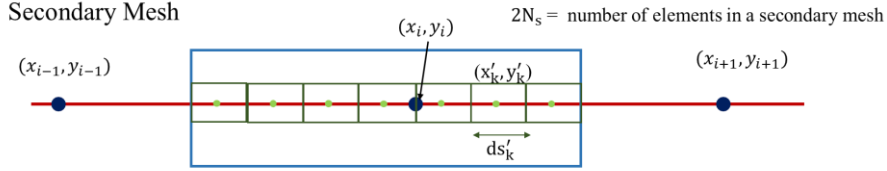
In the limit  $D \rightarrow 1$ ,  $S_1, S_2, \dots, S_{10}$ , as per equation (A 8), become singular, which arises when  $\mathbf{r}'$  approaches  $\mathbf{r}$ . This singularity is logarithmic and integrable. We handled this singularity by analytically evaluating the elliptic integrals using the following asymptotic expansion of the elliptic integrals (Lee and Leal, 1982):

$$K = \ln\left(\frac{4}{D'}\right) + \frac{1}{2}\left(\ln\left(\frac{4}{D'}\right) - 1\right) D'^2 + \frac{9}{64}\left(\ln\left(\frac{4}{D'}\right) - \frac{7}{6}\right) D'^4, \quad (\text{A 13 a})$$

$$E = 1 + \frac{1}{2}\left(\ln\left(\frac{4}{D'}\right) - \frac{1}{2}\right) D'^2 + \frac{3}{16}\left(\ln\left(\frac{4}{D'}\right) - \frac{13}{12}\right) D'^4, \quad (\text{A 13 b})$$

where  $D' = (1 - D^2)^{0.5}$ . Equations (A 13) are used when  $D' \leq 10^{-3}$ , else  $K$  and  $E$  are evaluated using numerically.





$$\mathbf{X}'_k = \frac{(N_s + 1 - k) \frac{(\mathbf{X}_{i-1} + \mathbf{X}_i)}{2} + (k)\mathbf{X}_i}{N_s + 1}, \quad 1 \leq k \leq N_s$$

$$\mathbf{X}'_k = \frac{(N_s + 1 - k)\mathbf{X}_i + (k) \frac{(\mathbf{X}_{i+1} + \mathbf{X}_i)}{2}}{N_s + 1}, \quad N_s + 1 \leq k \leq 2N_s$$

Here  $\mathbf{X}_i = (x_i, y_i)$  is a primary mesh point, while  $\mathbf{X}'_k = (x'_k, y'_k)$  is secondary mesh point.

$ds'_k$  is the size of the  $k^{th}$  secondary mesh point defined as

$$ds'_k = \frac{1}{2} \left( \sqrt{(x'_k - x'_{k-1})^2 + (y'_k - y'_{k-1})^2} + \sqrt{(x'_k - x'_{k+1})^2 + (y'_k - y'_{k+1})^2} \right)$$

This discretization ensures that the primary and secondary mesh point never coincide. The value of  $[f_0, f_1, \dots, f_9]$  at each secondary mesh point of the  $i^{th}$  primary cell is equal to the value of  $[f_0, f_1, \dots, f_9]$  for this primary mesh point.

(c)

Figure A.1. Schematic of the two meshes used in the calculation of the numerical integration of equation (3.1 a). The coefficients  $[f_0, f_1, \dots, f_9]$  are only evaluated at the primary mesh points and these values are assumed constant over the primary mesh cell. The summation in equation (A 9) is performed using the secondary mesh points, which are subdivisions to the primary mesh, to get an accurate estimate of the Green's function. This secondary mesh is used to for the numerical integral in equation (A 9).

## CHAPTER 3

# Slender body theory for particles with non-circular cross-sections with application to particle dynamics in shear flows

### 1. Introduction

Slender geometries are quite common in the realm of low Reynolds number fluid mechanics. Many microorganisms such as *E. coli* (Berg and Anderson 1973), *Chlamydomonas* (Bray 2000), *Paramecium* (Brennen and Winet 1977) or human spermatozoa (Suarez and Pacey 2006) use slender appendages to navigate through viscous fluid environments. The orientation distribution of plankton, some of which have elongated geometries, in the ocean is known to strongly influence the propagation of light in the deeper levels which can significantly influence the global carbon fixation (Guasto, Rusconi and Stocker 2012). Slender particles such as fibers are used to make fiber-reinforced composites that have enhanced tensile strength and increased anisotropic thermal conductivity (Tekce, Kumlutas & Tayman 2007). Slender body theory (Cox 1970; Batchelor 1970; Keller and Rubinow 1976; and Johnson 1980) provides a computationally inexpensive route to study the dynamics of slender particles in highly viscous flows. However, the influence of the force per unit length generated by the gradient in the imposed fluid velocity has not been previously embedded in this theory.

The force per unit length experienced by a slender filament with a circular cross-section at low Reynolds number, to leading order, is qualitatively similar to the viscous drag experienced by a long circular cylinder due to its relative motion with the local fluid velocity. Here, the existence of an additional force per unit length driven by the gradient in the imposed fluid velocity and its dependence on the shape of the cross-section is elucidated. In this study, the nature of the velocity disturbance is understood using a regular perturbation of the inner solution of the slender body theory (SBT) formulation. An integral equation is derived for the force per unit length experienced by the slender filament along with its dependence on the cross-sectional geometry. The force per unit length due to the non-circularity of the cross-section, has two components, one which is driven by the gradient in the imposed fluid velocity affecting three-lobed cross-sections (figure 1(c)) and

another driven by the motion of the particle relative to the fluid affecting two-lobed cross-sections (figure 1 (b)), a component first presented by Batchelor (1970). The additional force per unit length driven by the gradient in the fluid velocity is extremely important in the SBT formulation especially for computing the dynamics and rheology of thin particles in a linear flow field. A numerical calculation of the inner solution in a two-dimensional domain is proposed to extend our SBT formulation to particles with a general cross-sectional shape.

The current theory accurately predicts the resistance to rotation and translation of slender triaxial ellipsoids retaining accuracy even when the cross-section has a high-aspect ratio (section 4). In section 5, straight particles with three-lobed cross-sections, illustrated in figure 1 (c), are shown to rotate and translate quasi-periodically in a simple shear flow (SSF) because of the force per unit length driven by the imposed velocity gradient. In contrast, a straight particle with a combination of a two and a three-lobed cross-section, shown in figure 1 (d), can diffuse in space while rotating chaotically. This work allows for the inclusion of these dynamics which can potentially impact the rheology of a suspension of straight particles. In section 6, our theory is utilized to predict the dynamics of rings with non-circular cross-section, and the results remain accurate for cross-sections that deviate significantly from a circle or have aspect ratios as low as 10.

Slender body theory (SBT) allows for an approximate solution of the governing equation modeling a physical phenomenon that is affected by the presence of bodies which are long and thin. The governing equations of highly viscous flows (Stokes flow), potential flows and heat transfer have been solved using the SBT formulation for many applications. Potential flow problems that include animal locomotion (Lighthill (1960, 1971)), force on airship hulls (Munk, 1924), force on wings (Jones, 1946) and ship hydrodynamics (Newman, (1964, 1970)) have been solved using SBT. Steady state heat transfer in composites (Rocha and Acrivos, 1973 (a) & (b); Chen and Acrivos; Acrivos and Shaqfeh, 1988; Shaqfeh 1988; Fredrickson and Shaqfeh, 1989; Mackaplow and Shaqfeh. 1994;) and transient heat transfer in ground-source heat pumps (Beckers, Koch and Tester, 2014) are a few applications of SBT for steady state and transient heat conduction respectively. In the realm of highly viscous flows, problems involving flagellar hydrodynamics (Johnson and Brokaw, 1979), structure and rheology of fiber suspensions (Mackaplow and

Shaqfeh. (1996, 1998); Rahnama, Koch, Iso and Cohen (1993); Rahnama, Koch and Shaqfeh, (1995)) and separation of racemic mixtures of screw shaped particles (Kim and Rae, 1991) have been solved using existing SBT techniques for Stokes flow (Cox (1970); Batchelor (1970); Keller and Rubinow (1976); and Johnson (1980)).

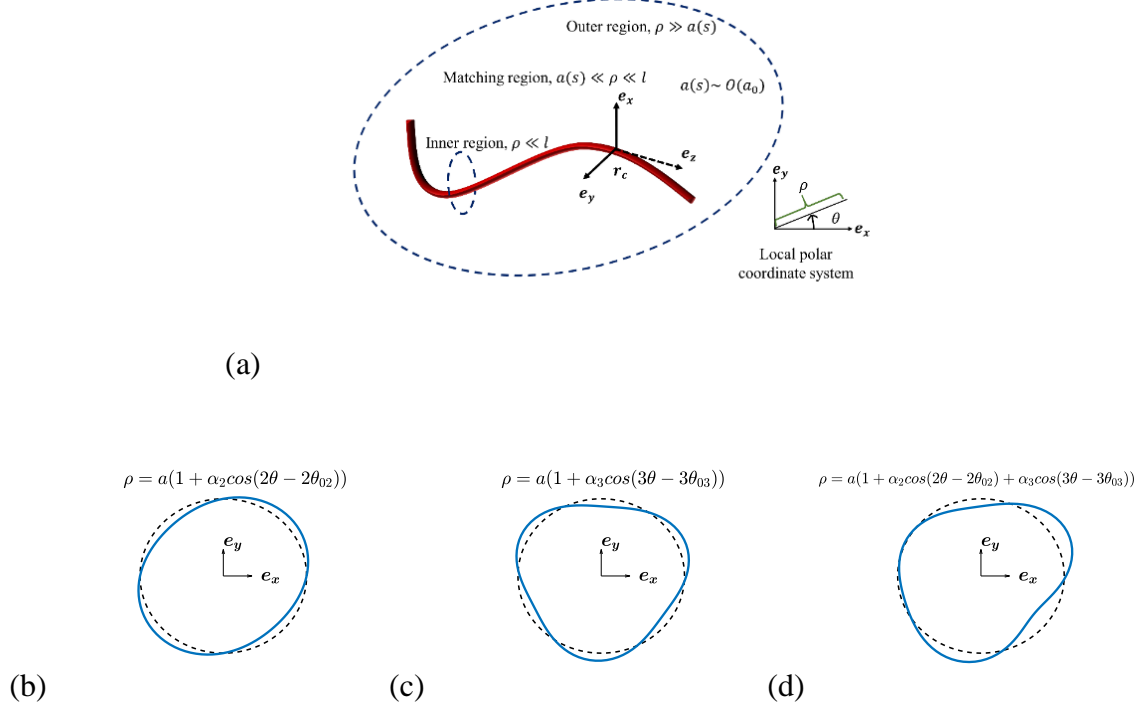


Figure 1. Local coordinate systems in the particle reference frame and the perturbed cross-sectional shapes studied here. (a) Local coordinate system for a general curved body.  $\mathbf{e}_z$  is along the tangent to the filament axis,  $\mathbf{e}_x$  is along the normal and  $\mathbf{e}_y$  is pointed along the binormal to the centerline of the slender body ( $\mathbf{r}_c$ ). (b) Schematic of a two-lobed shape (S-I), given by  $\rho = a(1 + \alpha_2 \cos(2\theta - 2\theta_{02}))$ . (c) Schematic of a three-lobed shape (S-II), given by  $\rho = a(1 + \alpha_3 \cos(3\theta - 3\theta_{03}))$ . (d) Schematic of a shape, which is a linear combination of the two and three lobed perturbations, given by  $\rho = a(1 + \alpha_2 \cos(2\theta - 2\theta_{02}) + \alpha_3 \cos(3\theta - 3\theta_{03}))$  (S-III shape). “ $a$ ” the radius of the equivalent circle is allowed to vary along the centerline of the filament.

The basic idea in SBT is to obtain the strength of a line of singularities placed along the centerline of the slender filament that approximates the field of interest around the filament far

away from the cross-sectional surface, termed as the outer region, i.e,  $a \ll \rho$ . Here  $\rho$  is the radial distance from the centerline of the slender filament, and “ $a$ ” is a measure of the cross-sectional size of the particle at a certain location along the centerline of the slender body as shown in figure 1 (a). The singularity for a potential flow problem is a point source of mass, for a heat transfer problem a point source of heat and for a Stokes flow problem a point force. The strength of the singularities is found by matching the field approximated in the outer region, termed as the outer solution, to a field obtained from the inner region (i.e,  $\rho \ll l$ , where  $l$  is the length of the slender filament). Placing higher order singularities along the centerline of the slender filament gives a better estimate of the field of interest. For a Stokes flow problem, which is the main topic of discussion in this paper, these singularities would include doublets, rotlets, sources, stresslets and quadrupoles (Johnson, 1980).

In Stokes flow, the force per unit length exerted by the body on the fluid (i.e. the strength of the singularity) is derived at each point along the centerline of the slender body in terms of the motion of the particle and the imposed fluid velocity. The length, “ $l$ ”, an appropriate velocity and the fluid viscosity are used to non-dimensionalize all variables throughout this paper unless mentioned otherwise. The force per unit length exerted by a slender body on the fluid, which is due to relative motion of the particle and fluid, can be expressed as a series in  $\epsilon = 1/\ln(2A)$  (Cox, 1970 and Batchelor, 1970), where  $A = l/(a_0)$  is the aspect ratio of the particle and  $a_0$  is the characteristic value of  $a(s)$ . The first term in this series arises only due to the local relative velocity between the particle and the fluid and is  $O(\epsilon)$  (Cox, 1970 and Batchelor, 1970). Cox (1970) was the first to demonstrate that the force per unit length is affected at  $O(\epsilon^2)$  by the centerline curvature (see equations (6.2) and (6.3) of his paper). Keller and Rubinow (1976) gave an integral equation for the force per unit length which can be iteratively solved to obtain higher order corrections to the force per unit length with errors of  $O(\epsilon^N)$ , where  $N$  is an integer such that  $N \geq 2$ . Johnson (1980) produced an integral equation for the force per unit length with errors of  $O(1/A^2)$  which also included the effects of the ends of the slender body (equation (19) of his paper). Johnson (1980) also described a method to incorporate the effect of centerline curvature in the inner solution (equation (31) of his paper).

Batchelor (1970) showed that the cross-sectional shape of the particle first affects the force per unit length at  $O(\epsilon^2)$ , the same order of importance as the centerline curvature of the body. Batchelor (1970) described how the force per unit length for an arbitrary cross-section can be found by solving for the longitudinal velocity field due to an equivalent circle of a certain radius, and the transverse velocity field due to an equivalent ellipse of certain dimensions and orientation. Batchelor (1954) provided the method to obtain the equivalent circular cylinder by solving the harmonic equation for the flow along the longitudinal direction. Batchelor (1970) described the procedure to obtain an equivalent ellipse by solving the biharmonic equation for the velocity field in the transverse plane around the cross-sectional shape in question.

Cox (1971) was the first to account for the effect of the gradient in the imposed velocity of a linear flow field on the force and torque acting on a slender cylinder with tapered ends, which was oriented such that the imposed velocity field at the particle centerline is exactly zero. Cox placed a force and dipole per unit length along the centerline of the body to approximate the velocity field in the outer region, while Keller and Rubinow (1976) employed a stresslet and rotlet per unit length for the same purpose. Singh, Koch, Subramanian and Stroock (2014) discuss the equivalence of these two formulations by showing that the variation of the force per unit length leads to a net stresslet and a rotlet on a slice of the particle. The rotlet per unit length can lead to a finite torque on the particle whereas a variable stresslet per unit length, which occurs when the particle cross-section varies along the longitudinal direction, can lead to a finite force acting on the particle of  $O(\epsilon^2/A^2)$ . A straight circular cylinder with a constant cross-section cannot experience a force per unit length at this orientation if the cross-section is circular. However, the force per unit length due to the velocity gradient can be non-zero if the cross-section is non-circular. This force per unit length, which will be  $O(\epsilon/A)$  as explained in section 3, can lead to a net force of  $O(\epsilon/A)$  acting on the particle.

In this paper, the additional  $O(\epsilon/A)$  contribution to the force per unit length in addition to Batchelor's correction of  $O(\epsilon^2)$  is derived in section 3. This calculation is especially important when considering motion of force and torque-free slender particles in SSF. In such scenarios, Batchelor's correction tends to zero for certain particle orientations, while Cox's (1971) correction predicts a much smaller effect on the particle rotation rate. Thus, both previous theories lead to an

incorrect qualitative behavior for particle geometries such as straight cylinders with elliptic cross-sections (Yarin, Gottlieb and Roisman 1997) or rings with 3-lobed cross-sections (Singh, Koch and Stroock, 2013) in SSF.

## 2. SBT solution for circular cross-section

In this section, the velocity disturbance created by a slender particle with a circular cross-section, when placed in a fluid moving with a velocity  $\mathbf{u}_\infty$  in the absence of the particle is described. This calculation will be used to obtain the effect of the cross-sectional shape in section 3. The slenderness parameter or the aspect ratio ( $A = l/(a_0)$ ), is defined as the ratio of the half-length of the filament ( $l$ ) and a measure of the radius of the cross-section ( $a_0$ ). The radius of the cross-section,  $a \sim O(a_0)$ , is allowed to vary along the longitudinal direction of the slender body. The position vector is denoted by  $\mathbf{r}$  and  $\mathbf{r}_c$  denotes the position of the centerline of the slender filament. A local coordinate system ( $\mathbf{e}_x, \mathbf{e}_y, \mathbf{e}_z$ ) is chosen based on the tangent ( $\mathbf{e}_z$ ), normal ( $\mathbf{e}_x$ ) and binormal ( $\mathbf{e}_y$ ) to the centerline of the slender body, as shown in figure 1 (a), and is mathematically given by

$$\mathbf{e}_z = \frac{\partial \mathbf{r}_c}{\partial s}, \mathbf{e}_x = \frac{1}{\kappa} \frac{\partial^2 \mathbf{r}_c}{\partial s^2}, \mathbf{e}_y = \mathbf{e}_z \times \mathbf{e}_x, \quad (2.1)$$

where  $\kappa$  is the local curvature of the body centerline and ' $s$ ' specifies the position along the centerline such that  $-1 \leq s \leq 1$  and  $|s|$  is the non-dimensional arc length measured from a point equidistant from the two ends of the filament.

where  $\kappa$  is the local curvature of the body centerline and “ $s$ ” specifies the position along the centerline such that  $-1 \leq s \leq 1$ , the extreme values of  $\pm 1$  being at the ends of the particle. A local polar coordinate system ( $\rho-\theta$ ), as shown in figure 1 (a), is defined in the  $\mathbf{e}_x - \mathbf{e}_y$  plane, where  $\theta$  is measured from  $\mathbf{e}_x$  and  $\rho$  is the normal distance from the centerline. The far-field fluid velocity is denoted by  $\mathbf{u}_\infty$ , which is allowed to vary with  $\mathbf{r}$ . The velocity on the particle surface ( $\mathbf{r} = \mathbf{r}_s$ ) is given by

$$\mathbf{u}(\mathbf{r} = \mathbf{r}_s) = \mathbf{U} + \boldsymbol{\omega} \times \mathbf{r}_s = (\mathbf{U} + \boldsymbol{\omega} \times \mathbf{r}_c) + \boldsymbol{\omega} \times (\mathbf{r}_s - \mathbf{r}_c), \quad (2.2)$$

where  $\mathbf{U}$  and  $\boldsymbol{\omega}$  are the particle velocity at the origin ( $\mathbf{r} = \mathbf{0}$ ) and angular velocity of the particle respectively. These definitions are valid for any cross-sectional shape. The rest of this section describes the slender body theory solution for a circular cross-section of radius “a”. The force per unit length and all the unknown constants in the inner solution, which are required for the perturbation analysis in section 3, are obtained in this section.

## 2.1 Velocity field in the inner region ( $\rho \ll 1$ )

Any curved slender body with  $O(1)$  curvature appears locally as a straight infinite cylinder to a first approximation. The velocity field in the inner region is obtained by assuming flow over an infinite cylinder. Thus, the flow along and transverse to the cylinder is solved separately. Any coupling between these flows arises due to curvature and finite aspect ratio of the particle and leads to algebraic  $O(1/A^2)$  corrections to the velocity disturbance (Johnson 1980) which are not discussed here. The functional form of the flow in the transverse plane is obtained by solving a two-dimensional Stokes flow problem that satisfies the no-slip condition on the particle surface. The far field boundary condition is applied later while asymptotically matching the velocity fields from the inner and outer regions to obtain any unknowns. The solution to the biharmonic equation ( $\nabla^4\psi = 0$ ) is used to obtain the functional form of the velocity field in the plane transverse to the slender dimension. The two-dimensional velocity field is obtained from the definition of the stream function, i.e.,  $u_\rho = \rho^{-1}d\psi/d\theta$  and  $u_\theta = -d\psi/d\rho$ . The solution around a circular cross-section of radius “a” in terms of the stream-function ( $\psi$ ) in polar coordinates is given by

$$\frac{\psi}{a} = \left(\frac{\tilde{\psi}}{a}\right) + [B \cos(\theta) + \hat{B} \sin(\theta)] \left[ \left(\frac{\rho}{a}\right) - \left(\frac{\rho}{a}\right)^{-1} - 2 \ln\left(\frac{\rho}{a}\right) \left(\frac{\rho}{a}\right) \right] + [(\mathbf{U} + \boldsymbol{\omega} \times \mathbf{r}_c) \cdot (\mathbf{e}_x \sin(\theta) - \mathbf{e}_y \cos(\theta))] \left[ \left(\frac{\rho}{a}\right)^{-1} + 2 \frac{\rho}{a} \ln\left(\frac{\rho}{a}\right) \right] - (\boldsymbol{\omega} \cdot \mathbf{e}_z) a \ln\left(\frac{\rho}{a}\right), \quad (2.3)$$

where  $\tilde{\psi}$  is the stream function that approaches the stream function of the imposed flow field for  $\rho \gg a$ , while satisfying the zero-velocity boundary condition on the particle surface.  $B$  and  $\hat{B}$  are obtained by matching this velocity field to the one from the outer region and depend on the force per unit length acting on the slender body, the imposed flow field and the particle velocities ( $\mathbf{U}$  and  $\boldsymbol{\omega}$ ). The velocity in polar coordinates in the inner region is given by

$$u_\rho = \frac{1}{\rho} \frac{\partial \psi}{\partial \theta} = \frac{1}{\rho} \frac{\partial \tilde{\psi}}{\partial \theta} + [ -B \sin(\theta) + \hat{B} \cos(\theta) ] \left[ 1 - \left( \frac{\rho}{a} \right)^{-2} - 2 \ln \left( \frac{\rho}{a} \right) \right] + [ (\mathbf{U} + \boldsymbol{\omega} \times \mathbf{r}_c) \cdot (\mathbf{e}_x \cos(\theta) + \mathbf{e}_y \sin(\theta)) ] \left[ \left( \frac{\rho}{a} \right)^{-2} + 2 \ln \left( \frac{\rho}{a} \right) \right], \quad (2.4)$$

$$u_\theta = -\frac{\partial \psi}{\partial \rho} = -\frac{\partial \tilde{\psi}}{\partial \rho} + [ B \cos(\theta) + \hat{B} \sin(\theta) ] \left[ 1 - \left( \frac{\rho}{a} \right)^{-2} + 2 \ln \left( \frac{\rho}{a} \right) \right] + [ (\mathbf{U} + \boldsymbol{\omega} \times \mathbf{r}_c) \cdot (\mathbf{e}_x \sin(\theta) - \mathbf{e}_y \cos(\theta)) ] \left[ \left( \frac{\rho}{a} \right)^{-2} - 2 - 2 \ln \left( \frac{\rho}{a} \right) \right] + \boldsymbol{\omega} \cdot \mathbf{e}_z a \left( \frac{\rho}{a} \right)^{-1}. \quad (2.5)$$

The velocity along the longitudinal direction is obtained by assuming negligible change in pressure along the longitudinal direction (i.e.  $\nabla^2 u_z = 0$ ). The velocity field along a slender filament with circular cross-section is given by

$$u_z = \tilde{u}_z + E \ln \left( \frac{\rho}{a} \right) + (\mathbf{U} + \boldsymbol{\omega} \times \mathbf{r}_c) \cdot \mathbf{e}_z + \left( \frac{\rho}{a} \right)^{-1} (\boldsymbol{\omega} \cdot \mathbf{e}_x a \sin(\theta) - \boldsymbol{\omega} \cdot \mathbf{e}_y a \cos(\theta)), \quad (2.6)$$

where  $\tilde{u}_z$  is the velocity field that approaches  $\mathbf{u}_\infty \cdot \mathbf{e}_z$  for  $\rho/a \gg 1$ , and equals zero on the particle surface,  $E$  is obtained by matching the inner region velocity field to the outer solution and depends on the imposed flow field, the particle velocities ( $\mathbf{U}$  and  $\boldsymbol{\omega}$ ) and the force per unit length on the filament. The overall error in equations (2.4) - (2.6) is the larger of  $O(1/A^2)$  and the order of errors in  $B, \hat{B}$  and  $E$ , determined by matching the inner velocity field to the outer solution.

## 2.2 Velocity field in the outer region ( $\rho \gg a(s)$ )

In the outer region, the velocity disturbance due to a slender filament is approximately captured by a suitable choice of Stokeslet distribution along the particle centerline ( $\mathbf{r}_c$ ) (Cox, 1970). A Stokeslet is a point force solution to the Stokes equations. The velocity disturbance created by a line of force per unit length is given by

$$\mathbf{u}(\mathbf{r}) \approx \mathbf{u}_\infty(\mathbf{r}) + \frac{1}{8\pi} \int_{\mathbf{r}_c} ds' \left( \frac{\mathbf{I}}{|\mathbf{r}-\mathbf{r}'|} + \frac{(\mathbf{r}-\mathbf{r}')(\mathbf{r}-\mathbf{r}')}{|\mathbf{r}-\mathbf{r}'|^3} \right) \cdot \mathbf{f}(\mathbf{r}'), \quad (2.7)$$

where  $\mathbf{r}$  is the point at which the velocity is evaluated,  $\mathbf{r}'$  takes all values along the centerline and  $ds'$  is the elemental length along the centerline of the slender body. Equation (2.7) has errors of

$O(1/A^2)$ . As  $\mathbf{r}' \rightarrow \mathbf{r}$ , the integrand in equation (2.7) diverges as  $\ln(\rho)$ . This diverging part of the integral in equation (2.7) is separated from the rest of the integral as shown by Keller and Rubinow (1976) and the resulting equation for  $\rho \ll 1$  is given by

$$\begin{aligned} \mathbf{u}(\mathbf{r}) \approx \mathbf{u}_\infty(\mathbf{r}) - \frac{1}{4\pi} (\mathbf{I} + \mathbf{e}_z \mathbf{e}_z) \cdot \mathbf{f}(\mathbf{r}) \left[ \ln\left(\frac{\rho}{2}\right) - \ln(\sqrt{1-s^2}) \right] - \frac{1}{4\pi} \mathbf{f} \cdot \mathbf{e}_z \mathbf{e}_z + \frac{1}{4\pi} \mathbf{f} \cdot \mathbf{e}_\rho \mathbf{e}_\rho + \\ \frac{1}{8\pi} \int_{-1}^1 ds' \left[ \left( \frac{\mathbf{I}}{|\mathbf{r}_c(s) - \mathbf{r}_c(s')|} + \frac{(\mathbf{r}_c(s) - \mathbf{r}_c(s'))(\mathbf{r}_c(s) - \mathbf{r}_c(s'))}{|\mathbf{r}_c(s) - \mathbf{r}_c(s')|^3} \right) \cdot \mathbf{f}(\mathbf{r}') - \left( \frac{\mathbf{I}}{|s-s'|} + \frac{\mathbf{e}_z \mathbf{e}_z}{|s-s'|} \right) \cdot \mathbf{f}(\mathbf{r}) \right], \end{aligned} \quad (2.8)$$

where  $\mathbf{e}_\rho$  is the radial vector in the  $\mathbf{e}_x - \mathbf{e}_y$  plane. The integral on the right-hand-side of equation (2.8) is shown to have a finite limit by Keller and Rubinow (1976). The  $\ln(\rho)$  term in equation (2.8), matches the  $\ln(\rho)$  of the inner solution in equations (2.4)- (2.6) and also corresponds to the velocity disturbance produced by an infinite cylinder with the same force per unit length at each point.

### 2.3 Matching region ( $a \ll \rho \ll 1$ )

The velocity produced from the inner solution for  $\rho \gg a$ , should asymptotically match the velocity field from the outer solution for  $\rho \ll 1$  as the velocity field cannot abruptly change in this matching region (i.e.  $a \ll \rho \ll 1$ ). Matching the velocity fields from the inner and outer solutions, using equations (2.4)-(2.6) and (2.8), yields the constants in the inner solution,  $\hat{B} = (\mathbf{U} + (\boldsymbol{\omega} \times \mathbf{r}_c)) \cdot \mathbf{e}_x + \frac{f_x}{8\pi}$ ,  $B = -(\mathbf{U} + (\boldsymbol{\omega} \times \mathbf{r}_c)) \cdot \mathbf{e}_y - \frac{f_y}{8\pi}$  and  $E = -\frac{4f_z}{8\pi}$ , and leads to an integral equation for the force per unit length given by

$$\begin{aligned} \frac{f(\mathbf{r})}{8\pi} = \frac{\epsilon}{2} \left( \mathbf{I} - \frac{\mathbf{e}_z \mathbf{e}_z}{2} \right) \cdot \left\{ \mathbf{U} + \boldsymbol{\omega} \times \mathbf{r}_c - \mathbf{u}_\infty(\mathbf{r}_c) - \frac{1}{8\pi} (\mathbf{I} - 3\mathbf{e}_z \mathbf{e}_z) \cdot \mathbf{f}(\mathbf{r}) - \frac{1}{4\pi} (\mathbf{I} + \mathbf{e}_z \mathbf{e}_z) \cdot \right. \\ \mathbf{f}(\mathbf{r}) \ln\left(\frac{\sqrt{1-s^2}}{\frac{a(s)}{a_0}}\right) - \frac{1}{8\pi} \int_{-1}^1 ds' \left[ \left( \frac{\mathbf{I}}{|\mathbf{r}_c(s) - \mathbf{r}_c(s')|} + \frac{(\mathbf{r}_c(s) - \mathbf{r}_c(s'))(\mathbf{r}_c(s) - \mathbf{r}_c(s'))}{|\mathbf{r}_c(s) - \mathbf{r}_c(s')|^3} \right) \cdot \mathbf{f}(\mathbf{r}') - \left( \frac{\mathbf{I}}{|s-s'|} + \frac{\mathbf{e}_z \mathbf{e}_z}{|s-s'|} \right) \cdot \mathbf{f}(\mathbf{r}) \right] \left. \right\}. \end{aligned} \quad (2.9)$$

The leading order force per unit length  $\mathbf{f} = 4\pi\epsilon(\mathbf{U} + \boldsymbol{\omega} \times \mathbf{r}_c - \mathbf{u}_\infty(\mathbf{r}_c)) \cdot \left( \mathbf{I} - \frac{\mathbf{e}_z \mathbf{e}_z}{2} \right) (1 + O(\epsilon))$ , suggests that a slender filament of any arbitrary cross-section experiences an  $O(\epsilon)$  viscous drag equal to the viscous drag per unit length experienced by a long cylinder due to its motion relative to the local fluid velocity. The higher order terms in equation (2.9) include the additional drag due to the relative motion of the particle and the local velocity as well as a contribution that comes from the velocity disturbance created by the particle itself.

### 3. SBT solution for non-circular cross-sections

In this section the  $O(\alpha\epsilon/A)$  force per unit length exerted by the filament for a slightly non-circular cross-section is derived along with the  $O(\alpha\epsilon^2)$  correction to the force per unit length derived by Batchelor (1970).  $\alpha$  is the perturbation parameter that quantifies the degree of non-circularity. The cross-sectional shapes that trigger these respective contributions are obtained from thought experiments. Finally, a strategy to extend our perturbation analysis to particles with  $\alpha \sim O(1)$  is demonstrated towards the end of this section.

#### 3.1 Regular perturbation of the inner solution

A slightly non-circular cross-section can be described by  $\rho = a(1 + \alpha h(s, \theta))$ , where  $\alpha \ll 1$ ,  $h(s, \theta)$  is a smooth and bounded function periodic in  $\theta$  with a period of  $2\pi/N$ , where  $N$  is any positive integer, such that  $\max|h(s, \theta)| \sim O(1)$  and  $|\partial h/\partial s| \sim O(1)$ . The derivative  $\partial h/\partial \theta$  cannot be zero, as that corresponds to a larger circular cross-section, thereby only changing the particle aspect ratio. The inner velocity field obtained in section 2 will be modified to satisfy the no slip boundary condition at the new surface,  $\rho = a(1 + \alpha h)$ . The additional velocity field in the transverse plane ( $\mathbf{e}_x - \mathbf{e}_y$  plane), is described using a stream function ( $\alpha \psi'$ ), such that  $\psi' \sim O(1)$  for  $\rho/a \sim O(1)$ .  $\psi'$  is given by an equation of the same form as equation (2.3), but with different constants from those obtained for  $\psi$ . The terms in  $\psi'$  corresponding to a decaying velocity field with increasing values of  $\rho/a$  can be obtained by satisfying the no-slip boundary condition at  $O(\alpha)$  for the velocity obtained using the stream function ( $\psi + \alpha\psi'$ ). These constants will depend on  $h$ ,  $\tilde{\psi}$ ,  $B$ ,  $\hat{B}$  and  $\mathbf{U}$  and  $\boldsymbol{\omega}$  all of which are either known or obtained from the analysis done for a slender

filament with a circular cross-section in section 2. The non-decaying terms in  $\psi'$  used during the matching process are given by

$$\alpha \psi' = \alpha \left[ -(C' \cos(\theta) + D' \sin(\theta)) \left( \left( \frac{\rho}{a} \right) \ln \left( \frac{\rho}{a} \right) \right) + (B' \cos(\theta) + \hat{B}' \sin(\theta)) \left( \left( \frac{\rho}{a} \right) - 2 \ln \left( \frac{\rho}{a} \right) \left( \frac{\rho}{a} \right) \right) \dots \right], \quad (3.1)$$

where  $C'$  and  $D'$  are constants that are obtained by satisfying the no-slip condition on the particle surface,  $\rho = a(1 + \alpha h)$ , while  $B'$  and  $\hat{B}'$  are obtained by matching with the outer solution and play the same role as  $B$  and  $\hat{B}$  played in the analysis for a circular cross-section. The “...” in equation (3.1) corresponds to the additional terms in the stream function necessary to satisfy the no-slip boundary condition on the particle surface that do not participate in the matching process. The corresponding terms in the fluid velocities used in the matching solution are given by

$$\alpha u'_\rho = \alpha \left[ (C' \sin(\theta) - D' \cos(\theta)) \left( \ln \left( \frac{\rho}{a} \right) \right) + (-B' \sin(\theta) + \hat{B}' \cos(\theta)) \left( 1 - 2 \ln \left( \frac{\rho}{a} \right) \right) \dots \right], \quad (3.2)$$

$$\alpha u'_\theta = \alpha \left[ (C' \cos(\theta) + D' \sin(\theta)) \left( 1 + \ln \left( \frac{\rho}{a} \right) \right) + (B' \cos(\theta) + \hat{B}' \sin(\theta)) \left( 1 + 2 \ln \left( \frac{\rho}{a} \right) \right) \dots \right]. \quad (3.3)$$

From equation (3.2) it can be easily seen that  $C'$  and  $D'$  do not enter the  $u_\rho$  boundary condition at  $O(\alpha)$ .  $C'$  and  $D'$ , which occur in the  $u_\theta$  boundary condition, are given by

$$C' = \frac{1}{\pi} \int_0^{2\pi} d\theta \cos(\theta) \left\{ -\frac{d}{d\alpha} \left( -\frac{\partial \tilde{\psi}}{\partial \rho} \Big|_{\rho=a(1+\alpha h(s,\theta))} \right)_{\alpha=0} + 4 h(\theta) \left[ -\frac{f_x}{8\pi} \sin(\theta) + \frac{f_y}{8\pi} \cos(\theta) \right] \right\}, \quad (3.4)$$

$$D' = \frac{1}{\pi} \int_0^{2\pi} d\theta \sin(\theta) \left\{ -\frac{d}{d\alpha} \left( -\frac{\partial \tilde{\psi}}{\partial \rho} \Big|_{\rho=a(1+\alpha h(s,\theta))} \right)_{\alpha=0} + 4 h(\theta) \left[ -\frac{f_x}{8\pi} \sin(\theta) + \frac{f_y}{8\pi} \cos(\theta) \right] \right\}. \quad (3.5)$$

The first terms in the integrands of equations (3.4) and (3.5) are of  $O(1/A)$  and are related to the force per unit length driven by the gradient in the imposed fluid velocity as will be explained in section (3.2). The remainder of the  $O(\epsilon)$  terms in the integrand of equations (3.4) and (3.5) occur due to the velocity disturbance created by the force per unit length of the unperturbed circular cross-section and are thereby driven by the motion of the particle relative to the local fluid velocity.

The function  $h(s, \theta)$  is expanded as a Fourier series to understand the effect of the cross-sectional shapes that affect  $C'$  and  $D'$ .  $h(s, \theta)$  is given by

$$h(s, \theta) = \sum_{m=1}^{\infty} h_m(s) \cos(m(\theta - \theta_{0m})), \quad (3.6)$$

where coefficients  $h_m$ , and  $\theta_{0m}$ , for  $m = 1, 2, \dots$ , are constants obtained using the orthogonality of  $\cos(m(\theta - \theta_{0m}))$ . The effects of the Fourier modes of  $h$  can be summed up to get the overall effect of the shape as the analysis is done at linear order in  $\alpha$ . The cross-sectional shape,  $\rho = a(1 + \alpha h_m \cos(m\theta - m\theta_{0m}))$ , corresponding to the  $m^{th}$  Fourier mode has an  $m$ -fold rotational symmetry and  $m$ -lobes where one of the lobes makes an angle of  $\theta_{0m}$  with  $e_x$ . The first Fourier mode only changes the position of the cross-section without distorting the shape at linear order in  $\alpha$ . Thus, particles with only the first Fourier mode can be studied using the SBT formalism explained in section two, by redefining the particle centerline so that it passes through the new center of the cross-section. The other Fourier modes can affect the force per unit length in a non-trivial way. Substituting equation (3.6) in equations (3.4) and (3.5), suggests that only the second Fourier mode will affect  $C'$  and  $D'$  at  $O(\epsilon)$ . The corresponding cross-sectional shape  $\rho = a(1 + \alpha h_2 \cos(2\theta - 2\theta_{02}))$  is approximately an ellipse of eccentricity  $\sqrt{4\alpha h_2}$  whose major axis is at an angle  $\theta_{02}$  as shown in figure 1 (b). The Fourier modes of a shape that affect  $C'$  and  $D'$  at  $O(1/A)$  depend on the specific nature of  $\tilde{\psi}$  as can be seen by substituting  $\rho = a(1 + \alpha h)$  in the expression for  $(-\partial \tilde{\psi} / \partial \rho)$ . If the imposed velocity field has terms that scale with  $\rho^N$ , for  $N \geq 1$ , then the

$(N - 2)^{\text{th}}$ ,  $(N)^{\text{th}}$  and  $(N + 2)^{\text{th}}$  Fourier modes of  $h$  will affect  $C'$  and  $D'$  (equation (S 1.4) of appendix). If  $N = 1$ , which corresponds to a linear imposed velocity field, then only the third Fourier mode will affect the  $O(1/A)$  term in equations (3.4) and (3.5) and the corresponding three-lobed cross-sectional shape is given by  $\rho = a(1 + \alpha h_3 \cos(3\theta - 3\theta_{03}))$  which is shown in figure 1 (c). If the imposed fluid velocity changes on the length scale of the particle cross-sectional size, then the contribution of the terms in  $\tilde{\psi}$  which scale with  $\rho^{N+1}$  to  $C'$  and  $D'$  will be  $O(1/A^N)$ , which is algebraically smaller than the contribution to  $C'$  and  $D'$  due to a linear flow field for  $N \geq 2$ . Therefore, in the remainder of the paper the focus is only on a linear flow field, i.e.  $\tilde{\psi}$  grows as  $\rho^2$ . In this case, the cross-sectional shapes shown in figures 1(b)-(d) can affect the force per unit length due to non-circularity.

Thought experiments are presented using two-dimensional Stokes flow problems to gain physical insight into why only the second and third Fourier mode perturbations to a circle change the force per unit length acting on a long cylinder. Consider a two-dimensional obstacle, whose shape is a second Fourier mode perturbation to a circle, that is placed in a uniform flow field. This body experiences a lift force, unless the imposed fluid velocity is along one of its two axes of symmetries as shown in figure 2 (a). The third and higher Fourier mode perturbations to a circle have at least a two-fold rotational symmetry in a two-dimensional space. An  $N$ -fold rotational symmetry means that the shape looks the same after rotating it by any integer multiple of  $2\pi/N$ . These cross-sections cannot generate a lift force in a 2-D uniform flow along at least two non-colinear directions,  $\mathbf{n}_1$  and  $\mathbf{n}_2$  as shown in figure 2 (b), due to fore-aft symmetry. Thereby such a cross-section should experience no lift for all cross-sectional orientations by linear superposition. This is analogous to our result obtained earlier that only slender particles with cross-sections with a second Fourier mode perturbation to a circle will experience an additional force per unit length.

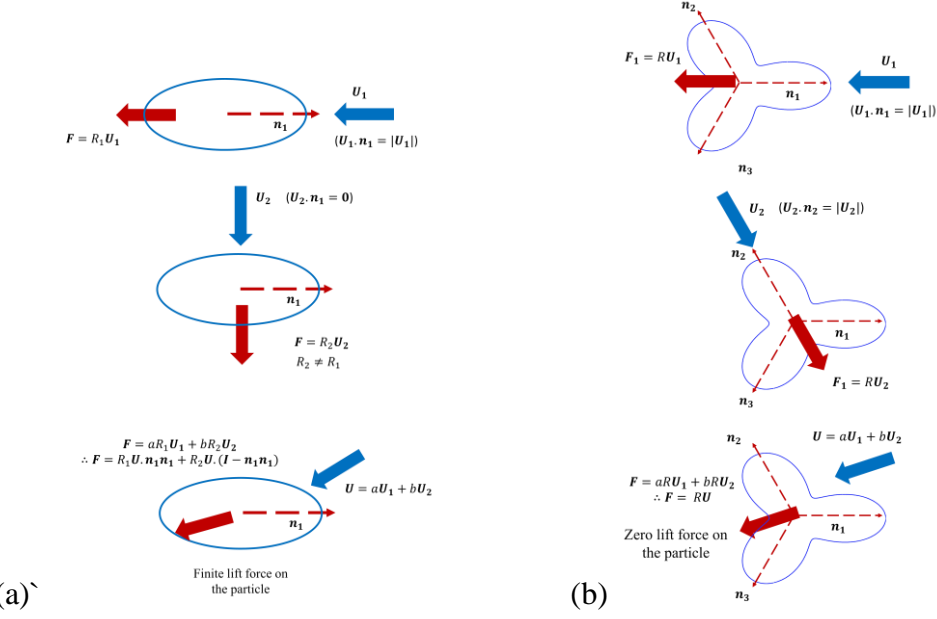


Figure 2. Schematic of thought experiments to intuitively understand the importance of the second Fourier mode perturbation to a circle. (a) Finite lift on a second Fourier mode perturbation of a circle. (b) Zero lift force on a cross-section with a three lobed cross-section which is obtained from the third Fourier mode perturbation to a circle. This zero lift is true for the third and any higher Fourier mode perturbation to a circle.

To gain insight into the force per unit length driven by the gradient in the imposed fluid velocity, consider a cross-section placed in a general linear flow field and note that at  $O(\alpha)$  the influence of the Fourier mode perturbations can be linearly superimposed. Only the extensional component of the flow influences the force per unit length,  $\tilde{\mathbf{f}}$ . Using the linearity of Stokes equations,  $\tilde{\mathbf{f}}$  is given by

$$\tilde{\mathbf{f}} = \xi_1 \mathbf{E}_\infty : \mathbf{n}_k \mathbf{n}_k \mathbf{n}_k + \xi_2 \mathbf{E}_\infty \cdot \mathbf{n}_k, \quad (3.7 \text{ a})$$

where  $\mathbf{E}_\infty$  is the straining tensor of the linear flow field and  $\mathbf{n}_k = [\cos(\frac{2\pi k}{n}), \sin(\frac{2\pi k}{n})]$  with  $k = 0, 1, \dots, (n-1)$  being the orientations along the lines of symmetry of the  $n^{th}$  Fourier mode perturbation to the circle ( $n \geq 2$ ). Choosing  $\mathbf{E}_\infty = \begin{bmatrix} 0 & 1 \\ 1 & 0 \end{bmatrix}$ ,  $\tilde{\mathbf{f}}$  can be written as

$$\tilde{\mathbf{f}} = \begin{bmatrix} \left(2 \cos^2\left(\frac{2\pi}{n}k\right)\xi_1 + \xi_2\right) \sin\left(\frac{2\pi}{n}k\right) \\ \left(2 \sin^2\left(\frac{2\pi}{n}k\right)\xi_1 + \xi_2\right) \cos\left(\frac{2\pi}{n}k\right) \end{bmatrix} = \begin{bmatrix} 0 \\ \xi_2 \end{bmatrix}_{k=0} \quad (3.7 \text{ b})$$

where the second equality gives the value  $\tilde{\mathbf{f}}$  at  $k = 0$ .  $\tilde{\mathbf{f}}$  as per equation (3.7 b) can be identical and non-zero for  $\forall k \in \{0, 1, \dots, (n - 1)\}$  only for the third Fourier mode perturbations to a circle. Identical values of  $\tilde{\mathbf{f}}$  for any other Fourier mode perturbation would require  $\xi_1 = \xi_2 = 0$  implying  $\tilde{\mathbf{f}} = \mathbf{0}$ . This implies that at linear order in the perturbation parameter, the force per unit length is only affected by the third Fourier mode perturbation to a circle. One can get a visual picture for the existence of  $\tilde{\mathbf{f}} = [0 \ \xi_2]$ , using our linear perturbation analysis for  $u'_\theta$ . For  $\mathbf{E}_\infty = \begin{bmatrix} 0 & 1 \\ 1 & 0 \end{bmatrix}$ , the perturbation to the tangential velocity  $\alpha_3 u'_\theta = -\alpha_3(4 \cos(2\theta) \cos(3\theta))$  is required to satisfy the no-slip condition on the particle surface. The direction of  $u'_\theta$  shown in figure 3, suggests that  $u'_\theta$  points along  $-\mathbf{e}_y$  for  $\theta \in \{(0, \pi/6), (\pi/4, 3\pi/4), (5\pi/6, 7\pi/6), (5\pi/4, 7\pi/4), (11\pi/6, 2\pi)\}$  and points along  $\mathbf{e}_y$  for the remaining narrow portions of angular space. A net average velocity along  $(-\mathbf{e}_y)$  is required to satisfy the no-slip boundary condition which leads to the force  $\tilde{\mathbf{f}} = (0, \xi_2)$  along that direction.

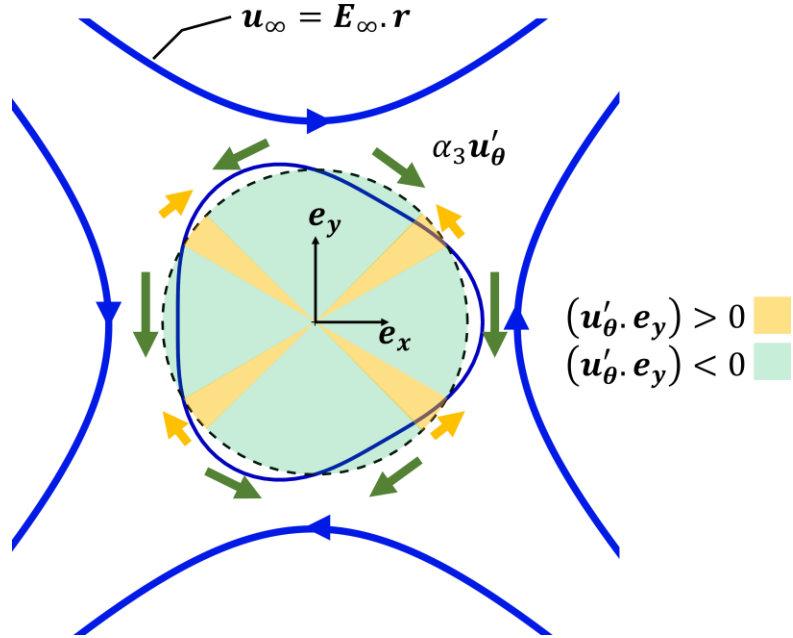


Figure 3. Direction of the perturbation to the tangential velocity on the particle surface  $\alpha_3 u'_\theta = -\alpha_3(4 \cos(2\theta) \cos(3\theta))$  necessary to satisfy the no-slip condition suggesting a need for a force along  $\mathbf{e}_y$ .

The additional terms in the longitudinal velocity field used during the matching process are given by

$$\alpha u'_z = \alpha e'_0 + \alpha E' \ln\left(\frac{\rho}{a}\right) + \dots, \quad (3.8)$$

where  $e'_0$  is obtained from the no-slip boundary condition and  $E'$  is determined by matching the inner solution to the outer solution in a similar manner to obtaining  $E$ . Substituting  $\rho = a(1 + \alpha h)$  in equation (2.8), it can be shown that there is no term of  $O(\alpha)$  which does not depend on  $\theta$ , and therefore  $e'_0$  is zero.

The velocity field in the inner region for a cross-section given by  $\rho = a(1 + \alpha h)$ , which could be obtained from equations (2.4)-(2.6), (3.2), (3.3) and (3.8), is given by

$$\mathbf{u}_i^{inner} = \mathbf{u}_i + \alpha \mathbf{u}'_i, \quad (3.9)$$

where  $i = \{\rho, \theta, z\}$ .

### 3.2 Matching the inner and outer velocity field for a slightly non-circular cross-section

Due to the linearity of Stokes equations, the additional force per unit length that arises from the perturbation of the circular cross-section must be of the form  $(\alpha \mathbf{f}')$ , where  $|\mathbf{f}'|$  is at most  $O(\epsilon^2)$ . The outer velocity disturbance created by  $\mathbf{f}'$  should also have a form similar to the velocity disturbance created by  $\mathbf{f}$ , i.e.

$$\begin{aligned} \mathbf{u}'(\mathbf{r}) \approx & -\frac{1}{4\pi} (\mathbf{I} + \mathbf{e}_z \mathbf{e}_z) \cdot \mathbf{f}'(\mathbf{r}) \left[ \ln\left(\frac{\rho}{2}\right) - \ln(\sqrt{1-s^2}) \right] - \frac{1}{4\pi} \mathbf{f}' \cdot \mathbf{e}_z \mathbf{e}_z + \frac{1}{4\pi} \mathbf{f}' \cdot \mathbf{e}_\rho \mathbf{e}_\rho + \\ & \frac{1}{8\pi} \int_{-1}^1 ds' \left[ \left( \frac{\mathbf{I}}{|\mathbf{r}_c(s) - \mathbf{r}_c(s')|} + \frac{(\mathbf{r}_c(s) - \mathbf{r}_c(s'))(\mathbf{r}_c(s) - \mathbf{r}_c(s'))}{|\mathbf{r}_c(s) - \mathbf{r}_c(s')|^3} \right) \cdot \mathbf{f}'(\mathbf{r}') - \left( \frac{\mathbf{I}}{|s-s'|} + \frac{\mathbf{e}_z \mathbf{e}_z}{|s-s'|} \right) \cdot \mathbf{f}'(\mathbf{r}) \right]. \end{aligned} \quad (3.10)$$

The complete velocity field,  $\mathbf{u} + \alpha\mathbf{u}'$ , is obtained by combining equations (2.8) and (3.10). On matching the velocity fields from the inner and outer region,  $\mathbf{f}'$  is given by the integral equation:

$$\begin{aligned}\mathbf{f}'(\mathbf{r}) = & \frac{\epsilon}{2} \left( \mathbf{I} - \frac{\mathbf{e}_z \mathbf{e}_z}{2} \right) \cdot \left( \frac{C'}{2} \mathbf{e}_y - \frac{D'}{2} \mathbf{e}_x - \frac{1}{8\pi} (\mathbf{I} - 3\mathbf{e}_z \mathbf{e}_z) \cdot \mathbf{f}'(\mathbf{r}) - \frac{1}{4\pi} (\mathbf{I} + \mathbf{e}_z \mathbf{e}_z) \cdot \right. \\ & \left. \mathbf{f}'(\mathbf{r}) \ln \left( \frac{\sqrt{1-s^2}}{\frac{a(s)}{a_0}} \right) - \frac{1}{8\pi} \int_{-1}^1 ds' \left[ \left( \frac{\mathbf{I}}{|r_c(s) - r_c(s')|} + \frac{(r_c(s) - r_c(s'))(r_c(s) - r_c(s'))}{|r_c(s) - r_c(s')|^3} \right) \cdot \mathbf{f}'(\mathbf{r}') - \left( \frac{\mathbf{I}}{|s - s'|} + \right. \right. \right. \\ & \left. \left. \left. \frac{\mathbf{e}_z \mathbf{e}_z}{|s - s'|} \right) \cdot \mathbf{f}'(\mathbf{r}') \right] \right). \quad (3.11)\end{aligned}$$

$\mathbf{f}'$  can be iteratively obtained with errors of  $O(\epsilon^{N+1})$  or errors of  $O(\epsilon^N/A)$  if  $h_2 = 0$ , where  $N \geq 2$ .  $\mathbf{f}'$  does not have a component along the longitudinal direction at linear order in  $\alpha$ . This can be understood on matching the  $O(\alpha)$  terms in the inner and outer velocity fields in  $u'_z$ , which results in  $E'$  being identically zero.

The integral equation for the net force per unit length,  $\mathbf{f}_{net} = \mathbf{f} + \alpha\mathbf{f}'$  is given by

$$\begin{aligned}\frac{(\mathbf{f}_{net})}{8\pi} = & \frac{\epsilon}{2} \left( \mathbf{I} - \frac{\mathbf{e}_z \mathbf{e}_z}{2} \right) \cdot \left\{ \mathbf{U} + \boldsymbol{\omega} \times \mathbf{r}_c - \mathbf{u}_\infty(\mathbf{r}_c) + \alpha \left( \frac{C'}{2} \mathbf{e}_y - \frac{D'}{2} \mathbf{e}_x \right) - \frac{1}{8\pi} (\mathbf{I} - 3\mathbf{e}_z \mathbf{e}_z) \cdot \right. \\ & (\mathbf{f}_{net}) - \frac{1}{4\pi} (\mathbf{I} + \mathbf{e}_z \mathbf{e}_z) \cdot (\mathbf{f}_{net}) \ln \left( \frac{\sqrt{1-s^2}}{\frac{a(s)}{a_0}} \right) - \frac{1}{8\pi} \int_{-1}^1 ds' \left[ \left( \frac{\mathbf{I}}{|r_c(s) - r_c(s')|} + \right. \right. \\ & \left. \left. \frac{(r_c(s) - r_c(s'))(r_c(s) - r_c(s'))}{|r_c(s) - r_c(s')|^3} \right) \cdot (\mathbf{f}_{net}(\mathbf{r}')) - \left( \frac{\mathbf{I}}{|s - s'|} + \frac{\mathbf{e}_z \mathbf{e}_z}{|s - s'|} \right) \cdot (\mathbf{f}_{net}(\mathbf{r})) \right] \right\}, \quad (3.12)\end{aligned}$$

where  $C'$  and  $D'$  are obtained from equations (3.2) and (3.3) respectively and have contributions of order  $\epsilon$  and/or  $1/A$  depending on the shape of the cross-section. The governing integral equation can be completely solved to get the value of the force per unit length correct to  $O(\epsilon^N) + O(\alpha\epsilon^{N+1}) + O(\alpha\epsilon^N/A)$ , where  $N$  is an integer greater than unity. Solving for the force per unit length to  $O(\epsilon) + O(\alpha\epsilon^2) + O(\alpha\epsilon/A)$ , equation (3.12) simplifies to

$$\mathbf{f} + \alpha \mathbf{f}' = 4\pi\epsilon(\mathbf{U} + \boldsymbol{\omega} \times \mathbf{r}_c - \mathbf{u}_\infty(\mathbf{r}_c)) \cdot \left( \mathbf{I} - \frac{\mathbf{e}_z \mathbf{e}_z}{2} \right) + 2\pi\epsilon\alpha(-D' \mathbf{e}_x + C' \mathbf{e}_y). \quad (3.13)$$

Equation (3.13) suggests that the force per unit length experienced by a slender filament due to non-circularity of the cross-section is affected at  $O(\alpha\epsilon^2)$  due to the velocity disturbance of the unperturbed circular cross-section and at  $O(\alpha\epsilon/A)$  due to the gradient in the imposed fluid velocity.

### 3.3 Extending the analysis to a general cross-sectional shape ( $\alpha \sim O(1)$ )

Here, a numerical calculation to determine the velocity disturbance by any cross-section is elucidated which can be used as the matching solution for SBT. This calculation involves the solution to the flow past an obstacle with the same shape as the particle cross-section in a two-dimensional domain with a size,  $\rho_\infty$ , that is much larger than the cross-sectional size ( $\rho_\infty \gg a$ ) as shown in figure 4. In this subsection, the fluid viscosity, a measure of the undisturbed fluid velocity far away from the obstacle and a length that is of the order of the size of the obstacle are used to non-dimensionalize any quantity of interest, such as the force per unit length.

The apparent hydrodynamic center of resistance (AHCOR<sup>1</sup>) of the cross-section is chosen as the center of the computational domain to avoid a solid body rotation at large separations from the particle. The AHCOR is defined as the point about which zero torque is acting on a two-dimensional obstacle translating in a concentric circular domain of size much larger than the obstacle with the outer boundary having zero velocity.

Consider a stationary obstacle experiencing a force per unit length  $\mathbf{f}$  placed in a fluid with an imposed velocity of  $\mathbf{u}_\infty \cdot (\mathbf{I} - \mathbf{e}_z \mathbf{e}_z)$ . The velocity field at the outer boundary is obtained from the asymptotic form predicted by SBT according to equations (2.8) and (3.11). This asymptotic form of the imposed fluid velocity in the region  $\rho \gg a$  is given by

---

<sup>1</sup> AHCOR is similar to the hydrodynamic center of resistance for three dimensional particles, which is defined as the point about which the torque acting on a body translating in a quiescent fluid is zero (Kim and Karrila, 1991). In a two-dimensional Stokes flow the velocity disturbance due to an obstacle grows logarithmically with the domain size and therefore a hydrodynamic center of resistance based on the above definition cannot be defined in the same manner.

$$\mathbf{u} = \mathbf{u}_\infty + \frac{2f}{8\pi} \cdot \left[ -\ln\left(\frac{\rho}{a}\right) (\mathbf{I} + \mathbf{e}_z \mathbf{e}_z) + (\mathbf{e}_\rho \mathbf{e}_\rho - 0.5(\mathbf{I} - \mathbf{e}_z \mathbf{e}_z)) + \mathbf{K} \right] + \mathbf{L}, \quad (3.14)$$

where  $\mathbf{K}$  is a second order tensor that depends only on the geometry of the particle cross-section and  $\mathbf{L}$  is a vector that arises due to the gradient of the imposed fluid velocity and therefore depends both on the geometry of the particle and  $\mathbf{u}_\infty$ .  $\mathbf{K}$  is symmetric (Batchelor 1970), such that  $K_{iz} = K_{zi} = 0$  for  $i = \{x, y\}$ , due to the decoupling of the longitudinal and the transverse flow fields around a long-slender body. The corresponding pressure for this velocity field in the region  $\rho \gg a$  is given by

$$p = \frac{4}{8\pi\rho} \mathbf{f} \cdot \mathbf{e}_\rho. \quad (3.15)$$

In equation (3.14),  $\mathbf{K}$  and  $\mathbf{L}$  are to be determined as part of the solution and therefore the velocity field at the outer boundary for a given  $f$  and  $\mathbf{u}_\infty$  cannot be specified a priori. Instead, the force per unit area  $\mathbf{t}$  acting on the outer boundary  $\rho = \rho_\infty$  is specified.  $\mathbf{t}$  is independent of  $a$ ,  $\mathbf{K}$  and  $\mathbf{L}$ , and given by

$$\mathbf{t} = \mathbf{t}_\infty - \frac{1}{\pi\rho_\infty} \mathbf{f} \cdot (\mathbf{e}_\rho \mathbf{e}_\rho), \quad (3.16)$$

where  $\mathbf{t}_\infty$  is the force per unit area that would act on the outer boundary due to  $\mathbf{u}_\infty \cdot (\mathbf{I} - \mathbf{e}_z \mathbf{e}_z)$  in the absence of the obstacle.

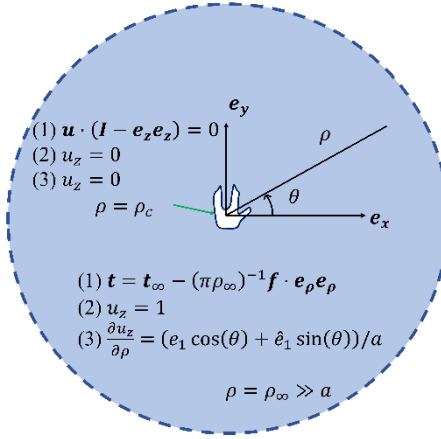


Figure 4. Schematic of the two-dimensional domain to obtain  $\mathbf{K}$  and  $\mathbf{L}$ , along with the boundary conditions for (1) the 2D Stokes flow equations in the transverse plane and the Laplace equation for the longitudinal velocity field  $\nabla^2 u_z = 0$  for computing (2)  $K_{zz}$  and (3)  $L_z$ .

$a$  and  $K_{ij}$  for  $i, j = \{x, y\}$  are obtained by solving the 2D Stokes equations with no-slip on the obstacle surface and  $\mathbf{t} = -(1/\pi\rho_\infty)\mathbf{f} \cdot (\mathbf{e}_\rho \mathbf{e}_\rho)$  on the outer boundary and matching the numerical velocity and  $\mathbf{u} \cdot (\mathbf{I} - \mathbf{e}_z \mathbf{e}_z)$  with  $\mathbf{L} = 0$  at the outer boundary.  $L_i$  for  $i = \{1, 2\}$  is calculated by equating  $\mathbf{u} = (\mathbf{u}_\infty + \mathbf{L}) \cdot (\mathbf{I} - \mathbf{e}_z \mathbf{e}_z)$  to the velocity field at the outer boundary obtained from the solution of the 2D Stokes equations with no slip on the obstacle surface and  $\mathbf{t} = \mathbf{t}_\infty$  at  $\rho = \rho_\infty$ .  $u_z$  at the outer boundary obtained from the solution of  $\nabla^2 u_z = 0$ , with no-slip on the obstacle and a constant value at  $\rho = \rho_\infty$ , is equated to  $u_z$  from equation (3.14) to obtain  $K_{zz}$ . Similarly,  $u_z$  at the outer boundary obtained from the solution of  $\nabla^2 u_z = 0$ , with no-slip on the obstacle and  $\partial u_z / \partial \rho$  corresponding to a linear vector field  $\mathbf{u}_\infty \cdot \mathbf{e}_z$  at  $\rho = \rho_\infty$ , is equated to  $u_z$  from equation (3.14) to obtain  $L_z$ . For arbitrary cross-sections the 2D Stokes flow equations and the 2D Laplace's equation can be solved using a finite element solver such as COMSOL or a two-dimensional boundary element method, by choosing a  $\rho_\infty$  which is sufficiently large such that the values of  $a$ ,  $\mathbf{K}$  and  $\mathbf{L}$  do not change on further increasing  $\rho_\infty$ . The final integral equation for the force per unit length exerted by a slender filament with an arbitrary cross-section is given by

$$\begin{aligned}
\frac{\mathbf{f}(\mathbf{r})}{8\pi} = & \frac{\epsilon}{2} \left( \mathbf{I} - \frac{\mathbf{e}_z \mathbf{e}_z}{2} \right) \\
& \cdot \left\{ \mathbf{U} + \boldsymbol{\omega} \times \mathbf{r}_c - \mathbf{u}_\infty(\mathbf{r}_c) + \frac{1}{4\pi} \mathbf{f}(\mathbf{r}) \cdot \mathbf{K} + \mathbf{L} - \frac{1}{8\pi} (\mathbf{I} - 3\mathbf{e}_z \mathbf{e}_z) \cdot \mathbf{f}(\mathbf{r}) \right. \\
& - \frac{1}{4\pi} (\mathbf{I} + \mathbf{e}_z \mathbf{e}_z) \cdot \mathbf{f}(\mathbf{r}) \ln \left( \frac{\sqrt{1-s^2}}{\frac{a(s)}{a_0}} \right) \\
& - \frac{1}{8\pi} \int_{-1}^1 ds' \left[ \left( \frac{\mathbf{I}}{|\mathbf{r}_c(s) - \mathbf{r}_c(s')|} + \frac{(\mathbf{r}_c(s) - \mathbf{r}_c(s'))(\mathbf{r}_c(s) - \mathbf{r}_c(s'))}{|\mathbf{r}_c(s) - \mathbf{r}_c(s')|^3} \right) \cdot \mathbf{f}(\mathbf{r}') \right. \\
& \left. \left. - \left( \frac{\mathbf{I}}{|s - s'|} + \frac{\mathbf{e}_z \mathbf{e}_z}{|s - s'|} \right) \cdot \mathbf{f}(\mathbf{r}) \right] \right\}. \quad (3.17)
\end{aligned}$$

Note that  $\mathbf{K}$  is related to the tensor  $\mathbf{K}_B$  and  $\ln(k_B)$ , which Batchelor (1970) mentions in equations (5.5) and (6.1) of his paper respectively, by the relation  $\mathbf{K}_B + 2\ln(k_B)\mathbf{e}_z\mathbf{e}_z = \mathbf{K} + (\mathbf{I} + \mathbf{e}_z\mathbf{e}_z)\ln(a/R_B)$ , where  $R_B$  is such that  $2\pi R_B$  is the perimeter of the cross-section. Batchelor (1970) shows that  $\mathbf{K}_B$  is a symmetric tensor, which implies that  $\mathbf{K}$  is also symmetric.  $\mathbf{K}_B$  has three unknowns such that  $\mathbf{K}_B \cdot \mathbf{e}_z = \mathbf{0}$ . These unknowns are written in terms of  $a$  and  $K_{ij}$ , where  $i, j = \{x, y\}$ , such that  $K_{xx} + K_{yy} = 0$ .  $K_{zz} = 2\ln(k_B) - 2\ln(a/R_B)$  captures the effect of the cross-sectional shape on the force and velocity field in the longitudinal direction. The influence of the cross-section on the velocity disturbance in the transverse plane can be decomposed into an isotropic component  $\ln(a)\mathbf{I}$  and a traceless component  $\mathbf{K} - K_{zz}\mathbf{e}_z\mathbf{e}_z$ . This length scale "a" which arises as part of the hydrodynamic calculation is therefore used instead of a purely geometric length scale  $R_B$ .

$\mathbf{K}$  can be represented in terms of  $\bar{\alpha}_2$ ,  $\theta_{02}$  and  $K_{zz}$  and is given by

$$\mathbf{K} = \begin{bmatrix} -0.5\bar{\alpha}_2 \cos(2\theta_{02}) & -0.5\bar{\alpha}_2 \sin(2\theta_{02}) & 0 \\ -0.5\bar{\alpha}_2 \sin(2\theta_{02}) & 0.5\bar{\alpha}_2 \cos(2\theta_{02}) & 0 \\ 0 & 0 & K_{zz} \end{bmatrix}. \quad (3.18 \text{ a})$$

$(\bar{\alpha}_2, \theta_{02})$ , similar to  $(\alpha_2, \theta_{02})$  of the regular perturbation theory, give the contribution to the second Fourier mode of the cross-sectional geometry.  $K_{zz}$ , which is zero to leading order in the perturbation analysis, can have a non-zero value for a general cross-sectional shape. This is because  $u_z$  can be affected by the details of the cross-section at  $O(\alpha^2)$  (See Appendix S.2 for details).  $\mathbf{L}$  can be represented in terms of  $\bar{\alpha}_3, \theta_{03}, L_z$  and the imposed fluid velocity and is given by

$$\mathbf{L} = \begin{bmatrix} 2\bar{\alpha}_3(\hat{a}_2 \cos(3\theta_{03}) - a_2 \sin(3\theta_{03})) \\ 2\bar{\alpha}_3(a_2 \cos(3\theta_{03}) + \hat{a}_2 \sin(3\theta_{03})) \\ L_{zx}e_1 + L_{zy}\hat{e}_1 \end{bmatrix}, \quad (3.18 \text{ b})$$

where the imposed velocity field  $(\mathbf{u}_\infty(\mathbf{r}) - \mathbf{u}_\infty(\mathbf{r}_c)) \cdot (\mathbf{I} - \mathbf{e}_z \mathbf{e}_z)$  is specified in terms of a stream function  $\psi_\infty$  given by

$$\frac{\psi_\infty}{a} = \tilde{a}_0 \left(\frac{\rho}{a}\right)^2 + (a_2 \cos(2\theta) + \hat{a}_2 \sin(2\theta)) \left(\frac{\rho}{a}\right)^2, \quad (3.18 \text{ c})$$

and  $(\mathbf{u}_\infty(\mathbf{r}) - \mathbf{u}_\infty(\mathbf{r}_c)) \cdot \mathbf{e}_z \mathbf{e}_z$  is given by

$$u_{\infty,z} = (e_1 \cos(\theta) + \hat{e}_1 \sin(\theta)) \frac{\rho}{a}. \quad (3.18 \text{ d})$$

$(\bar{\alpha}_3, \theta_{03})$ , similar to  $(\alpha_3, \theta_{03})$  of the regular perturbation theory, give the contribution to the third Fourier mode perturbation.  $\mathbf{L} \cdot \mathbf{e}_z$  is zero in the linear perturbation analysis but it is non-zero for a general cross-sectional geometry. The longitudinal component of  $-\mathbf{L}$  is the longitudinal velocity at which a particle must translate to avoid a longitudinal force per unit length when it is subjected to a simple shear flow with the stagnation streamline coinciding with the AHCOR. For the geometries studied in this paper,  $\mathbf{L} \cdot \mathbf{e}_z$  was found to be numerically small compared to the components of  $\mathbf{L}$  in the transverse plane.

#### 4. Resistance to motion of a triaxial ellipsoid

In this section our theory is utilized to obtain the Stokes hydrodynamic resistance tensor of triaxial ellipsoids of semi-axis lengths  $l_1, l_2$  and  $l_3$ , such that  $l_3 \gg l_1 > l_2$  ( $3$  is the longitudinal

direction, 1 is along the long axis of the elliptical cross-section and directions, [1,2,3] form a right-handed Cartesian coordinate system). By symmetry of the shape, the force,  $\mathbf{F}$  and the torque,  $\mathbf{T}$  acting on the ellipsoid are given as  $\mathbf{F} = \mathbf{R}^{FU} \cdot \mathbf{U}$ ,  $\mathbf{T} = \mathbf{R}^{L\omega} \cdot \boldsymbol{\omega}$ , where  $\mathbf{R}^{FU}$  and  $\mathbf{R}^{L\omega}$  are  $3 \times 3$  diagonal matrices that depend only on the particle geometry. The values of  $\mathbf{R}^{FU}$  and  $\mathbf{R}^{L\omega}$  for  $l_3/l_1 \gg 1$  and  $(l_1 - l_2)/l_1 \ll 1$  using the perturbation analysis in section (3.2) are given by

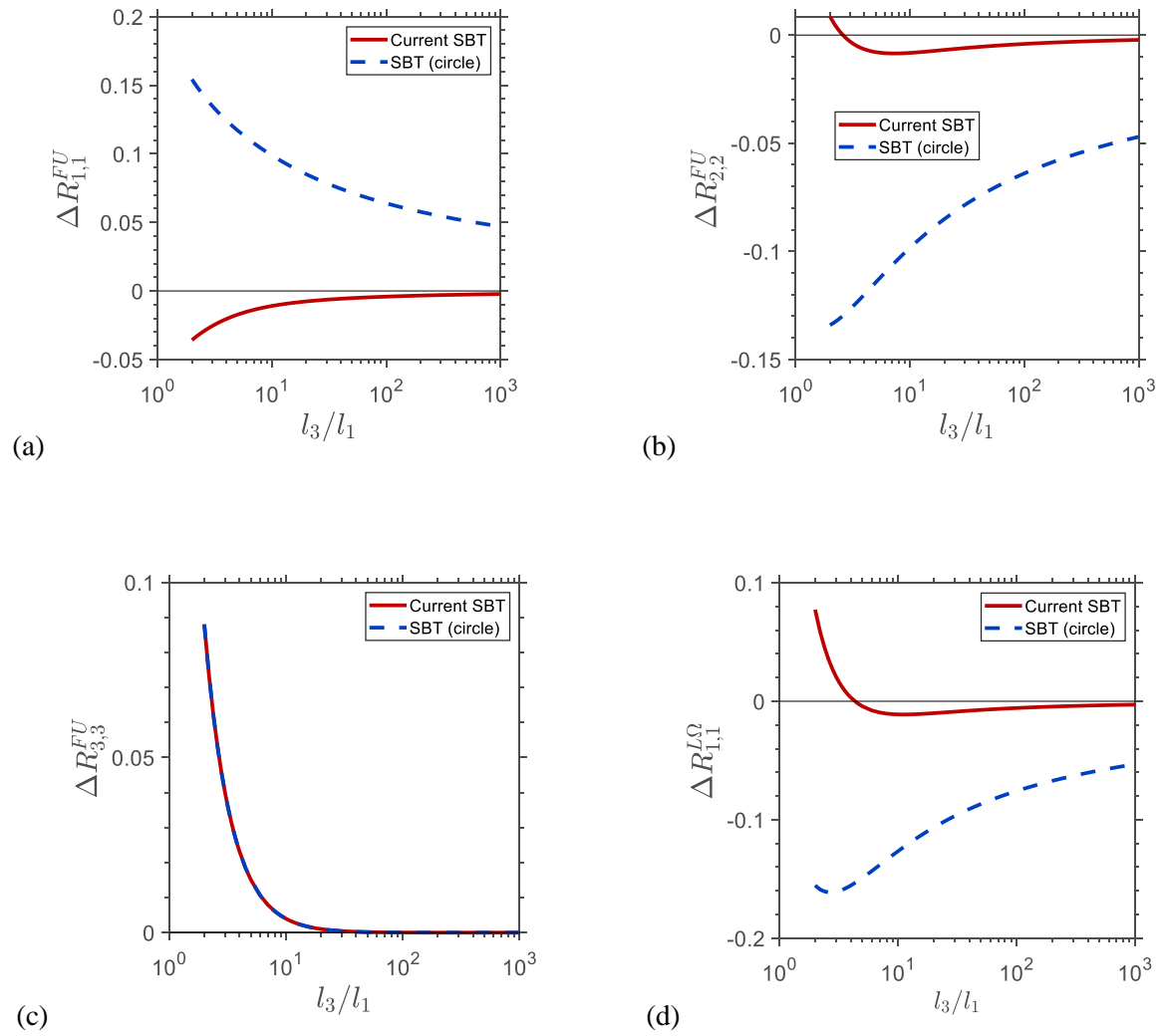
$$\mathbf{R}^{FU} = (8\pi) \frac{\epsilon(2l_3)}{2+\epsilon} \begin{bmatrix} 1 - \frac{\alpha_2 \epsilon}{2+\epsilon} & 0 & 0 \\ 0 & 1 + \frac{\alpha_2 \epsilon}{2+\epsilon} & 0 \\ 0 & 0 & \frac{1}{2} \frac{2+\epsilon}{2-\epsilon} \end{bmatrix}, \quad (4.1)$$

$$\mathbf{R}^{L\omega} = (8\pi) \frac{2l_3^3}{3} \frac{\epsilon}{2-\epsilon} \begin{bmatrix} 1 + \frac{\alpha_2 \epsilon}{2-\epsilon} & 0 & 0 \\ 0 & 1 - \frac{\alpha_2 \epsilon}{2-\epsilon} & 0 \\ 0 & 0 & \frac{(2-\epsilon)}{\epsilon} \left(\frac{a}{l_3}\right)^2 \end{bmatrix}, \quad (4.2)$$

where  $\epsilon = 1/\ln(2l_3/a)$ .  $a$  and  $\alpha_2$  are given by  $a = 0.5(l_1 + l_2)$  and  $\alpha_2 = (l_1 - l_2)/(2a)$  for  $(l_1 - l_2) \ll l_1$ . The results of equations (4.1) and (4.2) match exactly with the values obtained by Batchelor (1970) (equations (8.7), (8.8) and (8.10) of his paper).

For cross-sections with  $(l_1 - l_2) \sim O(l_1)$ ,  $\mathbf{R}^{FU}$  and  $\mathbf{R}^{L\omega}$  are determined using the numerical procedure in section (3.3) and the results retain great accuracy even for cross-sections with extreme aspect ratio. COMSOL, a finite element solver, was used to perform the 2D Stokes flow calculation.  $\mathbf{K}$  was estimated with an uncertainty of below 0.1 % when the size of the outer boundary ( $\rho_\infty$ ) was at least 30 times the cross-sectional dimension. Figure 5 shows the deviation of  $\mathbf{R}^{FU}$  and  $\mathbf{R}^{L\omega}$  predicted by our numerical procedure from the exact result for an ellipsoid given by Lamb (1932) for a high-aspect ratio elliptical cross-section with  $l_1/l_2 = 10$ . The deviation of the SBT for a circular cross-section from the exact result is also presented for comparison. Our SBT predicts  $\mathbf{R}^{FU}$  and  $\mathbf{R}^{L\omega}$  better than the SBT results for a circular cross-section and has errors less than about 1% for  $l_3/l_1 \gtrsim 10$ . The high level of accuracy shows the applicability of our methodology to accurately predict the resistance to motion of slender bodies with arbitrary cross-section.

$\mathbf{R}^{L\omega} : \mathbf{e}_3 \mathbf{e}_3$  needs special attention for a straight slender body because the force per unit length cannot generate a torque about its longitudinal axis. To obtain the effect of the cross-sectional geometry on  $\mathbf{R}^{L\omega} : \mathbf{e}_3 \mathbf{e}_3$ , a two-dimensional Stokes flow problem is solved to find the torque per unit length  $\mathbf{g} \propto a^2(s)$  acting on an ellipse with sides  $l_1$  and  $l_2$  which is rotating with a unit angular velocity parallel to  $\mathbf{e}_3$  with the velocity on the outer boundary set to zero (see figure 3). The torque per unit length is integrated by accounting for the variation of the cross-sectional size to attain the total torque on the ellipsoid, and thereby obtain  $\mathbf{R}^{L\omega} : \mathbf{e}_3 \mathbf{e}_3$  as depicted in figure 5 (f).



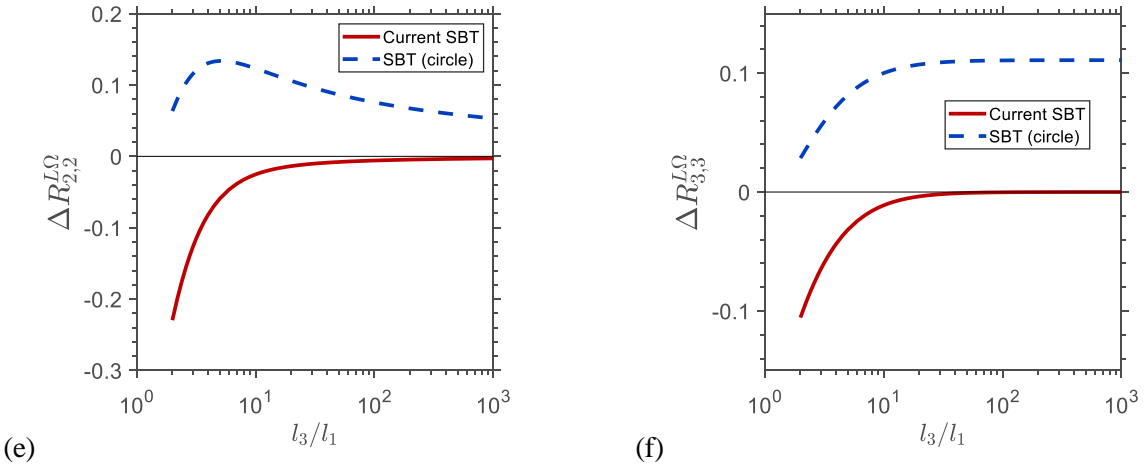


Figure 5. Variation of resistances,  $\mathbf{R}^{FU}$  and  $\mathbf{R}^{L\omega}$ , with  $l_3/l_1$  for an ellipsoid with  $l_1/l_2 = 10$ .

(a) – (f) Comparison of  $\Delta R_{ij}^k = (R_{ij}^k - (R_{ij}^k)_{exact}) / (R_{ij}^k)_{exact}$ , the deviation of different components of  $\mathbf{R}^{FU}$  and  $\mathbf{R}^{L\omega}$  predicted using the current SBT as well as the SBT for a circular cross-section from the exact result of Lamb (1932) ( $(R_{ij}^k)_{exact}$ ). Here  $i, j = \{1, 2, 3\}$  and  $k = \{\mathbf{FU}, \mathbf{L}\omega\}$ .

## 5. Translation of a straight slender body in a simple shear flow (SSF)

An axisymmetric straight particle rotates periodically in one of the Jeffery orbits depending on its initial orientation and has zero cross-stream drift relative to the fluid velocity at its center of mass. A straight particle with a three-lobed cross-section shown in figure 6 (a) rotates like a spheroid but translates quasi-periodically across streamlines with an  $O(\alpha/A)$  velocity. A straight particle with a combination of an elliptic (or two-lobed) and a three-lobed cross-section can rotate chaotically and translate diffusively. The calculations in this section can be used to extract the motion of straight fibers in viscous fluids which is important in the manufacturing process of fiber-reinforced composite materials or paper products. The half-length of the particle, the shear rate and the fluid viscosity are used to non-dimensionalize variables in this section.

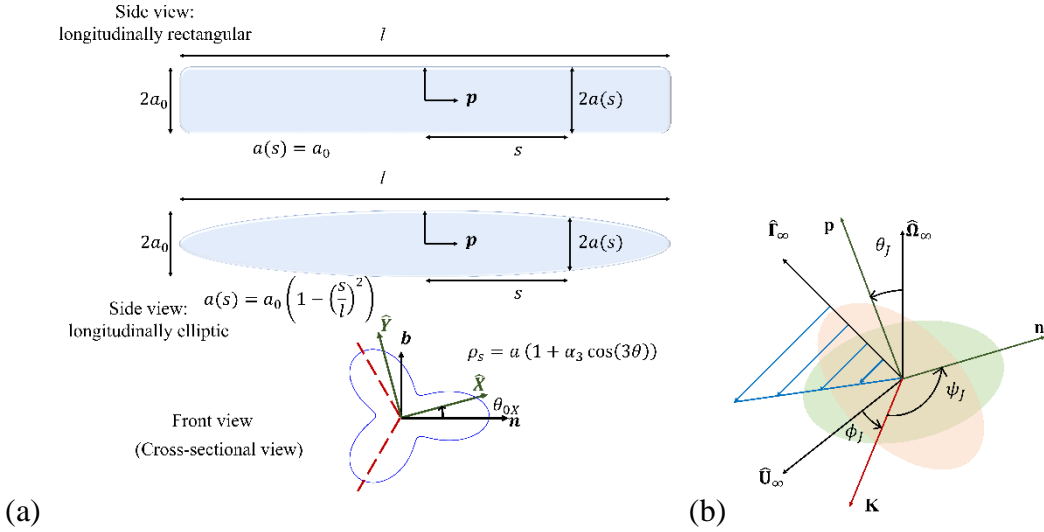


Figure 6. Schematic of the particle shape and the coordinate system used in the calculation. (a) Schematic of the slender particle that is longitudinally rectangular or elliptic. The cross-section of the particle is given by  $\rho_s = a(1 + \alpha_3 \cos(3\theta))$ , where  $\theta$  is measured from  $\mathbf{n}$ .  $\mathbf{n}$  is along one of the lines of symmetry of the cross-section,  $\hat{\mathbf{Y}}$  is a unit vector in the cross-sectional plane chosen such that  $\hat{\mathbf{Y}} \cdot \hat{\mathbf{U}}_\infty = 0$  and  $\hat{\mathbf{X}} = \hat{\mathbf{Y}} \times \mathbf{p}$ . (b) The fixed reference frame is defined along the flow ( $\hat{\mathbf{U}}_\infty$ ), vorticity ( $\hat{\boldsymbol{\Omega}}_\infty$ ) and the gradient ( $\hat{\mathbf{G}}_\infty$ ) direction of the SSF. The longitudinal direction of the particle is along  $\mathbf{p}$  and a reference vector in the transverse plane is  $\mathbf{n}$ .  $\mathbf{p}, \hat{\boldsymbol{\Omega}}_\infty, \mathbf{K} = \mathbf{p} \times \hat{\boldsymbol{\Omega}}_\infty, \mathbf{n}$  and  $\hat{\mathbf{U}}_\infty$  are used to define the Euler angles  $\theta_J, \phi_J, \psi_J$ .

### 5.1. Problem formulation and SBT solution

The cross-section of the slender particle studied here is a small perturbation to a circle given by  $\rho_s = a(1 + \alpha_3 \cos(3\theta))$ , where  $\alpha_3 \ll 1$  is the perturbation parameter and  $\theta$  is measured relative to a vector  $\mathbf{n}$  that is along one of the lines of symmetry of the cross-section. The second Fourier mode perturbation to a circle does not affect  $C'$  and  $D'$  for a torque-free particle in a SSF because the force per unit length it produces satisfies  $\mathbf{f} \cdot (\mathbf{I} - \mathbf{p}\mathbf{p}) = 0$ . The second Fourier mode perturbation to a circle affects the torque per unit length  $\mathbf{g}$  thereby influencing the rotational dynamics of a straight particle, which is discussed in section 5.3.

The size of the cross-section, “ $a$ ”, either varies with the longitudinal position,  $s$ , as  $\frac{a(s)}{a_0} = (1 - s^2)^{0.5}$  for a cross-section that is longitudinally elliptic or is a constant  $a = a_0$  for a cylinder. The force per unit length obtained from equation (3.17), is used to obtain the linear ( $\mathbf{U}$ ) and angular ( $\boldsymbol{\omega}$ ) velocity of the particle by applying the force-free ( $\int \mathbf{f}_{net} ds = 0$ ) and torque-free ( $\int (s\mathbf{p} \times \mathbf{f}_{net} + \mathbf{g})ds = 0$ ) condition on the particle respectively.  $\mathbf{g}$  is calculated by computing the stresses from a transverse velocity field obtained from the stream function  $\tilde{\psi}$  and the velocity field  $\tilde{u}_z$ .

$\boldsymbol{\omega}$  is not affected by a three-lobed perturbation of a circle at linear order in  $\alpha_3$  and thus, this particle rotates periodically, like a spheroid shown by Jeffery (1922). This holds true for cylinders with blunt ends and a three-lobed cross-section. The ends of a blunt cylinder significantly influence  $\boldsymbol{\omega}$  when the particle is near the flow-vorticity plane (Cox 1971), which can be computed using the force generated at the ends of the particle in the transverse direction,  $\mathbf{F}_{end}$ . Using linearity of Stokes flow, and the symmetry of the third and higher Fourier mode perturbations,  $\mathbf{g} \cdot (\mathbf{I} - \mathbf{p}\mathbf{p})$  and  $\mathbf{p} \times \mathbf{F}_{end}$  can be shown to be proportional to  $\mathbf{E} \cdot \mathbf{p} \times \mathbf{p}$  which is proportional to  $\boldsymbol{\omega}$  due to the straining component of a SSF for an axisymmetric particle (See Appendix S2). Therefore, straight particles with  $\alpha_2 = 0$ , in addition to circular cylinders shown by Cox (1971), rotate similar to an  $O(A/\sqrt{\ln(A)})$  aspect ratio spheroid. The exact relationship can be obtained from experiments or a numerical calculation. For a torque-free straight particle with a 3-lobed cross-section,  $\boldsymbol{\omega}$  is given by

$$\boldsymbol{\omega} = \boldsymbol{\omega}_\infty + \lambda_J \mathbf{p} \times (\mathbf{E} \cdot \mathbf{p}), \quad (5.1)$$

where  $\lambda_J$  is the rotation parameter of the particle that depends only on its geometry.  $\lambda_J = 1 - \frac{2}{A^2}$  for a slender particle that is longitudinally elliptic (Jeffery 1922, Cox 1971).  $\lambda_J = 1 - 0.65 \frac{\ln(A)}{A^2}$  for a cylinder, where the prefactor of 0.65 was obtained by fitting the asymptotic form of Cox (1971) to the experimental data of Anczurowskei and Mason (1968).

Unlike a spheroid or a circular cylinder, a slender particle with a three lobed cross-section drifts across streamlines due to the  $O(\alpha_3/A)$  force per unit length. The drift velocity of the particle

is confined to the plane normal to  $\mathbf{p}$ , as  $\mathbf{f}_{net} \cdot \mathbf{p} = 0$ . Thus, the drift velocity of this particle takes the form  $\mathbf{U}_p = U_x \hat{\mathbf{X}} + U_y \hat{\mathbf{Y}}$ , where  $U_x$  and  $U_y$  are the components of the drift velocity along  $\hat{\mathbf{X}}$  and  $\hat{\mathbf{Y}}$  respectively and  $(\hat{\mathbf{X}}, \hat{\mathbf{Y}}, \mathbf{p})$  form an orthogonal pair such that  $\hat{\mathbf{Y}} \cdot \hat{\mathbf{U}}_\infty = 0$ .  $U_x$  and  $U_y$  are given by

$$U_x = \alpha_3 a_0 U_0 [\mathbf{E}_\infty : \hat{\mathbf{X}} \hat{\mathbf{Y}} \sin(3\theta_{0X}) - 0.5 \mathbf{E}_\infty : \hat{\mathbf{X}} \hat{\mathbf{X}} \cos(3\theta_{0X})], \quad (5.2 \text{ a})$$

$$U_y = \alpha_3 a_0 U_0 [\mathbf{E}_\infty : \hat{\mathbf{X}} \hat{\mathbf{Y}} \cos(3\theta_{0X}) + 0.5 \mathbf{E}_\infty : \hat{\mathbf{X}} \hat{\mathbf{X}} \sin(3\theta_{0X})], \quad (5.2 \text{ b})$$

where  $U_0 = 1$  for a cylinder and  $U_0 = \pi/4$  for a spheroid,  $\theta_{0X}$  is the angle made by  $\hat{\mathbf{X}}$  with  $\mathbf{n}$  and  $\mathbf{E}_\infty = \frac{1}{2}(\nabla \mathbf{u}^\infty + (\nabla \mathbf{u}^\infty)^T)$  is the straining tensor.  $\mathbf{U}$  for the longitudinally elliptic particle differs from  $\mathbf{U}$  of a cylinder by a factor of  $\pi/4$  due to the difference in the integral of  $\int_{-1}^1 ds a(s)$  for the two cases. Only the results for a straight cylinder are presented in the following section, since both  $\mathbf{U}$  and  $\boldsymbol{\omega}$  are qualitatively similar for a longitudinally elliptic particle.

## 5.2. Quasi-periodic translation of particles

The motion of the particle shown in figure 6(a) is calculated by tracking its center of mass position and orientation. The orientation is given in terms of the Euler angles,  $(\theta_J, \psi_J, \phi_J)$ , shown in figure 6 (b) and defined using the longitudinal direction of the particle  $\mathbf{p} = (\sin(\phi_J) \sin(\theta_J), \cos(\theta_J), \cos(\phi_J) \sin(\theta_J))$ , a vector  $\mathbf{K} = (\cos(\phi_J), 0, -\sin(\phi_J))$  that is normal to both  $\mathbf{p}$  and  $\hat{\Omega}_\infty$  and  $\cos(\psi_J) = \mathbf{n} \cdot \mathbf{K}$ , where  $\mathbf{n}$  is a vector along one of the lines of symmetry of the cross-section as illustrated in figure 6 (a).  $(\mathbf{n}, \mathbf{b}, \mathbf{p})$  and  $(\hat{\mathbf{X}}, \hat{\mathbf{Y}}, \mathbf{p})$ , such that  $\hat{\mathbf{Y}} \cdot \hat{\mathbf{U}}_\infty = 0$ , form an orthogonal set. The angle  $\theta_{0X}$  in equation (5.4) equals  $\text{asin}(\hat{\mathbf{Y}} \cdot \mathbf{n})$ . Jeffery (1922) obtained the time variation of  $\phi_J$  and  $\theta_J$  that is given by

$$\tan(\phi_J) = A_e \tan\left(2\pi \frac{t}{T} + \tau\right), \quad (5.3 \text{ a})$$

$$\tan(\theta_J) = \frac{A_e C}{\sqrt{A_e^2 \cos^2(\phi_J) + \sin^2(\phi_J)}}, \quad (5.3 \text{ b})$$

where  $\phi_J \in [0, 2\pi]$ ,  $\theta_J \in [0, \pi]$ ,  $C$  is the orbit constant,  $\tau$  is the phase angle,  $T = 2\pi(A_e + A_e^{-1})$  is the period of rotation of  $\mathbf{p}$  and  $A_e$  is the effective aspect ratio of the particle defined as  $A_e = \sqrt{(1 + \lambda_J)/(1 - \lambda_J)}$ . A thin cylinder ( $A \gg 1$ ) spends most of its time such that  $\mathbf{p}$  is near the flow-vorticity plane ( $\phi_J \rightarrow \pi/2$ ). The rate of change of  $\psi_J$  is given by

$$\frac{d\psi_J}{dt} = -\frac{1}{2}\lambda_J \cos(\theta_J) \cos(2\phi_J) \quad (5.3 \text{ c})$$

According to equation (5.3 c),  $\psi_J$  changes over a timescale of  $O((1 + (A_e C)^2)^{0.5})$  which varies with the orbit constant,  $C$ , and contrasts from the fixed  $O(T)$  time scale over which  $\theta_J$  and  $\phi_J$  change. Therefore, there are uncountably infinite orbits where  $\psi_J$  rotates quasiperiodically while only countably infinite orbits where  $\psi_J$  has a period that is a multiple of  $T$ . The quasiperiodic rotation of  $\psi_J$  demonstrates that the  $(\psi_J, \phi_J)$  space is filled completely over time as seen in figures 7 (b) and (c). Discrete peaks in the frequency spectrum obtained by the Fast-Fourier transformation  $\hat{\psi}_J$  is used to establish the quasi-periodic nature of the system as shown in figure 7 (d).

The average velocity of the particle is zero because of the symmetry of the orbits relative to the SSF. The quasiperiodic translation is quantified using the root mean square (RMS) velocity of the particle given by

$$\langle (\mathbf{U} \cdot \boldsymbol{\zeta})^2 \rangle^{1/2} = \lim_{N \rightarrow \infty} \frac{1}{\sqrt{NT}} \left( \sqrt{\int_0^{NT} (\mathbf{U} \cdot \boldsymbol{\zeta})^2 dt} \right), \quad (5.4)$$

where  $\boldsymbol{\zeta} \in \{\widehat{\boldsymbol{\Omega}}_\infty, \widehat{\boldsymbol{\Gamma}}_\infty\}$  and  $N$  should be sufficiently large such that the results are invariant on increasing  $N$ . The mean-square velocity can also be obtained by averaging in the  $(\psi_J, \phi_J)$  space given by

$$\langle (\mathbf{U} \cdot \boldsymbol{\zeta})^2 \rangle = \int_0^{2\pi} d\phi_J \left( \frac{1}{2\pi} \right) \left( \frac{A_e(1-\lambda)}{1+\lambda \cos(2\phi_J)} \right) \int_0^{2\pi} d\psi_J \frac{1}{2\pi} (\mathbf{U} \cdot \boldsymbol{\zeta})^2. \quad (5.5)$$

The RMS velocity in the gradient ( $\hat{\Gamma}_\infty$ ) and vorticity ( $\hat{\Omega}_\infty$ ) direction for  $\alpha_3 = 0.1$  are shown in figure 8 (a) and (b) respectively as a function of  $C$  for varying particle aspect ratios. The RMS velocities computed from equation (5.5) match the values obtained from time averaging over 500 tumbling events reaffirming the quasi-periodic nature of the system. For  $C \rightarrow 0$  the particle is symmetric about the flow-gradient plane and therefore cannot translate in the vorticity direction as evident in figure 8 (b). In this orbit  $\hat{X} = \hat{U}_\infty$  and  $\hat{Y} = \hat{\Gamma}_\infty$  thereby leading to the highest value of  $U_y$  among the orbits as per equation (5.2). Therefore,  $\langle (\mathbf{U} \cdot \hat{\Gamma}_\infty)^2 \rangle$  is highest when  $C = 0$  and monotonically decreases with increasing  $C$  as seen in figure 8 (a). A peak is observed in  $\langle (\mathbf{U} \cdot \hat{\Omega}_\infty)^2 \rangle$  for  $C \sim O(1/A)$  before the value plateaus for large  $C \gg 1$ .

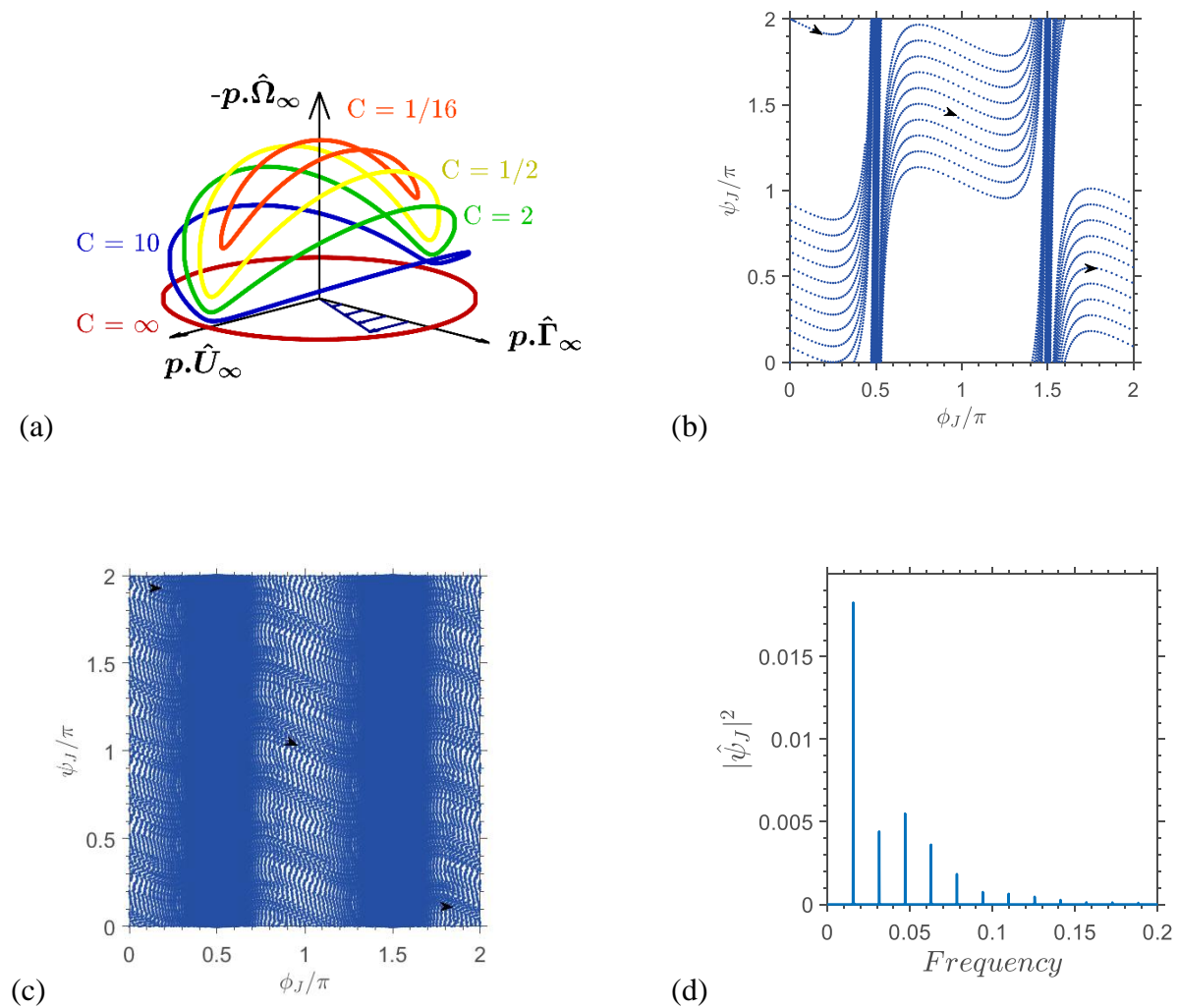


Figure 7. Trajectory of the orientation of the particle. (a) Orientational trajectory of  $\mathbf{p}$  ( $\lambda_J = 0.98$ ) for various initial conditions specified by the orbit constant,  $C$ . Change in  $(\psi, \phi)$  during (b) 10 and (c)  $10^3$  tumbling events respectively for a cylinder with  $A = 20$  and  $C = 0.1$ . (d) Frequency spectrum obtained from the Fast Fourier transformation of  $\psi_J(t)$  for  $C = 0.1$  and  $A = 20$ .

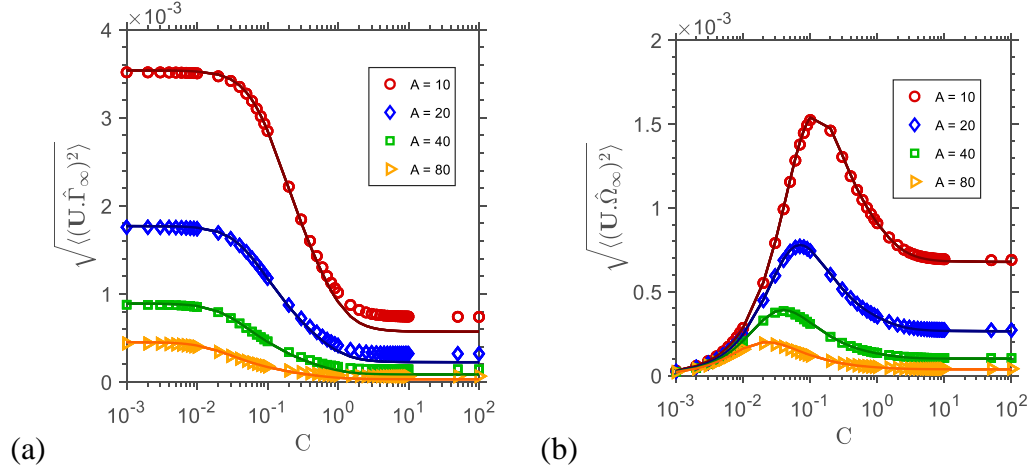
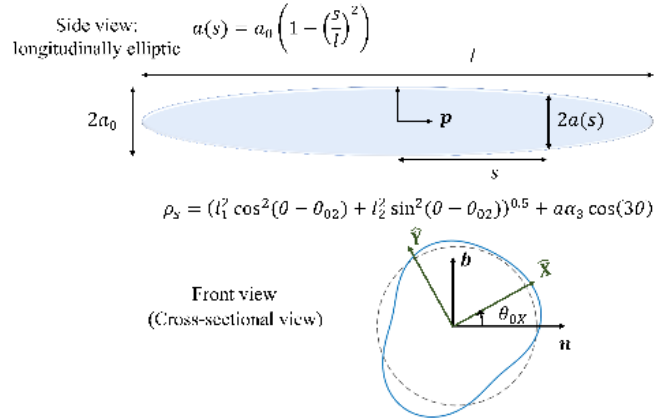


Figure 8. Particle RMS velocity variation with particle aspect ratio,  $A$ , and orbit constant,  $C$  for  $\alpha_3 = 0.1$ . RMS velocity of the particle in (a) the gradient direction and (b) the vorticity direction averaged over 500 tumbling events. Solid lines are phase-space integration using equation (5.5), while the symbols are the results of the time integration (equation 5.4).

These qualitatively new results predicting cross-stream drift due to cross-sectional asymmetries can be compared to the drift velocities observed for curved fibers (Wang et al. 2012) and screw like particles (Kim and Rae 1991). Curved fibers with an aspect ratio 20 and a curvature of unity migrate in the gradient direction with an average velocity of  $1.7 \times 10^{-3}$  (Wang et al. 2012). The drift velocity of screw shaped particles is shown to be  $O(10^{-4})$ , where the length and time are non-dimensionalized using the length of the screw along its axis and the inverse of the shear rate respectively (The diameter of the screw was 1, the diameter of the filament was 0.1, and the screw had two turns.) Both these values which are numerically comparable to the values in figure 8 (a) suggest that the translation of slender bodies caused by cross-sectional modifications can have a similar magnitude to the effects of the shape of the centerline.

### 5.3.Diffusive translation of particles

Chaotic rotation and diffusive translation of a straight particle with a cross-section that is a combination of an ellipse and a third Fourier mode perturbation to a circle is demonstrated. The cross-section is given by  $\rho_s = (l_1^2 \cos^2(\theta - \theta_{02}) + l_2^2 \sin^2(\theta - \theta_{02}))^{0.5} + a\alpha_3 \cos(3\theta)$ , where  $l_1, l_2$  are lengths of the semi-major axes of an ellipse such that  $l_1 > l_2$ ,  $a$  is the radius of the equivalent circle of the ellipse with semi-axes  $l_1, l_2$  obtained from the analysis in section (3.3) and  $\alpha_3$  is the amplitude of the third Fourier mode perturbation to the equivalent circle. The cross-section is chosen to be longitudinally elliptic (i.e.,  $a/a_0 = l_1/l_{1,0} = l_2/l_{2,0} = (1 - s^2)^{0.5}$ ) with  $\theta_{02} = 0$  as such particles are known to rotate chaotically when  $\alpha_3 = 0$  (Yarin et al. 1997). The rotational motion of such particles can be described using Jeffery's (1922) equations of motion since the third Fourier mode perturbation does not alter  $\omega$  as shown earlier. Yarin et al. (1997) demonstrated chaotic rotation of a particle with  $\alpha_3 = 0$ ,  $l_{1,0} = 2/10$  and  $l_{2,0} = 1/10$  (an ellipsoid). Such a particle with a finite  $\alpha_3 = 0.2$  would translate diffusively in addition to rotating chaotically. This particle has  $a_0 = 1.5/10$ ,  $\mathbf{K}$  is represented in terms of  $\bar{\alpha}_2 = 0.33$ ,  $\theta_{02}$  and  $K_{zz} = 0$ ; and  $\mathbf{L}$  is represented in terms of  $\bar{\alpha}_3 = 0.20$ ,  $\theta_{03} = 0$  and  $L_z = 0$ , according to equation (3.18). The values  $\bar{\alpha}_2 = 0.33$ ,  $\bar{\alpha}_3 = \alpha_3$  and  $\theta_{03} = 0$  are accurate within 7% error for  $\forall \alpha_3 \leq 0.2$  and arbitrary  $\theta_{02}$ .



(a)

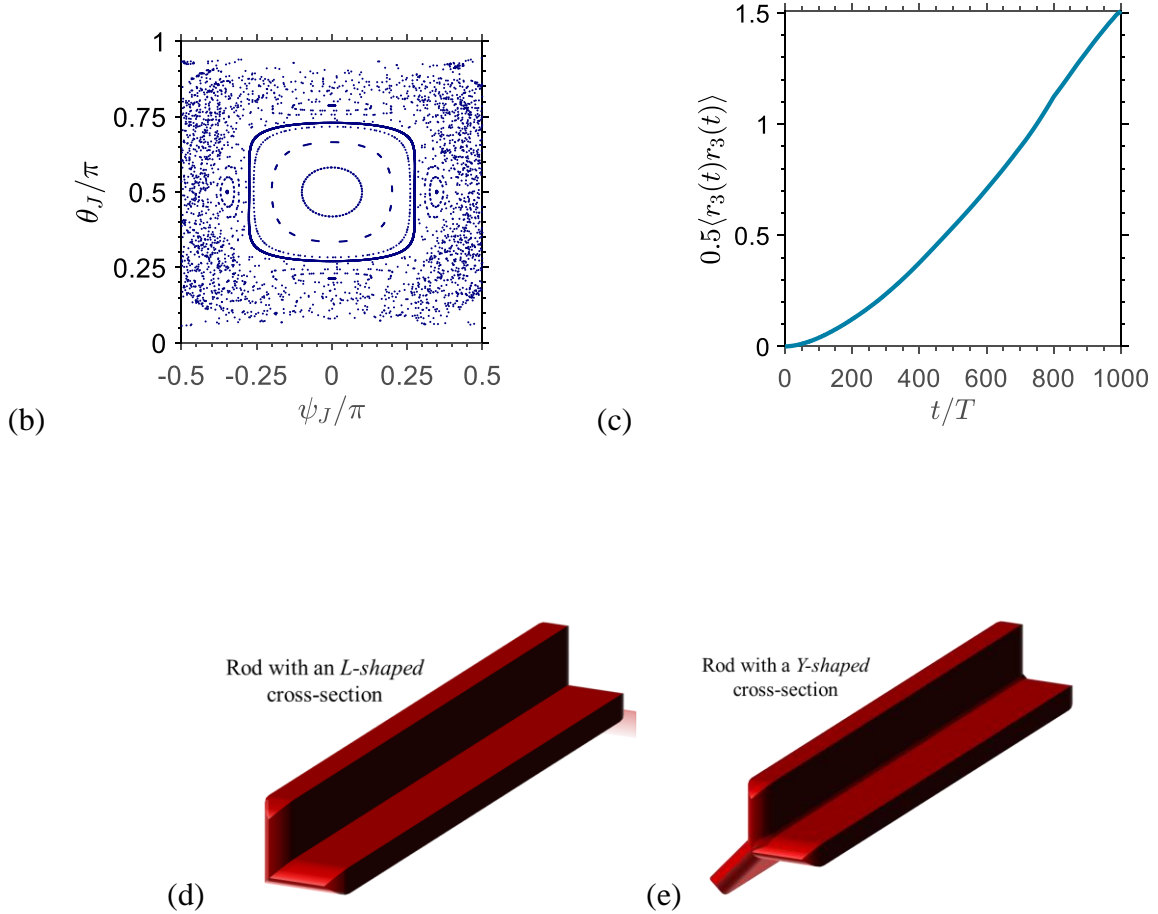


Figure 9. Shape and chaotic dynamics of particles. (a) Representative shape that can rotate and translate chaotically in a SSF. (b) Poincare map sampled when  $\phi_J$  is a multiple of  $\pi$  for the shape in (a) with  $\alpha_3 = 0.1$ ,  $l_{1,0} = 2/10$  and  $l_{2,0} = 1/10$  that shows the chaotic sea. The closed loops represent trajectories in which  $(\phi_J, \theta_J, \psi_J)$  change quasi-periodically. A detailed Poincare map can be seen in figure 6 (a) of Yarin et al. (1997). (c) Variation of  $\langle r_3(t)r_3(t) \rangle$  with the time, suggests a diffusive behavior of the particle position. (d) A straight rod with an *L-shaped*, which can rotate chaotically and migrate diffusively. (e) A straight rod with a *Y-shaped* cross-section that can rotate periodically and translate quasi-periodically. These particles can be fabricated using photolithography (Foulds and Parameswaran 2006) or 3D printing (Raney and Lewis 2015).

The particle motion is obtained using the numerical procedure mentioned in Yarin et al. (1997) for ellipsoids. The Poincare map sampled when  $\phi_J$  is a multiple of  $\pi$  shows the chaotic sea as seen in figure 9 (b). A particle whose orientation starts within the sea will span it after enough time.

The simulation was carried out for a time of  $10^4 T$ , where  $T$  is the time period of rotation of a spheroid of the same aspect ratio,  $A = 1/a_0$ . The diffusivity in the gradient ( $D_{33}$ ) and vorticity ( $D_{22}$ ) direction, obtained from the position of the particle, is given by

$$D_{ij} = \frac{1}{2} \lim_{t \rightarrow \infty} \frac{d}{dt} \langle r_i(t) r_j(t) \rangle. \quad (5.6)$$

The variation of  $\langle r_3 r_3 \rangle$  with time shown in figure 9 (c) suggests a ballistic motion at short times and a diffusive behavior for long times with a diffusivity of  $4 \times 10^{-5}$ . The diffusivity in the vorticity direction  $D_{22} = 6 \times 10^{-8}$  is of much smaller magnitude. The current case is particularly interesting as the particle is self-dispersive at zero-Reynolds number without Brownian diffusion or inter-particle interactions. This gradient diffusivity is numerically comparable to the gradient diffusivity of a fiber of the same length and aspect ratio  $A$  due to interparticle interactions when the dimensional particle number density  $n^* L^{*3} \approx 0.37$ , where  $L^*$  is the dimensional length of the particle (Rahnama et al. 1993; Lopez and Graham 2007). Similarly, the gradient diffusivity of curved fibers with aspect ratios of about 20 is  $O(10^{-5})$  (Wang et al. 2014), again of a magnitude similar to the influence of the cross-section.

The orientational dynamics in this section illustrated for straight cylinders which are longitudinally elliptic can be extended to other straight bodies with tapered ends using results from a complimentary study of Cox (1971). Cox (1971) obtained the  $O(1/(\ln(A) A^2))$  torque acting on a stationary body with tapered ends and a circular cross-section held stationary in the flow-vorticity plane of the simple shear flow. This torque can be matched with the torque required to rotate the particle in a quiescent fluid to obtain  $\boldsymbol{\omega}$ . On applying a regular perturbation of the inner solution of Cox (1971) one can extend his result to a slightly non-circular cross-section. The details can be found in Cox (1971) which is discussed in section (S. 3) of the appendix.

For a cylinder with blunt edges, which is a more practical case, the analysis of Cox (1971) breaks down because the ends of the cylinder generate an  $O(1/A^2)$  torque on the particle. The torque on a stationary cylinder with blunt ends is equal to  $2\mathbf{p} \times \mathbf{F}_{end}$ , where  $\mathbf{F}_{end}$  is the force acting on an end of the particle. For a general shaped cross-section, one can find a second order tensor  $\mathbf{A}$ , such that  $\mathbf{F}_{end} = \mathbf{A} \cdot \mathbf{g}$ .  $\mathbf{A}$  can be derived by taking 3 random orientations and finding

$\mathbf{F}_{end}$  from experiments or numerical solutions of the Stokes equations. The part of  $\boldsymbol{\omega} \cdot (\mathbf{I} - \mathbf{p}\mathbf{p})$  driven by the straining part of the SSF, can be obtained by equating  $2\mathbf{p} \times \mathbf{F}_{end}$  to the torque required to rotate a particle in a quiescent fluid  $8\pi\boldsymbol{\omega} \cdot (\mathbf{I} - \mathbf{p}\mathbf{p})/(3\ln(A))$ .  $\boldsymbol{\omega} \cdot \mathbf{p}$  can be obtained by matching the torque due to  $\mathbf{g} \cdot \mathbf{p}$  to  $4\pi\boldsymbol{\omega} \cdot \mathbf{p}\mathbf{p} \int ds a^2$  (Cox 1971). This can allow us to model the rotational dynamics of straight particles with a general cross-section and blunt edges using the SBT formulation. This calculation of the orientation dynamics of straight particles is important in predicting the structure and rheology of fiber suspensions which could be useful in paper-manufacturing research.

A straight rod with an *L-shaped* cross-section shown in figure 9 (d) has a finite value of  $\bar{\alpha}_2$  and  $\bar{\alpha}_3$  and thereby rotates and translates chaotically (a non-zero  $\bar{\alpha}_2$  is similar to an equivalent elliptic cross-section). A straight rod with a *Y-shaped* cross-section shown in figure 9 (e) has a non-zero value of  $\bar{\alpha}_3$  while  $\bar{\alpha}_2 = 0$  and therefore rotates periodically and translates quasi-periodically. These rods could be fabricated via multi-step photolithography (Foulds and Parameswaran, 2006) or 3D printing (Raney and Lewis 2015) opening a pathway to experimentally verify our results and observe interesting dynamics. Einarsson et al. (2016) measured the rotational motion of non-axisymmetric particles formed by connecting multiple micro-rods, which can simulate particles with two or three lobed cross-sections. The results presented here demonstrate the nature of cross-sectional shapes that can be used to control the rotational and translational dynamics of straight particles in a SSF.

## 6. Motion of rings in a simple shear flow (SSF)

In this section, the SBT is used to predict the dynamics of rings with non-circular cross-sections and the results are verified using boundary element method (BEM) calculations. The influence of the cross-sectional geometry on the rotational and translational motion of rings is established using analytical expressions. Rings with cross-sections that have  $\bar{\alpha}_2 \neq 0$  rotate and translate periodically with no net migration over time if the contribution to the third Fourier mode,  $\bar{\alpha}_3$ , is below a critical value that depends on the aspect ratio. On the other hand, rings with a  $\bar{\alpha}_3 \neq 0$  can attain an equilibrium orientation and can drift indefinitely in the gradient direction if the aspect ratio is above a critical value that depends on  $\bar{\alpha}_3$ . Such rings can self-align without

application of external forces or torques, thereby creating a highly anisotropic structure that can be contrasted with the dispersed particle orientation in a suspension of rotating particles. Here, the length is non-dimensionalized using the radius of the ring  $R$ . The shear rate of the SSF and the viscosity of the fluid are used to non-dimensionalize other quantities of interest such as the force per unit length and the linear and angular velocity of the particle.

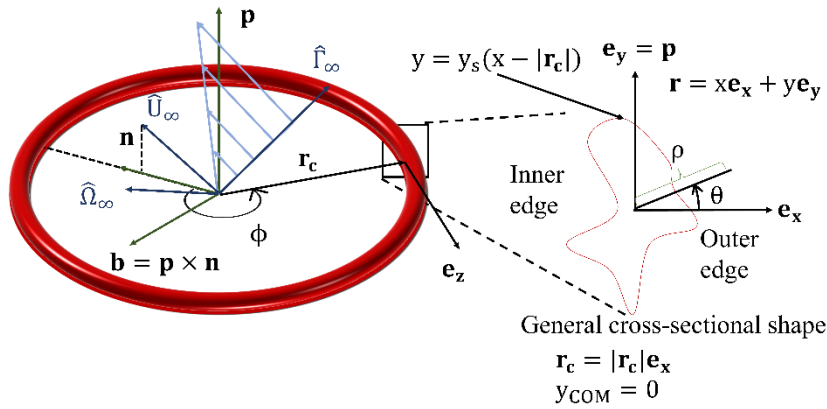


Figure 10. Geometry of a ring and the four coordinate systems, namely the global coordinate system  $(\hat{U}_\infty, \hat{\Omega}_\infty, \hat{\Gamma}_\infty)$ , the particle coordinate system  $(\mathbf{n}, \mathbf{b}, \mathbf{p})$ , the local Cartesian coordinate system  $(\mathbf{e}_x, \mathbf{e}_y, \mathbf{e}_z)$  and the local polar coordinate system  $(\rho, \theta)$  in the cross-section plane.

## 6.1 Coordinate system

The global coordinate system is defined along the flow ( $\hat{U}_\infty$ ), vorticity ( $\hat{\Omega}_\infty$ ) and gradient ( $\hat{\Gamma}_\infty$ ) directions of a SSF as shown in figure 10. The coordinate system relative to the particle is defined along the axis of symmetry,  $\mathbf{p}$ , a vector  $\mathbf{n} = (\mathbf{I} - \mathbf{p}\mathbf{p}) \cdot \hat{U}_\infty$  and a vector  $\mathbf{b} = \mathbf{p} \times \mathbf{n}$ . The local coordinate system  $(\mathbf{e}_x, \mathbf{e}_y, \mathbf{e}_z)$ , is defined such that  $\mathbf{e}_y = \mathbf{p}$ ,  $\mathbf{e}_z$  is tangent to the centerline of the ring cross-section,  $\mathbf{r}_c$ , and  $\mathbf{e}_x = \mathbf{e}_y \times \mathbf{e}_z$  (normal to the centerline of the ring cross-section). Here,  $\mathbf{r}_c$  is the separation vector of the centerline of the ring cross-section relative to the center of mass (COM) of the ring. The center of the cross-section is chosen to coincide with the apparent hydrodynamic center of the cross-section described in section (3.3). The azimuthal angle  $\phi$ , measured from  $\mathbf{n}$  in the plane of the ring (i.e.,  $\mathbf{n} - \mathbf{b}$  plane), determines the position along the

centerline of the ring cross-section. A local polar coordinate system ( $\rho$ - $\theta$ ) is defined in the  $e_x - e_y$  plane, where  $\theta$  is measured from  $e_x$  and  $\rho$  is the normal distance from  $r_c$ . The aspect ratio of the ring is  $A = l/a$ , where  $a$  is the radius of the unperturbed circular cross-section.

## 6.2 Dynamics of rings with slightly non-circular cross-sections

The functional form of the angular velocity ( $\omega$ ) of a ring in an unbounded linear flow field using the linearity of Stokes flow is given by

$$\omega = 0.5\epsilon: W_\infty + \lambda p \times (E_\infty \cdot p), \quad (6.1)$$

where  $p$  is the particle orientation,  $W_\infty = 0.5(\nabla u_\infty - (\nabla u_\infty)^T)$  is the vorticity tensor,  $E_\infty = 0.5(\nabla u_\infty + (\nabla u_\infty)^T)$  is the strain rate and  $\lambda$  is the rotation parameter (Bretherton (1962) and Jeffery (1922)). The drift velocity ( $U - u_\infty(r_{COM})$ ) of the particle relative to the fluid velocity at its centre-of-mass (COM) can be written as

$$U - u_\infty(r_{COM}) = \eta_1 E_\infty \cdot p + \eta_2 (ppp: E_\infty), \quad (6.2)$$

where  $\eta_1$  and  $\eta_2$  are the translation parameters that depend only on the particle geometry (Brenner 1964; Singh, et al. 2013). The values of the dynamic parameters of the particle,  $\lambda$ ,  $\eta_1$  and  $\eta_2$  can be obtained by applying the force-free ( $\int f_{net}(\phi) R d\phi = \mathbf{0}$ ) and torque-free ( $\int ((r - r_{COM}) \times f_{net}(\phi) + g) R d\phi = \mathbf{0}$ ) conditions on the particle, where  $g = \int ds_c (r - r_c) \times (\sigma \cdot \tilde{n}) + (r_c - r_{COM}) \times \int ds_c \cos(\theta) / A (\sigma \cdot \tilde{n})$ ,  $\sigma$  is the stress tensor obtained from the solution of the 2D Stokes equations and  $\nabla^2 u_z = 0$  with  $u = u_\infty$  on the outer boundary and no-slip on the particle surface,  $\tilde{n}$  is the unit normal to the surface of the particle and  $ds_c$  is the elemental length along the cross-sectional contour (see appendix S.4 for details). For rings, equation (3.12) can be solved analytically using elliptic integrals to obtain  $f_{net}$  with errors of  $O(1/A^2)$  (see appendix S.4 for details).  $\lambda$ ,  $\eta_1$  and  $\eta_2$  are given by

$$\lambda = -1 - \frac{\alpha_3 \cos(3\theta_{03})}{A} + \frac{(\ln(8A) - 1.5)}{A^2} C_\lambda + O\left(\frac{\alpha_3^2}{A}\right) + O\left(\frac{\alpha_2^2}{A}\right) + O\left(\frac{\alpha_2 \alpha_3}{A}\right), \quad (6.3)$$

$$\eta_1 = -\frac{2}{3} \frac{\alpha_3 \sin(3\theta_{03})}{A} \frac{(\ln(8A) - K_{zz}/2 - 3)}{\ln(8A) - K_{zz}/3 - 17/6} + O\left(\frac{\alpha_2^2}{A}\right) + O\left(\frac{\alpha_3^2}{A}\right) + O\left(\frac{\alpha_2 \alpha_3}{A}\right), \quad (6.4)$$

$$\eta_2 = \frac{17}{12} \frac{\alpha_3 \sin(3\theta_{03})}{A} \frac{(\ln(8A) - 7K_{zz}/17 - 99/34)}{\ln(8A) - K_{zz}/3 - 17/6} + \frac{\alpha_2 \sin(2\theta_{02})}{4 \ln(8A) - 10} + O\left(\frac{\alpha_2^2}{\ln(8A)}\right) + O\left(\frac{\alpha_3^2}{A}\right) + O\left(\frac{\alpha_2 \alpha_3}{\ln(8A)}\right), \quad (6.5)$$

where  $C_\lambda = A^2 (\int d\phi \mathbf{g} \cdot \hat{\boldsymbol{\Omega}}_\infty) / (2\pi^2) \sim O(1)$ ,  $\mathbf{g}$  being the torque per unit length computed when  $\mathbf{p} = \hat{\boldsymbol{\Gamma}}_\infty$ .  $K_{zz}$  is the effect of the cross-sectional shape on the longitudinal velocity field ( $\mathbf{e}_z$ ) as described in section (3.3) and is zero at  $O(\alpha_2)$  and  $O(\alpha_3)$ . The part of the value of  $\lambda$  equal to  $-1 - \alpha_3 \cos(3\theta_{03})/A$ , is the contribution due to  $\mathbf{f}_{net}$  and the  $O(\ln(8A)/A^2)$  term is the contribution due to  $\mathbf{g}$ . Both of these terms are crucial for particles that can self-align in a simple shear flow for which  $\lambda + 1$  crosses zero. For a general cross-sectional shape equations (6.3) - (6.5) can be used if  $(\alpha_2, \alpha_3)$  are replaced with  $(\bar{\alpha}_2, \bar{\alpha}_3)$ , where  $(\bar{\alpha}_2, K_{zz}, \bar{\alpha}_3)$  are related to  $\mathbf{K}$  and  $\mathbf{L}$  according to equation (3.18). For a circular cross-section  $C_\lambda = 1.5$  and this value maintains great accuracy when  $\bar{\alpha}_2$  and  $\bar{\alpha}_3$  are small.

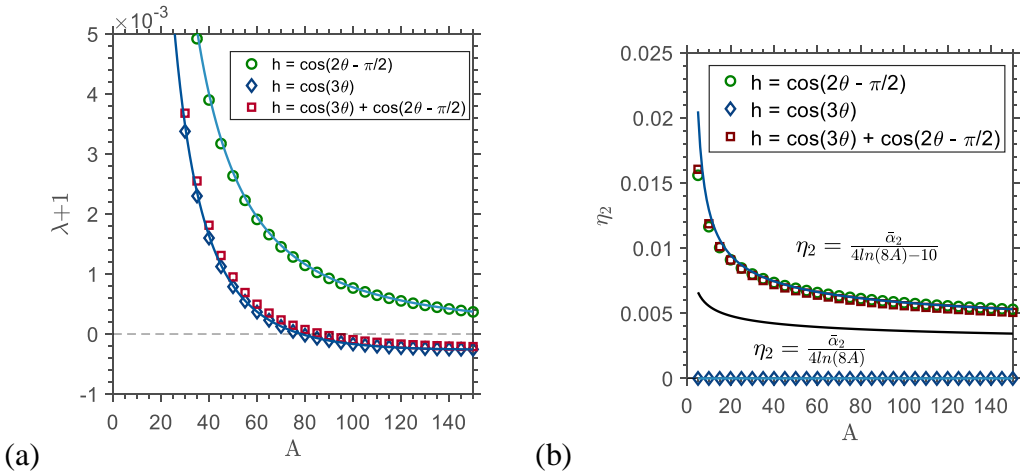


Figure 11. Comparison of SBT with the numerical results obtained from BEM calculations (Borker et al. 2018). Variation of (a)  $\lambda$  and (b)  $\eta_2$ , with aspect ratio,  $A$  (solid lines), and verification with the boundary element method calculations (symbols) for shapes shown in figure 1 (b)-(d). The cross-sectional shape is defined as  $\rho_c = a(1 + 0.1h)$ .

$\lambda$  and  $\eta_2$  obtained from equations (6.3), (6.5) using  $(\bar{\alpha}_2, \bar{\alpha}_3, K_{zz}) = (0.0975, 0.0945, 0.0)$  (as obtained using the numerical calculation in section 3.3 instead of  $(\alpha_2, \alpha_3) = (0.1, 0.1)$ ), compare well with the numerical values obtained from boundary element method (BEM) described in Borker et al. (2018) as shown in figure 11. Figure 11 (a) shows that  $\lambda$  for shapes S-1 and S-3 are nearly identical and close to the SBT prediction. This result confirms the prediction of SBT that at linear order in  $\alpha$ ,  $\lambda$  is only affected by the perturbation to a circle given by  $h(\theta) = \cos(3\theta - 3\theta_{03})$ .  $\lambda$  and  $\eta_2$  are accurately predicted because the integral equation (3.12) is solved with algebraic errors of  $O(1/A^2)$ . For comparison,  $\eta_2$  obtained from the leading order solution  $\bar{\alpha}_2/(4 \ln(8A))$  is only qualitatively accurate as seen in figure 11 (b).

### 6.3 Dynamics of rings that can self-align in a SSF

The translational and rotational motion of rings with an arbitrary cross-sectional shape can be specified using equations (6.1) – (6.5) and requires only the solution of a 2D Stokes flow problem mentioned in section (3.3). The time evolution of the orientation and position of a ring has four qualitatively different states: (i) continuous periodic tumbling without cross-stream translation ( $\bar{\alpha}_3 < C_\lambda(\ln(8A) - 1.5)/A$ ,  $\sin(2\theta_{02}) = 0$ ,  $\sin(3\theta_{03}) = 0$ ), (ii) continuous periodic tumbling with periodic translation ( $\bar{\alpha}_3 < C_\lambda(\ln(8A) - 1.5)/A$  &  $(\bar{\alpha}_2 \sin(2\theta_{02}) \neq 0$  or  $\bar{\alpha}_3 \sin(3\theta_{03}) \neq 0$ )), (iii) equilibrium orientation without cross-stream translation ( $\bar{\alpha}_3 \geq C_\lambda(\ln(8A) - 1.5)/A$ ,  $\bar{\alpha}_3 \neq 0$ ,  $\sin(2\theta_{02}) = 0$ ,  $\sin(3\theta_{03}) = 0$ ), and (iv) equilibrium orientation with a net translation in the gradient direction of the SSF ( $\bar{\alpha}_3 \geq C_\lambda(\ln(8A) - 1.5)/A$ ,  $\bar{\alpha}_3 \neq 0$  &  $(\alpha_2 \sin(2\theta_{02}) \neq 0$  or  $\sin(3\theta_{03}) \neq 0$ ). Cases (i) and (ii) can be studied using traditional SBT formulations of Cox (1970) and Batchelor (1970) respectively and are not treated here. The qualitative nature of ring dynamics in cases (iii) and (iv) cannot be captured using any previous SBT formulations to the best of our knowledge.

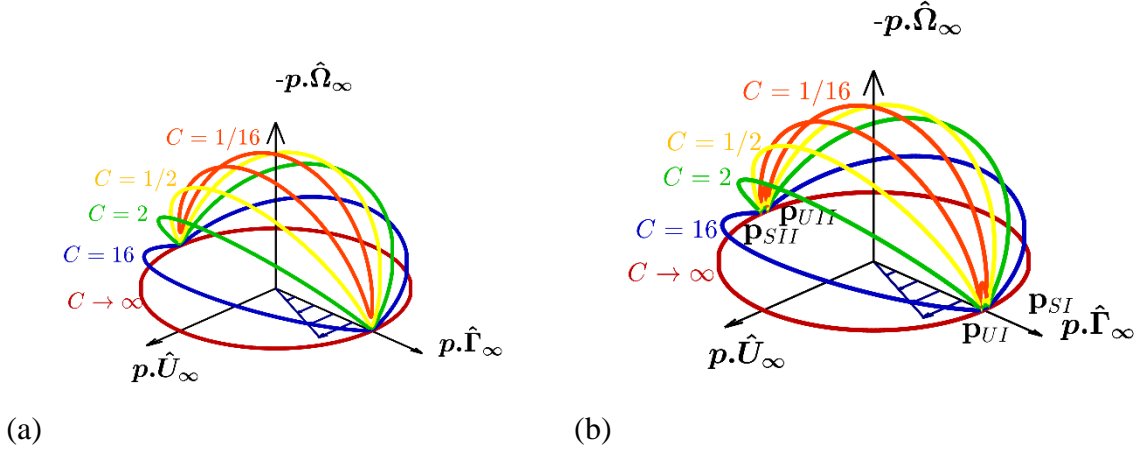


Figure 12. Trajectories traced by the orientation vector of a ring ( $\mathbf{p}$ ) (a) with a circular cross-section and an aspect ratio  $A = R/a = 100$  and (b) with the three-lobed cross section shown in figure 1 (c) with  $\bar{\alpha}_3 = 0.3$ ,  $\theta_{03} = 0$  and  $A = R/a = 100$ . This high value of  $\alpha_3$  was chosen to yield a visually apparent difference between the stable ( $\mathbf{p}_{SI}, \mathbf{p}_{SII}$ ) and unstable ( $\mathbf{p}_{UI}, \mathbf{p}_{UPI}$ ) nodes.

A ring with the cross-section shown in figure 1 (c) (S-II shape) shows qualitatively different rotational dynamics from a ring with a circular or S-I shaped cross-section. Such rings attain an equilibrium orientation, as shown in figure 12 (b), instead of rotating continuously in Jeffery orbits as shown in figure 12 (a). The particle orientation,  $\mathbf{p}$ , aligns along one of the two stable nodes ( $\mathbf{p}_{SI}, \mathbf{p}_{SII}$ ) in the flow-gradient plane which are very close to the gradient direction, as shown in figure 12 (b). This was first shown by Singh et al. (2013) for rings with S-II shaped cross-sections with  $\theta_{03} = 0$ . Rings with an S-II shaped cross-section can in general align for a non-zero  $\theta_{03}$  as evident from equation (6.6), which can be confirmed based on the physical explanation of alignment given in Borker et al. (2018).

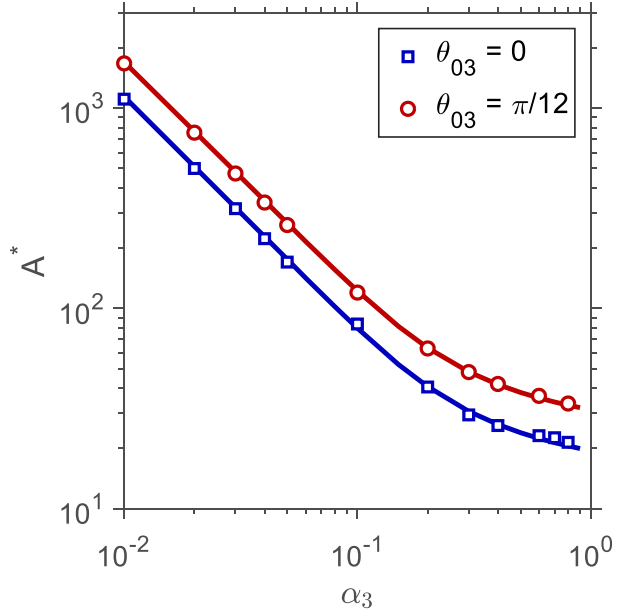


Figure 13. Variation of the critical aspect ratio,  $A^*$ , vs  $\alpha_3$  from SBT (lines) compared with BEM results of Borker et al. (2018) (symbols) for  $\theta_{03} = 0$  and  $\theta_{03} = \pi/12$ .  $\bar{\alpha}_3$  lies in the range  $0.01 \leq \bar{\alpha}_3 \leq 0.27$  for  $0.01 \leq \alpha_3 \leq 0.9$ .

The critical aspect ratio,  $A^*$ , defined as the value of  $A$  for which  $\lambda = -1$ , is a quantity of interest as it is the lowest aspect ratio at which a ring with a given cross-sectional shape can align. A lower value of  $A^*$  would also mean that the ring will be less prone to bending and buckling, thus improving the structural integrity of the particle. Previously, a large number of computationally expensive boundary element method calculations would have been required to compute  $A^*$ . However, the current theory can be used to calculate  $A^*$  from equation (6.6) when  $\lambda = -1$  and is the solution to the equation given by

$$\frac{1}{A^{*2}} (A^* \bar{\alpha}_3 \cos(3\theta_{03}) - C_\lambda(\ln(8A^*) - 1.5)) = 0, \quad (6.6)$$

where  $\bar{\alpha}_3$  is obtained from the solution of the 2D Stokes flow problem mentioned in section (3.3). Equation (6.6) only requires the solution of two 2D Stokes flow problems and a solution to a Laplace's equation to obtain  $\bar{\alpha}_3$  and  $C_\lambda$ . Figure 13 compares the prediction of  $A^*$  from equation (6.6) with the BEM predictions for rings with a cross-section given by  $\rho = a(1 +$

$\alpha_3 \cos(3\theta - 3\theta_{03}))$ . The accurate prediction of  $A^*$  suggests that the current SBT framework can be used as a computationally inexpensive alternative to search for shapes that can self-align at the least  $A^*$ . Furthermore, equation (6.3) suggests that cross-sections with  $\theta_{03} = 0$  (i.e. a fore-aft symmetric shape) and a large value of  $\bar{\alpha}_3$ , should have a smaller  $A^*$  than fore-aft asymmetric shapes. The Y-shaped cross-section in Borker et al. (2018) which has the lowest reported value of  $A^* = 8.9$  has features similar to the 3-lobed cross-section with  $\theta_{03} = 0$ .

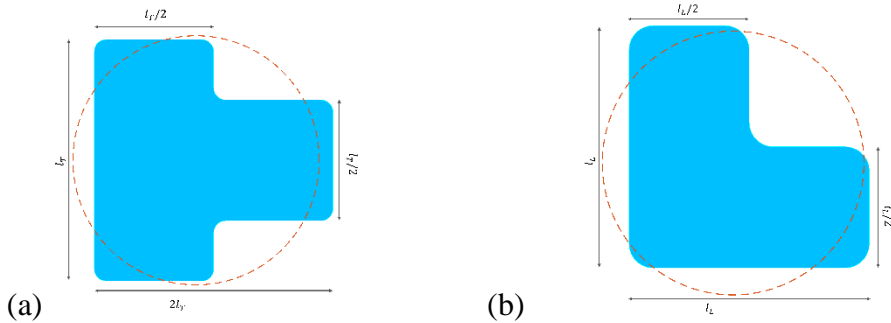
Rings with S-II shaped cross-sections can migrate across streamlines in the gradient direction for non-zero values of  $\theta_{03}$ . These migrating rings could be deposited by flowing the suspension of particles along a surface allowing one to control the roughness or scratch resistance of the underlying surface (Isla et al. 2003). This drift velocity is given by  $\eta_2(\mathbf{p}_s \cdot \hat{\mathbf{U}}_\infty)(\mathbf{p}_s \cdot \hat{\mathbf{F}}_\infty)^2 \approx \eta_2(0.5|1 + \lambda|)^{0.5}$ . The  $O(\bar{\alpha}_2 \sin(2\theta_{02}) / \ln(A))$  drift due to the second Fourier mode perturbation is  $O(A / \ln(A))$  larger than the drift due to the third Fourier mode perturbation. Therefore, shapes with  $\theta_{03} \rightarrow 0$ , which increases  $|\lambda + 1|$ , and  $\theta_{02} \rightarrow \pi/4$ , which maximizes  $\eta_2$ , should generate the highest drift velocities. The cross-section which led to the highest drift shown in figure 9 (a) of Borker et al. (2018) also has a clear resemblance to a shape which is a combination of the second and third Fourier mode with  $\theta_{02} = \pi/4$ .

Rings with the cross-sections shown in figure 14 (a) or (b) can align in a SSF at relatively low aspect ratios (Borker et al. 2018). These rings are of practical interest due to the ease of fabrication using multi-step photolithography (Foulds and Parameswaran, 2006) or optofluidic fabrication (Paulson, Di Carlo and Chung 2015), which can allow for testing the rheology of a suspension of such particles. Here, SBT is utilized to predict the dynamics of individual particles and the results are compared with the numerical predictions obtained using the boundary element method (BEM) detailed in Borker et al. (2018). COMSOL, a finite element solver, was used to perform the 2D Stokes flow calculation presented in section (3.3). The values of  $\mathbf{K}$  and  $\mathbf{L}$ , which were estimated with an uncertainty below 0.1 % when the size of the outer boundary ( $\rho_\infty$ ) was at least 50 times the cross-sectional dimension, are reported in table 1. Figure 14 (c) and (d) show the variation of  $\lambda$  with  $A$  obtained from the BEM calculation and the corresponding SBT prediction for rings with *T-shaped* and *L-shaped* cross-sections, respectively. The SBT precisely mimics the BEM results even at low aspect ratios near the critical aspect ratio,  $A^*$ , which is possible by using the numerical

procedure in section (3.3) and solving the integral in equation (3.17) with errors of  $O(1/A^2)$  using elliptic integrals (appendix S. 4).  $\eta_1$  and  $\eta_2$  are zero for a ring with a *T-shaped* cross-section due to mirror symmetry about a plane normal to  $\mathbf{p}$ . Figures 14 (e) and (f) show the accuracy of SBT to predict the variation of  $\eta_1$  and  $\eta_2$  with  $A$  for rings with the *L-shaped* cross-section. The force per unit length  $\mathbf{f}$  obtained from equation (3.17) is also in excellent agreement with the BEM results for both *L* and *T shaped* cross-sections for  $A \gtrsim 10$  as shown in figure 14 (g)-(h) by the value of  $\mathbf{f}$  at  $\phi = 0.2\pi$ ,  $\mathbf{p} \cdot \hat{\Omega}_\infty = 0$  and  $\mathbf{p} \cdot \hat{\Gamma}_\infty = \cos(0.2\pi)$ . The dependence of  $\mathbf{f}$  on  $\phi$  can be derived using the linearity of the governing equations (Borker et al. 2018) and the imposed boundary conditions and is presented in the appendix (S.4).

Table 1.  $\mathbf{K}$  and  $\mathbf{L}$  values for rings with *T-shaped* and *L-shaped* cross-sections represented in terms of  $(\bar{\alpha}_2, \theta_{02}, K_{zz})$  and  $(\bar{\alpha}_3, \theta_{03}, L_{zx}, L_{zy})$ .

<i>T-shaped</i> ring ( $a = 1.055 \times l_T$ )	$(\bar{\alpha}_2, \theta_{02}, K_{zz})$	$(0.0345, 0, -0.05532)$
	$(\bar{\alpha}_3, \theta_{03}, L_{zx}, L_{zy})$	$(0.157, 0, -8.1 \times 10^{-4}, 0)$
<i>L-shaped</i> ring ( $a = 0.5446 \times l_L$ )	$(\bar{\alpha}_2, \theta_{02}, K_{zz})$	$(0.1534, -\pi/4, -0.05512)$
	$(\bar{\alpha}_3, \theta_{03}, L_{zx}, L_{zy})$	$(0.1366, -\pi/12, 1.4 \times 10^{-3}, 1.4 \times 10^{-3})$



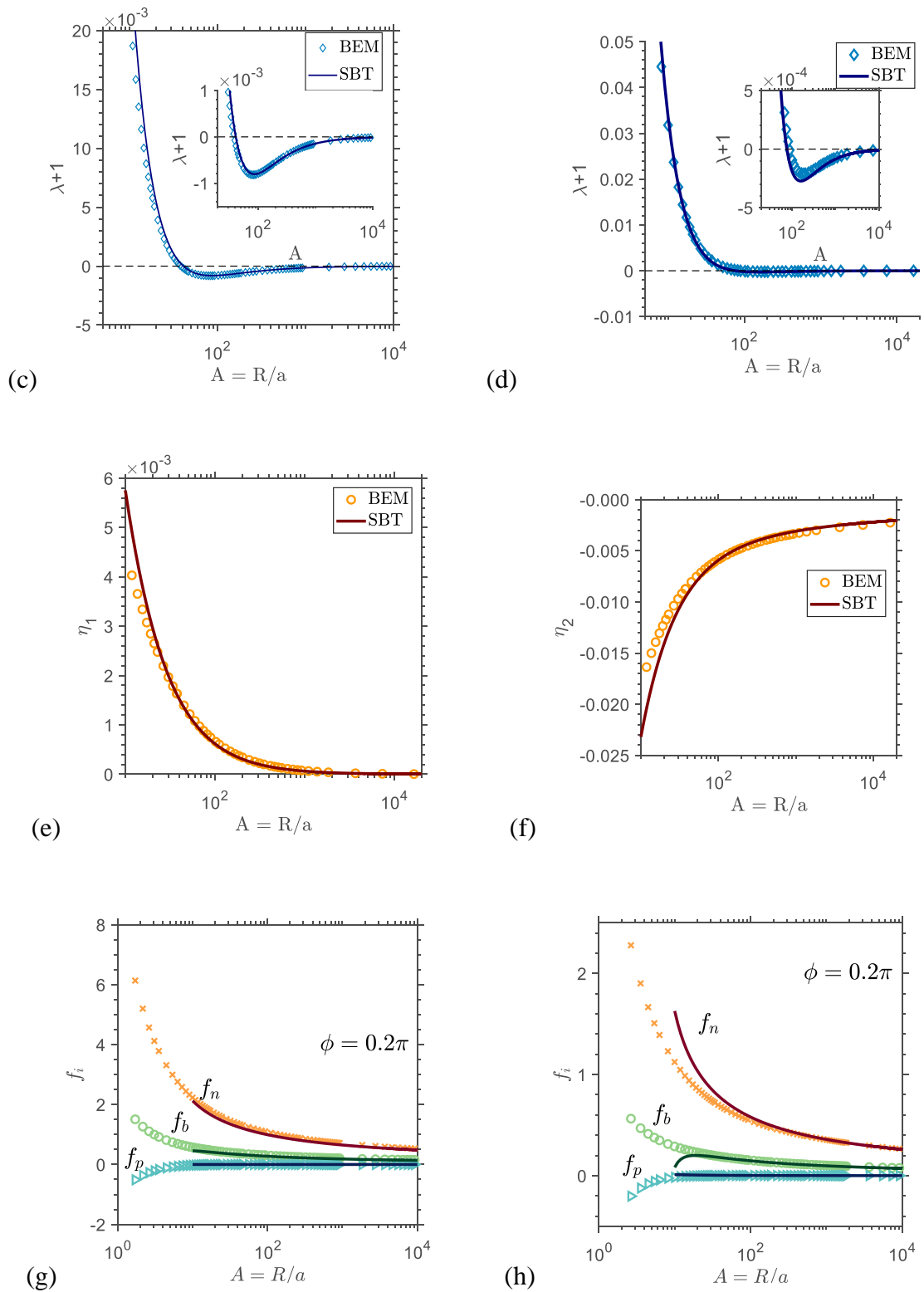


Figure 14. Application of current SBT to predict dynamics of rings with cross-sections which deviate significantly from a circle. (a) A “T-shaped” and (b) an “L-shaped” cross-section proposed

in Borker et al. (2018). Rings with these cross-sections (shaded regions) can align in a SSF at finite aspect ratios. The equivalent circle obtained from the analysis in section (3.3) is shown using dotted lines. Comparison of  $\lambda$  vs  $A$  variation from BEM for rings with (c) *T-shaped* and (d) *L-shaped* cross-sections with the SBT prediction from equation (6.3). Comparison of the variation of (e)  $\eta_1$  and (f)  $\eta_2$  with  $A$  obtained from BEM calculations for rings with an *L-shaped* cross-section with the SBT predictions from equations (6.4) - (6.5). Force per unit length variation with  $A$  at  $\phi = 0.2\pi$ ,  $\mathbf{p} \cdot \hat{\Omega}_\infty = \mathbf{0}$  and  $\mathbf{p} \cdot \hat{\Gamma}_\infty = \cos(0.2\pi)$  for a ring with (g) *T-shaped* and (h) *L-shaped* cross-sections. Symbols are results from the BEM calculations, the solid lines are the corresponding values obtained from the current SBT formulation.

Figures 14 (g)-(h) suggest that our slender body theory accurately predicts  $\mathbf{f}$  which can in turn be utilized to simulate hydrodynamic interactions between various rings, especially the ones that can self-align. This calculation is important for obtaining the rheology of a suspension of rings and also estimating the influence of surrounding particles on the self-aligning characteristics of such a ring. A ring aligned near the flow-vorticity plane has weak hydrodynamic interactions with other aligned rings and therefore the suspension should have a highly anisotropic microstructure, which can be expected to be retained at higher particle concentrations due to excluded volume interactions.

## 7. Conclusion

In this work, a slender-body-theory is developed for a thin, curved body with an arbitrary cross-section that allows one to solve for the velocity, pressure and force per unit length exerted by the particle on the fluid. The derivation is based on asymptotically matching the velocity field of an infinitely long cylinder in the inner region to the velocity field due to a line of forces in the outer region. Our theory accounts for the force per unit length associated with the gradient in the imposed fluid velocity which previously had not been embedded into SBT formulations. The features of the cross-sectional shape that display this qualitatively different force per unit length are described using regular perturbation of the inner solution. A cross-section that has two lobes or three lobes (figures 1 (b) and (c) respectively) will change the force per unit length by  $O(\epsilon^2)$  or  $O(\epsilon/A)$ , respectively. Thought experiments that give physical insight into the special nature of the two and three lobed cross-sections were illustrated. A 2D Stokes flow problem was formulated

that can be numerically solved to extend our theory to arbitrary cross-sectional shapes which deviate significantly from a circle. Our analysis also captures the force per unit length driven by the relative velocity of the particle and the fluid for a non-circular cross-section, which was first derived by Batchelor (1970).

A slender cylinder that has a significant contribution to  $\alpha_2$  and  $\alpha_3$ , e.g. an *L-shaped* cross-section (figure 8 d), rotates and translates chaotically, while a cylinder with a finite contribution to  $\alpha_3$  along with  $\alpha_2 = 0$ , e.g. a *Y-shaped* cross-section (figure 8 e), rotates periodically and translates quasi-periodically. Our theory accurately predicted the resistance to translation and rotation for a triaxial ellipsoids even for high-aspect ratio cross-sections as shown by comparison with the exact results of Lamb (1932). In this case, the current method provides a computationally inexpensive alternative to other available approaches such as slender ribbon theory (Koens and Lauga, 2016) or boundary element method (Youngren & Acrivos, 1975; Kim & Karilla, 1991; Pozrikidis, 2002). The dynamics of rings with different cross-sectional shapes in a simple shear flow was used to further validate our theory by comparing the results with boundary element method calculations of Singh et al. (2013) and Borker et al. (2018). The perturbation analysis described in this paper could be extended to Stokes flow with fluid inertia (Khayat and Cox, 1989), potential flow (Lighthill 1960, 1971) and heat transfer (Beckers et al. 2015) to find the impact of the gradients in the respective background fields. The solution of the respective two-dimensional problem, similar to the problem described in section (3.3), could be used to extend the result to a general cross-sectional shape.

The advancement in nano-fabrication shows promise of utilizing micro and nanoscale objects with high-aspect ratio appendages to aid in targeted drug delivery, material assembly (Sacanna et al 2013) or water treatment (Gao and Wang 2014; Soler and Sanchez 2014). These slender micromachines would be subject to velocity gradients and our current work can be utilized to simulate their dynamics and thereby learn about optimal propulsion mechanism under a background flow field.

Our theory can also be utilized to understand slender particle dynamics in various linear flow fields. The results of section (5) suggest that the effects of the cross-section can have magnitudes similar to the effects of the curvature of the centerline of curved slender bodies. The current theory

can be used to study the motion of straight particles in a simple shear flow (SSF), which has a rich dynamical structure. A sampling of such results were presented in section (5) for straight cylinders with mirror symmetry about the longitudinal direction where the  $O(\alpha_3/A)$  force per unit length induced a net translation. The  $O(\alpha_3/A)$  force per unit length, being proportional to  $a$ , will also induce an  $O(\alpha_3/A)$  angular velocity to any particle that lacks mirror symmetry about the longitudinal direction. This  $O(\alpha_3/A)$  angular velocity, which is important when the particle is near the flow-vorticity plane, has a much stronger scaling than the  $O(\ln(A)/A^2)$  contribution from the dipole per unit length. Such particles can also translate with an  $O(1)$  velocity arising from asymmetry along the longitudinal direction leading to velocities an order of magnitude larger than the ones presented in section (5). Furthermore, such asymmetric particles that have an additional contribution to  $\alpha_2$  could also rotate and translate chaotically. The motion of straight cylinders can be explored using the current SBT formalism along with the solution of Cox (1971). Our work gives insight into the geometry of cross-sections that are important and the tools to explore the motion of such slender shapes in a shear flow.

The force per unit length acting on rings with non-circular cross-section, presented in section 6, can be used to simulate hydrodynamic interactions between multiple rings to obtain the structure and rheology of a suspension of rings. The particular case of interest is obtaining the rheology of rings that can attain an equilibrium orientation in a SSF, which has never been explored. A suspension of such aligned rings has the possibility of attaining high degrees of anisotropy due to alignment of all particles in the same orientation, which could be useful to manufacture highly anisotropic materials. Hydrodynamic interactions between rings can be captured by using equation (3.12) or (3.17) with the velocity disturbance produced by other rings included in the  $\mathbf{u}_\infty$  term and solving for the force per unit length up to  $O(1/\ln(2A))$ .

## 8. Appendix

### S.1 General form of the velocity field in the inner problem of slender body theory

The general solution to a 2-D biharmonic equation ( $\nabla^4 \psi = 0$ ) for flow in the transverse plane of an infinite cylinder such that  $\rho$  at the cross-sectional surface is single valued with  $\theta$  is given by

$$\begin{aligned} \frac{\psi}{a} = & \tilde{a}_0 \left(\frac{\rho}{a}\right)^2 + b_0 \left(\frac{\rho}{a}\right)^2 \ln \left(\frac{\rho}{a}\right) + c_0 + d_0 \log \left(\frac{\rho}{a}\right) + \left[ a_1 \left(\frac{\rho}{a}\right)^3 + b_1 \left(\frac{\rho}{a}\right)^{-1} + c_1 \left(\frac{\rho}{a}\right) + \right. \\ & \left. d_1 \left(\frac{\rho}{a}\right) \ln \left(\frac{\rho}{a}\right) \right] \cos(\theta) + \left[ \hat{a}_1 \left(\frac{\rho}{a}\right)^3 + \hat{b}_1 \left(\frac{\rho}{a}\right)^{-1} + \hat{c}_1 \left(\frac{\rho}{a}\right) + \hat{d}_1 \left(\frac{\rho}{a}\right) \ln \left(\frac{\rho}{a}\right) \right] \sin(\theta) + \\ & \sum_{n=2}^{\infty} \left[ a_n \left(\frac{\rho}{a}\right)^n + b_n \left(\frac{\rho}{a}\right)^{n+2} + c_n \left(\frac{\rho}{a}\right)^{-n} + d_n \left(\frac{\rho}{a}\right)^{-n+2} \right] \cos(n\theta) + \sum_{n=2}^{\infty} \left[ \hat{a}_n \left(\frac{\rho}{a}\right)^n + \hat{b}_n \left(\frac{\rho}{a}\right)^{n+2} + \right. \\ & \left. \hat{c}_n \left(\frac{\rho}{a}\right)^{-n} + \hat{d}_n \left(\frac{\rho}{a}\right)^{-n+2} \right] \sin(n\theta), \end{aligned} \quad (\text{S 1.1})$$

where  $\psi$  is the stream function,  $\tilde{a}_0, a_n, b_n, c_n, d_n, \hat{a}_n, \hat{b}_n, \hat{c}_n$  and  $\hat{d}_n$ , for  $n = 0$  to  $\infty$ , are constants (Sadeh, 1967). The two-dimensional velocity field can be obtained from the definition of the stream function, i.e.,  $u_\rho = \rho^{-1} \partial \psi / \partial \theta$  and  $u_\theta = -\partial \psi / \partial \rho$ .

The velocity along the longitudinal direction can be obtained by assuming negligible change in pressure along the longitudinal direction (i.e.  $\nabla^2 u_z = 0$ ). The general solution to this harmonic is given by

$$u_z = e_0 + f_0 \ln \left(\frac{\rho}{a}\right) + \sum_{n=1}^{\infty} \left[ e_n \left(\frac{\rho}{a}\right)^n + f_n \left(\frac{\rho}{a}\right)^{-n} \right] \cos(n\theta) + \sum_{n=1}^{\infty} \left[ \hat{e}_n \left(\frac{\rho}{a}\right)^n + \right. \\ \left. \hat{f}_n \left(\frac{\rho}{a}\right)^{-n} \right] \sin(n\theta), \quad (\text{S 1.2})$$

where  $e_0, e_n, f_n, \hat{f}_n, \hat{e}_n$ , for  $n = 1$  to  $\infty$ , are constants.

The general functional form of the terms  $\tilde{u}_z$  and  $\tilde{\psi}$  in polar coordinates required for doing the perturbation analysis and obtaining  $C'$  and  $D'$  (equations (3.4) and (3.5)) can be obtained from equations (S 1.1) and (S 1.2) respectively.  $\tilde{u}_z$  needs to be zero at the particle surface and match the imposed flow field for  $\rho/a \gg 1$  and therefore can only have a constant term, and terms of the

form,  $((\rho/a)^n - (\rho/a)^{-n}) \cos(n\theta)$  and  $((\rho/a)^n - (\rho/a)^{-n}) \sin(n\theta)$ , where  $n$  is any positive integer. Likewise,  $\tilde{\psi}$  can be obtained from the general expression mentioned in equation (S 1.1), such that the corresponding velocity field satisfies the no-slip boundary condition on the particle surface (i.e.,  $\partial\tilde{\psi}/\partial\theta = 0$  and  $\partial\tilde{\psi}/\partial\rho = 0$  at  $\rho = a$ ). The expression for  $\tilde{u}_z$  and  $\tilde{\psi}$  for a general imposed flow field and a circular cross-section are given as

$$\tilde{u}_z = \sum_{n=1}^{\infty} (e_n \cos(n\theta) + \hat{e}_n \sin(n\theta)) \left[ \left(\frac{\rho}{a}\right)^n - \left(\frac{\rho}{a}\right)^{-n} \right], \quad (\text{S 1.3})$$

where  $e_n$  and  $\hat{e}_n$  can be obtained by matching to the imposed velocity field for  $\rho \gg a(s)$ .

$$\begin{aligned} \frac{\tilde{\psi}}{a} = & \tilde{a}_0 \left( \left(\frac{\rho}{a}\right)^2 - 2 \ln \left(\frac{\rho}{a}\right) \right) + b_0 \left( \left(\frac{\rho}{a}\right)^2 - 1 \right) \ln \left(\frac{\rho}{a}\right) + c_0 + a_1 \left[ \left(\frac{\rho}{a}\right)^3 - \left(\frac{\rho}{a}\right)^{-1} - \right. \\ & \left. 4 \left(\frac{\rho}{a}\right) \ln \left(\frac{\rho}{a}\right) \right] \cos(\theta) + \hat{a}_1 \left[ \left(\frac{\rho}{a}\right)^3 - \left(\frac{\rho}{a}\right)^{-1} - 4 \left(\frac{\rho}{a}\right) \ln \left(\frac{\rho}{a}\right) \right] \sin(\theta) + \sum_{n=2}^{\infty} (a_n \cos(n\theta) + \\ & \hat{a}_n \sin(n\theta)) \left[ \left(\frac{\rho}{a}\right)^n + (n-1) \left(\frac{\rho}{a}\right)^{-n} - n \left(\frac{\rho}{a}\right)^{-n+2} \right] + (b_n \cos(n\theta) + \hat{b}_n \sin(n\theta)) \left[ \left(\frac{\rho}{a}\right)^{n+2} + \right. \\ & \left. (n) \left(\frac{\rho}{a}\right)^{-n} - (n+1) \left(\frac{\rho}{a}\right)^{-n+2} \right], \end{aligned} \quad (\text{S 1.4})$$

where  $\tilde{a}_0, b_0, a_1, \hat{a}_1, a_n, \hat{a}_n, b_n$  and  $\hat{b}_n$ , with  $n \geq 2$  are constants obtained by matching to the imposed velocity field for  $\rho \gg a$ .

## S.2 Effect of the cross-section on the velocity field in the longitudinal direction

The force per unit length in the longitudinal direction is first affected by the details of the cross-section at  $O(\epsilon^2 \alpha^2)$ , which can be seen by substituting  $\rho = a(1 + \alpha h(s, \theta))$  in equation (S 1.3) and performing the matching with the outer solution at  $O(\alpha^2)$ . Here the perturbation parameter  $\alpha \ll 1$ ,  $h(s, \theta)$  is a smooth and bounded function periodic in  $\theta$  with a period of period  $2\pi/N$ , where  $N$  is any positive integer, such that  $\max|h(s, \theta)| \sim O(1)$  and  $|\partial h/\partial s| \sim O(1)$ . The terms in the inner solution of the longitudinal velocity field at  $O(\alpha)$ , which will be matched with an outer solution are given by

$$\alpha u'_z = \alpha \left( e'_0 + E' \ln \left( \frac{\rho}{a} \right) \right), \quad (\text{S } 2.1)$$

where  $u'_z \sim O(1)$ .  $E'$  is determined, in a manner similar to  $E$ , by matching to an outer velocity field, and  $e'_0$  is determined by satisfying the no-slip boundary condition on the particle surface. From the form of the longitudinal velocity field in equation (S 1.3) it can be easily shown that  $e'_0 = 0$ . This in turn results in  $E' = 0$  and so there is no effect on the force per unit length in the longitudinal direction (i.e.  $f'_z = 0$ ). The terms in the inner solution of the longitudinal velocity field at  $O(\alpha^2)$ , which will be matched with an outer solution which will have a form similar to equation (S 2.1) and is given by

$$\alpha^2 u''_z = \alpha^2 \left( e''_0 + E'' \ln \left( \frac{\rho}{a} \right) \right), \quad (\text{S } 2.2)$$

where  $u''_z \sim O(1)$ .  $E''$  is determined by matching to an outer velocity field and  $e''_0$  is determined by satisfying the no-slip boundary condition on the particle surface.  $e''_0$  can be finite unlike  $e'_0$  which must be zero to satisfy the no-slip boundary condition. On matching with an outer velocity field one can easily see that the force per unit length in the longitudinal direction due to the perturbation in the cross-sectional shape is of  $O(\alpha^2 \epsilon^2)$ . This influence of the cross-section on  $u_z$  for a general cross-section is captured by  $K_{zz}$  mentioned in section (3.3).

### S.3 Dipole per unit length for straight particles

Consider a straight particle with a cross-section given by  $\rho_s = (l_1^2 \cos^2(\theta - \theta_{02}) + l_2^2 \sin^2(\theta - \theta_{02}))^{0.5} + a\alpha_3 \cos(3\theta)$ , where  $l_1, l_2$  are lengths of the semi-major axes of an ellipse such that  $l_1 > l_2$ ,  $a$  is the radius of the equivalent circle of the ellipse with semi-major axes  $l_1, l_2$  obtained from the analysis mentioned in section (3.3) and  $\alpha_3$  generates a third Fourier mode perturbation to a circle. We look at a specific example of a particle that is longitudinally elliptic (i.e.,  $a/a_0 = l_1/l_{1,0} = l_2/l_{2,0} = (1 - s^2)^{0.5}$ ) and has  $\theta_{02} = 0$ . Using the analysis presented in section (3.3),  $a_0, \mathbf{K}$ , represented in terms of  $(\bar{\alpha}_2, \theta_{02}, K_{zz} = 0)$  and  $\mathbf{L}$ , represented in terms of  $(\bar{\alpha}_3, \theta_{03} = 0)$  are obtained. For small perturbations from a circle, one can obtain  $a_0 = 0.5(l_{1,0} + l_{2,0})$ ,  $\bar{\alpha}_2 \approx (l_{1,0} - l_{2,0})/(2a_0)$  and  $K_{zz} = 0$ , valid when  $(l_{1,0} - l_{2,0})/(l_{1,0}) \ll 1$ , where the second

subscript refers to  $s = 0$  position. These asymptotic values of  $a$ ,  $\bar{\alpha}_2$ ,  $\bar{\alpha}_3$  are used for the analysis in the remainder of the section.

The angular velocity of this particle obtained from the analysis of Jeffery (1922) in terms of  $\bar{\alpha}_2$  can be written as

$$\begin{aligned}\omega_{\hat{X}} &= \frac{\gamma_5}{A^2} + \frac{2\bar{\alpha}_2}{A^2} (-\gamma_5 \cos(2\theta_{02}) + (\gamma_3 + \gamma_4) \sin(2\theta_{02})), \\ \omega_{\hat{Y}} &= \gamma_3 - \frac{\gamma_3 + \gamma_4}{A^2} - \frac{2\bar{\alpha}_2}{A^2} (\gamma_5 \sin(2\theta_{02}) + (\gamma_3 + \gamma_4) \cos(2\theta_{02})), \\ \omega_p &= -\frac{\gamma_2}{2} + \bar{\alpha}_2 (\gamma_2 \cos(2\theta_{02}) - \gamma_1 \sin(2\theta_{02})),\end{aligned}\tag{S 3.1}$$

where  $\gamma_2 = \nabla \mathbf{u}_{\infty} : \hat{Y} \hat{X}$ ,  $\gamma_3 = \nabla \mathbf{u}_{\infty} : \hat{X} p$ ,  $\gamma_4 = \nabla \mathbf{u}_{\infty} : p \hat{X}$ ,  $\gamma_5 = \nabla \mathbf{u}_{\infty} : p \hat{Y}$ . Here  $p$  is along the longitudinal direction of the particle  $\hat{Y}$  is chosen such that it has zero projection along the flow direction (i.e.,  $\hat{Y} \cdot \hat{U}_{\infty} = 0$ ) and  $\hat{X} = \hat{Y} \times p$ . Equation (S 3.1) is equivalent to equation (5.1) for  $\alpha_2 = 0$  with  $\lambda_J = 1 - 2/A^2$ . The torque per unit length exerted by the particle on the fluid,  $\mathbf{g} = \int dl \mathbf{r} \times \tilde{\mathbf{n}} \cdot (\nabla \mathbf{u}^{\text{inner}} + (\nabla \mathbf{u}^{\text{inner}})^T)$ , where  $dl$  is the integral over the cross-sectional contour and  $\tilde{\mathbf{n}}$  is the outward normal to the surface.  $\mathbf{u}^{\text{inner}} = \mathbf{e}_z \times \nabla_{2D}(\psi + \alpha\psi')$ , is obtained from the inner solution of slender body theory presented in section (3).  $\mathbf{g}$  is given by

$$\begin{aligned}g_{\hat{X}} &= 2\pi a^2 (-\gamma_5 + \bar{\alpha}_2 (\gamma_5 \cos(2\theta_{02}) - (\gamma_3 + \gamma_4) \sin(2\theta_{02}))), \\ g_{\hat{Y}} &= 2\pi a^2 ((\gamma_4 + \gamma_3) + \bar{\alpha}_2 (\sin(2\theta_{02}) (\gamma_5) + \cos(2\theta_{02}) (\gamma_4 + \gamma_3))), \\ g_p &= 4a^2 \pi \left( \frac{\gamma_2}{2} + \omega_z + \bar{\alpha}_2 (-\cos(2\theta_{02}) \gamma_2 + \sin(2\theta_{02}) \gamma_1) \right),\end{aligned}$$

(S 3.2)

where  $a$  is the radius of the equivalent circle of the local cross-section. The  $O(1)$  term in  $\omega_{\hat{Y}}$  (i.e.,  $\gamma_3$ ) arises by setting the torque produced by the  $O(1/\ln(2A))$  force per unit length  $\mathbf{f}_{net}$  to zero.  $O(1/A^2)$  terms in  $\omega_{\hat{X}}$  and  $\omega_{\hat{Y}}$  as well as  $\omega_{\hat{P}}$  are driven by the torque per unit length,  $\mathbf{g}$ , as can be seen by the similarity of these terms from equations (S 3.1) and (S 3.2). This analysis is not straightforward but a result from a complimentary study by Cox (1971) can be used to obtain the  $O(1/A^2)$  terms in  $\mathbf{g}$ ,  $\omega_{\hat{X}}$  and  $\omega_{\hat{Y}}$ , which we shall describe briefly in the next paragraph.

Cox (1971) obtained the torque acting on a slender particle with a circular cross-section with tapered ends held stationary ( $\boldsymbol{\omega} = \mathbf{0} = \mathbf{U}$ ) such that  $\mathbf{p}$  lies in the flow vorticity plane. At this orientation the torque on the particle is a linear, homogeneous function of  $\mathbf{g}$ . In Cox's terminology, the torque on the particle can be given by

$$\mathbf{G} = - \int ds (\mathbf{g} + s\mathbf{p} \times \tilde{\mathbf{f}}), \quad (\text{S 3.3})$$

where  $\tilde{\mathbf{f}}$  is given by

$$\tilde{\mathbf{f}} = \tilde{\mathbf{f}}_0 + \frac{\tilde{\mathbf{f}}_1}{\ln(A)}. \quad (\text{S 3.4})$$

$\tilde{\mathbf{f}}_0$ , obtained by ensuring that the  $O(1/A^2)$  velocity field has no terms that grow as  $\ln(\rho)$ , is equal to  $\mathbf{p} \times (d\mathbf{g}/ds \cdot (\mathbf{I} - \mathbf{p}\mathbf{p}))$  with  $\bar{\alpha}_2 = 0$  (Cox 1971). This ensures that the torque produced by  $\mathbf{g}$  exactly cancels the torque due to  $\tilde{\mathbf{f}}_0$  and the torque on the body is equal to the torque produced by a force per unit length equal to  $-\tilde{\mathbf{f}}_1/\ln(A)$ .  $\tilde{\mathbf{f}}_1$ , obtained by matching the  $\ln(\rho)$  term of the  $O(1/(A^2 \ln(A)))$  inner and outer velocity fields, is equal to  $\mathbf{p} \times (d\mathbf{g}/ds \cdot (\mathbf{I} - \mathbf{p}\mathbf{p}))$  with  $\bar{\alpha}_2 = 0$  (Cox 1971). Since  $\tilde{\mathbf{f}}$  is driven by  $\mathbf{g}$ , we can perform Cox's analysis for any general orientation  $\mathbf{p}$  if we know  $\mathbf{g}$ , which as mentioned previously can be derived solely from the inner solution and is given by equation (S 3.2) for  $\bar{\alpha}_2 = 0$ . The angular velocity can be obtained by matching the torque in equation (S 3.2) to the torque required to rotate the particle with an angular velocity  $\boldsymbol{\omega}$  in a

quiescent fluid, which is equal to  $8\pi\omega \cdot (\mathbf{I} - \mathbf{p}\mathbf{p})/(3\ln(A)) + 4\pi\omega \cdot \mathbf{p}\mathbf{p} \int ds a^2$ . This analysis yields  $\boldsymbol{\omega}$  in equation (S 3.1) when  $\bar{\alpha}_2 = 0$ .

For a finite  $\bar{\alpha}_2$  we can obtain the complete inner solution in terms of the stream function  $\psi + \alpha_2\psi'_2$  and a longitudinal velocity field  $u_z + \bar{\alpha}_2 u'_z$ . This inner velocity field can be used to derive the torque per unit length,  $\mathbf{g}$ , given in equation (S 3.2). Using the exact procedure mentioned in Cox's analysis for a finite  $\bar{\alpha}_2$ , the force per unit length,  $\tilde{\mathbf{f}}_{\text{net}}$ , like  $\tilde{\mathbf{f}}$  is Cox's analysis, can be written as

$$\tilde{\mathbf{f}}_{\text{net}} = \tilde{\mathbf{f}}_0 + \frac{\tilde{\mathbf{f}}_1}{\ln(A)} + \bar{\alpha}_2 \left( \tilde{\mathbf{f}}'_0 + \frac{\tilde{\mathbf{f}}'_1}{\ln(A)} \right).$$

(S 3.5)

$\tilde{\mathbf{f}}_0 + \bar{\alpha}_2 \tilde{\mathbf{f}}'_0$  should equal  $\mathbf{p} \times (d\mathbf{g}/ds \cdot (\mathbf{I} - \mathbf{p}\mathbf{p}))$ , to ensure that there is no  $\ln(\rho)$  term in the  $O(1/A^2)$  velocity field. And this equality naturally ensures that the torque due to  $\tilde{\mathbf{f}}_0 + \bar{\alpha}_2 \tilde{\mathbf{f}}'_0$  exactly cancels the torque due to  $\mathbf{g}$  in equation (S 3.2). This torque balance is true for a straight particle with arbitrary cross-section and tapered ends. Thereby the total torque acting on the particle is equal to the torque produced by  $\tilde{\mathbf{f}}_1/\ln(A) + \bar{\alpha}_2 \tilde{\mathbf{f}}'_1/\ln(A)$ .  $\tilde{\mathbf{f}}_1 + \bar{\alpha}_2 \tilde{\mathbf{f}}'_1$  is obtained by matching the  $\ln(\rho)$  term of the  $O(1/(A^2 \ln(A)))$  velocity field with the inner solution and is equal to  $2\mathbf{p} \times (d\mathbf{g}/ds \cdot (\mathbf{I} - \mathbf{p}\mathbf{p}))$ . The factor of 2 in the above expression arises because there is an additional  $\ln(\rho)$  term in the inner solution similar to the terms with  $C'$  and  $D'$  in equation (3.1) of the main text which is absent while doing the matching for a circular cross-section. Thus,  $\mathbf{G}$  scales as  $\mathbf{g}/\ln(A)$  and the result of Cox (1970) can be generalized if we obtain  $\mathbf{g}$  due to the slight perturbation to a circular cross-section. This can be done analytically as shown in equation (S 3.2) or numerically using the solution of a 2D Stokes equation in the cross-sectional plane (section (3.3)) and a harmonic equation for the velocity field in the longitudinal direction ( $\nabla^2 u_p = 0$ ).

The ends of a straight particle with blunt ends lead to an  $O(1/A^2)$  torque on the particle, which is larger than the  $O(1/(A^2 \ln(A)))$  torque for tapered ended particles shown in the above analysis. Thus, the dynamics of blunt ended particles in a simple shear flow would critically

depend on the shape of the ends. We quantify the effect of the ends on  $\omega$  using a thought experiment similar to the one in section (3.1). For the thought experiment, only the effect of the straining component of the SSF is required as the rotational component forces a torque-free particle to perform a solid body rotation.

Consider a blunt-ended slender particle with a cross-section which has an  $N^{th}$  Fourier mode perturbation to a circle placed in a straining flow of strain rate  $E$ . Using symmetry of each Fourier mode and linearity of the flow field, the torque per unit length on the particle,  $\mathbf{g}$ , in the transverse direction can be given by

$$\begin{aligned}\mathbf{g} \cdot (\mathbf{I} - \mathbf{p}\mathbf{p}) &= (\mathbf{p} \times \mathbf{n})[\tilde{\chi}_1 \mathbf{p} \cdot \mathbf{E} \cdot \mathbf{p} + \tilde{\chi}_2 \mathbf{p} \cdot \mathbf{E} \cdot \mathbf{n} + \tilde{\chi}_3 \mathbf{n} \cdot \mathbf{E} \cdot \mathbf{n} + \tilde{\chi}_4 (\mathbf{p} \times \mathbf{n}) \cdot \mathbf{E} \cdot (\mathbf{p} \times \mathbf{n})] \\ &\quad + \mathbf{n}[\tilde{\chi}_5 \mathbf{p} \cdot \mathbf{E} \cdot (\mathbf{p} \times \mathbf{n}) + \tilde{\chi}_6 \mathbf{n} \cdot \mathbf{E} \cdot (\mathbf{p} \times \mathbf{n})] + \tilde{\chi}_7 (\mathbf{p} \cdot \mathbf{E}) \times \mathbf{p} + \tilde{\chi}_8 (\mathbf{n} \cdot \mathbf{E}) \times \mathbf{p}\end{aligned}$$

(S 3.6)

where  $\tilde{\chi}_i$ ,  $i = 1, 2, \dots, 8$  are geometric parameters and  $\mathbf{n}$  is the orientation along one of the lines of symmetry of the cross-section. Similarly, using the linearity of the flow field and the cross-sectional shape, the force generated at the ends of the particle in the transverse direction,  $\mathbf{F}_{end}$ , can be written as

$$\begin{aligned}\mathbf{F}_{end} &= \mathbf{n}[\tilde{\xi}_1 \mathbf{p} \cdot \mathbf{E} \cdot \mathbf{p} + \tilde{\xi}_2 \mathbf{p} \cdot \mathbf{E} \cdot \mathbf{n} + \tilde{\xi}_3 \mathbf{n} \cdot \mathbf{E} \cdot \mathbf{n} + \tilde{\xi}_4 (\mathbf{p} \times \mathbf{n}) \cdot \mathbf{E} \cdot (\mathbf{p} \times \mathbf{n})] \\ &\quad + (\mathbf{p} \times \mathbf{n})[\tilde{\xi}_5 \mathbf{p} \cdot \mathbf{E} \cdot (\mathbf{p} \times \mathbf{n}) + \tilde{\xi}_6 \mathbf{n} \cdot \mathbf{E} \cdot (\mathbf{p} \times \mathbf{n})] + \tilde{\xi}_7 \mathbf{p} \cdot \mathbf{E} \cdot (\mathbf{I} - \mathbf{p}\mathbf{p}) \\ &\quad + \tilde{\xi}_8 \mathbf{n} \cdot \mathbf{E} \cdot (\mathbf{I} - \mathbf{p}\mathbf{p})\end{aligned}$$

(S 3.7)

where  $\tilde{\xi}_i$ , for  $i = 1, 2, \dots, 8$ , are parameters which depend on the shape of ends of the particle.  $\omega$  is linear in  $\mathbf{g} \cdot (\mathbf{I} - \mathbf{p}\mathbf{p})$  and  $\mathbf{p} \times \mathbf{F}_{end}$ . The symmetry of the Fourier modes implies that  $\mathbf{g} \cdot (\mathbf{I} - \mathbf{p}\mathbf{p})$  and  $\mathbf{F}_{end}$  given respectively by equations (S 3.6) and (S 3.7) should be identical if  $\mathbf{n}$  is along *any other* line of symmetry. It can be easily shown, similar to the analysis in section (3.3), that  $\tilde{\xi}_i$  and  $\tilde{\chi}_i$ , for  $i = 1, \dots, 7$ , are non-zero only for the second Fourier mode perturbations to a circle. For the

third and higher Fourier mode perturbations,  $\mathbf{g} \cdot (\mathbf{I} - \mathbf{p}\mathbf{p})$  and  $\mathbf{p} \times \mathbf{F}_{end}$  are proportional to  $\mathbf{E} \cdot \mathbf{p} \times \mathbf{p}$  which is proportional to  $\boldsymbol{\omega}$  due to the straining component of a SSF for an axisymmetric particle. Therefore, for straight particles with cross-sections that have  $\alpha_2 = 0$ , the angular velocity of the particle is similar to the angular velocity of an  $O(A/\sqrt{\ln(A)})$  aspect ratio spheroid as shown for a circular cylinder by Cox (1971). The exact relationship can be obtained from experiments or a numerical solution wherein we obtain the torque acting on the particle at two different orientations.

#### S.4 Force per unit length on a slender ring

The force per unit length acting on a ring with a non-circular cross-section,  $\rho = a(1 + \alpha h(\theta))$ , is the solution of equation (3.12) from the main text in which  $C'$  and  $D'$  can be obtained using equation (3.4) and (3.5) respectively. The stream-function  $\tilde{\psi}$ , required in equations (3.4) and (3.5), for a SSF, is given by

$$\tilde{\psi} = \tilde{a}_0 \left( \left( \frac{\rho}{a} \right)^2 - 2 \ln \left( \frac{\rho}{a} \right) \right) + (a_2 \cos(2\theta) + \hat{a}_2 \sin(2\theta)) \left( \left( \frac{\rho}{a} \right)^2 + \left( \frac{\rho}{a} \right)^{-2} - 2 \right) \quad (\text{S 4. 1})$$

where  $\tilde{a}_0$ ,  $a_2$ , and  $\hat{a}_2$  are constants such that the velocity field produced by  $\tilde{\psi}$  approaches the value for the SSF for  $\rho \gg a$ .  $\tilde{a}_0 = 0.25a((\gamma_3 - \gamma_4) \cos(\phi) - \gamma_5 \sin(\phi))$ ,  $a_2 = -0.25a[(\gamma_3 + \gamma_4) \cos(\phi) + \gamma_5 \sin(\phi)]$ ,  $\hat{a}_2 = 0.25a[\gamma_1(1 + \cos^2(\phi)) + \gamma_2 \cos(\phi) \sin(\phi)]$ , where the constants  $\gamma_i$ , with  $i = \{1, 2, \dots, 5\}$ , are related to the gradient of the imposed SSF and are given by

$$\gamma_1 = \nabla \mathbf{u}_\infty \cdot \mathbf{n} \mathbf{n}, \gamma_2 = \nabla \mathbf{u}_\infty \cdot \mathbf{n} \mathbf{b}, \gamma_3 = \nabla \mathbf{u}_\infty \cdot \mathbf{n} \mathbf{p}, \gamma_4 = \nabla \mathbf{u}_\infty \cdot \mathbf{p} \mathbf{n}, \gamma_5 = \nabla \mathbf{u}_\infty \cdot \mathbf{p} \mathbf{b}. \quad (\text{S 4.2})$$

Thus,  $C'$  and  $D'$  are given by

$$C' = \frac{1}{\pi} \int_0^{2\pi} d\theta \cos(\theta) g(\theta) \left\{ 8[a_2 \cos(2\theta) + \hat{a}_2 \sin(2\theta)] + 4 \left[ -\frac{f_x}{8\pi} \sin(\theta) + \frac{f_y}{8\pi} \cos(\theta) \right] \right\},$$

(S 4.3 a)

$$D' = \frac{1}{\pi} \int_0^{2\pi} d\theta \sin(\theta) g(\theta) \left\{ 8[a_2 \cos(2\theta) + \hat{a}_2 \sin(2\theta)] + 4 \left[ -\frac{f_x}{8\pi} \sin(\theta) + \frac{f_y}{8\pi} \cos(\theta) \right] \right\}.$$

(S 4.3 b)

The function  $g(\theta)$ , defining the contour of the cross-section, can be written in terms of Fourier modes in  $\theta$ , as shown in section 3. From equations (S 4.3 a) and (S 4.3 b), it can be easily seen that  $C'$  and  $D'$  are only affected for  $h(\theta) = \cos(2\theta - 2\theta_{02})$  and  $h(\theta) = \cos(3\theta - 3\theta_{03})$ , which are the second and the third Fourier modes respectively. For a cross-sectional shape given by  $\rho_c = a(1 + \alpha_2 \cos(2\theta - 2\theta_{02}) + \alpha_3 \cos(3\theta - 3\theta_{03}))$ , where  $\alpha_i \ll 1$  for  $i = \{2, 3\}$ , we have  $(C'_2, D'_2)$  and  $(C'_3, D'_3)$ , similar to  $(C', D')$ , corresponding to the second and the third Fourier mode respectively.  $(C'_2, D'_2)$  and  $(C'_3, D'_3)$  are given by

$$C'_2 = 2 \left[ -\frac{f_x}{8\pi} \sin(2\theta_{02}) + \frac{f_y}{8\pi} \cos(2\theta_{02}) \right], \quad (\text{S 4.4 a})$$

$$D'_2 = 2 \left[ \frac{f_x}{8\pi} \cos(2\theta_{02}) + \frac{f_y}{8\pi} \sin(2\theta_{02}) \right], \quad (\text{S 4.4 b})$$

$$C'_3 = 4[a_2 \cos(3\theta_{03}) + \hat{a}_2 \sin(3\theta_{03})], \quad (\text{S 4.4 c})$$

$$D'_3 = 4[a_2 \sin(3\theta_{03}) - \hat{a}_2 \cos(3\theta_{03})]. \quad (\text{S 4.4 d})$$

For this cross-sectional shape the force per unit length contribution due to a circular cross-section and the second and the third Fourier mode perturbations can be obtained analytically from equation (3.12) using elliptic integrals with errors of  $O(1/A^2)$ ,  $O(\alpha_2/A^2)$  and  $O(\alpha_3/A^2)$  respectively.

For rings with a cross-sectional shape which does not vary with  $\phi$  (in other words, the ring is axisymmetric), one can deduce the azimuthal dependence of the force per unit length  $\mathbf{f}_{net}$  in the following way if the imposed flow field is linear. This azimuthal dependence can be obtained by using the linearity of the Stokes flow equations and the linearity of the imposed SSF as explained in more detail in section 3 of Borker, Stroock and Koch (2018). Using the linearity of this system and the constraint that  $\mathbf{f}_{net}$  must be a real vector, we can argue that  $\mathbf{f}_{net}$  must be linear

in the relative translational velocity  $\mathbf{U} = \mathbf{U}_p - \mathbf{u}_\infty(\mathbf{r}_{com})$  of the particle and the fluid; a relative rotation rate  $\boldsymbol{\omega} = \boldsymbol{\omega}_p - \boldsymbol{\epsilon}: \mathbf{W}_\infty$  of the particle and the fluid, where  $\mathbf{W}_\infty = 0.5(\nabla \mathbf{u}_\infty - (\nabla \mathbf{u}_\infty)^T)$ ; and a rate of strain  $\mathbf{E}_\infty = 0.5(\nabla \mathbf{u}_\infty + (\nabla \mathbf{u}_\infty)^T)$  of the fluid. The azimuthal variation of  $\mathbf{f}_{net}$  is given by

$$\begin{aligned}
\mathbf{f}_{net} = & C_1 \mathbf{U} + C_2 \mathbf{p} \mathbf{p} \cdot \mathbf{U} + C_3 \mathbf{r}_c \mathbf{r}_c \cdot \mathbf{U} + C_4 \mathbf{r}_c \mathbf{p} \cdot \mathbf{U} + C_5 \mathbf{p} \mathbf{r}_c \cdot \mathbf{U} + C_6 (\mathbf{r}_c \times \mathbf{p})(\mathbf{r}_c \times \mathbf{p}) \cdot \mathbf{U} \\
& + C_7 \boldsymbol{\omega} \times \mathbf{p} + C_8 \boldsymbol{\omega} \times \mathbf{r}_c + C_9 (\mathbf{r}_c \times \mathbf{p}) \mathbf{r}_c \cdot \boldsymbol{\omega} + C_{10} (\mathbf{r}_c \times \mathbf{p}) \mathbf{p} \cdot \boldsymbol{\omega} + (C_{11} (\boldsymbol{\omega} \times \mathbf{p}) \\
& + C_{12} (\boldsymbol{\omega} \times \mathbf{r}_c)) \times (\mathbf{r}_c \times \mathbf{p}) + C_{13} (\boldsymbol{\omega} \times \mathbf{r}_c) \cdot \mathbf{p} \mathbf{p} + C_{14} (\boldsymbol{\omega} \times \mathbf{p}) \cdot \mathbf{r}_c \mathbf{p} + C_{15} (\boldsymbol{\omega} \times \mathbf{r}_c) \\
& \cdot \mathbf{p} \mathbf{r}_c + C_{16} (\boldsymbol{\omega} \times \mathbf{p}) \cdot \mathbf{r}_c \mathbf{r}_c + C_{17} \mathbf{p} \mathbf{p} : \mathbf{E}^\infty + C_{18} \mathbf{p} \mathbf{r}_c \mathbf{p} : \mathbf{E}^\infty + C_{19} \mathbf{p} \mathbf{r}_c \mathbf{r}_c : \mathbf{E}^\infty + C_{20} \mathbf{p} \\
& \cdot \mathbf{E}^\infty + C_{21} \mathbf{r}_c \mathbf{p} \mathbf{p} : \mathbf{E}^\infty + C_{22} \mathbf{r}_c \mathbf{r}_c \mathbf{p} : \mathbf{E}^\infty + C_{23} \mathbf{r}_c \mathbf{r}_c \mathbf{r}_c : \mathbf{E}^\infty + C_{24} \mathbf{r}_c \cdot \mathbf{E}^\infty \\
& + C_{25} \mathbf{p} (\mathbf{r}_c \times \mathbf{p}) : \mathbf{E}^\infty (\mathbf{r}_c \times \mathbf{p}) + C_{26} \mathbf{r}_c (\mathbf{r}_c \times \mathbf{p}) : \mathbf{E}^\infty (\mathbf{r}_c \times \mathbf{p}) \\
& + C_{27} (\mathbf{r}_c \times \mathbf{p}) (\mathbf{r}_c \times \mathbf{p}) : \mathbf{E}^\infty \mathbf{p} + C_{28} (\mathbf{r}_c \times \mathbf{p}) (\mathbf{r}_c \times \mathbf{p}) : \mathbf{E}^\infty \mathbf{r}_c,
\end{aligned}$$

(S 4.5)

where  $C_1, C_2 \dots, C_{28}$  are constants which are independent of the azimuthal position and depend only on the cross-sectional shape and the radius of the ring. For a general particle orientation  $\mathbf{p}$ , equation (S 4.5) can be simplified to obtain the azimuthal dependence of  $\mathbf{f}_{net}$  given by

$$\begin{aligned}
\mathbf{f}_{net} \cdot \mathbf{n} = & f_{net,n0} + f_{net,n1} \cos(\phi) + f_{net,n2} \cos(2\phi) + f_{net,n3} \cos(3\phi) \\
& + f_{net,n4} \sin(\phi) + f_{net,n5} \sin(2\phi) + f_{net,n6} \sin(3\phi),
\end{aligned}$$

$$\begin{aligned}
\mathbf{f}_{net} \cdot \mathbf{b} = & f_{net,b0} + f_{net,b1} \cos(\phi) + f_{net,b2} \cos(2\phi) + f_{net,b3} \cos(3\phi) \\
& + f_{net,b4} \sin(\phi) + f_{net,b5} \sin(2\phi) + f_{net,b6} \sin(3\phi),
\end{aligned}$$

$$\mathbf{f}_{net} \cdot \mathbf{p} = f_{net,p0} + f_{net,p1} \cos(\phi) + f_{net,p2} \cos(2\phi) + f_{net,p3} \sin(\phi) + f_{net,p4} \sin(2\phi),$$

(S 4.6)

where  $f_{net,ij}$ , with  $i = \{n, b, p\}$  and  $j = \{1, 2, \dots, 6\}$  depend only on the cross-sectional shape and the radius of the ring. We can write  $\mathbf{f}_{net} = \mathbf{f} + \alpha_2 \mathbf{f}'_2 + \alpha_3 \mathbf{f}'_3$ , where  $\mathbf{f}$ ,  $\mathbf{f}'_2$  and  $\mathbf{f}'_3$  are the force

per unit length due to the unperturbed, the second and the third Fourier mode perturbation to a circle respectively. Since the azimuthal variation given by equation (S 4.6) is true for any cross-sectional shape,  $\mathbf{f}$ ,  $\mathbf{f}'_2$  and  $\mathbf{f}'_3$  follow this azimuthal variation with the corresponding constants  $f_{ij}$ ,  $f'_{2,ij}$  and  $f'_{3,ij}$  respectively, with  $i = \{n, b, p\}$  and  $j = \{1, 2, \dots, 6\}$ , such that  $f_{net,ij} = f_{ij} + \alpha_2 f'_{2,ij} + \alpha_3 f'_{3,ij}$ . On substituting the azimuthal variation of  $\mathbf{f}_{net}$  from equation (S 4.6) and using the fact that  $s = R\phi$ , the integral in equation (3.12) can be expressed in terms of elliptic integrals, thereby avoiding an iterative process. The constants  $f_{ij}$ ,  $f'_{2,ij}$  and  $f'_{3,ij}$  can be obtained in terms of a small parameter,  $\epsilon_R = 1/\ln(8A)$ . We utilize  $\mathbf{f}_{net}$  to obtain the translational and rotational dynamics on a force and torque free ring with a non-circular cross-section.

The constants  $f_{ij}$ , which give the force per unit length for a ring with a circular cross-section, are given by

$$\begin{aligned}\frac{f_{n0}}{8\pi} &= \frac{U_n \epsilon_R}{8} \frac{\left(3 - \frac{17}{2} \epsilon_R\right)}{\left(1 - \frac{5}{2} \epsilon_R - \epsilon_R^2\right)} \\ \frac{f_{n1}}{8\pi} &= -\frac{7\gamma_1 \epsilon_R}{16} \frac{\left(1 - \frac{16}{3} \epsilon_R + \frac{1211}{180} \epsilon_R^2\right)}{\left(1 - \frac{151}{30} \epsilon_R + \frac{514}{90} \epsilon_R^2\right)\left(1 - \frac{5}{2} \epsilon_R\right)} \\ \frac{f_{n2}}{8\pi} &= \frac{f_{b5}}{8\pi} = \frac{U_n \epsilon_R}{8} \frac{\left(1 - \frac{7}{2} \epsilon_R\right)}{\left(1 - \frac{5}{2} \epsilon_R - \epsilon_R^2\right)} \\ \frac{f_{n3}}{8\pi} &= \frac{f_{b6}}{8\pi} = -\frac{\gamma_1 \epsilon_R}{16} \frac{\left(1 - \frac{25}{6} \epsilon_R\right)}{\left(1 - \frac{151}{30} \epsilon_R + \frac{514}{90} \epsilon_R\right)} \\ \frac{f_{n4}}{8\pi} &= \frac{-\omega_p \epsilon_R}{4(1 - 2\epsilon_R)} - \frac{5\gamma_2 \epsilon_R}{16} \frac{\left(1 - \frac{773}{150} \epsilon_R + \frac{1387}{225} \epsilon_R^2\right)}{\left(1 - \frac{151}{30} \epsilon_R + \frac{514}{90} \epsilon_R^2\right)(1 - 2\epsilon_R)}\end{aligned}$$

$$\frac{f_{n5}}{8\pi} = -\frac{f_{b2}}{8\pi} = \frac{U_b\epsilon_R}{8} \frac{\left(1 - \frac{7}{2}\epsilon_R^2\right)}{\left(1 - \frac{5}{2}\epsilon_R - \epsilon_R^2\right)}$$

$$\frac{f_{n6}}{8\pi} = -\frac{f_{b3}}{8\pi} = -\frac{\gamma_2\epsilon_R}{16} \frac{\left(1 - \frac{25}{6}\epsilon_R\right)}{\left(1 - \frac{151}{30}\epsilon_R + \frac{514}{90}\epsilon_R^2\right)}$$

$$\frac{f_{b0}}{8\pi} = \frac{U_b\epsilon_R}{8} \frac{\left(3 - \frac{17}{2}\epsilon_R\right)}{\left(1 - \frac{5}{2}\epsilon_R - \epsilon_R^2\right)}$$

$$\frac{f_{b1}}{8\pi} = \frac{\omega_p\epsilon_R}{4(1-2\epsilon_R)} - \frac{\gamma_2\epsilon_R}{16} \frac{\left(1 - \frac{507}{90}\epsilon_R + \frac{718}{90}\epsilon_R^2\right)}{\left(1 - \frac{151}{30}\epsilon_R + \frac{514}{90}\epsilon_R^2\right)(1-2\epsilon_R)}$$

$$\frac{f_{b4}}{8\pi} = -\frac{\gamma_1\epsilon_R}{16} \frac{\left(1 - \frac{88}{30}\epsilon_R - \frac{253}{180}\epsilon_R^2\right)}{\left(1 - \frac{151}{30}\epsilon_R + \frac{514}{90}\epsilon_R^2\right)\left(1 - \frac{5}{2}\epsilon_R\right)}$$

$$\frac{f_{p0}}{8\pi} = \frac{U_p\epsilon_R}{\epsilon_R + 2}$$

$$\frac{f_{p1}}{8\pi} = -\frac{(\omega_b + \gamma_4)\epsilon_R}{2 - 3\epsilon_R}$$

$$\frac{f_{p3}}{8\pi} = \frac{(\omega_n - \gamma_5)\epsilon_R}{2 - 3\epsilon_R}$$

$$f_{p2}=f_{p4}=0.$$

(S 4.7)

The force per unit length,  $\mathbf{f}$ , obtained in equation (S 4.7) with  $\mathbf{u}_\infty = 0$  agrees exactly with the expressions for a translating and rotating torus given in Johnson and Wu (1979). The components of the force per unit length,  $\mathbf{f}'_2$ , for a non-circular cross-section with the second Fourier mode perturbation (i.e.  $\rho = a(1 + \alpha_2 \cos(2\theta - 2\theta_{02}))$ ), are given by

$$f'_{2,n0} = -\frac{1}{8} \frac{(1-3\epsilon_R)}{\left(1-\frac{5}{2}\epsilon_R-\epsilon_R^2\right)} \left( 2f_{p1} \sin(2\theta_{02}) + \cos(2\theta_{02}) (2f_{n0} + f_{n2} + f_{b5}) \right)$$

$$\begin{aligned} f'_{2,n1} = & -\sin(2\theta_{02}) \left[ \frac{\epsilon_R}{2} \frac{f_{p0}}{\left(1-\frac{5}{2}\epsilon_R\right)} + \frac{\epsilon_R}{4} \frac{f_{p2} \left(1-\frac{52}{15}\epsilon_R\right)}{\left(1-\frac{151}{30}\epsilon_R+\frac{514}{90}\epsilon_R^2\right)} \right] \\ & + \frac{\cos(2\theta_{02}) \epsilon_R}{\left(1-\frac{5}{2}\epsilon_R\right)\left(1-\frac{151}{30}\epsilon_R+\frac{514}{90}\epsilon_R^2\right)} \left[ -\frac{3}{8} f_{n1} \left(1-\frac{481}{90}\epsilon_R+\frac{1808}{270}\epsilon_R^2\right) \right. \\ & \left. - \frac{f_{b4}}{8} \left(1-\frac{41}{10}\epsilon_R+\frac{248}{90}\epsilon_R^2\right) - \frac{f_{n3}}{4} \left(1-\frac{52}{15}\epsilon_R\right) \left(1-\frac{5}{2}\epsilon_R\right) \right] \end{aligned}$$

$$f'_{2,n2} = f'_{2,b5} = -\frac{1}{8} \frac{(1-\epsilon_R)}{\left(1-\frac{5}{2}\epsilon_R-\epsilon_R^2\right)} (2f_{p1} \sin(2\theta_{02}) + \cos(2\theta_{02}) (2f_{n0} + f_{n2} + f_{b5}))$$

$$f'_{2,n3} = f'_{2,b6} = \frac{\epsilon_R}{4} \frac{\sin(2\theta_{02}) f_{p2} \left(1-\frac{8}{3}\epsilon_R\right)}{\left(1-\frac{151}{30}\epsilon_R+\frac{514}{90}\epsilon_R^2\right)} + \frac{\cos(2\theta_{02}) \epsilon_R \left(1-\frac{8}{3}\epsilon_R\right)}{1-\frac{151}{30}\epsilon_R+\frac{514}{90}\epsilon_R^2} \left( \frac{-f_{n1} + f_{b4} - 2f_{n3}}{8} \right)$$

$$f'_{2,n4} = f'_{2,b1} = -\frac{\epsilon_R}{8} \frac{\left(1-\frac{52}{15}\epsilon_R\right)}{\left(1-\frac{151}{30}\epsilon_R+\frac{514}{90}\epsilon_R^2\right)} [2f_{p4} \sin(2\theta_{02}) + \cos(2\theta_{02}) (f_{b1} + f_{n4} + 2f_{n6})]$$

$$f'_{2,n5} = -f'_{2,b2} = -\frac{1}{8} \frac{(1-\epsilon_R)}{\left(1-\frac{5}{2}\epsilon_R-\epsilon_R^2\right)} (2f_{p3} \sin(2\theta_{02}) + \cos(2\theta_{02}) (2f_{b0} + f_{n5} - f_{b2}))$$

$$f'_{2,n6} = -f'_{2,b3} = -\frac{\epsilon_R}{8} \frac{\left(1 - \frac{8}{3}\epsilon_R\right)}{1 - \frac{151}{30}\epsilon_R + \frac{514}{90}\epsilon_R^2} [2f_{p4} \sin(2\theta_{02}) + \cos(2\theta_{02})(f_{b1} + f_{n4} + 2f_{n6})]$$

$$f'_{2,b0} = -\frac{1}{8} \frac{(1 - 3\epsilon_R)}{\left(1 - \frac{5}{2}\epsilon_R - \epsilon_R^2\right)} \left(2f_{p3} \sin(2\theta_{02}) + \cos(2\theta_{02})(2f_{b0} + f_{n5} - f_{b2})\right)$$

$$\begin{aligned} f'_{2,b4} &= \sin(2\theta_{02}) \left[ -\frac{\epsilon_R}{2} \frac{f_{p0}}{\left(1 - \frac{5}{2}\epsilon_R\right)} + \frac{\epsilon_R}{4} \frac{f_{p2} \left(1 - \frac{52}{15}\epsilon_R\right)}{\left(1 - \frac{151}{30}\epsilon_R + \frac{514}{90}\epsilon_R^2\right)} \right] \\ &\quad + \frac{\cos(2\theta_{02})\epsilon_R}{\left(1 - \frac{5}{2}\epsilon_R\right) \left(1 - \frac{151}{30}\epsilon_R + \frac{514}{90}\epsilon_R^2\right)} \left[ -\frac{1}{8} f_{n1} \left(1 - \frac{41}{10}\epsilon_R + \frac{248}{90}\epsilon_R^2\right) \right. \\ &\quad \left. - \frac{3f_{b4}}{8} \left(1 - \frac{481}{90}\epsilon_R + \frac{1808}{270}\epsilon_R^2\right) + \frac{f_{n3}}{4} \left(1 - \frac{52}{15}\epsilon_R\right) \left(1 - \frac{5}{2}\epsilon_R\right) \right] \end{aligned}$$

$$\frac{f'_{2,p0}}{8\pi} = \epsilon_R \frac{f_{p0} \cos(2\theta_{02}) - 0.5(f_{n1} + f_{b4}) \sin(2\theta_{02})}{2 + \epsilon_R}$$

$$\frac{f'_{2,p1}}{8\pi} = \epsilon_R \frac{f_{p1} \cos(2\theta_{02}) - 0.5(2f_{n0} + f_{b5} + f_{n2}) \sin(2\theta_{02})}{2 - 3\epsilon_R}$$

$$\frac{f'_{2,p2}}{8\pi} = \epsilon_R \frac{f_{p2} \cos(2\theta_{02}) - 0.5(f_{n1} + f_{n3} - f_{b4} + f_{b6}) \sin(2\theta_{02})}{2 - \frac{13}{3}\epsilon_R}$$

$$\frac{f'_{2,p3}}{8\pi} = \epsilon_R \frac{f_{p3} \cos(2\theta_{02}) - 0.5(2f_{b0} - f_{b2} + f_{n5}) \sin(2\theta_{02})}{2 - 3\epsilon_R}$$

$$\frac{f'_{2,p4}}{8\pi} = \epsilon_R \frac{f_{p4} \cos(2\theta_{02}) - 0.5(f_{b1} + f_{n4} + f_{n6} - f_{b3}) \sin(2\theta_{02})}{2 - \frac{13}{3}\epsilon_R}$$

(S 4.8)

The components of the force per unit length,  $\mathbf{f}'_3$ , for a non-circular cross-section with the third Fourier mode perturbation (i.e.  $\rho = a(1 + \alpha_3 \cos(3\theta - 3\theta_{03}))$ ), are given by

$$\frac{f'_{3,n0}}{8\pi} = \frac{(\gamma_3 + \gamma_4)a \sin(3\theta_{03}) \epsilon_R}{8} \frac{(1 - 3\epsilon_R)}{\left(1 - \frac{5}{2}\epsilon_R - \epsilon_R^2\right)}$$

$$\frac{f'_{3,n1}}{8\pi} = \frac{7\gamma_1 a \cos(3\theta_{03}) \epsilon_R}{16} \frac{1 - \frac{155}{30}\epsilon_R + \frac{184}{30}\epsilon_R^2}{\left(1 - \frac{151}{30}\epsilon_R + \frac{514}{90}\epsilon_R^2\right)\left(1 - \frac{5}{2}\epsilon_R\right)}$$

$$\frac{f'_{3,b0}}{8\pi} = \frac{(\gamma_5)a \sin(3\theta_{03}) \epsilon_R}{8} \frac{(1 - 3\epsilon_R)}{\left(1 - \frac{5}{2}\epsilon_R - \epsilon_R^2\right)}$$

$$\frac{f'_{3,b1}}{8\pi} = \frac{f'_{3,n4}}{8\pi} = \frac{\gamma_2 a \cos(3\theta_{03}) \epsilon_R}{16} \frac{1 - \frac{52}{15}\epsilon_R}{\left(1 - \frac{151}{30}\epsilon_R + \frac{514}{90}\epsilon_R^2\right)}$$

$$\frac{f'_{3,n2}}{8\pi} = \frac{f'_{3,b5}}{8\pi} = \frac{(\gamma_3 + \gamma_4)a \sin(3\theta_{03}) \epsilon_R}{8} \frac{(1 - \epsilon_R)}{\left(1 - \frac{5}{2}\epsilon_R - \epsilon_R^2\right)}$$

$$\frac{f'_{3,b2}}{8\pi} = -\frac{f'_{3,n5}}{8\pi} = -\frac{\gamma_5 a \sin(3\theta_{03}) \epsilon_R}{8} \frac{1 - \epsilon_R}{1 - \frac{5}{2}\epsilon_R - \epsilon_R^2}$$

$$\frac{f'_{3,n3}}{8\pi} = \frac{f'_{3,b6}}{8\pi} = \frac{\gamma_1 a \cos(3\theta_{03}) \epsilon_R}{16} \frac{1 - \frac{8}{3}\epsilon_R}{\left(1 - \frac{151}{30}\epsilon_R + \frac{514}{90}\epsilon_R^2\right)}$$

$$\frac{f'_{3,b3}}{8\pi} = -\frac{f'_{3,n6}}{8\pi} = -\frac{\gamma_2 a \cos(3\theta_{03}) \epsilon_R}{16} \frac{1 - \frac{8}{3}\epsilon_R}{\left(1 - \frac{151}{30}\epsilon_R + \frac{514}{90}\epsilon_R^2\right)}$$

$$\frac{f'_{3,b4}}{8\pi} = \frac{5\gamma_1 a \cos(3\theta_{03})\epsilon_R}{16} \frac{1 - \frac{727}{150}\epsilon_R + \frac{768}{150}\epsilon_R^2}{\left(1 - \frac{151}{30}\epsilon_R + \frac{514}{90}\epsilon_R^2\right)\left(1 - \frac{5}{2}\epsilon_R\right)}$$

$$f'_{3,p0} = \frac{3\epsilon_R}{4} \frac{\gamma_1 a \sin(3\theta_{03})}{2 + \epsilon_R}$$

$$f'_{3,p1} = -\frac{\epsilon_R a \cos(3\theta_{03})}{2(2 - 3\epsilon_R)} (\gamma_3 + \gamma_4)$$

$$f'_{3,p2} = \frac{a \sin(3\theta_{03}) \epsilon_R}{4\left(2 - \frac{13}{3}\epsilon_R\right)} \gamma_1$$

$$f'_{3,p3} = -\frac{\epsilon_R a \cos(3\theta_{03})}{2(2 - 3\epsilon_R)} \gamma_5$$

$$f'_{3,p4} = \frac{\epsilon_R a \sin(3\theta_{03})}{4\left(2 - \frac{13}{3}\epsilon_R\right)} \gamma_2.$$

(S 4.9)

The force per unit length given by (S 4.7) – (S 4.9) can be used for cross-sections with negligibly small values of  $K_{zz}$  by replacing  $(\alpha_{02}, \alpha_{03}, \theta_{02}, \theta_{03})$  with the corresponding values obtained from the analysis in section (3.3) of the main text. For slightly non-circular cross-sections,  $K_{zz}$  is  $O(\alpha_2^2)$  as shown in section (S 2). It remains small even for cross-sections with larger deviations from a circle and was found to be below 0.05 for all the cross-sections studied in the paper. Thus, the analytical expressions developed here maintain great accuracy.

The values of the dynamic parameters of the particle,  $\lambda$ ,  $\eta_1$  and  $\eta_2$  are obtained by applying the force-free ( $\int \mathbf{f}_{net}(\phi) R d\phi = \mathbf{0}$ ) and torque-free ( $\int ((\mathbf{r} - \mathbf{r}_{COM}) \times \mathbf{f}_{net}(\phi) + \mathbf{g}) d\phi = \mathbf{0}$ ) conditions on the particle, where  $\mathbf{g} = \int ds_c (\mathbf{r} - \mathbf{r}_c) \times (\boldsymbol{\sigma} \cdot \hat{\mathbf{n}}) + (\mathbf{r}_c - \mathbf{r}_{COM}) \times \int ds_c \cos(\theta) / A(\boldsymbol{\sigma} \cdot \hat{\mathbf{n}})$ ,  $\boldsymbol{\sigma}$  is the stress tensor obtained from the solution of two 2D Stokes flow problems

mentioned in section (3.3) with  $\mathbf{u} = \mathbf{u}_\infty$  on the outer boundary,  $\tilde{\mathbf{n}}$  is the unit normal to the surface of the particle and  $ds_c$  is the elemental length along the cross-sectional contour. To understand the form of  $\mathbf{g}$ , consider the torque computed directly from the stresses:

$$\iint dA (\mathbf{r} - \mathbf{r}_{COM}) \times (\boldsymbol{\sigma} \cdot \tilde{\mathbf{n}}) = \int d\phi \int ds_c \left(1 + \frac{\cos(\theta)}{A}\right) (\mathbf{r} - \mathbf{r}_{COM}) \times (\boldsymbol{\sigma} \cdot \tilde{\mathbf{n}})$$

(S 4.10)

Equation (S 4.10) is modified to have a term with an  $O(1/A)$  moment arm about the center of the cross-section ( $\mathbf{g}$ ) and another that has an  $O(1)$  moment arm  $((\mathbf{r} - \mathbf{r}_{COM}) \times \mathbf{f}_{net})$ . The inner integral can be rewritten in the form

$$\begin{aligned} & \int ds_c \left(1 + \frac{\cos(\theta)}{A}\right) (\mathbf{r} - \mathbf{r}_{COM}) \times (\boldsymbol{\sigma} \cdot \tilde{\mathbf{n}}) \\ &= \int ds_c (\mathbf{r} - \mathbf{r}_c) \times (\boldsymbol{\sigma} \cdot \tilde{\mathbf{n}}) + (\mathbf{r}_c - \mathbf{r}_{COM}) \times \int ds_c \frac{\cos(\theta)}{A} (\boldsymbol{\sigma} \cdot \tilde{\mathbf{n}}) \\ &+ (\mathbf{r}_c - \mathbf{r}_{COM}) \times \mathbf{f}_{net} + O\left(\frac{1}{A^3}\right), \end{aligned}$$

where  $\mathbf{f}_{net} = \int ds_c \boldsymbol{\sigma} \cdot \tilde{\mathbf{n}}$ . The two integrals on the right-hand side correspond to the torque per unit length  $\mathbf{g} = \int ds_c (\mathbf{r} - \mathbf{r}_c) \times (\boldsymbol{\sigma} \cdot \tilde{\mathbf{n}}) + (\mathbf{r}_c - \mathbf{r}_{COM}) \times \int ds_c \cos(\theta) / A (\boldsymbol{\sigma} \cdot \tilde{\mathbf{n}})$ . The second term is present because of finite curvature of the slender body. The above two integrals can be obtained from the solution of 2D Stokes flow equations and  $\nabla^2 u_z = 0$ , similar to the one in section (3.3), wherein the outer boundary has  $\mathbf{u} = \mathbf{u}_\infty$  and the inner boundary satisfy a no-slip velocity. The dynamic parameter  $\lambda$  is obtained by matching the torque acting on the particle when it is placed in a simple shear flow with  $\mathbf{p} = \hat{\Gamma}_\infty$  to the torque of required to rotate a ring in a quiescent flow  $(4\pi^2 \boldsymbol{\omega} / (\ln(8A) - 1.5))$ . On simplifying the torque free condition  $\lambda$  is given by

$$\lambda = -1 - \frac{\alpha_3 \cos(3\theta_{03})}{A} + \frac{(\ln(8A) - 1.5)}{2\pi^2} \int d\phi \mathbf{g} \cdot \hat{\boldsymbol{\Omega}}_\infty = -1 - \frac{\alpha_3 \cos(3\theta_{03})}{A} + \frac{(\ln(8A) - 1.5)}{A^2} C_\lambda,$$

where  $C_\lambda = A^2(\int d\phi \mathbf{g} \cdot \widehat{\boldsymbol{\Omega}}_\infty)/(2\pi^2) \sim O(1)$ . This integral can be performed analytically for a circular cross-section by solving for  $\sigma$  corresponding to a transverse velocity field specified by  $\tilde{\psi}$  and a longitudinal velocity field specified by  $\tilde{u}_z$  given by equations (S 1.4) and (S 1.3) respectively yielding  $C_\lambda = 1.5$ .  $C_\lambda = 1.5$  was also found to be a good approximation for the shapes studied in section (6.3).

# CHAPTER 4

## Rheology of a dilute suspension of tumbling rings

### 1. Introduction

High-aspect ratio particle suspensions are useful in a number of practical applications such as fabrication of high-strength composites using fibers or mica flakes (Mansouri, et al., 2005), using conducting fibers for production of conducting optical films used in touchscreen devices (De, et al., 2009) or making paper using fiber suspension (Lundell, et al., 2011). The quality of the final product crucially depends on the orientational dynamics of individual particles during the processing step which is influenced by the shape of individual particles as well as interactions between particles even at small particle number densities ( $n \ll 1$ ). The dilute suspension rheology of high-aspect ratio fibers in a simple shear flow, which is a linear approximation to many processing flows such as injection molding or spin casting, has been extensively studied using experiments (Anczurowski & Mason, 1968; Stover, et al., 1992), theory and numerical simulations (Mackaplow & Shaqfeh, 1996). Theoretical analysis describing the influence of pairwise interactions gives insight into the physical mechanisms governing the suspension rheology (Mackaplow & Shaqfeh, 1996) and the steady state orientation distribution of particles (Rahnama, et al., 1995) thereby aiding the design of processing equipment using fiber suspensions. However, a dilute rheology calculation including pairwise particle interactions is absent for any other high-aspect ratio particle. Reported orientational distribution for disc suspensions (Anczurowski & Mason, 1968) are questionable since their measurements for dilute fiber suspensions ( $n \sim O(10^{-2})$  comparable to their disc measurements) were found to be strongly affected by secondary flows in the Coutte device (Stover, et al., 1992). Furthermore, high-aspect ratio discs have solid-body contact in shear flows (Singh, et al., 2014) at dilute concentrations ( $n \ll 1$ ) with a frequency that is comparable to the strongest hydrodynamic interactions suggesting a new mechanism driving the rheology of discs, as well as other planar particles, namely collisions. Dilute rheology study for high-aspect ratio discs does not exist partly due to the high computational cost involved in using finite-volume or boundary element methods. High aspect ratio rings provide a convenient way to

explore the effect of collisions on the dilute rheology and orientational statistics using slender body theory to compute the velocity disturbances.

In this, work the dilute rheology of a suspension of tori is established using numerical simulations which captures both hydrodynamic interaction and collision between two particles. Hydrodynamic interactions are modeled in the slender body theory framework and collisions are modeled using a short-range repulsive force as described in section (2). Particle collisions have a dominating effect towards setting the steady state orientation distribution of the rings and thereby also influencing the rheology. The shear rate dependence on the suspension rheology is established in section (3) using Brownian Dynamics simulations of a single ring. The shear rate of the simple shear flow  $\gamma$ , the fluid viscosity  $\mu_f$  and the radius of the torus  $R$  is used to non-dimensionalize any quantity of interest. The aspect ratio of the ring  $A$  is defined as the ratio of  $R$  and the cross-sectional radius  $a$ , implying  $A = R/a$ . Furthermore, discs and fibers used for comparison in the remainder of the paper have the radius and half-length equal to the ring radius, both having the same aspect ratio as the ring.

Rings have higher surface area to volume ratio compared to high-aspect ratio discs or fibers, making them useful in drug delivery and catalysis (Wittstock, et al., 2010) due to a shorter diffusion pathway. Furthermore, a hexagonal closed lattice of slender rings has a volume fraction of  $\pi^2/(2\sqrt{3}A)$  making even concentrated suspension of rings highly porous. Ring suspensions could be used to fabricate porous materials for hydrogen fuel storage,  $CO_2$  capture or electrochemical reactors (Qi, et al., 2014) using simple processing flow techniques. Rings can be fabricated using a variety of materials organic polysaccharides to inorganic nanoparticles using the vortex ring freezing technique (An, et al., 2016), allowing for experimental validation of our results and also allowing the exploration of the suspension rheology at higher particle concentrations. Additionally, high aspect ratio rings allow the use of slender body theory (Borker & Koch, in press) for calculating the hydrodynamic interactions between particles drastically reducing the computational cost compared to finite-volume or boundary-element method simulations required for discs. Rings can be thought of as a bent fiber or a disc with a hole and is a natural geometry to understand how particle shape influences suspension rheology.

Before elucidating the simulation strategy, Jeffery's solution (Jeffery, 1922) describing the motion of axisymmetric particles is discussed. The rate of change of the orientation of the axis of symmetry  $\mathbf{p}$  of any axisymmetric particle is given by

$$\dot{\mathbf{p}} = \mathbf{p} \cdot \mathbf{R}_\infty + \lambda(\mathbf{E}_\infty \cdot \mathbf{p} - \mathbf{E}_\infty : \mathbf{p}\mathbf{p}\mathbf{p}) \quad (1.1)$$

where  $\mathbf{R}_\infty = 0.5(\nabla\mathbf{u}_\infty - (\nabla\mathbf{u}_\infty)^T)$  is the vorticity tensor,  $\mathbf{E}_\infty = 0.5(\nabla\mathbf{u}_\infty + (\nabla\mathbf{u}_\infty)^T)$  is the rate of strain tensor and  $\lambda$  is a geometric parameter which is equal to  $-1 + 1.5(\ln(8A) - 1.5)/A^2$  for high aspect ratio rings (Borker & Koch, in press),  $-1 + 2.24(1 + 0.21A^{-0.5})/A^{1.5}$  for thin discs (Singh, et al., 2014) and  $1 - 0.65\ln(A)/A^2$  for fibers (Cox, 1971). In our calculations,  $\lambda$  is accurately calculated using boundary element method (BEM) calculations (Borker, et al., 2018).

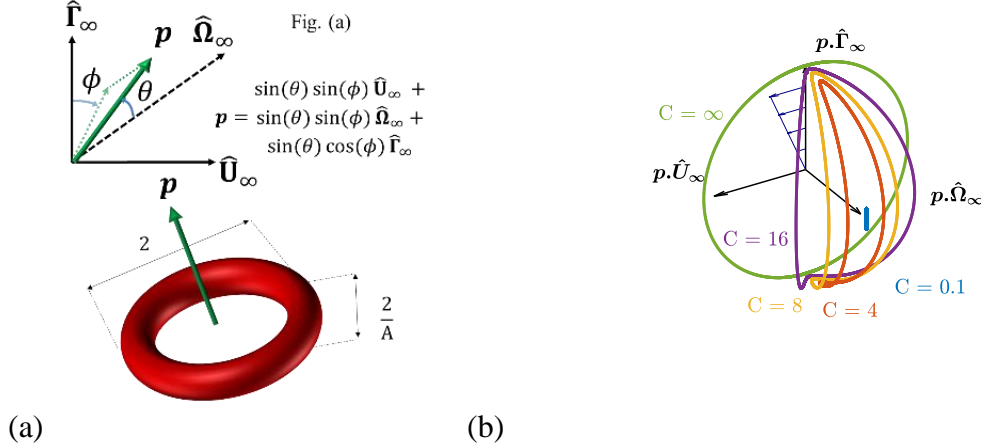


Figure 1 (a) Coordinate system and definition of the azimuthal ( $\phi$ ) and polar ( $\theta$ ) angles. (b) Jeffery orbits of a tumbling torus with  $A = 40$  with  $\lambda = -1 + 4 \times 10^{-3}$  and  $\phi_T \approx 0.045$ .

The solution of equation (1.1) is given by

$$\tan(\phi) = \phi_T \tan\left(\frac{t}{T} + \tau\right), \quad (1.2)$$

$$\tan(\theta) = \frac{C \phi_T}{\sqrt{\phi_T^2 \cos^2(\phi) + \sin^2(\phi)}}, \quad (1.3)$$

where  $T = 4\pi/\sqrt{1 - \lambda^2}$  is the time period of rotation of the ring,  $\phi_T = 2\pi/T \approx \sqrt{(1 + \lambda)/2}$ , (also referred to as the effective aspect ratio by some authors),  $\tau$  is the phase angle and  $C$  is the orbit constant.  $T$  is  $O(A\sqrt{\epsilon})$  for rings,  $O(A^{-0.75})$  for discs and  $O(A\sqrt{\epsilon})$  for fibers, where  $\epsilon = 1/\ln(8A)$ . The orientation trajectories of equation (1.1) are closed loops known as Jeffery orbits specified by  $C$  and are shown in figure 1 (b) for an  $A = 40$  torus. One characteristic of high-aspect ratio rings is that the orbits are pinched near the gradient direction.  $\tilde{\theta} = \pi/2 - \theta$  gives the measure of the tilt of ring relative to the flow vorticity plane (or the tilt of  $\mathbf{p}$  from  $\hat{\Gamma}_\infty$ ). Equation (1.2) suggests that  $\phi \sim O(\phi_T) \ll 1$  most of the times and has an  $O(1)$  value only when the  $\mathbf{p}$  tumbles across the flow-vorticity plane, which happens with a probability of  $O(\phi_T)$ . The value of  $\theta$  when  $\phi \rightarrow \phi_T$  is  $O(\text{atan}(C))$  implying that  $\mathbf{p}$  makes a small angle with  $\hat{\Gamma}_\infty$  only when  $C \gg O(\phi_T^{-1})$  and  $\mathbf{p}$  makes an  $O(1)$  angle only when  $C \sim O(1)$  or smaller. When  $\mathbf{p}$  crosses the flow-vorticity plane (i.e.,  $\phi = \pi/2$ ),  $\theta = \text{atan}(C\phi_T)$  implying  $\mathbf{p}$  makes a small angle with  $\hat{\Omega}_\infty$  when  $C \sim O(1)$  and an  $O(1)$  angle when  $C \gg O(\phi_T^{-1})$ . In other words, if  $\theta$  and  $\phi$  are set to random  $O(1)$  values, the orbit constant would most likely be  $O(\phi_T^{-1})$  or larger. The hydrodynamic velocity disturbance created by the particle is approximately proportional to the tilt of the ring relative to the flow-vorticity plane. Therefore, a ring in the orbits with  $C \gg O(\phi_T^{-1})$  generates an  $O(\epsilon)$  disturbance when it is tumbling (i.e.  $\mathbf{p}$  crossing the flow-vorticity plane) and a much smaller  $O(\phi_T\epsilon)$  disturbance when it is in the temporarily aligned. On the other hand, rings rotating in orbits with  $C$  of  $O(1)$  or smaller, will generate an  $O(\epsilon)$  velocity disturbance all the time. However, since most of the orientational space is filled with the  $C \gg \phi_T^{-1}$  orbits pairwise hydrodynamic interactions, interparticle collisions and Brownian motion tends to force the steady state orientation distribution to accumulate in near the  $C \gg \phi_T^{-1}$  orbits.

The hydrodynamic stresslet tensor  $\mathbf{S}_{Hyd}$  equal to the symmetric part of the first moment of the stress acting on the particle is used to quantify the anisotropic change in the suspension stress due to the presence of a rigid particle.  $\mathbf{S}_{Hyd}$  is computed from an area integral over the particle surface and is given by

$$\mathbf{S}_{Hyd} = \int dA \left( \frac{\mathbf{r}(\boldsymbol{\sigma} \cdot \mathbf{n}) + (\boldsymbol{\sigma} \cdot \mathbf{n})\mathbf{r}}{2} - \frac{\boldsymbol{\sigma} : \mathbf{n}\mathbf{r}}{3} \mathbf{I} \right), \quad (1.4)$$

where  $\boldsymbol{\sigma} = -p_{inner} \mathbf{I} + (\nabla \mathbf{u}_{inner} + (\nabla \mathbf{u}_{inner})^T)$  is the stress tensor,  $\mathbf{u}_{inner}$  and  $p_{inner}$  being the velocity field and the pressure of the complete inner solution of the SBT;  $\mathbf{n}$  is the outward unit normal to the surface,  $\mathbf{r}$  is the position vector and  $dA$  is the elemental area on the particle surface.  $\langle \mathbf{S}_{Hyd} \rangle$  is the ensemble average stresslet tensor which averages  $\mathbf{S}_{Hyd}$  over the steady state orientation distribution and can be expressed in terms of the  $\mathbf{E}_\infty$  and moments of  $\mathbf{p}$  for an axisymmetric particle as

$$\langle \mathbf{S}_{Hyd} \rangle = \xi_1 \mathbf{E}_\infty + \xi_2 \mathbf{E}_\infty : \langle \mathbf{p} \mathbf{p} \rangle \mathbf{I} + \xi_3 (\mathbf{E}_\infty \cdot \langle \mathbf{p} \mathbf{p} \rangle + \langle \mathbf{p} \mathbf{p} \rangle \cdot \mathbf{E}_\infty) + \xi_4 \mathbf{E}_\infty : \langle \mathbf{p} \mathbf{p} \mathbf{p} \mathbf{p} \rangle, \quad (1.5)$$

where  $\xi_i$  for  $i = \{1,2,3,4\}$  are  $O(\epsilon)$  constants that depend only on the particle geometry, with  $\xi_1 + \xi_3 \sim O\left(\frac{1}{A^2}\right)$  (Kim & Karilla, 1991).  $\xi_i$  are obtained using SBT (A1), instead of BEM calculations, to remain consistent with the additional stresslet contributions due to pairwise interactions computed in the following section using the SBT framework.  $\langle \mathbf{S}_{Hyd} \rangle$  requires information about the orbit distribution which is set either by pairwise hydrodynamic interactions or weak Brownian motion explained in the next two sections.

## 2. Rheology of pairwise interacting non-Brownian rings

### 2.1. Simulation strategy for pairwise particle interactions

The dilute suspension rheology can be calculated by monitoring the particle positions, orientations and the stresslet tensor of two rings which are initially widely separated along  $\hat{\mathbf{U}}_\infty$  for all possible interactions of this two-particle system. A boundary element method approach to solve this problem requires resolving the  $O(1/A)$  length scale of the ring cross-section, leading to  $O(A^2)$  number of mesh elements and therefore, solution of  $O(A^2)$  integral equations at each time step which have complications in inverting a highly dense matrix with  $O(A^4)$  elements. A finite volume approach, in addition to resolving the cross-section, suffers from the requirement of a large domain size at each time step. In this study, we use slender body theory to simulate the hydrodynamic interaction (HI) and a short-range repulsive force to simulate collisions. The flow, vorticity and gradient direction of the simple shear flow (SSF) form the global coordinate system shown in figure 1 (a).

Consider two particles with orientations  $\mathbf{p}_I$  and  $\mathbf{p}_{II}$  and center-of-mass positions located at  $\mathbf{r}_{I,COM}$  and  $\mathbf{r}_{II,COM}$  respectively. A slender body theory (SBT) formulation is used to compute the velocity disturbance  $\mathbf{u}'_\infty$  at  $\mathbf{r}$  produced by a nearby particle, termed as the first refection, obtained from a path integral over the centerline of the ring cross-section given by

$$u'_{\infty,i}(\mathbf{r}) = \frac{1}{8\pi} \int_0^{2\pi} ds f_j \left( \frac{\delta_{ij}}{r''} + \frac{r''_i r''_j}{r''^2} \right), \quad (2.1)$$

where  $ds$  being the magnitude of the elemental change along the centerline;  $\mathbf{r}'' = \mathbf{r} - \mathbf{r}'$ ,  $\mathbf{r}'$  being a position on the centerline of the second ring;  $\mathbf{f} = \mathbf{f}_{SSF} + \mathbf{f}_{col}$ ,  $\mathbf{f}_{SSF}$  being the force per unit length exerted by the particle on the fluid obtained from the SBT solution of a single force-and-torque-free ring in a SSF (Borker & Koch, in press); and  $\mathbf{f}_{col}$  being the force per unit length imparted to the particle due to the  $O(1)$  rotational and translational velocities imparted by collisions given in equation (2.4). The rheology of fibers can be accurately predicted by only considering the first reflection (Mackaplow & Shaqfeh, 1996) and should therefore also accurately predict the hydrodynamic interaction of high-aspect ratio rings. Velocity disturbance produced by subsequent reflections (i.e. the velocity disturbance produced by the force per unit length induced by the previous reflection) will be smaller by a factor of  $O(\epsilon)$  due to the high aspect ratio of the particle.  $\mathbf{u}'_\infty$  induces an angular velocity  $\boldsymbol{\omega}_{HI}$ , a translational velocity  $\mathbf{U}_{HI}$  and a force per unit length  $\mathbf{f}_{HI} = 4\pi\epsilon(\mathbf{U}_{HI} + \boldsymbol{\omega}_{HI} \times (\mathbf{r}_c - \mathbf{r}_{I,COM}) - \mathbf{u}'_\infty) \cdot (\mathbf{I} - 0.5 \mathbf{e}_z \mathbf{e}_z)$ .  $\mathbf{f}_{HI}$  is given by (Borker & Koch, in press) with errors of  $O(1/A^2)$ .  $\mathbf{U}_{HI}$  and  $\boldsymbol{\omega}_{HI}$  are obtained by applying the force and torque free conditions respectively. In addition,  $\mathbf{f}_{HI}$  also exerts a stresslet required to calculate the increase in the fluid viscosity and normal stress differences in the suspension.

In addition to HI, collisions are important at dilute particle concentrations. The lubrication force between nearly touching rings is qualitatively similar to the lubrication force between two colliding cylinders which is  $O\left(\dot{\delta}/(A^2\delta)\right)$  (Yamane, et al., 1994),  $\delta$  being the distance of minimum separation between the cylinders and  $\dot{\delta}$  is the rate of change of  $\delta$ . The stresses due to the SSF driving the two rings together acts over the entire length fo the particle and therefore the contact force must be  $O(1)$ . Harlen and coworkers (Harlen, et al., 1999) argued that in an  $O(1)$  time  $\delta$  changes by a factor of  $\exp(-A^2)$ , which for practical purposes would imply a solid body contact

between the cylinders. Therefore, lubrication is too weak to prevent solid-body contact. The  $O(\sqrt{\ln(A)}/A^2)$  ideal collision frequency of fibers (Singh, et al., 2011) is much smaller than the  $O(\sqrt{\ln(A)}/A)$  frequency of the most important interactions, those between an aligned and a tumbling fiber (Rahnama, et al., 1995), which implies that collisions are not very important at particle concentrations  $n \ll 1$ . However, rings have two longitudinal dimensions, and thereby the ideal collision frequency is  $O(\sqrt{\ln(A)}/A)$  (Singh, et al., 2011). This collision frequency is comparable to the  $O(\sqrt{\ln(A)}/A)$  frequency of interactions between tumbling and aligned rings which have the strongest contribution to the steady state orientation distribution and the suspension rheology. This suggests that tumbling-aligned encounters involving both solid-body collision and hydrodynamic interactions are the predominant form of pairwise interaction for any planar, curved slender particle. Furthermore, collisions lead to an  $O(1)$  change in  $\mathbf{p}$  compared to the  $O(\epsilon)$  change in  $\mathbf{p}$  of an aligned ring due to a purely hydrodynamic interaction with a neighboring tumbling ring, making the contribution of collisions stronger than HIs<sup>2</sup>.

The collision event near the point of contact is simulated by applying a short-range repulsive force,  $\mathbf{F}_{col}$  that prevents particles from passing through each other and depends only on the distance of minimum separation of the tori  $\delta$ .  $\mathbf{F}_{col}$  acts on one or two points on the rings, the latter case happening when one ring enters the hole of the other ring or when both rings are parallel to each other. The functional dependence of  $\mathbf{F}_{col}$  on  $\delta$  was chosen to be similar to  $\mathbf{F}_{col}$  used to simulate collision of two discs used by Meng & Higdon (2008) and is given by

<sup>2</sup> The mean squared change in the orientation is a measure of the change in  $\mathbf{p}$  due to PI and scales as the change in  $\mathbf{p}$  due to an interaction times the occurrence frequency of that interaction (Rahnama, et al., 1995). The interaction frequency of two aligned fibers is  $O(1)$  but the change in the orientation of either particle due to HI is only  $O(\epsilon\phi_T)$  leading to a mean squared change in orientation of  $O(\epsilon^2\phi_T^2) = O(\epsilon/A^2)$  which is smaller compared to both  $O(\epsilon^{1.5}/A)$  and  $O(1/(\sqrt{\epsilon}A))$  values corresponding to a hydrodynamic and a collisional interaction of an aligned and a tumbling ring.

$$\mathbf{F}_{col} = \frac{8\pi}{A^2} C_p \frac{\delta_{min}}{\delta} \left( \eta - \frac{\eta^2}{2} \right)^3 \mathbf{d}$$

(2.2)

where,  $\eta = 1 - \delta/\delta_{min}$ ,  $\mathbf{d}$  is a unit vector normal to the collision surface pointing towards the surface of each torus and  $C_p$  is an  $O(1)$  constant chosen to be unity for our simulations. The functional form of  $\mathbf{F}_{col}$  on  $\delta$  is reported to have little impact on the overall dynamics and the suspension rheology as long as it is steep and the force acts for  $\delta_{min} \leq O(1/A)$  ((Meng & Higdon, 2008), (Yamamoto & Matsuoka, 1997)).  $\delta_{min}$  was chosen to be  $10^{-2}/A$  and  $\mathbf{F}_{col}$  is capped to a maximum value corresponding to  $\delta = 10^{-2}\delta_{min}$  for all our simulations to prevent the time-step from becoming extremely small. For  $\delta < 0$  (i.e. overlapping rings) we set  $\mathbf{F}_{col}$  to a value corresponding to  $\delta = 10^{-4}\delta_{min}$ , which creates a discontinuity at  $\delta = 0$  and prevents the simulation from progressing. Less than about 0.1% of our simulations prematurely terminated because of capping the collisional force. Additionally, for cases with two contact points a region of size  $O(1/A)$  around one of the contact points is excluded to avoid the two contact points from being close to each other.  $\mathbf{F}_{col}$  is applied at the centerline of the ring cross-section instead of the exact point of contact, which only creates errors of  $O(1/A^2)$  in the computation of the angular velocity. The linear ( $\mathbf{U}_{col}$ ) and angular ( $\boldsymbol{\omega}_{col}$ ) velocities of the particle due to collision obtained by applying the force and torque free condition respectively on the particle are

$$\begin{aligned} \mathbf{U}_{col} &= \frac{1}{6\pi^2\epsilon_R} \mathbf{F}_{col} \cdot \left( \frac{1 - \frac{17}{6}\epsilon_R}{1 - \frac{5}{2}\epsilon_R - \epsilon_R^2} (\mathbf{I} - \mathbf{p}\mathbf{p}) + \frac{3}{4} \frac{1}{1 + \frac{\epsilon_R}{2}} \mathbf{p}\mathbf{p} \right), \\ \boldsymbol{\omega}_{col} &= \frac{1}{4\pi^2\epsilon_R} \left( (\mathbf{r}_{c,col} - \mathbf{r}_{COM}) \times \mathbf{F}_{col} \right) \cdot \left( \frac{\mathbf{I} - \mathbf{p}\mathbf{p}}{1 - 1.5\epsilon_R} + \frac{\mathbf{p}\mathbf{p}}{1 - 2\epsilon_R} \right), \end{aligned} \quad (2.3)$$

where  $\mathbf{r}_{c,col}$  is the position of the centerline of the ring corresponding to the point of minimum separation and  $\mathbf{r}_{COM}$  is the center of mass of the ring. The collision induces a force per unit length  $\mathbf{f}_{col}$  which is given by

$$\frac{f_{col,n}}{8\pi} = \frac{U_{col,n}\epsilon_R(3 + \cos(2\phi))}{8} + \frac{U_{col,b}\epsilon_R \sin(2\phi)}{8} - \frac{\omega_{col,p} \sin(\phi)}{4},$$

$$\begin{aligned} \frac{f_{col,b}}{8\pi} &= \frac{U_{col,n}\epsilon_R \sin(2\phi)}{8} + \frac{U_{col,b}\epsilon_R(3 - \cos(2\phi))}{8} + \frac{\omega_{col,p}\epsilon_R \cos(\phi)}{4}, \\ \frac{f_{col,p}}{8\pi} &= \frac{U_{col,p}\epsilon_R}{2} + \frac{\omega_{col,n}\epsilon_R \sin(\phi)}{2} - \frac{\omega_{col,b}\epsilon_R \cos(\phi)}{2}. \end{aligned} \quad (2.4)$$

$\mathbf{f}_{col}$  is included while computing the velocity disturbance in equation (2.1) and is important when the particles collide. Particle collisions also exert a stresslet  $\mathbf{S}_{col}$  which is given by

$$\mathbf{S}_{col} = \frac{\mathbf{r}_{col}\mathbf{F}_{col} + \mathbf{F}_{col}\mathbf{r}_{col}}{2} - \frac{1}{3}(\mathbf{r}_{col} \cdot \mathbf{F}_{col})\mathbf{I}. \quad (2.5)$$

$\mathbf{S}_{col}$  has a stronger  $O(1)$  scaling in comparison to the  $O(\epsilon)$  scaling of  $\mathbf{S}_f$  and therefore dominates the rheology.

The particle position and orientation are obtained by solving a set of ordinary differential equations given by

$$\frac{d\mathbf{r}_{k,COM}}{dt} = \mathbf{u}_\infty(\mathbf{r}_{k,COM}) + \mathbf{U}_{HI} + \mathbf{U}_{col}, \quad (2.6)$$

$$\frac{d\mathbf{p}_k}{dt} = \mathbf{p}_k \cdot \mathbf{R}_\infty + \lambda(\mathbf{E}_\infty \cdot \mathbf{p}_k - \mathbf{E}_\infty \cdot \mathbf{p}_k \mathbf{p}_k \mathbf{p}_k) + (\boldsymbol{\omega}_{HI} + \boldsymbol{\omega}_{col}) \times \mathbf{p}_k, \quad (2.7)$$

where  $k = \{I, II\}$ . The Runge-Kutta method with adaptive time-stepping is used to march forward in time. The initial positions of the center of mass of the two particles were chosen to be the origin ( $\mathbf{r}_{I,COM} = 0$ ) and  $\mathbf{r}_{II,COM} = -\Delta\mathbf{r}_0$ . The initial orientations  $\mathbf{p}_{I,0}$  and  $\mathbf{p}_{II,0}$  are specified in terms of the phase angles  $(\tau_I, \tau_{II})$  chosen uniformly between  $[0, 2\pi]$  and the orbit constants  $(C_I, C_{II})$  chosen from the steady state orbit distribution discussed towards the end of this subsection.  $\Delta\mathbf{r} \cdot \hat{\mathbf{r}}_\infty$  was chosen with a uniform probability between  $[0, L_3]$  and  $\Delta\mathbf{r} \cdot \hat{\boldsymbol{\Omega}}_\infty$  was chosen with a uniform probability from  $[-L_2, L_2]$ .  $\Delta\mathbf{r}_0 \cdot \hat{\mathbf{U}}_\infty = -10$  simulated an initial large separation between the two particles. The simulation is run until  $\Delta\mathbf{r} \cdot \hat{\mathbf{U}}_\infty = 10$ , which is a sufficiently large distance to reduce interparticle interactions. The average value of  $\mathbf{X}$  per unit concentration due to pairwise interactions (i.e.  $\langle \mathbf{X} \rangle_{PI}/n$ ) is evaluated from the flux of the particles passing through the  $\hat{\boldsymbol{\Omega}}_\infty - \hat{\mathbf{r}}_\infty$  plane ensembled averaged over the steady state orbit distribution of the two particles and is given by

$$\frac{\langle \mathbf{X} \rangle_{PI}}{n} = \int_{\hat{\Omega}_\infty - \hat{\mathbf{r}}_\infty} dA (\Delta \mathbf{r}_0) \cdot \hat{\mathbf{r}}_\infty \int dC_b^I p(C_b^I) \int \frac{d\tau_I}{2\pi} \int dC_b^{II} p(C_b^{II}) \int \frac{d\tau_{II}}{2\pi} \int_{-\infty}^{\infty} dt \left( \mathbf{X}(t) - \mathbf{X}_J(t) \right), \quad (2.8)$$

where  $i \in \{I, II\}$  being the indices for the two particles in the simulation;  $\mathbf{X}_J$  is the value of  $\mathbf{X}$  evaluated in the absence of a second particle and  $p(C_b)$  is the steady state probability distribution of the modified orbit constant  $C_b = C/(C + 1)$ . Because of 6 degrees of freedom in equation (2.8), Monte-Carlo integration is used to evaluate the integral which simplifies to

$$\frac{\langle \mathbf{X} \rangle_{PI}}{n} = \sum_j \frac{A_j}{N_j} \sum_{k=1}^{N_j} (\Delta \mathbf{r}_0)_k \cdot \hat{\mathbf{r}}_\infty \int_{-\infty}^{\infty} dt \left( \mathbf{X}_k(t) - \mathbf{X}_{J,k}(t) \right) = \sum_j A_j \sum_{k=1}^{N_j} \frac{I_k}{N_j}, \quad (2.9)$$

where  $I_k$  is equal to the product of the time integral times the relative velocity of the particles,  $A_j$  is the area of the  $j^{th}$  region in the gradient-vorticity plane in which the points are chosen with uniform probability and  $C_b$  for both particles are chosen from the steady state orbit distribution  $p(C_b)$ . The flow vorticity plane is split into multiple regions of area  $A_j$  to establish convergence of physically relevant quantities such as orientational dispersion, hydrodynamic diffusivity and the stresslet tensor in a systematic way. The standard deviation of the inner summation  $\sigma_{I,j}$  for the  $j^{th}$  region is given by

$$\sigma_{I,j}^2 = \frac{1}{N_j} \sum_{k=1}^{N_j} \left( I_k - \sum_{k=1}^{N_j} \frac{I_k}{N_j} \right)^2, \quad (2.10)$$

The expression for  $\langle \mathbf{X} \rangle_{PI}$  with the standard error within 95% confidence limits is given by

$$\frac{\langle \mathbf{X} \rangle_{PI}}{n} = \sum_j A_j \left\{ \frac{1}{N_j} \sum_{k=1}^{N_j} I_k \pm 1.96 \frac{\sigma_{I,j}}{\sqrt{N_j}} \right\}. \quad (2.11)$$

$$\sigma_{I,j}$$

Pairwise interactions lead to a transient change in the orientation of both particles which can be quantified using the orientational dispersion of the particles defined below. The dispersion in the  $\phi$  direction can be written as  $\langle \phi^2 \rangle = \langle \phi^2 \rangle_J + n(\langle \phi^2 \rangle_{PI}/n)$ , where the subscript  $J$  refers to the contribution to  $\langle \phi^2 \rangle$  for an isolated particle undergoing Jeffery rotation with the steady state orbit distribution set by pairwise interactions. The subscript  $PI$  corresponds to the effect of the transient change in the particle's orientation during the interaction.  $\langle \phi^2 \rangle_{PI}/n$  is given by

$$\frac{\langle \phi^2 \rangle_{PI}}{n} = \sum_j \frac{A_j}{N_j} \sum_{k=1}^{N_j} (\Delta \mathbf{r}_0)_k \cdot \hat{\Gamma}_\infty \int_{-\infty}^{\infty} dt \left( \phi - \phi(t, \tau_i)(1 - H(t - t_{HI})) - \phi(t, \tau_f)H(t - t_{HI}) \right)^2, \quad (2.12)$$

where  $H(t - t_{HI})$  is the Heaviside step-function and  $t_{HI}$  is the time when  $(\Delta \mathbf{r}) \cdot \hat{\mathbf{U}}_\infty = 0$ ;  $\tau_i$  and  $\tau_f$  is the phase angle before and after the interaction respectively. Similarly, the dispersion in  $\theta$  can be expressed as  $\langle \theta^2 \rangle = \langle \theta^2 \rangle_J + n(\langle \theta^2 \rangle_{PI}/n)$  where  $\langle \theta^2 \rangle_{PI}/n$  is given by

$$\frac{\langle \theta^2 \rangle_{PI}}{n} = \sum_j \frac{A_j}{N_j} \sum_{k=1}^{N_j} (\Delta \mathbf{r}_0)_k \cdot \hat{\Gamma}_\infty \int_{-\infty}^{\infty} dt \left( \theta - \theta(t, \tau_i, C_i)(1 - H(t - t_{HI})) - \theta(t, \tau_f, C_f)H(t - t_{HI}) \right)^2, \quad (2.13)$$

where  $C_i$  and  $C_f$  are the orbit constants before and after the interaction respectively. The idea of equation (2.13) is that the time integral of  $\theta(t, \tau_i, C_i) H(t - t_{HI})$  will be exactly equal to  $\theta(t, \tau_f, C_f) H(t - t_{HI})$  when averaged over all trajectories, although it will not be equal for every individual trajectory. This is because of detailed balance in which for every interaction involving a change of the orbit constant from  $C_i$  to  $C_f$  there should exist an equivalent trajectory for which the orbit constant changes from  $C_f$  to  $C_i$ . This should hold true when  $p(C_b)$  has reached steady state.

The stresslet in a dilute suspension of rings can be expressed as  $\langle \mathbf{S} \rangle = \langle \mathbf{S}_{Hyd} \rangle + n(\langle \mathbf{S}_p \rangle/n + \langle \mathbf{S}_f \rangle/n + \langle \mathbf{S}_{col} \rangle/n)$ , where  $\langle \mathbf{S}_p \rangle$  is the stresslet driven by the transient change in the particles orientation due to PIs,  $\langle \mathbf{S}_f \rangle$  the stresslet induced by  $\mathbf{f}_{HI}$ , and  $\langle \mathbf{S}_{col} \rangle$  is the stresslet imparted from particle collisions ( $\mathbf{F}_{col}$ ).  $\langle \mathbf{S}_p \rangle$  is expressed as

$$\begin{aligned} \frac{\langle \mathbf{S}_p \rangle}{n} = & \sum_j \frac{A_j}{N_j} \sum_{k=1}^{N_j} (\Delta \mathbf{r}_0)_k \\ & \cdot \hat{\mathbf{r}}_\infty \int_0^\infty dt \left[ \mathbf{S}_{Hyd}(\phi, \theta) - \mathbf{S}_{Hyd}(\phi_J(t, \tau_i), \theta(t, \tau_i, C_i)) (1 - H(t)) \right. \\ & \left. - \mathbf{S}_{Hyd}(\phi_J(t, \tau_f), \theta(t, \tau_f, C_f)) H(t) \right] \end{aligned} \quad (2.14)$$

$\langle \mathbf{S}_f \rangle$  is the ensemble average of  $\mathbf{S}_f = \int ds ((\mathbf{f}_{HI} \mathbf{r}_c + \mathbf{r}_c \mathbf{f}_{HI})/2 - (\mathbf{r}_c \cdot \mathbf{f}_{HI}) \mathbf{I}/3)$ , given by

$$\frac{\langle \mathbf{S}_f \rangle}{n} = \sum_j \frac{A_j}{N_j} \sum_{k=1}^{N_j} (\Delta \mathbf{r}_0)_k \cdot \hat{\mathbf{r}}_\infty \int_{-\infty}^\infty dt \mathbf{S}_f, \quad (2.15)$$

and  $\langle \mathbf{S}_{col} \rangle$  is given by

$$\frac{\langle \mathbf{S}_{col} \rangle}{n} = \sum_j \frac{A_j}{N_j} \sum_{k=1}^{N_j} (\Delta \mathbf{r}_0)_k \cdot \hat{\mathbf{r}}_\infty \int_{-\infty}^\infty dt \mathbf{S}_{col}. \quad (2.16)$$

Equation (2.15) faces the problem of a non-integrable area integral over the  $\hat{\mathbf{r}}_\infty - \hat{\Omega}_\infty$  plane because  $\mathbf{S}_f$  scales with  $\Delta r^{-3}$ ,  $\Delta r$  being the measure of the distance away from the particle. To prevent this divergent behavior, a term  $\mathbf{S}_f^{RN}$  with the same  $\Delta r^{-3}$  behavior as  $\mathbf{S}_f$  leading to a similar non-integrable divergent expression.  $\mathbf{S}_f^{RN}$  is the stresslet computed for particle I, which is fixed at the origin and its orientation following Jeffery's equation (1.1), such that particle II moves along its original streamline rotating with Jefferey's rotation rate following equation (1.1). The ensemble average of  $\mathbf{S}_f^{RN}$  should be zero because this artificial calculation is computing the net stresslet exerted by the presence of other particles in the suspension correct to  $O(n)$ . The renormalized equation for evaluating  $\langle \mathbf{S}_f \rangle$  is given by

$$\frac{\langle \mathbf{S}_f \rangle}{n} = \sum_j \frac{A_j}{N_j} \sum_{k=1}^{N_j} (\Delta \mathbf{r}_0)_k \cdot \hat{\mathbf{r}}_\infty \int_{-\infty}^\infty dt (\mathbf{S}_f - \mathbf{S}_f^{RN}). \quad (2.15)$$

Evaluating the time integration using equation (2.15) isolates the influence of the pairwise interaction for each trajectory, and also minimizes the statistical uncertainty of the Monte-Carlo procedure since the  $\Delta r^{-3}$  part of  $\mathbf{S}_f$  and  $\mathbf{S}_f^{RN}$  exactly cancels out for  $\Delta r \gg 1$  leading to a term which decays as  $\Delta r^{-6}$  thereby leading to a convergent summation.  $\langle \mathbf{S}_p \rangle$  does not require renormalization because the linearized change in the stress due to change in orientation does not have a net ensemble change in the particle's orientation.

PIs can also displace the particle in  $\hat{\Gamma}_\infty - \hat{\Omega}_\infty$  plane which across many particle interactions is approximately diffusive in nature. The corresponding hydrodynamic diffusivity in the gradient ( $D_{33}$ ) and vorticity ( $D_{22}$ ) direction are given by

$$\frac{D_{22}}{n} = \sum_j \frac{A_j}{N_j} \sum_{k=1}^{N_j} (\Delta \mathbf{r}_0)_k \cdot \hat{\Gamma}_\infty \left( ((\Delta \mathbf{r}_\infty)_k - (\Delta \mathbf{r}_0)_k) \cdot \hat{\Omega}_\infty \right)^2, \quad (2.16)$$

$$\frac{D_{33}}{n} = \sum_j \frac{A_j}{N_j} \sum_{k=1}^{N_j} (\Delta \mathbf{r}_0)_k \cdot \hat{\Gamma}_\infty \left( ((\Delta \mathbf{r}_\infty)_k - (\Delta \mathbf{r}_0)_k) \cdot \hat{\Gamma}_\infty \right)^2, \quad (2.17)$$

where  $(\Delta \mathbf{r}_\infty)_k \cdot \hat{\Omega}_\infty$  and  $(\Delta \mathbf{r}_\infty)_k$  are the separation of the center of mass of the two particles in the vorticity and gradient directions after the interaction (i.e., when  $(\Delta \mathbf{r}_\infty)_k \cdot \hat{\mathbf{U}}_\infty \rightarrow \infty$ ).

Which are the most important hydrodynamic interactions? There are two components to this question one that deals with the relative separation between the particles and one that deals with the orientations of both the particles. In a simple shear flow the rate of particle interactions is proportional to its initial separation in the gradient direction  $h_0 = \Delta \mathbf{r}_0 \cdot \hat{\Gamma}_\infty$ . When  $h_0 \gg 1$ , the interaction is purely hydrodynamic and the angular velocity induced by the disturbance of a second ring is  $O(1/h_0^3)$  and the time of interaction is inversely proportional to  $h_0$ . This leads to an angular displacement of  $O(1/h_0^4)$ . The mean squared change in the particle orientation scales as  $\int dh_0 h_0 (1/h_0^2)^2 \propto h_0^{-2}$  is therefore convergent and small for  $h_0 \gg 1$ . When  $h_0 \ll 1$ , the angular velocity induced by HI is  $O(\epsilon)$  and collisions is  $O(1)$ . The time of interaction is again inversely proportional to  $h_0$ . The particle orientation changes by  $O(1/h_0)$ , which implies the possibility of multiple tumbles, but the changes in  $(\phi, \theta)$ , which are bounded between  $[0, 2\pi)$  and  $[0, \pi]$

respectively, are only  $O(1)$ . This implies the mean squared change in the particle orientation equal to  $\int dh_0 h_0^2 \propto h_0^2$  is also convergent and small for  $h_0 \ll 1$ . When  $h_0 \sim O(1)$ , particle collisions also lead to an  $O(1)$  change in the particle orientation leading to an  $O(1)$  mean squared angular displacement. Therefore, the most important interactions required to obtain the steady state orientation distribution have  $h_0 \sim O(1)$  and therefore also interact for an  $O(1)$  time. A similar scaling analysis for the diffusivity shows the convergence of the integral in equation (2.8).

Interacting rings change their rate of rotation from Jeffery's prediction (equation (1.1)) and also change the orbit constant  $C$  during the course of the interaction. Collisions tend to change the angle by an  $O(1)$  amount and was found to be the dominant contribution in determining the steady state orientation distribution. The Jeffery orbits are pinched near the gradient and vorticity directions due to high aspect ratio of the ring most of the orientational space is filled with orbits with orbit constant  $C \gtrsim O(\phi_T^{-1})$  as seen in figure 1 (b). This implies that PIs will move the particles near the  $C \approx O(\phi_T^{-1})$  orbit. This can be more formally proven by considering a modified orbit constant  $C_b = C/(C + 1)$  because it is bounded between 0 and 1, unlike  $C$ . Let  $(\theta, \phi)$  change by an amount  $(\Delta\theta, \Delta\phi)$  during an interaction with a second particle and let the change in the modified orbit constant be  $\Delta C_b$ . The new orientation after the interaction should satisfy equation (1.3) giving

$$\tan(\theta + \Delta\theta) = \frac{C_b + \Delta C_b}{1 - (C_b + \Delta C_b)} \cdot \frac{\phi_T}{\sqrt{\phi_T^2 \cos^2(\phi + \Delta\phi) + \sin^2(\phi + \Delta\phi)}}. \quad (2.17)$$

Equation (2.15 a) can be simplified for small values of  $\Delta\theta$  and  $\Delta\phi$  giving the relationship

$$\sec^2(\theta) \Delta\theta \approx \tan(\theta) \left( \frac{\Delta C_b}{C_b(1 - C_b)} + \frac{\sin(\phi) \cos(\phi) \Delta\phi}{\phi_T^2 \cos^2(\phi) + \sin^2(\phi)} \right). \quad (2.18)$$

On rearranging equation (2.18) and using the fact that  $\phi \sim O(\phi_T)$  and  $\theta \sim O(\arctan(C))$ , obtained from Jeffery's analysis, the scaling of  $\Delta C_b$  is given by  $\Delta C_b = \left\{ C_b(1 - C_b)O\left(\frac{\Delta\phi}{\phi_T}\right) + [C_b^2 + (1 - C_b)^2]O(\Delta\theta) \right\}$ . Since  $\Delta C_b$  is at most  $O(1)$ ,  $C_b(1 - C_b)$  should be  $O(\phi_T)$  which happens when either  $C_b \rightarrow O(\phi_T)$  or  $1 - C_b \rightarrow O(\phi_T^{-1})$ .  $C_b \rightarrow O(\phi_T)$ , requires both  $C_b$  and  $\Delta C_b$  to remain  $O(\phi_T)$ , which is not possible based on the expression for  $\Delta C_b$ . Thus,  $1 - C_b \rightarrow O(\phi_T)$  or  $\langle C \rangle \rightarrow O(\phi_T^{-1})$ , which is very similar to Leal and Hinch's distribution for weak Brownian

motion discussed in section (3). Furthermore, the unsteady Jeffery rotation implies that rings in the  $C \sim O(\phi_T^{-1})$  orbit spend most of the time aligned close to the flow-vorticity plane. However, two rings nearly aligned in flow vorticity plane have a collision frequency of  $O(1/A^2)$ , which is much smaller than the  $O(\sqrt{\ln(A)}/A)$  collision frequency of a tumbling and an aligned ring. Furthermore, the  $O(\epsilon\phi_T)$  velocity disturbance of an aligned ring changes the orientation of another aligned ring in its vicinity by  $O(\epsilon\phi_T) = O(1/(\sqrt{\ln(A)} A))$ . Therefore, the most dominant interactions are the collisional interactions of a temporarily aligned and a tumbling ring. This observation is used to derive scaling arguments in the forthcoming subsection.

The procedure used to obtain the steady state orientation distribution is described now. The initial orientation is based on the probability distribution resulting from Jeffery rotation and weak anisotropic rotary diffusion. The corresponding probability distribution of  $C_b = C/(C + 1)$  is

$$p(C_b) = \frac{4C_b A_{eff}^2 \zeta_1}{\left(4 \left(\frac{C_b}{1 - C_b}\right)^2 A_{eff}^2 \zeta_1 + 1\right)^{3/2} (1 - C_b)^3}, \quad (2.19)$$

where  $\zeta_1$  is ratio of the  $\theta\theta$  and  $\phi\phi$  diffusivity components (Rahnama, Koch and Shaqfeh 1995). A dilute suspension of fibers attains a steady state orbit distribution specified by equation (2.19) with  $\zeta_1 \sim O(1)$  (Stover, Koch and Cohen 1992; Rahnama, Koch and Shaqfeh 1995). The orbit distribution can be specified in terms of a set  $S_c$  of  $N_{set}$  particles chosen to have  $C_b$  values following the orbit distribution specified by (2.19). Two values of  $C_b$  are randomly chosen from  $S_c$  and assigned to the two particles being simulated. The values of  $C_b$  for each particle are replaced by the new  $C_b$  values attained by the corresponding particle at the end of the interaction. This procedure is continued until  $\langle \cos^2(\theta) \rangle$  reaches a statistical steady state value as a function of the number of such simulations  $N_{sim}$ .  $N_{set}$  was chosen to be 200 so that  $S_c$  has enough points to represent a smooth  $p(C_b)$  and small enough to require  $O(N_{set}/2) = O(10^2)$  interactions for each particle or  $O(N_{set}^2/2) \equiv O(10^4)$  total number of computations to reach a statistical steady state orbit distribution.

In addition to the orbit distribution, the probability of an interaction itself is proportional to  $\Delta r \cdot \hat{\Gamma}_\infty$  due to the SSF, and therefore most interactions are the ones where  $\Delta r \cdot \hat{\Gamma}_\infty \gg 1$ . However,

these interactions have a negligible effect on the steady state orientation distribution due to weak HI of particles that decays as  $|\Delta\mathbf{r}|^{-2}$ . The most important interactions, as shown earlier, are the ones for which  $\Delta\mathbf{r} \cdot \hat{\mathbf{r}}_\infty \sim O(1)$ . Therefore,  $\Delta\mathbf{r} \cdot \hat{\mathbf{r}}_\infty$  was chosen between  $(0, L_3]$  with a probability of  $2\Delta\mathbf{r} \cdot \hat{\mathbf{r}}_\infty/L_3^2$  while  $\Delta\mathbf{r} \cdot \hat{\Omega}_\infty$  was chosen with a uniform probability between  $[-L_2, L_2]$  and, where  $L_2$  and  $L_3$  specify the bounds of the initial position along  $\hat{\Omega}_\infty$  and  $\hat{\mathbf{r}}_\infty$  respectively. Instead of starting with a large value of  $L_2$  and  $L_3$ , an initial value of  $L_2 = 1$  and  $L_3 = 1$  is chosen, which corresponds to the ideal collision cross-section of a tumbling and an aligned ring, to attain an intermediate steady state distribution  $p(C_b)$  which is quantified by obtaining the ensemble average value of  $\langle \cos^2(\theta) \rangle$ . This approach reduces the computational time by avoiding, during the initial transient period, calculation of a large number of cases which make small contributions to the final steady state orientation distribution.

Figure (2 a) shows the variation of  $\langle \cos^2(\theta) \rangle$  with the number of simulation  $N_{sim}$  for  $A = 40$  torus with  $(L_2, L_3) = (2, 1)$  and a starting distribution specified by equation (2.16) with  $\zeta_1 = 1$ . The mean value of  $\langle \cos^2(\theta) \rangle$  approaches a value of 0.0946 with a standard deviation of the mean equal to 15 %. On further increasing the domain size  $(L_2, L_3) = (2, 2)$ ,  $\langle \cos^2(\theta) \rangle$  has mean value of 0.0951, which is less than 1 % larger than the steady state value for the  $(L_2, L_3) = (1, 1)$  domain. The region in the  $\hat{\mathbf{r}}_\infty - \hat{\Omega}_\infty$  plane corresponding to  $(L_2, L_3) = (2, 1)$  is the ideal collision cross-section of an aligned ring and a temporarily tumbling ring which has a dominant contribution in setting the steady state orientation distribution.  $\langle \mathbf{S}_{Hyd} \rangle$  vs of  $A$  is shown in figure (2 b) based on the steady state orbit distribution set by PIs. Rings tumble with a frequency of  $O(\phi_T) = O(1/(A\sqrt{\epsilon}))$  due to PI and exert a much larger  $O(\epsilon)$  stresslet compared to the  $O(\phi_T\epsilon)$  stresselt of a nearly aligned ring and therefore,  $\langle \mathbf{S}_{Hyd} \rangle$  scales as  $O(\sqrt{\epsilon}/A)$ , similar to a suspension of fibers. The orientation distribution set by PIs is very similar to the distribution set by weak Brownian motion which is discussed in section (3).

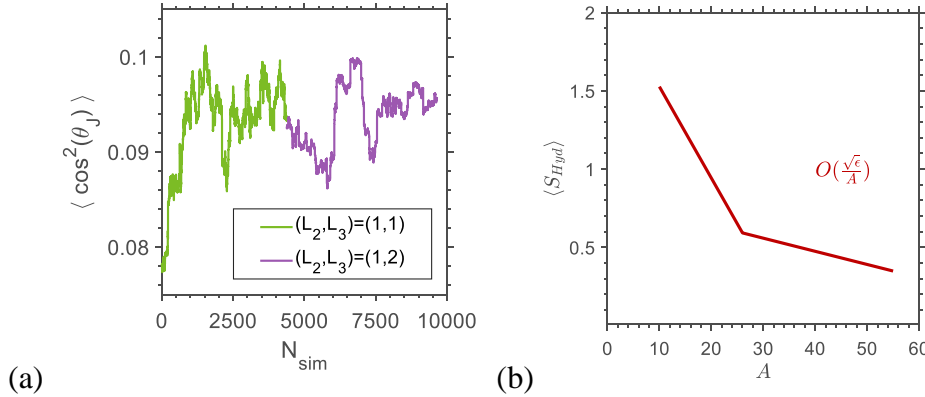


Figure 2  $\langle \cos^2(\theta_j) \rangle$  vs  $N_{sim}$  (a) for  $A = 40$  tori with different values of  $(L_2, L_3)$  (the mean and standard deviation were evaluated after 1500 simulations in each region); (b)  $\langle S_{Hyd} \rangle$  vs  $A$  for a torus with the steady state orientation distribution

## 2.2. $O(n^2)$ rheology of hydrodynamically interacting rings

At dilute particle concentrations ( $n \ll 1$ ) pairwise hydrodynamic interactions as well as collisions are important in determining the orientational dispersion, hydrodynamic diffusivity and the rheology of rings. The dependence of each of these quantities on the aspect ratio  $A$  of the ring is cannot be obtained based on purely scaling arguments. The steady state orientation distribution tends to move rings near the  $C_\infty$  orbits as explained earlier in section (3.1). The transient change in the particles orientational dynamics is quantified through  $\langle \phi^2 \rangle_{PI}$  and  $\langle \theta^2 \rangle_{PI}$  defined in equations (2.10) and (2.11) respectively and shown in figure 3 (a) for different particle aspect ratios. Collisions between a tumbling an aligned ring occurring with an  $O(\phi_T)$  frequency lead to a scaling of  $\langle \phi^2 \rangle_{PI}$  and  $\langle \theta^2 \rangle_{PI}$  of  $n\sqrt{\ln(8A)}/A$ .

The center of mass of a tumbling torus gets displaced from its original fluid streamline due to the presence of other particles. The displacements are stochastic in nature and the overall translation of the particle in the suspension on a length scale than its size appears to be diffusive in nature. This motion can be quantified using the hydrodynamic diffusivity and its components in the gradient ( $D_{33}$ ) and vorticity ( $D_{22}$ ) directions are shown in figure 3 (b). The scaling for the diffusivity per unit particle density due to collisions is obtained by simply multiplying the square of the  $O(1)$  displacement in its position in the gradient or vorticity direction with the  $O(\phi_T)$

interaction frequency. The contribution to the diffusivity due to HI is  $O(\epsilon^2 \phi_T)$  obtained from the  $O(\epsilon)$  displacement of an aligned ring caused by a HI with a tumbling ring and  $\phi_T$  is the frequency of such interactions.

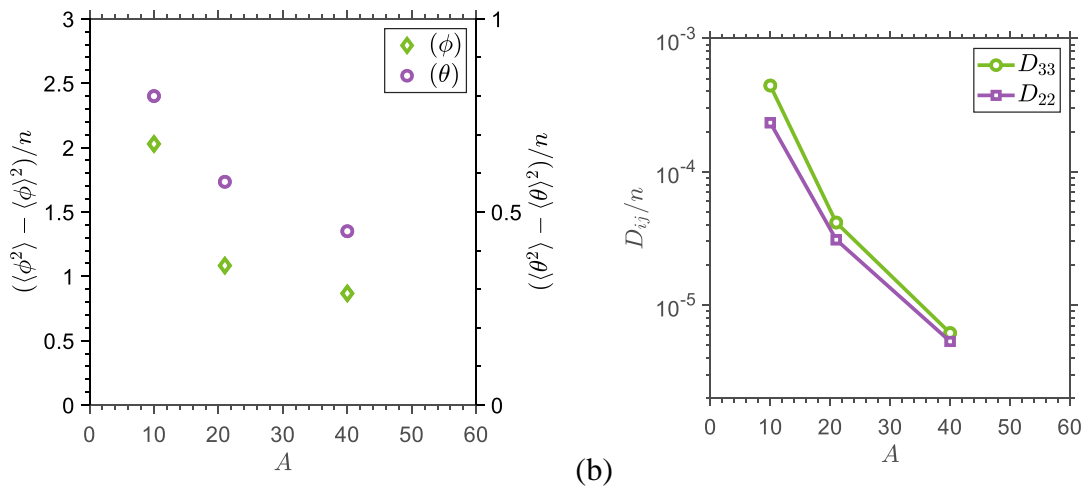
The stresslet due to pairwise interactions  $\langle \mathbf{S}_{PI} \rangle$  is proportional to  $n$  and the stresslet per unit concentration ( $\langle \mathbf{S}_{PI} \rangle/n$ ) is given by

$$\frac{\langle \mathbf{S}_{PI} \rangle}{n} = \frac{\langle \mathbf{S}_p \rangle}{n} + \frac{\langle \mathbf{S}_f \rangle}{n} + \frac{\langle \mathbf{S}_{col} \rangle}{n}, \quad (2.20)$$

where  $\langle \mathbf{S}_p \rangle$  is the contribution due to change of particle orientation,  $\langle \mathbf{S}_f \rangle$  is the contribution from the force per unit length induced by the presence of a neighboring ring and  $\langle \mathbf{S}_{col} \rangle$  is the contribution from collisions computed from equations (2.12)-(2.13) respectively. The scaling for each can be derived from the interactions of a tumbling and an aligned ring which occur with a probability of  $O(\phi_T) \sim O(1/(\sqrt{\epsilon}A))$ . The collisions happen from the rotation caused by the simple shear flow and therefore the collision force is  $O(1)$ , which implies that  $\langle \mathbf{S}_{col} \rangle/n \sim O(\phi_T) \sim O(1/(\sqrt{\epsilon}A))$ . The  $O(1)$  change in the orientation of the aligned ring due to collision with a tumbling ring contributes to  $O(\epsilon\phi_T) \sim O(\sqrt{\epsilon}/A)$  value of  $\langle \mathbf{S}_p \rangle/n$ . Similarly,  $\mathbf{f}_{HI}$  is  $O(\epsilon)$  because of collisions leading to an  $O(\epsilon\phi_T) \sim O(\sqrt{\epsilon}/A)$  scaling for  $\langle \mathbf{S}_f \rangle/n$ . Therefore, the total stresslet due to HI is  $O(n/(\sqrt{\epsilon}A))$  mainly due to collisions as seen in figure 3 (c). For the aspect ratios considered in the study the value of  $\epsilon$  lies between (0.228, 0.164) suggesting that the  $\langle \mathbf{S}_p \rangle$ ,  $\langle \mathbf{S}_f \rangle$ , and  $\langle \mathbf{S}_{col} \rangle$  will have similar numerical values. The values of  $\langle \mathbf{S}_p \rangle$ ,  $\langle \mathbf{S}_f \rangle$ , and  $\langle \mathbf{S}_{col} \rangle$ , are shown in figure 3 (c).  $\langle \mathbf{S}_f \rangle$  and  $\langle \mathbf{S}_{col} \rangle$  are similar in magnitudes and much larger than  $\langle \mathbf{S}_p \rangle$ , which implies that the  $O(n^2)$  viscosity correction to the viscosity has major contributions from the hydrodynamic velocity disturbances and actual solid body contacts, as opposed to the transient change in the particles orientation from Jeffery's equations.

A single particle rotating in Jeffery orbits cannot generate normal stresses because the orientation trajectory of the particle is symmetric about the gradient-vorticity ( $\hat{\mathbf{r}}_\infty - \hat{\mathbf{\Omega}}_\infty$ ) plane. Suspensions where particles have purely hydrodynamic interactions also cannot have normal stress differences at dilute concentrations because the microstructure is symmetric about the  $\hat{\mathbf{r}}_\infty - \hat{\mathbf{\Omega}}_\infty$

plane and remains invariant upon reversal of the shear flow due to Stokes flow reversibility. Collisions break Stokes flow reversibility because collisional force is non-zero when the particles approach each other and is zero when they move apart. This is a stark distinction from the dilute fiber suspension for which collisions are rare at dilute concentrations and most interactions are purely hydrodynamics. The first and second normal stress differences are given by  $\langle N_1 \rangle = n^2 (\langle S_{PI} \rangle / n) : (\hat{U}_\infty \hat{U}_\infty - \hat{\Gamma}_\infty \hat{\Gamma}_\infty)$  and  $\langle N_2 \rangle = n^2 (\langle S_{PI} \rangle / n) : (\hat{\Gamma}_\infty \hat{\Gamma}_\infty - \hat{\Omega}_\infty \hat{\Omega}_\infty)$  respectively and their variation with the aspect ratio is shown in figure 3 (d) and (e).  $\langle N_2 \rangle$  is negative and  $\langle N_1 \rangle$  is positive and both have major contributions from  $\langle S_p \rangle$ . A tumbling ring either delays or advances the tumbling phase of a temporarily aligned when the particle make solid-body contact. This breaks the symmetry of the Jeffery orbit leading to finite normal stress differences. Furthermore,  $\langle N_2 \rangle$  is much smaller in magnitude than  $\langle N_1 \rangle$ . These results are consistent with the normal stresses arising in semi-dilute fiber suspensions due to particle contact (Snook, et al., 2014). The normal stress differences in a sheared suspension of non-Brownian axisymmetric fibers should also be proportional to  $n^2$  rather than  $n$  as reported by many experimental studies which are summarized in (Petrie, 1999). This discrepancy is mostly due the fact that most of those studies were carried out over a small range of number densities and therefore the quadratic behavior was difficult to assert.



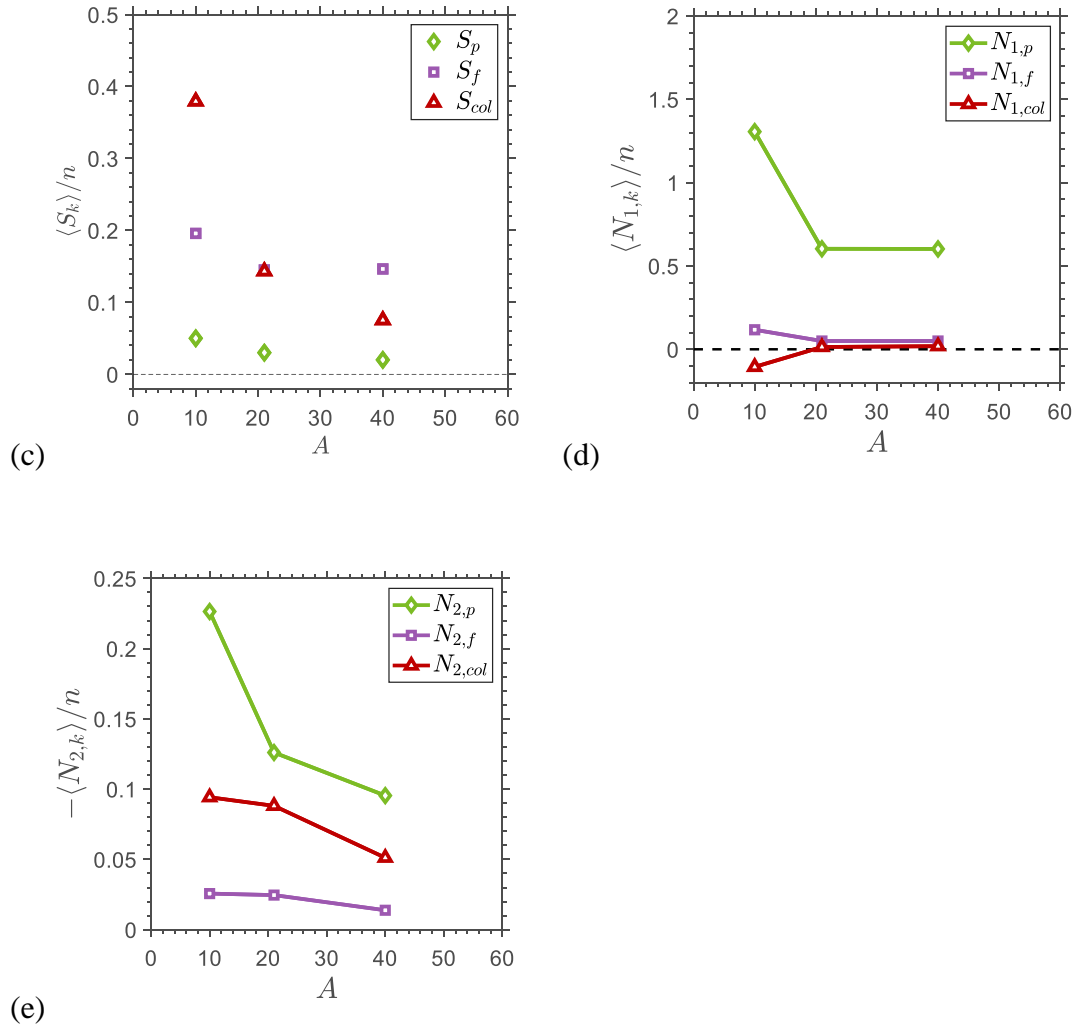


Figure 3 Rheological properties of a suspension of tori due to interparticle interactions. (a) Orientational dispersion; (b) hydrodynamic diffusivity in the gradient ( $D_{33}$ ) and vorticity ( $D_{22}$ ) direction; (c)  $\langle S_p \rangle$ ,  $\langle S_f \rangle$ , and  $\langle S_{col} \rangle$ ; (d)  $\langle N_1 \rangle$  and (e)  $\langle N_2 \rangle$  as a function of the particle aspect ratio.

### 3. Rheology of isolated Brownian rings

#### 3.1. Brownian Dynamics (BD) simulation strategy

Rotary Brownian Dynamics simulations of an axisymmetric particle with a rotary diffusivity  $D_r$  is carried out using the procedure outlined in Gabdoulline & Wade (Gabdoulline & Wade, 1998). A rotary Peclet number  $Pe = \gamma/D_r$  quantifies the strength of Brownian motion, where  $D_r$

is the non-dimensional rotary diffusivity of the particle given by  $D_r = k_B T(2 - 3\epsilon)/(8\pi^2 \mu_f \epsilon R^3)$ . The rotational displacement at each Brownian time step  $\Delta t_B$  is given by

$$\mathbf{p}(t + \Delta t_B) - \mathbf{p}(t) = \int_t^{t + \Delta t_B} dt' \left[ \dot{\mathbf{p}}_J(t') + \frac{\Delta \mathbf{p}_B(t)}{\Delta t_B} \right] \quad (3.1)$$

where  $\dot{\mathbf{p}}_J = \mathbf{p} \cdot \mathbf{R}_\infty + \lambda(\mathbf{E}_\infty \cdot \mathbf{p} - \mathbf{E}_\infty : \mathbf{p}\mathbf{p})$  is the rotation rate induced by the SSF given by equation (1.1). The Brownian displacement  $\Delta \mathbf{p}_B$  is such that  $\langle \Delta \mathbf{p}_B \rangle = 0$ ,  $\langle \Delta \mathbf{p}_B \Delta \mathbf{p}_B \rangle = (2D_r \Delta t_B)^{0.5} (\mathbf{I} - \mathbf{p}\mathbf{p})$ . Solving equation (3.1) is equivalent to solving the Fokker-Planck for the orientation probability distribution  $P(\mathbf{p})$  ((Gabdoulline & Wade, 1998), (Kim & Karilla, 1991)). The quantity  $P(\mathbf{p}) d\mathbf{p}$  gives the fraction of systems in differential region  $d\mathbf{p}$  around  $\mathbf{p}$  and is used to obtain the ensemble average of any quantity of interest  $\mathbf{X}$  which is given by

$$\langle \mathbf{X} \rangle = \int d\mathbf{p} P(\mathbf{p}) \mathbf{X}. \quad (3.2)$$

A Runge-Kutta method with an adaptive time stepping method was used to solve the integral equation (3.1) during each Brownian step  $\Delta t_B$ . The mean squared value of the dimensional angular step is given by  $\sqrt{2(\gamma \Delta t_B) D_r}$  which in non-dimensional form is expressed as  $\sqrt{2\Delta t_B/Pe}$ . For  $Pe < 1$ , a variable Brownian time step  $\Delta t_B = 10^{-2}Pe$  guarantees that the mean-squared value of the Brownian angular step,  $\sqrt{2\Delta t_B/Pe} = \sqrt{2\Delta t_B/Pe}$ , is smaller than unity. For  $Pe \gg 1$ ,  $\sqrt{2\Delta t_B/Pe}$  should be much smaller than  $\phi_T$ . Choosing  $\Delta t_B = 10^{-2}$  for all  $Pe > 1$ , satisfies  $\sqrt{2\Delta t_B/Pe} \ll \phi_T$  required for  $Pe \gg 1$  and  $\sqrt{2\Delta t_B/Pe} \ll 1$  for  $Pe \sim O(1)$ . The steady state orientation distribution is attained in an  $O(Pe)$  time for  $Pe \ll 1$  and an  $O(Pe \phi_T^2)$  time for  $Pe \gg 1$  (Leahy, et al., 2015). The simulation was terminated after a time  $10^5$  for  $1 \leq Pe \leq 10^5$  and after a time  $10^5 Pe$  for  $Pe < 1$ .

The BD simulation is verified by confirming the convergence to the asymptotic limits as  $Pe \rightarrow 0$  and  $Pe \gg \phi_T^{-3}$ . For the low  $Pe$  limit the moments  $\mathbf{p}$  obtained from the solution to the Fokker-Plank equation for  $P(\mathbf{p})$  are

$$\langle \mathbf{p}\mathbf{p} \rangle = \frac{1}{3} \mathbf{I} - \frac{1}{15} \frac{\mathbf{E}_\infty}{D_r} + O(Pe^2),$$

$$\langle p_i p_j p_k p_l \rangle = \frac{1}{15} (\delta_{ij}\delta_{kl} + \delta_{ik}\delta_{jl} + \delta_{il}\delta_{jk}) + O(Pe), \quad (3.3)$$

(Kim & Karilla, 1991). The BD simulation results are within 3% from the values in equation (1.3) for  $Pe < 1$ . On the other hand, for the high  $Pe$  limit, the orientation distribution for tumbling particles ( $Pe \gg \phi_T^{-3}$ ) matches the distribution of Leal and Hinch (Leal & Hinch, 1971). The moments of  $\mathbf{p}$  obtained from the BD simulations match the asymptotic values with a maximum error of 5% for  $Pe \gtrsim 10 \phi_T^{-3}$ . Therefore, the BD simulations were performed only for  $1 < Pe \leq 10\phi_T^{-3}$ .

### 3.2. Structure and rheology of isolated Brownian rings

Brownian torques try to make particles attain an isotropic orientation distribution and compete with the SSF which tries to distort the distribution. Brownian motion influences  $\langle \mathbf{S}_{Hyd} \rangle$  through change in  $\mathbf{p}$ , but also has a more direct contribution termed as the Brownian stress  $\langle \mathbf{S}_{Brow} \rangle = 3D_r M_r^{-1} \lambda (\langle \mathbf{p}\mathbf{p} \rangle - \mathbf{I}/3)$  that arises by virtue of angular velocity associated with the diffusion process across the gradients in the orientation probability distribution. Here,  $M_r = (2 - 3\epsilon)/(8\pi^2\epsilon)$  is the rotary mobility of the axisymmetric particle. The relative increase in the suspension viscosity  $\Delta\mu$  is equal to  $n(\langle \mathbf{S}_{Brow} \rangle + \langle \mathbf{S}_{Hyd} \rangle)$ , where  $\langle \mathbf{S}_{Hyd} \rangle = \langle \mathbf{S}_{Hyd} \rangle : \hat{\mathbf{U}}_\infty \hat{\mathbf{f}}_\infty$  and  $\langle \mathbf{S}_{Brow} \rangle = \langle \mathbf{S}_{Brow} \rangle : \hat{\mathbf{U}}_\infty \hat{\mathbf{f}}_\infty$ . The scalars  $\langle \mathbf{S}_{Hyd} \rangle$  and  $\langle \mathbf{S}_{Brow} \rangle$  are henceforth referred to as the hydrodynamic stresslet and the Brownian stresslet respectively, to be distinguished from the respective stresslet tensors.

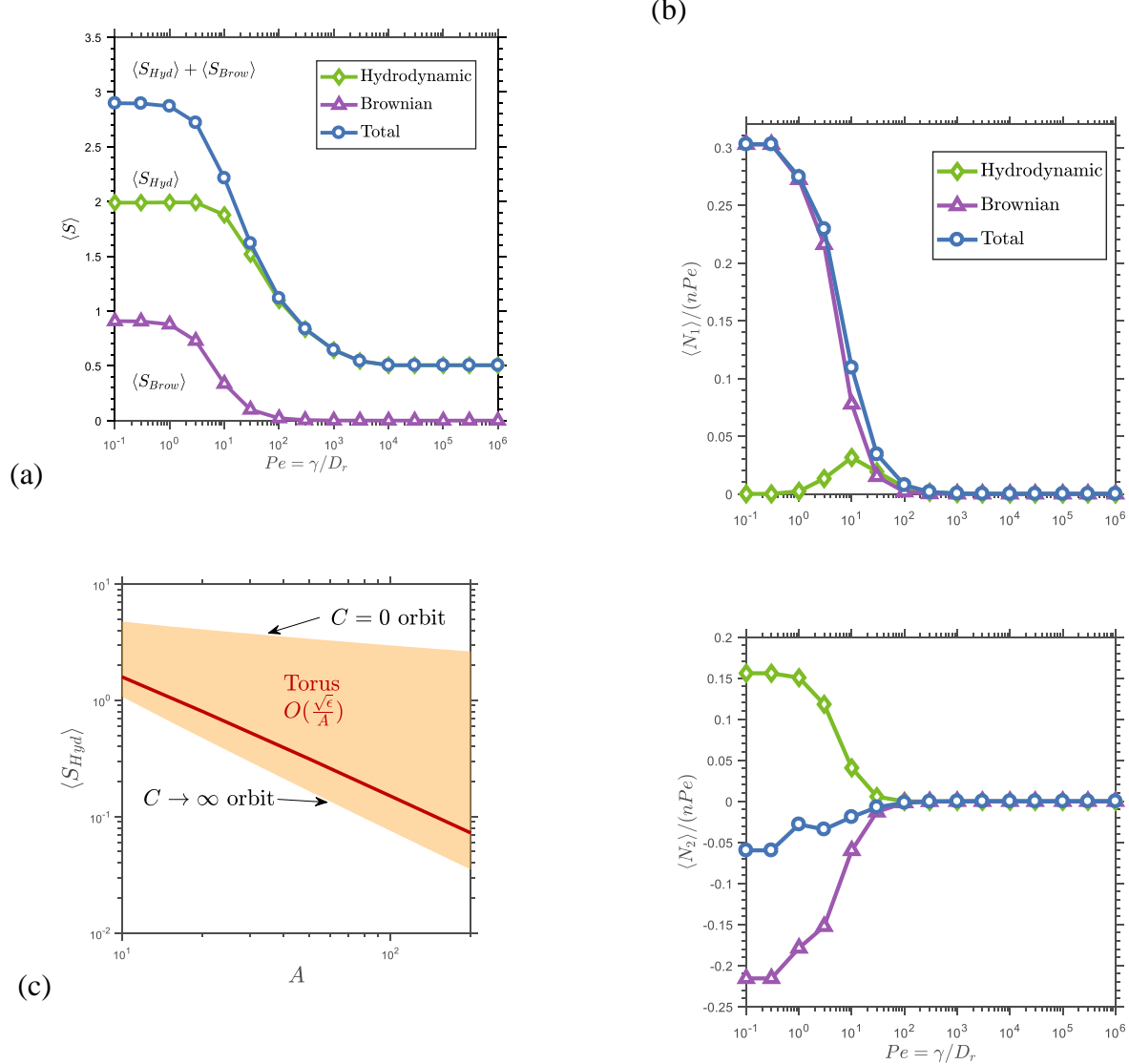


Figure 4 (a) The two contributions of the stresslet  $\langle \mathbf{S}_{Brow} \rangle$  and  $\langle \mathbf{S}_{Hyd} \rangle$  as a function of the  $Pe$  number. (b) The non-dimensional normal stress difference coefficients  $\langle N_1 \rangle/Pe$  and  $\langle N_2 \rangle/Pe$  vs  $Pe$ . The aspect ratio of the ring is  $A = 26$  corresponding to  $\lambda = -1 + 8.62 \times 10^{-3}$ . (c)  $\langle \mathbf{S}_{Hyd} \rangle$  due to a single ring with the  $Pe \rightarrow \infty$  orbit distribution along with the range of values the  $\mathbf{S}_{Hyd}$  averaged over the time period of rotation achieved for any orbit distribution specified by the orbit constant  $C$  which varies from 0 to  $\infty$ .

At dilute concentrations a suspension exhibits a typical shear thinning behavior, similar to a fiber suspension as shown in figure 4 (a) depicting the variation of the flow-gradient component of the stresslet tensor  $\langle \mathbf{S} \rangle$ :  $\hat{\mathbf{U}}_\infty \hat{\mathbf{F}}_\infty = \langle \mathbf{S} \rangle$ .  $\langle S_{Brow} \rangle \propto Pe^{-1}$ , going to a zero value for  $Pe \gg 1$  and approaching a constant  $\lambda M_r^{-1}/5$ , for  $Pe \ll 1$ , since  $(\langle \mathbf{p} \mathbf{p} \rangle - \mathbf{I}/3) \rightarrow Pe \lambda \mathbf{E}/(15) + O(Pe^2)$  (Brenner, 1974).  $\langle S_{Hyd} \rangle$  also approaches a constant  $O(\epsilon)$  at low  $Pe$  since the even moments of  $\mathbf{p}$  at leading order are isotropic tensors (Brenner, 1974). At high  $Pe$  ( $Pe \gg \phi_T^{-3}$ ), the Brownian motion has very little influence on the angular velocity of the particle and its only role is to set the orbit distribution (Leal & Hinch, 1971). For this orbit distribution  $\langle S_{Hyd} \rangle$  is  $O(\epsilon \phi_T) \sim O(\sqrt{\epsilon}/A)$ , which is smaller than the low- $Pe$  limit by a factor of  $O(\phi_T) \sim O(1/(A\sqrt{\epsilon}))$ , thereby giving the familiar shear thinning behavior observed for dilute particle suspensions.

Brownian motion also generates normal stress differences given by  $\langle N_1 \rangle = n \langle \mathbf{S} \rangle : (\hat{\mathbf{U}}_\infty \hat{\mathbf{U}}_\infty - \hat{\mathbf{F}}_\infty \hat{\mathbf{F}}_\infty)$  and  $\langle N_2 \rangle = n \langle \mathbf{S} \rangle : (\hat{\mathbf{F}}_\infty \hat{\mathbf{F}}_\infty - \hat{\mathbf{\Omega}}_\infty \hat{\mathbf{\Omega}}_\infty)$ . The non-dimensional normal stress difference coefficients  $\psi_1 = \langle N_1 \rangle/Pe$  and  $\psi_2 = \langle N_2 \rangle/Pe$  have a low and high  $Pe$  plateaus as shown in figure 4 (b) similar to a suspension of Brownian fibers. The low  $Pe$  limit values of the normal stress differences, derived from the perturbation of the Fokker Plank equation (Brenner, 1974), are given by

$$\frac{\psi_1^{Brow}}{n} = \frac{\langle N_1^{Brow} \rangle}{nPe} = \frac{24\pi^2 \epsilon}{2-3\epsilon} \frac{\lambda^2}{90} + O(Pe), \quad (3.4 a)$$

$$\frac{\psi_2^{Brow}}{n} = \frac{\langle N_2^{Brow} \rangle}{nPe} = -\lambda \frac{24\pi^2 \epsilon}{2-3\epsilon} \frac{\lambda^2}{630} \left( -\frac{3}{2} + \frac{7}{2\lambda} \right) + O(Pe), \quad (3.4 b)$$

$$\frac{\psi_1^{Hyd}}{n} = \frac{\langle N_2^{Hyd} \rangle}{nPe} = -\xi_3 \frac{\lambda}{30} - \xi_4 \frac{\lambda}{105} + O(Pe), \quad (3.4 c)$$

and  $\psi_1^{Hyd} = \langle N_1^{Hyd} \rangle / Pe = 0 + n O(Pe)$ . These values match the simulation results within 2% error for  $Pe \lesssim 1$ .  $\psi_1$  is positive and has major contribution from Brownian motion, while  $\psi_2$  is negative and much smaller in magnitude than  $\psi_1$  which is similar to Brownian fibers (Petrie, 1999).  $\psi_2$  has a negative contribution from  $\langle S_{Brown} \rangle$  and a positive contribution from  $\langle S_{Hyd} \rangle$  which is slightly less in magnitude. The shear flow alone cannot generate normal stress differences owing to the reversibility of Stokes flow. Thereby, the normal stress differences in the high  $Pe$  limit are zero.

The low-Pe rheology for rings is very similar to that for discs.  $\langle S \rangle$  for discs is  $O(1)$  at low  $Pe$  and differs by a factor of  $O(\epsilon)$  which is not very small for moderate aspect ratio rings. In shear dominated flows,  $Pe \gg \phi_T^{-3}$ ,  $\langle S \rangle$  for a disc is equal to  $10.3A^{-0.75}$  (Singh, et al., 2014) which is larger than the  $O(1/(A\sqrt{\epsilon}))$  stresslet of a ring. This results from the decreased period induced in cylindrical discs by the stresses near their sharper edges. For  $A = 26$  the high Pe plateau for a Brownian ring is 44% lower than the corresponding value for a disc. Similarly, at  $Pe \ll 1$ ,  $\psi_1/n$  is  $32/90$  for a disc which is close to the values for  $A = 26$  ring shown in figure 4 (b).  $\psi_2/n$  is  $-16/63$  for a disc (Brenner, 1974) which seems to be larger in magnitude than the corresponding value for a ring.

Figure 4 (c) shows  $\langle S_{Hyd} \rangle$  for a single ring whose orbit distribution is set by weak Brownian motion ( $Pe \gg \phi_T^{-3}$  orbit distribution). In this regime,  $\mathbf{p}$  is nearly aligned along the gradient direction most of the time and the weak Brownian motion moves the particle across different orbits. Because of the pinching of the orbits near the gradient direction,  $\mathbf{p}$  only needs to change by  $O(\phi_T)$  to sample most of the orbits. Therefore, the time required to span various orbits is  $O(Pe\phi_T^{-2})$  which is the relaxation time due to Brownian motion. The normal stress differences in this regime take on very small,  $O(Pe^{-1})$ , values. The colored region shows the range of stresslet value accessible to a rings rotating in Jeffery orbits. The  $O(\epsilon)$  upper bound of  $\langle S_{Hyd} \rangle$  is set by rings rotating in  $C_0$  orbit and the  $O(\sqrt{\epsilon}A^{-1})$  lower bound of  $\langle S_{Hyd} \rangle$  is set by tumbling rings in the  $C_\infty$  orbit. The weak Brownian motion tends to accumulate the rings near the  $C_\infty$  orbit similar to the effect of pairwise interactions and therefore the stresslet for  $A \lesssim 200$  remains of  $O(A\sqrt{\epsilon})$  as shown in figure 4 (d). The orbit distribution set by weak Brownian motion will be sustained if the

$O(Pe\phi_T^{-2})$  relaxation time of Brownian motion is much smaller than the  $O(n^{-1})$  relaxation time of pairwise interactions, i.e.  $n \ll Pe\phi_T^{-2} = Pe \ln(8A) / A^2$ .

#### 4. Conclusion

In this work, the rheology of a suspension of high aspect ratio ( $A \gg 1$ ) non-Brownian rings is calculated using numerical simulations accounting for pairwise far-field hydrodynamic interactions through slender-body-theory formulation and particle collisions using a short-range repulsive force. The steady state orbit distribution of rings at dilute particle concentrations  $n \ll 1$  was mainly set by collisions between particles which changed the particle's orientation by  $O(1)$  as opposed to the  $O(\epsilon)$  change in the orientation caused by purely hydrodynamic interactions. The dispersion of particle orientations which exists due to periodic rotation of the particle in Jeffery orbits is further enhanced by pairwise interactions primarily through collisions. The hydrodynamic diffusivity in the gradient ( $D_{33}$ ) and vorticity ( $D_{22}$ ) directions were found to be of the same order of magnitude and scaled as  $n\phi_T = n\sqrt{\ln(8A)} / A$ . Collisions also played a key role in determining the rheology of the suspension which was characterized by the relative increase in the suspension viscosity  $\Delta\mu = (\mu - \mu_f)/\mu_f$ , the first ( $N_1$ ) and second ( $N_2$ ) normal stress differences.  $\Delta\mu = n(0.1 + n)$  where the aspect ratio dependence of the  $O(n^2)$  term, derived from pairwise interactions, is proportional to the  $O(\sqrt{\ln(8A)} / A)$  collision frequency of a tumbling and an aligned ring.  $N_1$  was found to be positive and  $N_2$  was found to negative and much smaller than  $N_1$ . The normal stress differences are non-zero because collisions break Stokes flow reversibility and therefore  $N_1$  and  $N_2$  should be proportional to  $n^2$ , rather than  $n$ .

The rheology of Brownian ring suspension was also established through Brownian Dynamics simulation of a single ring. Suspension of rings shows shear thinning behavior with the  $O(\epsilon)$  low- $Pe$  plateau of  $\Delta\mu$  being larger than the  $O(\phi_T\epsilon)$  high- $Pe$  plateau by a factor of  $\frac{A}{\sqrt{\epsilon}}$ . Similarly, the normal stress-difference coefficients  $\psi_1 = \frac{N_1}{Pe}$  and  $\psi_2 = \frac{N_2}{Pe}$  also have a similar shear thinning behavior with increasing  $Pe$  as  $\Delta\mu$ , but have zero high- $Pe$  plateau due to Stokes flow reversibility described in section 2. Because Brownian motion breaks the symmetry of Jeffery orbits  $N_1$  and  $N_2$  are proportional to  $n$ , rather than  $n^2$  for non-Brownian rings. Furthermore, the orbit distribution set by weak Brownian motion  $Pe \gg \phi_T^{-3}$  is very similar to the distribution set

by pairwise interactions for  $A \geq 21$ , thereby having rheology which is very similar to non-Brownian rings described in section (3.2). The non-Brownian particle rheology presented in section (2) should also be accurate even for Brownian rings when the relaxation time of the orientation distribution due to Brownian motion,  $Pe^{-1}\phi_T^{-2}$ , is much larger than the  $O(n^{-1})$  relaxation time set by pairwise interactions (i.e.  $1 \gg n \gg Pe^{-1}\phi_T^{-2}$ ).

Our pairwise interaction simulations suggest that collisions strongly affect the rheology of ring suspensions. In general particle collisions should be important in determining suspension rheology at dilute concentrations ( $Pe^{-1}\phi_T^{-2} \ll n \ll 1$ ) for all high-aspect ratio particles other than suspension of straight fibers. Our work demonstrates an efficient methodology for quantifying the effect of particle geometry on the suspension rheology. In this work, rings were demonstrated to have a much smaller  $\Delta\mu$  than a suspension of discs of the same radius and a much larger  $\Delta\mu$  than a suspension of fibers of the same half-length. The dilute rheology of non-axisymmetric high-aspect ratio particles, such as bent fibers, or planar flakes should still be dominated by collisions, and the current simulation strategy with two additional orientational degrees of freedom for interacting pair of particles should aid in obtaining the respective properties.

## 5. Appendix

### A.1 $\xi_i$ values for a torus

The geometric parameters  $\xi_i$  required to compute the hydrodynamic stresslet from equation (3.1) are given by

$$\begin{aligned}\xi_1 &= 8\pi^2 \left( \left(1 + \frac{1}{2A^2}\right) (-f_{n1} + f_{b4}) + \frac{1}{2A^2} \right), \\ \xi_2 &= -8\pi^2 \left( \left(1 + \frac{1}{2A^2}\right) \left(\frac{1}{3}f_{n1} - \frac{2}{3}f_{b4}\right) + \frac{1}{4A^2} \right), \\ \xi_2 &= -\xi_1 + \frac{7\pi^2}{A^2}, \\ \xi_4 &= \frac{8\pi^2}{3} \left(1 + \frac{1}{2A^2}\right) \frac{\epsilon}{2\epsilon - 5} + \frac{8\pi^2}{A^2} - 2(\xi_1 + \xi_3) + (\xi_1 - \xi_2),\end{aligned}\quad (A.1.1)$$

where  $f_{n1} = -\frac{\epsilon}{16} \frac{(1-\frac{88}{30}\epsilon-\frac{253}{180}\epsilon^2)}{(1-\frac{151}{30}\epsilon+\frac{514}{90}\epsilon^2)(1-\frac{5}{2}\epsilon)}$  and  $f_{b4} = -\frac{7\epsilon}{16} \frac{(1-\frac{16}{3}\epsilon+\frac{1211}{180}\epsilon^2)}{(1-\frac{151}{30}\epsilon+\frac{514}{90}\epsilon^2)(1-\frac{5}{2}\epsilon)}$  (Borker & Koch, in press).

Equation (A 1.1) is derived by matching the stresslet obtained from equation (3.1) to the stresslet calculated from the inner velocity field ( $\mathbf{u}_{inner}$ ) in the SBT formulation and is given by

$$\langle \mathbf{S}_{Hyd} \rangle = \int_0^{2\pi} dA \left( \frac{\mathbf{r}(\boldsymbol{\sigma} \cdot \mathbf{n}) + (\boldsymbol{\sigma} \cdot \mathbf{n})\mathbf{r}}{2} - \frac{\boldsymbol{\sigma} : \mathbf{n}\mathbf{r}}{3} \mathbf{I} \right). \quad (A 1.2)$$

Here  $\boldsymbol{\sigma} = 2(\nabla \mathbf{u}_{inner} + (\nabla \mathbf{u}_{inner})^T)$ ,  $\mathbf{n}$  is the unit normal to the surface and  $\mathbf{r}$  is the position vector. Matching equations (A 1.2) with equation (1.5) gives the result mentioned in (A 1.1).

## CHAPTER 5

### Passively tunable shear rheology using self-aligning particles

Self-aligning particles (SAPs) are rigid bodies that can attain an equilibrium orientation without application of any external forces or torques in a simple shear flow, which is a linear approximation to a pressure driven flow found in many natural and industrial processes. Self-alignment of particles could be a technologically revolutionary behavior because it allows for creation of materials with *perfect anisotropy* using current processing flow techniques like injection molding, spin-casting or extrusion as shown in figure 1 (b). The orientational order of SAPs allows for the fabrication of functional materials with great control over the mechanical, optical, electrical, or thermal properties of the final product. For instance, SAPs embedded during the curing process can be used to fabricate lightweight high strength materials with a layered microstructure, mimicking that of an abalone shell, which can also withstand crack propagation (Lin, et al., 2006) thereby making them useful for making bulletproof armor. Conducting self-aligning rings can also be used instead of fibers to fabricate optical films because it provides an easy route to have uniform planar conductivity desirable in many applications (De, et al., 2009).

In this work, the *rheology* of a suspension of SAPs is demonstrated for the first time using ring-shaped geometries shown in figure 1 (a) which were chosen due to accessibility to fabrication using multi-step photolithography (Foulds & Parameswaran., 2006) and ability to self-align at a moderate aspect ratio  $A = 26$  (Borker, et al., 2018). SAPs have unconventional rheological properties that include a sharp drop in the intrinsic viscosity, hydrodynamic diffusivity and orientational dispersion compared to a suspension of tori of the same aspect ratio. These suspension properties as a function of the particle aspect ratio  $A$ , defined in figure 1 a, exhibit a phase transition like behavior near a critical aspect ratio  $A^*$  at dilute particle concentrations. Our study demonstrates, for the first time, how small change in the geometry of individual particles (i.e. O(1) change in  $A$ ) can drastically change the macroscopic properties of the suspension.

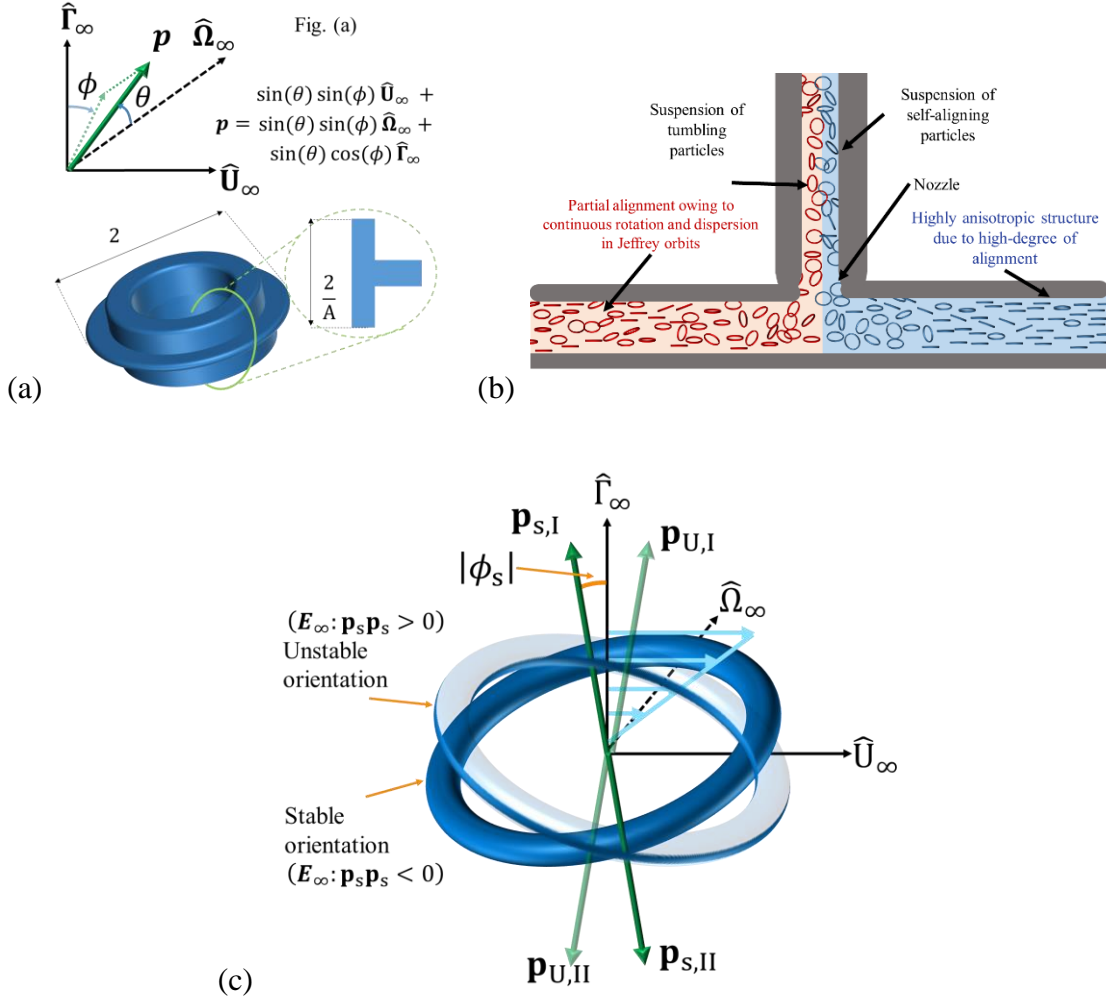


Figure 1 Single particle rheology and orientational dispersion along with geometry of rings studied in this work. (a) Coordinate system and a ring geometry that can align at aspect ratios,  $A \geq A^*$  and rotate more slowly than an equivalent tumbler (ET) for  $A < A^*$ . (b) Schematic of an injection molding system with self-aligning particles on the right, and tumbling particles on the left, demonstrates the difference in the micro-structure. (c) The stable ( $\mathbf{p}_{S,I}, \mathbf{p}_{S,II}$ ) (solid ring) and unstable ( $\mathbf{p}_{U,I}, \mathbf{p}_{U,II}$ ) (translucent ring) nodes of SAP orientation. The neutrally stable nodes  $\mathbf{p} = \pm \hat{\mathbf{\Omega}}_\infty$  are not shown for clarity of the figure. Here  $\mathbf{p}$  is normal to the plane of the ring.

Most particles, whether globular (sphere-like) or thin (rod-like or disc-like), tend to rotate continuously in a simple shear flow (SSF) because of the angular velocity imparted by the non-zero shear stresses acting on the particles. Thin particles spend a long time with their longitudinal direction(s) normal to the gradient direction ( $\hat{\Gamma}_\infty$ ), but eventually rotate continuously (referred as

the tumbling phase). However, rings with a blunt inner and a sharper outer edge, such as the one shown in figure 1 (a), can self-align without application of any external torques. Such self-aligning particles (SAPs) break the usual intuition of a fluid dynamicist by utilizing the fluid pressure to generate a counter-vorticity rotation (Borker, et al., 2018) which balances the shear stress induced rotation. The plane of a SAP subtends an angle  $|\phi_S| \ll 1$  with the flow-vorticity ( $\hat{\mathbf{U}}_\infty - \hat{\boldsymbol{\Omega}}_\infty$ ) plane and is therefore nearly aligned along the fluid lamellae as shown in figure 1(c). This flow-alignment implies that a self-aligning ring always exerts a smaller stress than an equivalent torus of the same aspect ratio, referred henceforth as an equivalent tumbler (ET), during its tumbling phase thereby leading to the unusual rheological properties described in this work. The radius of the ring  $R$ , defined as half the extent of the ring in its plane, the shear rate of the SSF  $\gamma$  and the fluid viscosity  $\mu_f$  are used to non-dimensionalize all quantities of interest. The aspect ratio the ring  $A$  is defined as the ratio of  $R$  and half the extent of the ring along its axis of symmetry.

The angular velocity  $\boldsymbol{\omega}$  of a ring equals  $\boldsymbol{\omega}_\infty + \lambda \mathbf{p} \times \mathbf{E}_\infty \cdot \mathbf{p}$ , where  $\lambda$  is the rotation parameter that only depends on the cross-sectional shape and the aspect ratio  $A$ ,  $\boldsymbol{\omega}_\infty = 0.5 \nabla \times \mathbf{u}_\infty$  and  $\mathbf{E}_\infty = 0.5(\nabla \mathbf{u}_\infty + (\nabla \mathbf{u}_\infty)^T)$  is the rate of strain tensor,  $\mathbf{u}_\infty$  being the imposed SSF. The rotation parameter  $\lambda$  for high aspect ratio rings is given by

$$\lambda = -1 + \Delta\lambda \approx -1 + \frac{C_\lambda(1-1.5\epsilon)}{\epsilon A^2} - \frac{C_\alpha}{A}, |\Delta\lambda| \ll 1 \quad (1)$$

where  $A$  is the aspect ratio of the particle,  $\epsilon = 1/\ln(8A) \ll 1$  is a slenderness parameter that arises in the slender body theory (SBT) treatment of the ring,  $C_\lambda$  is a positive  $O(1)$  parameters that depend only on the cross-sectional geometry and  $C_\alpha \approx C_\lambda \ln(8A^*)/A^*$ ,  $A^*$  being the critical aspect ratio at which  $\Delta\lambda = 0$ . Geometric constants  $(C_\alpha, C_\lambda)$  equal to  $(0.23, 1.5)$  for a T-ring and  $(0, 1.5)$  for a torus are obtained from SBT analysis (Borker & Koch, in press) and confirmed with boundary element method (BEM) calculations (Singh, et al., 2013). The ring attains an equilibrium orientation when  $|\lambda| \geq 1$  and rotates in periodic Jeffery orbits (Jeffery, 1922) with a time period  $T = 4\pi/\sqrt{1-\lambda^2} = 2\pi/\phi_T$  otherwise,. A rotating high-aspect ratio particle remains orientated

near the  $\widehat{\mathbf{U}}_\infty - \widehat{\boldsymbol{\Omega}}_\infty$  plane for a time of approximately  $T/2 \gg 1$  before tumbling.  $\phi_T^3$  is a measure of the angle subtended by a rotating ring with the  $\widehat{\mathbf{U}}_\infty - \widehat{\boldsymbol{\Omega}}_\infty$  plane during its nearly aligned phase. The time period of rotation of a torus  $T_t$  changes gradually as shown in figure 1 (d) and a similar gradual increase in the magnitude of  $T$  is observed for other high-aspect ratio shapes such as discs and fibers. The shape of the  $T$  vs  $A$  graph changes dramatically due to fine-scale cross-sectional features of a ring. A T-ring rotates like an ET when  $1 \ll A \ll A^* \approx 26$ , rotates much slower than an ET for  $A^* - A \sim O(1)$  and self-aligns for  $A \geq A^*$  with an angle  $\phi_S = 0.5\text{acos}(-1/\lambda) \approx \sqrt{-\Delta\lambda/2}$  as shown in figure 1 (c). A Taylor series expansion of equation (1) for  $\epsilon \ll 1$  and  $\Delta A = A - A^* \sim O(1)$  is used to derive the scaling of  $T$  and  $\phi_S$  in figure 1 (d). Figure 1 (d) demonstrates a steep divergence of the time period and a steep decrease in  $|\phi_S|$  near  $A^*$  which is a characteristic of the family of SAPs. A tumbling T-ring with  $A$  slightly smaller than  $A^*$  is referred to as a nearly aligning particle (NAP) because it spends much more time aligned than an ET. The rheology of NAPs is also dramatically different from ETs due to a diverging time period.

Because of alignment, SAPs have zero orientational dispersion at infinite dilution, while rotating particles have a finite root-mean-square (RMS) orientation of  $O(1/\sqrt{T})$  (Brenner, 1974) as shown in figure 1 (e). The average dispersion in figure 1 (e) is evaluated for an orientation distribution set by weak Brownian motion ( $Pe \gg \phi_T^{-3}$ ) (Leal & Hinch, 1971) which is also similar to the distribution obtained due to pairwise interactions. The dispersion value drops sharply for T-rings due to a diverging  $T$  leading to a phase transition to an ordered microstructure at  $A = A^*$  in an infinitely dilute suspension. SAPs have *perfect anisotropy* as they can fully transmit the anisotropy of the particle geometry to the suspension, as shown in the schematic in figure 1 (b). This characteristic of SAPs can be exploited to tune properties such as conductivity of the suspension.

The second order *stresslet-tensor*  $\mathbf{S}_{Hyd}$  which is the symmetric deviatoric part of the first moment of the stresses exerted by the particle on the fluid can be used to obtain the rheology of the suspension. The increase in the suspension viscosity ( $\mu$ ) relative to the fluid viscosity  $\Delta\mu =$

---

<sup>3</sup> The effective aspect ratio  $r_{eff} = \sqrt{(1 + \lambda)/(1 - \lambda)} \approx \sqrt{\Delta\lambda/2}$  defined by (Leal & Hinch, 1971) is approximately equal to  $\phi_T$  when  $\Delta\lambda \ll 1$ . However,  $\phi_T = 0.5\sqrt{1 - \lambda^2} \approx \sqrt{\Delta\lambda/2}$  a measure of an angle is used due to its similarity with  $|\phi_S| \approx \sqrt{-\Delta\lambda/2}$  for SAPs.

$(\mu - \mu_f)/\mu_f$  which quantifies the increase in the stress required to shear a suspension due to the presence of particles, is equal to  $n\langle S_{Hyd} \rangle = n\langle \mathbf{S}_{Hyd} \rangle : \hat{\mathbf{U}}_\infty \hat{\mathbf{F}}_\infty$ . The angular brackets refer to the ensemble average over the steady state orientation distribution of the particles. Using the linearity of the Stokes equations and the imposed shear flow, the hydrodynamic stresslet exerted by the particle on the fluid is given by  $\langle \mathbf{S}_{Hyd} \rangle = \xi_1 \mathbf{E}_\infty + \xi_2 \mathbf{E}_\infty : \langle \mathbf{p} \mathbf{p} \rangle \mathbf{I} + \xi_3 (\mathbf{E}_\infty \cdot \langle \mathbf{p} \mathbf{p} \rangle + \langle \mathbf{p} \mathbf{p} \rangle \cdot \mathbf{E}_\infty) + \xi_4 \mathbf{E}_\infty : \langle \mathbf{p} \mathbf{p} \mathbf{p} \mathbf{p} \rangle$ , where  $\xi_i$  for  $i = \{1,2,3,4\}$  are  $O(\epsilon)$  constants that depend only on the particle geometry, with  $\xi_1 + \xi_3 \sim O\left(\frac{1}{A^2}\right)$ .  $\langle S_{Hyd} \rangle = 0.5(\xi_1 + \xi_3 - \xi_3 \langle \cos^2(\theta) \rangle + 0.5\xi_4 \langle \sin^4(\theta) \sin^2(2\phi) \rangle)$  and has a constant  $O(1/A^2)$  contribution and a variable contribution that depends on the particles orientational dynamics. For SAPs,  $\langle S_{Hyd} \rangle \sim O(\epsilon|\phi_S|^2) + O(1/A^2)$  corresponding to their equilibrium orientation while for rotating particles  $\langle S_{Hyd} \rangle$  has an  $O(\epsilon\phi_T)$  contribution arising mainly from the  $O(\epsilon)$  stresslet during the small  $O(\phi_T)$  duration of the particle's tumbling phase and a much smaller  $O(\epsilon\phi_T^2)$  contribution during its  $O(1)$  aligned state. This implies that the tumbling of high-aspect ratio particles is responsible for most of the stress in suspensions. SAPs therefore can completely utilize the high-aspect feature of the particle by attaining a permanent orientation.

Using the scaling of  $\phi_T$  with  $A$  discussed earlier, while a torus generates an  $O(\sqrt{\epsilon}/A)$  stresslet, a NAP generates an  $O(1/A^2) + O((\Delta A/A)^{0.5}\sqrt{\epsilon}/A)$  stresslet leading to a sharp drop in  $\langle S_{Hyd} \rangle$  near  $A^*$  as shown in figure 1 (f). SAPs have a stresslet value that scales as  $O(C_\alpha \epsilon \Delta A/A^2) + O(1/A^2)$  for  $A \gtrsim A^*$ , and  $O(\epsilon/A)$  for  $A \gg A^*$  as seen in figure 1 (f). The  $O(\epsilon/A)$  scaling of  $\langle S_{Hyd} \rangle$  for SAPs with  $A$  for  $A \gg A^*$  is similar to that of ETs, however the magnitude of the  $\langle S_{Hyd} \rangle$  differs by a factor of  $O(C_\alpha) = O(\ln(8A^*)/A^*)$ . In addition to the shear stresses, the first ( $N_1 = n\langle \mathbf{S}_{Hyd} \rangle : (\hat{\mathbf{U}}_\infty \hat{\mathbf{U}}_\infty - \hat{\mathbf{F}}_\infty \hat{\mathbf{F}}_\infty)$ ) and second ( $N_2 = n\langle \mathbf{S}_{Hyd} \rangle : (\hat{\mathbf{F}}_\infty \hat{\mathbf{F}}_\infty - \hat{\Omega}_\infty \hat{\Omega}_\infty)$ ) normal stress differences, which are zero for tumbling particles due to Stokes flow reversibility, are finite for a SAP, as seen in figure 1 (g). In most purely hydrodynamic Stokes suspensions, including dilute suspension of ETs, the microstructure is symmetric about the  $\hat{\mathbf{F}}_\infty - \hat{\Omega}_\infty$  plane and remains invariant upon reversal of shear due to Stokes flow reversibility. Alignment breaks this symmetry and the stable and unstable fixed points exchange identities upon shear reversal. An infinitesimal disturbance is then sufficient to break Stokes flow reversibility, leading to non-zero  $N_1$  and  $N_2$ . The  $O(\epsilon|\phi_S|)$  force per unit length is restricted to the plane of the ring and directed towards its

center of mass. Since the plane of the ring is aligned near the flow-vorticity plane, the moment of the force along  $\hat{\Gamma}_\infty$  is smaller than  $\hat{U}_\infty$  and  $\hat{\Omega}_\infty$ , making  $N_1 \approx 7\epsilon|\phi_S|/16 > 0$  and  $N_2 \approx -\epsilon|\phi_S|/16 < 0$ .

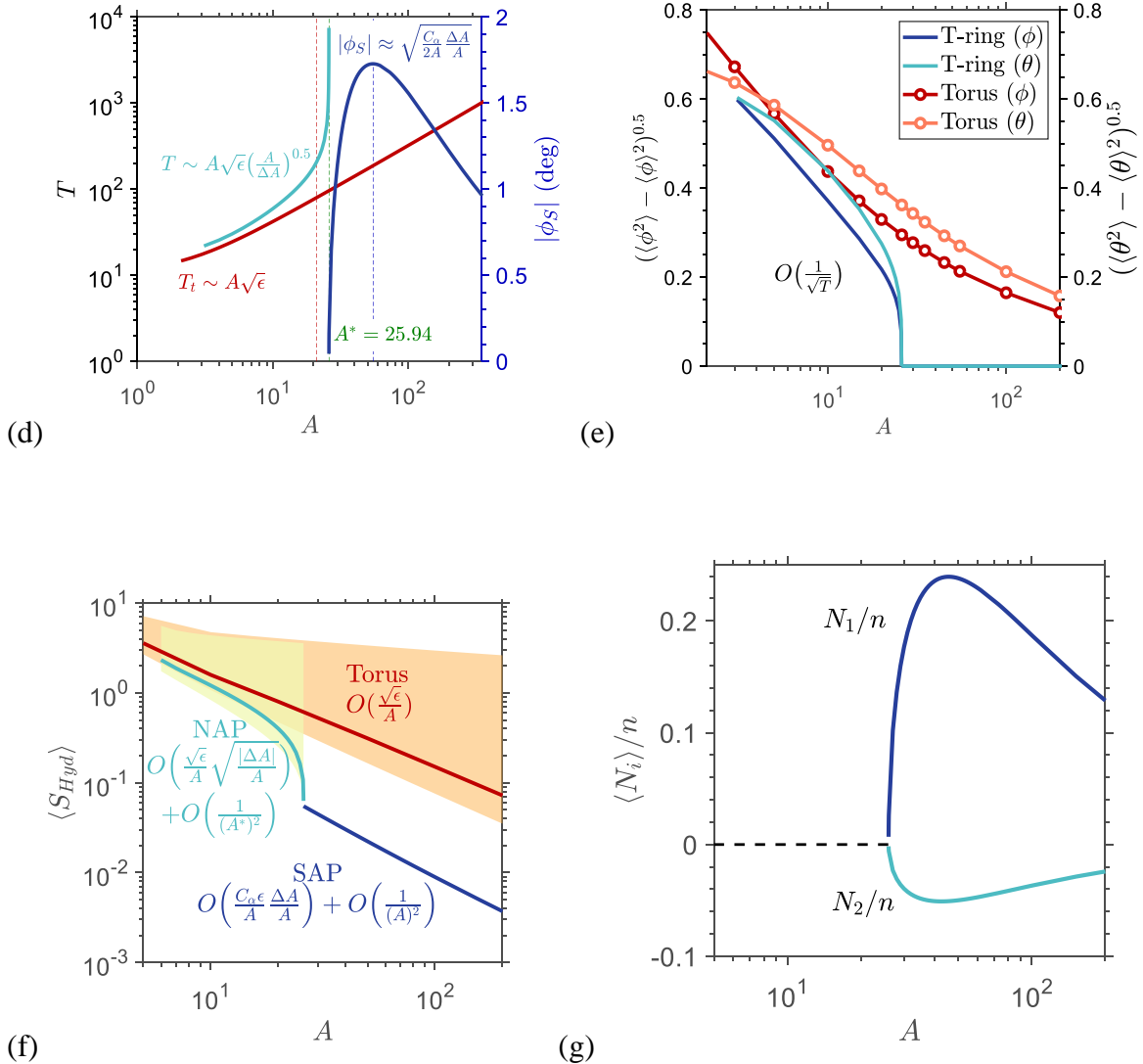


Figure 1 (d) Time period of rotation,  $T$ , and  $T_t$ , of NAPs and ETs respectively and the aligning angle  $|\phi_S|$ ; (e) orientational dispersion of the azimuthal ( $\phi$ ) and polar angles ( $\theta$ ) (f)  $\langle S_{Hyd} \rangle$ ; and (g)  $\{N_1, N_2\}$  as a function of  $A$  for T-rings and equivalent tori obtained from slender-body-theory (Borker & Koch) using both the force and dipole per-unit-length. Scaling laws are derived in the

SBT framework. The normal stress-differences peak at the aspect ratio for which  $|\phi_S|$  is the highest. The dotted lines in (d) correspond to  $A = 21, 26$  and  $55$ . The SBT values have a maximum error of 5% when validated with respect to BEM results. The SBT values are used instead of BEM results to be consistent with the  $O(n^2)$  rheology results obtained using pairwise calculations discussed later in the paper.

The flow-alignment of SAPs imparts unconventional rheological properties to the suspension. A SAP has an unstable node ( $\mathbf{p}_{U,I}$ ) in close proximity at an angular separation of  $2|\phi_S|$  from the stable or equilibrium orientation ( $\mathbf{p}_{S,I}$ ) as shown in figure 1 (c). This suggests the possibility that small disturbances such as those due to hydrodynamic interactions or Brownian motion could rotate the particle towards the unstable node leading to a tumble. This leads to some fundamental questions of practical importance. How robust is the self-aligning behavior under secondary effects? What is the critical shear rate required to flow align a Brownian ring? What is the change in the orientational order of SAPs due to secondary effects of Brownian motion or pairwise interactions? What happens in a suspension with a mixture of SAPs and tumbling particles? How does a bounding wall influence motion of self-aligning particles? These questions are addressed in the remainder of the text.

The randomizing effects of rotary Brownian motion compete with the flow-aligning effect of the shear flow. This competition is characterized by the Peclet number  $Pe = \gamma/D_r$ , where  $D_r$  is the rotary diffusivity of the particle. Effects of Brownian motion are assessed using rotary Brownian Dynamics simulations ( (Gabdoulline, 1998) and S.1) and the scaling laws are obtained at high  $Pe$  ( $Pe \gg \phi_T^{-3}$  and  $Pe \gg |\phi_S|^{-3}$  for tumbling and aligning particles respectively) from a semi-analytical solution of the Fokker-Plank equation in orientational space (Brenner, 1974). A SAP with  $A = 55$ , which has the maximum separation between the stable and unstable nodes (i.e.  $2|\phi_S|$ ) among a family of T-rings, is used demonstrate the difference in the shear rheology of SAPs and ETs. A measure of dispersion of the ring orientation away from the flow-vorticity plane is the flow-alignment parameter,  $k = 1.5 \left( 1 - \left\langle (\mathbf{p} \cdot \hat{\mathbf{l}}_\infty)^2 \right\rangle \right)$ , whose value is 0 when the ring is perfectly aligned in the flow vorticity plane and 1 for a perfectly isotropic suspension. The effects of the self-aligning behavior have little impact for  $Pe < 10^3$  as seen from the indistinguishable values of  $k$  for a SAP and an ET in figure 2 (a). For  $Pe \geq 10^3$   $k$  for a SAP sharply deviates from the

value for an ET suggesting this is a flow-regime in which self-alignment would create suspensions with near perfect anisotropy. The flow-alignment parameter,  $k \propto Pe^{-1}$  for  $Pe \gg |\phi_S|^{-1}$ , settling at a values of  $1.5|\phi_S|^2$  at  $Pe \gtrsim O(|\phi_S|^{-3})$  for SAPs while  $k \propto Pe^{-1/3}$  for  $1 \ll Pe \ll \phi_T^{-3}$ , settling at  $k \approx 3.63\phi_T$  at  $Pe \gg \phi_T^{-3}$  (Brenner, 1974) as shown in figure 2 (a). Using the aspect ratio dependence of  $|\phi_S|$  and  $\phi_T$  the ratio of  $k$  for SAPs and ETs is  $O(\Delta A \sqrt{\epsilon}/A^2) + O(\sqrt{\epsilon}/A)$  for  $\Delta A \ll A^*$  and  $O(\sqrt{\epsilon})$  for  $A \gg A^*$  demonstrating the difference in the degree of flow-alignment of SAPs and ETs in the high-shear flow regime. The special case of T-rings with  $A = A^*$  have  $k \propto Pe^{-1/3}$  for  $Pe \gg 1$  (figure S X) and this power law behavior gives greater control in tuning the orientation order of the suspension through change in the shear rate than SAPs at other aspect ratios. In summary, SAPs can robustly retain their flow-alignment above a critical  $Pe_C = |\phi_S|^{-3}$  and achieve a greater degree of alignment than ETs. In dimensional terms, a self-aligning ring with a  $1\mu m$  radius with  $A = 55$  requires a shear rate of at least  $47 s^{-1}$  for retaining alignment in a viscous fluid like glycerin ( $\mu \approx 1 \text{ Pa s}$ ).

Brownian motion alters the hydrodynamic stresslet,  $\langle S_{Hyd} \rangle$ , by changing the steady state orientation distribution and also has a more direct contribution to the rheology through a Brownian stresslet,  $\langle S_{Brow} \rangle = 3\lambda D_r M_r^{-1} (\langle \mathbf{p}\mathbf{p} \rangle - \mathbf{I}/3)$ , arising from the angular velocity associated with the diffusion process across the gradient in the orientational probability. Here  $M_r$  is the rotary mobility of the axisymmetric particle (Brenner, 1974). The increase in the suspension viscosity due to Brownian particles is  $\Delta\mu = n(\langle S_{Hyd} \rangle + \langle S_{Brow} \rangle)$ , where  $\langle S_{Brow} \rangle = \langle S_{Brow} \rangle : \hat{\mathbf{U}}_\infty \hat{\mathbf{\Gamma}}_\infty$ . The effect of self-alignment on  $\langle S_{Hyd} \rangle$  and  $\langle S_{Brow} \rangle$  is negligible at  $Pe \ll |\phi_S|^{-3}$ , similar to its effect on  $k$ , because Brownian motion is sufficiently strong to overcome the flow-induced angular velocity differences that lead to self-alignment.  $\langle S_{Brow} \rangle$  is  $O(Pe^{-1})$  for  $Pe \gg 1$  and therefore has a negligible contribution for shear dominated flows as shown in figure 2 (b). Figure 2 (b) suggests that the total stresslet for a SAP suspension, or equivalently the intrinsic suspension viscosity, can be changed from an  $O(\epsilon)$  value in the low-shear regime to an  $O(\epsilon|\phi_S|^2) = O(C_\alpha \epsilon \Delta A / A^2) + O(1/A^2)$  for  $A \gtrsim A^*$  in the high-shear regime. The  $O(\epsilon|\phi_S|^2)$  high- $Pe$  net-stresslet for a SAP is also much smaller than the  $O(\epsilon\phi_T)$  value for an ET, being almost a factor of  $10^{-1}$  smaller at  $A =$

55. Additionally, SAPs have access to a larger range of values of  $k$  and  $\langle S_{Hyd} \rangle$  compared to ETs. Brownian motion induces normal stress differences because collisions with fluid molecules which are irreversible in nature. The normal stress differences of SAPs are larger than those for ETs, but the difference is most evident only for  $Pe \gtrsim |\phi_S|^{-3}$ , where SAPs have a finite value in contrast with the zero value of ETs as seen in figure 2 (c). At such Peclet numbers, the SAP remains near its equilibrium orientation, thereby retaining the asymmetry about the flow-vorticity plane that ensures finite normal stress differences. Particles with larger  $|\phi_S|$  values would have larger high-Pe normal stress difference plateaus. However, this finite value is much smaller than the  $O(\epsilon)$  normal stress differences in the weak shear ( $Pe \rightarrow 0$ ) regime.

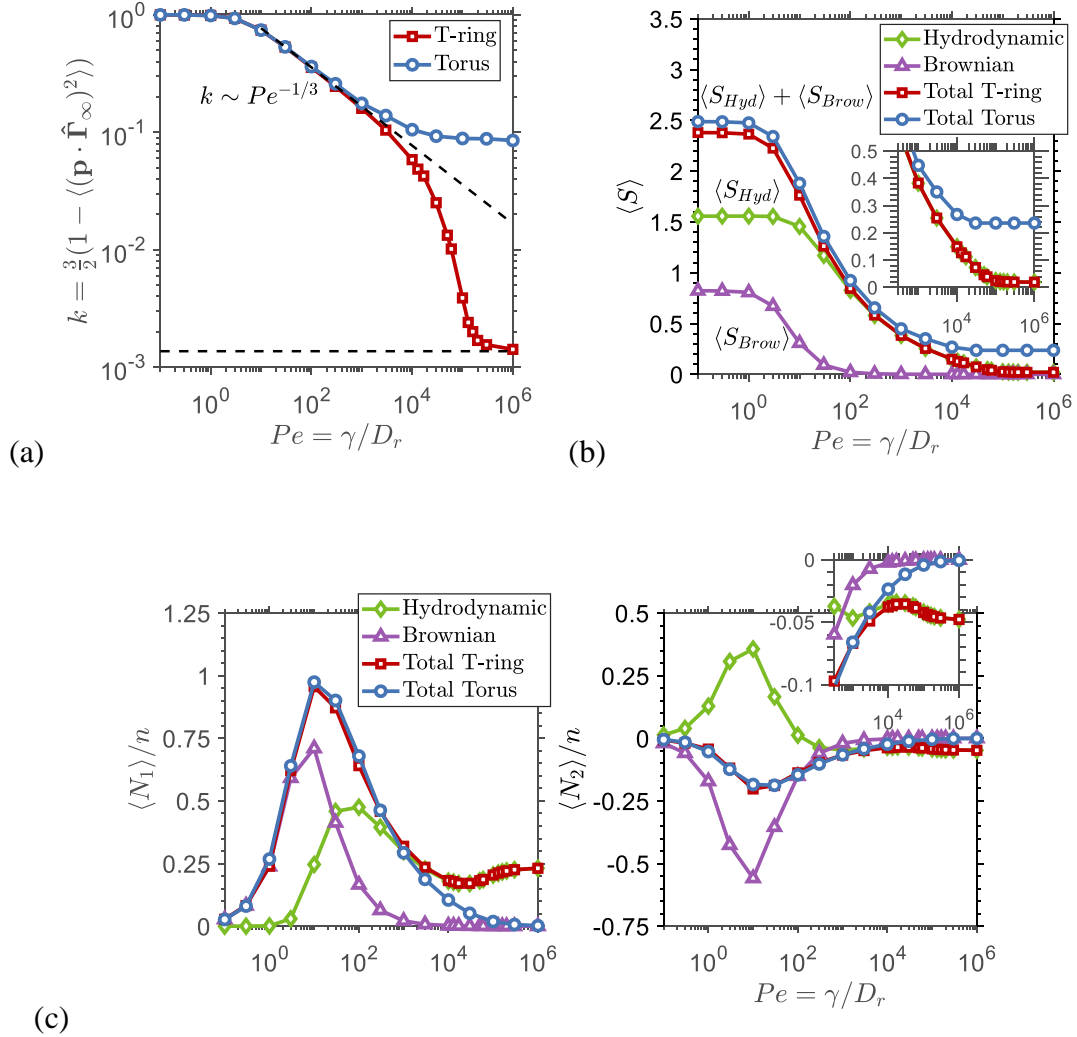


Figure 2 Effect of Brownian motion on SAPs. (a) Orientational order parameter,  $k = 1.5 \left(1 - \langle (\mathbf{p} \cdot \hat{\mathbf{r}}_\infty)^2 \rangle\right)$ ; (b) Hydrodynamic  $\langle S_{Hyd} \rangle$  and Brownian stresslet  $\langle S_{Brow} \rangle$ ; and (c) First ( $N_1$ ) and second ( $N_2$ ) normal stress differences as a function of  $Pe$  for a SAP with  $A = 55$  and  $\phi_S = -0.03$  and an ET with  $\phi_T = 0.034$ .

The equilibrium orientation of SAPs can also be disturbed by pairwise interactions (PIs) between particles. PIs give the  $O(n^2)$  corrections to  $\Delta\mu$  and the normal stress differences thereby changing the rheology of suspensions of SAPs from those presented in figure 1. PIs are simulated using slender body theory (SBT) for hydrodynamic interactions (HIs) and a short-range repulsive force to model solid-body collisions as detailed in Chapter 4 and appendix (S 2). In the SBT formulation, the force-per-unit circumference is obtained by computing the velocity disturbance created by a neighboring ring using the Green's function convoluted with the leading order force per unit length acting on a force-and-torque free ring in an unbounded SSF. Here, we only discuss pairwise interactions of non-Brownian rings and the results should hold true when the  $O(n^{-1})$  relaxation time for the orientation distribution set by PIs is much smaller than the  $O(Pe|\phi_S|^2)$  relaxation time of Brownian motion (i.e.,  $((Pe|\phi_S|)^{-2} \ll n)$ .

The most important interactions are the ones where the particles are separated by an  $O(1)$  distance in the gradient direction and therefore interact for an  $O(1)$  time (Rahnama, et al., 1993). The physical processes governing the orientational dispersion and rheology due to PIs are different for SAPs and ETs. In a suspension of tumblers, the most important interactions are solid-body collisions between a tumbling particle and a temporarily aligned particle changing  $\mathbf{p}$  by  $O(1)$  (Chapter 4). On the contrary, hydrodynamic interactions rather than collisions are the dominant mechanism driving dispersion of SAP orientation from its equilibrium value. Solid-body collisions of SAPs occurs with a frequency of  $O(\phi_S^2)$  and each collision changes  $\mathbf{p}$  by  $O(|\phi_S|)$  leading to an RMS change in  $\mathbf{p}$  of  $O(\phi_S^2)$  which is much smaller than the corresponding  $O(\epsilon|\phi_S|)$  value due to HIs. Therefore, the RMS change in  $\mathbf{p}$  of a SAP in a dilute sea of other SAPs is  $O(\epsilon|\phi_S|)$  and this value is smaller than the  $2|\phi_S|$  angular separation between the stable and the unstable nodes of the particle. This scaling argument suggesting SAPs rarely tumble due to pairwise interactions is confirmed from the PI simulations. Figure 3 (a) shows the orientational dispersion of the polar  $(\langle \theta^2 \rangle - \langle \theta \rangle^2)/n$  and the azimuthal  $(\langle \phi^2 \rangle - \langle \phi \rangle^2)/n$  angles as a function of  $A$  for T-rings.

Additionally, the mean azimuthal angle  $\langle \phi \rangle$  due to pairwise interactions is smaller than its equilibrium  $-|\phi_S|$  (i.e.  $\langle \phi \rangle < -|\phi_S|$ ) indicating that HIs push  $\mathbf{p}$  away from the unstable node. This is remarkable, because not only is the HI weak but it also seems to make the particle less prone to tumbling by pushing it away from the unstable nodes. The dilute theory predicting the orientational distribution of hydrodynamically interacting high-aspect fibers works well even when the number density  $n \sim O(1)$  (Rahnama, et al., 1995). This suggests that the results in figure 3 (a) should hold true even when  $n \sim O(1)$  which corresponds to a concentrated regime. Even for  $n = 1$ , the value of the orientational dispersion of  $\phi$  and  $\theta$  is still small compared to the corresponding values for ETs (shown in figure S 2) implying the retention of the near *perfect anisotropy* of the suspension as shown in the schematic in figure 1 (a). The small dispersion also means that particle aggregation should be drastically reduced in comparison to ETs important in maintaining homogeneity within the suspension.

PIs lead to translational as well as orientational dispersion of suspended particles. The translational hydrodynamic diffusivities of SAPs in the gradient ( $D_{33}$ ) and the vorticity ( $D_{22}$ ) directions are shown in figure 3 (b). SAPs have much smaller values of  $D_{22}$  and  $D_{33}$  compared to ETs because SAPs have weak hydrodynamic interactions while ETs have much stronger interactions due to collisions. A stream of SAPs can be injected locally in a channel and the small diffusivity would ensure that these particles remain within a narrow stream due to small translational diffusivities. This has applications in manufacturing composites with particles embedded in a small portion of the material. The diffusivity for rotating particles can be computed from the square of  $O(1)$  displacement due to collisions multiplied with the  $O(\phi_T)$  collision frequency. This leads to a sharper decrease in the diffusivity values for a NAP compared to an ET.

PIs can also change suspension viscosity and the relative increase in the suspension viscosity with the  $O(n^2)$  corrections can be expressed as

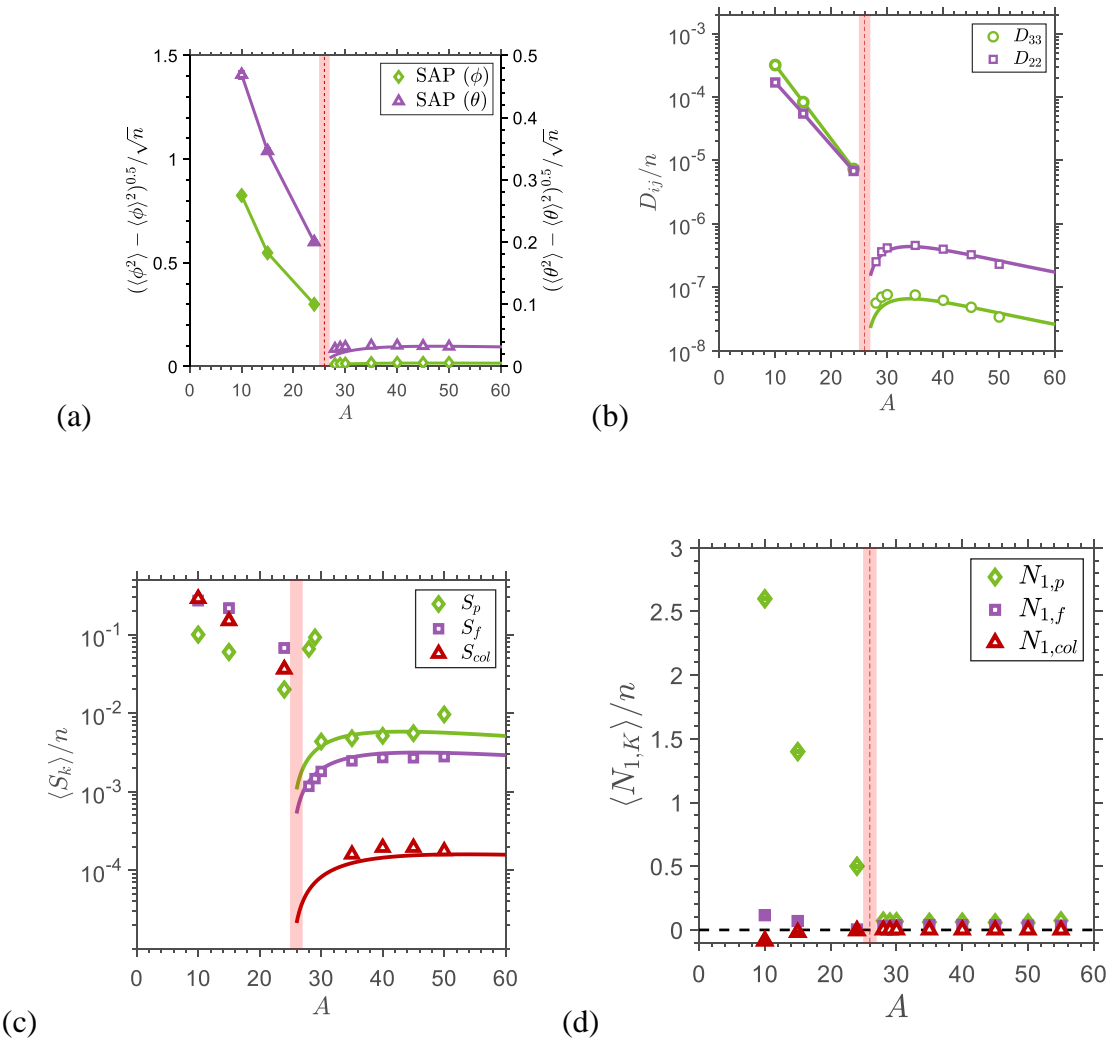
$$\Delta\mu = \frac{\mu - \mu_f}{\mu_f} = n \left[ \langle S_{Hyd} \rangle + n \left( \frac{\langle S_{PI} \rangle}{n} \right) \right], \quad (2)$$

where  $\langle S_{PI} \rangle$  is the stresslet induced by pairwise interactions which is proportional to  $n$ .  $\langle S_{PI} \rangle$  is comprised of three components, one driven by a transient change in  $S_{Hyd}$  through change in the

particle orientation ( $\langle S_p \rangle$ ), another induced from the change in the force per unit length associated with the fluid velocity disturbance created by neighboring particles ( $\langle S_f \rangle$ ) and a third associated with collisional forces ( $\langle S_{col} \rangle$ ) (See appendix S2 for mathematical definitions). The  $O(\epsilon^2 |\phi_S|^2)$  scaling for  $\langle S_p \rangle$  arises from the PI-induced change in the value of the term,  $\xi_4 \langle \sin^4(\theta) \sin^2(2\phi) \rangle$ , in  $\langle S_{Hyd} \rangle$  relative to its equilibrium value of  $4\xi_4 |\phi_S|^2$ . The force-per-unit length induced by a second SAP is proportional to the  $O(\epsilon |\phi_S|)$  velocity disturbance of the second particle and the slender parameter  $\epsilon$  (Borker & Koch, in press), suggesting an  $O(\epsilon^2 |\phi_S|)$  scaling of  $\langle S_f \rangle$ .  $\langle S_{col} \rangle / n$ , should scale with the product of the  $O(\phi_S)$  relative particle velocity, the  $O(\phi_S)$  collision cross-sectional area and the  $O(\epsilon |\phi_S|)$  collision force, and is  $O(\epsilon |\phi_S|^3)$  (Singh, et al., 2011). The collisional contribution in a suspension of SAP is negligible while the other two components are of similar magnitude as shown in figure 3 (c). Additionally, the first and second normal stress differences also deviate from their equilibrium values as shown in figures 3 (d) and (e) following the same scaling arguments discussed for the shear stress. Pairwise interactions lead to a mean change in the particle's orientation away from the unstable node thereby making increasing the magnitudes of both normal stress-differences. For tumblers, the much stronger collisional interactions make the scaling proportional to the  $O(\phi_T)$  collisional frequency. This leads to the sharp drop in  $\langle S_{PI} \rangle$  and the normal stress differences near the critical aspect ratio for  $A < A^*$ . The slight dip near  $A > A^*$  with  $\Delta A \sim O(1)$  is potentially associated with the decrease in strength of the interaction as  $A \rightarrow A^{*+}$  and the decrease in separation between the stable and the unstable points.

Figure 3 (f) shows the variation of  $\Delta\mu$  with the number density  $n$  for an  $A = 40$  SAP,  $A = 21$  torus and an  $A = 40$  equivalent torus.  $\Delta\mu$  for SAPs is much smaller than the equivalent torus.  $\Delta\mu$  has two contributions, the  $O(n)$  contribution which is set by the steady state orbit distribution and an  $O(n^2)$  contribution driven by pairwise interactions. The coefficient of the  $O(n)$  and  $O(n^2)$  terms in  $\Delta\mu$  have similar values for SAPs. The  $O(n^2)$  coefficient of SAPs is smaller than ETs by a factor of about 1/10. Furthermore, the PI calculation for SAPs should accurately describe the rheology of a suspension until  $n \sim O(1)$ . On the contrary in a suspension of tumblers there are much stronger collisional interactions between multiple particles when  $n \sim O(1)$ , which corresponds to a concentrated regime for rings. In this regime,  $\Delta\mu$  should be much greater than the value predicted by our simulations and therefore a much larger separation between the values of  $\Delta\mu$  for SAPs and

ETs. At  $n = 1$  the viscosity of the SAP increases by barely 2% while that of a suspension of ETs is at least twice the fluid viscosity. Thus, flowing a suspension of SAP is significantly easier than a suspension of tumblers and this effect is enhanced with increasing particle number densities.



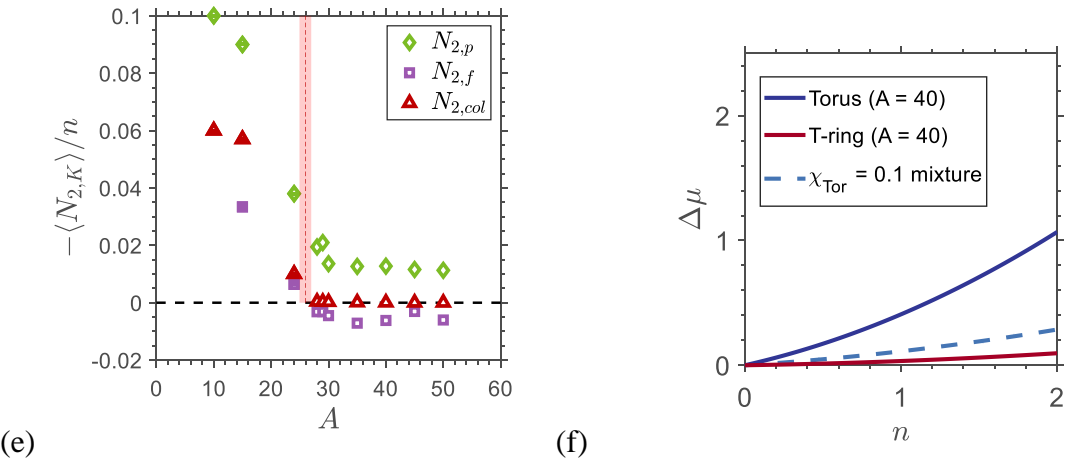


Figure 3 :Figure\_rheology Effect of pairwise interactions on the orientational order and rheology of SAPs.: (a) Root mean square orientational displacement, (b) Hydrodynamic translational diffusivity, (c) stresslet contributions ( $\langle S_p \rangle, \langle S_f \rangle, \langle S_{col} \rangle, \langle S_{PI} \rangle$ ), (d) first ( $\langle N_1 \rangle$ ) and (e) second ( $\langle N_2 \rangle$ )normal stress difference for a suspension of self-aligning rings, rotating T-rings and tori as functions of particle aspect ratio,  $A$ . (f)  $\Delta\mu$  as a function of  $n$  for a suspension of  $A = 40$  T-rings, tori and a mixture of T-rings and tori with the torus particle fraction  $\chi_{Tor} = 0.1$ .

The difference in magnitudes of  $\Delta\mu$ ,  $D_{ij}$  and orientational dispersion between SAPs and ETs can be utilized to passively tune the suspension properties by inserting a small fraction ( $\chi$ ) of tumbling particles in a suspension of SAPs. When  $\chi \ll 1$ , the relative increase in the viscosity for the mixture can be expressed as  $(\Delta\mu)_{mix} \approx n \left[ \langle S_{Hyd} \rangle_{SAP} (1 - \chi) + \langle S_{Hyd} \rangle_{ET} \chi + n \left( (1 - \chi)^2 \frac{\langle S_{PI} \rangle_{SAP-SAP}}{n} + \chi(1 - \chi) \frac{\langle S_{PI} \rangle_{SAP-ET}}{n} + \chi^2 \frac{\langle S_{PI} \rangle_{ET-ET}}{n} \right) \right]$ , where the subscripts correspond to the values obtained for a single SAP; a single ET; the interactions of two SAPs, a SAP and an ET, and two ETs respectively. Figure 3 (f) shows  $(\Delta\mu)_{mix}$  for a suspension of  $A = 40$  SAPs with small amount of tori ( $\chi = 0.1$ ).

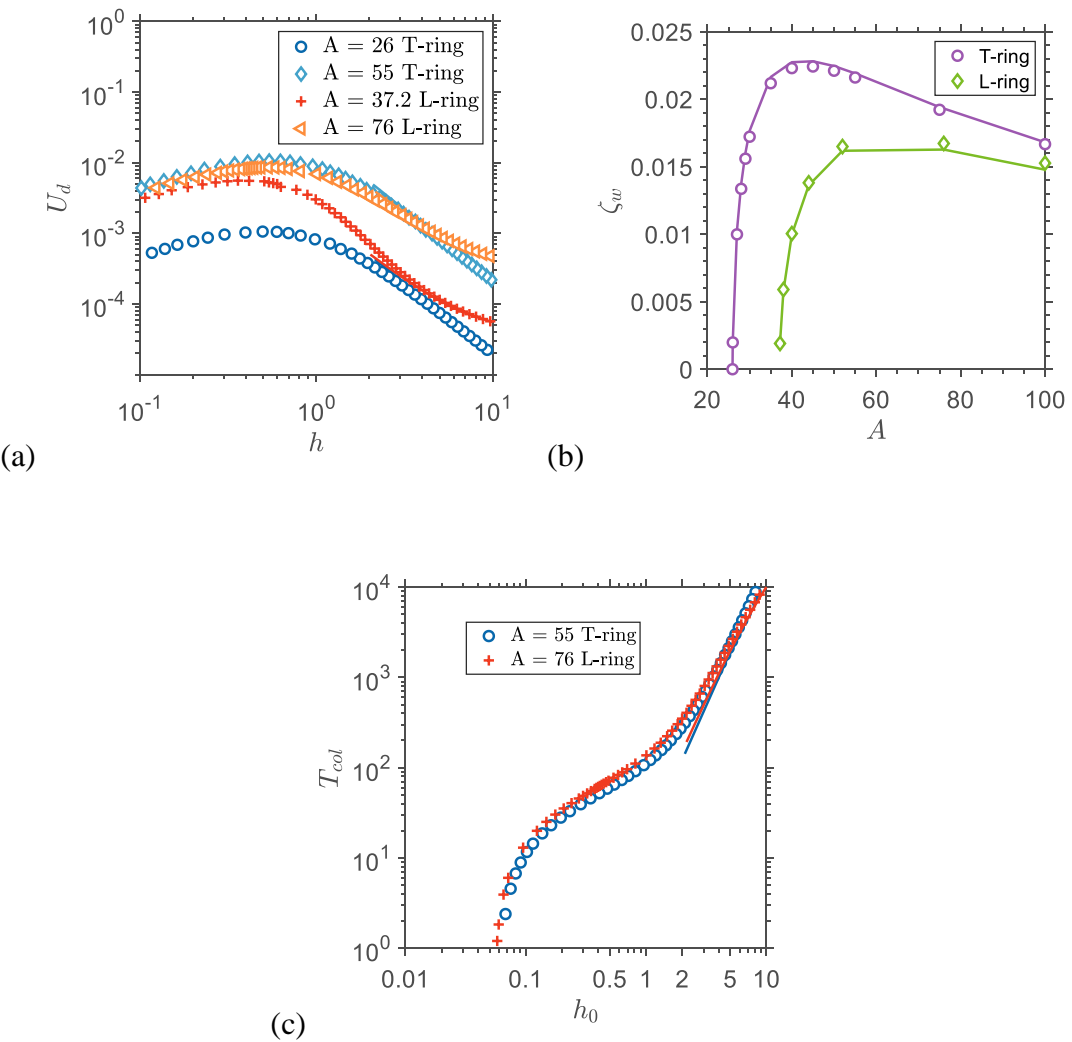


Figure 4 SAP-wall interactions: (a) Drift velocity of the particle versus distance from the wall  $h$  using simulation (symbols) and  $U_d + \zeta_w/h^2$  (line). (b)  $\zeta_w$  as a function of aspect ratio  $A$  where the symbols are obtained by fitting the simulated  $h(t)$  with the solution of  $-dh/dt = U_d + \zeta_w/h^2$  and lines corresponds to an approximate dipole solution using SBT (see section S3). (c)  $T_{col}$ , the time required for the particle to collide with the wall, vs the initial distance from the wall  $h_0$ .

In material processing flows or rheometers, particles often encounter bounding walls. To study, the resulting dynamics, the center of mass (COM) of a ring is placed at an initial separation  $h_0 \gg 1$  away from the wall. A tumbling ring performs time-periodic translation associated with the periodic change in its orientation without a net change in its COM position in the gradient direction,  $h$  (Yang & Leal, 1984). In stark contrast, a SAP steadily migrates towards the wall by

virtue of its equilibrium orientation. This migration is captured by computing the velocity disturbance created by placing image singularities (Blake & Chwang, 1974) along the centerline of an image ring, based on the force-per-unit length,  $f_{SSF}$ , in an unbounded SSF. The velocity disturbance created by the image-ring is similar to a point force dipole when  $h \gg 1$  because the original ring is force-and-torque-free. Therefore, the wall induces a migration velocity in the negative gradient direction which scales as  $h^{-2}$ . The separation from the wall thus approximately satisfies  $-dh/dt = U_d + \zeta_w/h^2$ , where the first and second terms are the drift velocities induced by particle asymmetry and the wall respectively.  $\zeta_w \sim O(\epsilon|\phi_S|)$  quantifies the strength of the dipole and is obtained analytically as shown in figure 4 (b) using the velocity disturbance created by the image ring in the limit for  $h \gg 1$  (S 7). The solution to the simple ordinary differential equation predicts the particle's drift velocity accurately for  $h \gtrsim 2$  as shown in figure 4 (a) for both T and L rings. An L-ring is a fore-aft asymmetric ring obtained by slicing the T-ring shape in figure 1 (a) in half. L-rings have an inherent drift in the gradient direction due to lack of mirror-symemtry about a plane normal to  $\mathbf{p}$ . The model assumes that  $\mathbf{p} = \mathbf{p}_s$  which is found to be true in the simulations until  $h < 1$ . T-rings were found to drift faster than L-rings for  $h \sim O(1)$  due to a larger value of  $|\phi_S|$  and a stronger wall interaction, but L-rings take a lesser time to approach the wall if  $h_0 \gg 1$ . SAPs should accumulate near the wall at distance  $h$  satisfying  $(1/A) \ll h < 1$ , thereby forming a thin concentrated layer whose structure will depend on the details of the particle geometry, Brownian motion, HI with other particles and surface forces, in addition to the hydrodynamic forces. The simplified model can be used to engineer systematic particle deposition on the wall which has potential applications in imparting tunable optical and scratch resistance properties to the surfaces (Isla, et al., 2003). The model also suggests  $h \rightarrow 0$  in a time equal to  $3(h_0^3)/\zeta_w$  for T-rings and  $U_d^{-1}\tilde{h}((h_0)\tilde{h}^{-1} - \tan(h_0\tilde{h}^{-1}))$  for L-rings, where  $\tilde{h} = (\zeta_w/U_d)^{0.5}$  is the height at which the wall induced drift velocity equals  $U_d$  as shown in figure 4 (g).

In conclusion, our work demonstrates a new class of particle suspensions that have a much smaller effective viscosities, hydrodynamic diffusivities and orientation dispersion in comparison to suspensions of tumbling particles. Such suspensions also pave the way for passively tuning rheological properties using the geometry of individual particles. Discs are known to strongly align near the flow vorticity plane for  $n \sim O(1)$  under shear due to excluded volume interactions (Meng & Higdon, 2008). The excluded volume of a rings is only about 15% smaller than that of a

circumscribing disc (Wensink & Avendaño, 2016). Furthermore, rings are known to transition to a smectic liquid crystal phase at  $n \approx 0.8$  for  $A \approx 17$  (Carlos Avendaño, 2016). These findings suggest that self-aligning rings should retain orientational order for almost all values of  $n$  and high shear rates unlike fiber or disc suspensions, offering a unique route to synthesizing materials with tunable properties using existing processing flow technologies. Our work should motivate researchers to experimentally observe this new and exciting regime of flowing suspensions whose properties will be distinct from their tumbling counterparts, thereby opening new avenues in material synthesis. T-rings and L-rings with feature sizes of a few microns could be fabricated using photolithography (Foulds & Parameswaran., 2006). A Coutte cell with a gap of at least 5 particle diameters is sufficient to ignore wall effects and observe alignment for a time that is at least 10 times the rotational period of an equivalent torus. Finally, the large holes in rings lead to a very small maximum packing fractions which can therefore be used to make highly porous materials. Such porous materials have applications in storage of hydrogen or  $CO_2$ .

## 1. Appendix

### 1.1 Brownian Dynamics simulation for rotational diffusion of axisymmetric particles

Rotary Brownian Dynamics (BD) simulations of an axisymmetric particle with a rotary diffusivity  $D_r$  is carried out using the procedure outlined in Gabdoulline & Wade (Gabdoulline, 1998). The rotational displacement at each Brownian time step  $\Delta t$  is given by

$$\mathbf{p}(t + \Delta t) - \mathbf{p}(t) = \int_t^{t + \Delta t} dt' \left[ \dot{\mathbf{p}}_J(t') + \frac{\Delta \mathbf{p}_B(t)}{\Delta t} \right] \quad (S\ 1.1)$$

where the rotation rate induced by the simple shear flow is  $\dot{\mathbf{p}}_J = \boldsymbol{\omega}_\infty + \lambda(\mathbf{E}_\infty - \mathbf{E}_\infty : \mathbf{p}\mathbf{p})$ ,  $\boldsymbol{\omega}_\infty$  being the vorticity and  $\mathbf{E}_\infty = 0.5(\nabla \mathbf{u}_\infty + (\nabla \mathbf{u}_\infty)^T)$  being the strain rate. The Brownian displacement  $\Delta \mathbf{p}_B$  is such that  $\langle \Delta \mathbf{p}_B \rangle = 0$ ,  $\langle \Delta \mathbf{p}_B \Delta \mathbf{p}_B \rangle = (2D_r \Delta t)^{0.5}(\mathbf{I} - \mathbf{p}\mathbf{p})$ . Solving equation (S1.1) is equivalent to solving the Fokker-Planck equation for the orientation probability distribution  $P(\mathbf{p})$  ((Gabdoulline, 1998), (Kim & Karilla, 1991)). The quantity  $P(\mathbf{p})d\mathbf{p}$  gives the

fraction of systems in the differential region  $d\mathbf{p}$  around  $\mathbf{p}$  and is used to obtain the ensemble average of any quantity of interest  $X$  which is given by

$$\langle X \rangle = \int d\mathbf{p} P(\mathbf{p})X. \quad (S 1.2)$$

A Runge-Kutta method with adaptive time stepping is used to solve equation (S 1.1). The Brownian time-step  $\Delta t$  should be much smaller than the inverse of the non-dimensional rotary diffusivity  $D_r$  at low  $Pe$  and much smaller than the inverse of the shear rate at high  $Pe$ . Additionally, the angular step  $\sqrt{2\Delta t D_r}$  should be much smaller than unity at low  $Pe$  and much smaller than measure of the angle subtended by the particle at high  $Pe$ , which is  $|\phi_s|$  for SAPs and  $\phi_T$  for rotating particles. These conditions are enforced by choosing  $\Delta t = 0.1$  for  $Pe = 1/D_r \geq 1$  and  $\Delta t = 10^{-2}Pe$  for  $Pe < 1$ . The steady state orientation distribution is attained in an  $O(Pe)$  time for  $Pe \ll 1$  and an  $O(Pe \phi_T^2)$  or  $O(Pe |\phi_s|)$  time for  $Pe \gg 1$  (Hinch & Leal, 1973). Therefore, the simulation was terminated after a time  $10^3Pe$  for  $Pe \leq 1$ ; and  $10^3Pe \phi_T^2$  for tumbling particles and  $Pe \phi_S^2$  for SAPs for  $Pe \geq 1$ . For the special case of  $|\phi_s| = 0$  a steady state orientation distribution was reached in a time of  $0.1Pe$ .

The BD simulation is additionally verified by confirming the convergence to the asymptotic limits as  $Pe \rightarrow 0$  and  $Pe \gg \phi_T^{-3}$  for tumbling particles or  $Pe \gg |\phi_s|^{-3}$  for aligning particles. For the low  $Pe$  limit the moments  $\mathbf{p}$  obtained from the solution to the Fokker-Planck equation for  $P(\mathbf{p})$  yields

$$\langle \mathbf{p}\mathbf{p} \rangle = \frac{1}{3}\mathbf{I} - \frac{1}{15}\frac{\mathbf{E}_\infty}{D_r} + O(Pe^2),$$

$$\langle p_i p_j p_k p_l \rangle = \frac{1}{15} (\delta_{ij}\delta_{kl} + \delta_{ik}\delta_{jl} + \delta_{il}\delta_{jk}) + O(Pe), \quad (S 1.3)$$

(Kim & Karilla, 1991; Brenner, 1974). The BD simulation results are within 3% from the values in equation (S 1.3) for  $Pe < 0.1$ . On the other hand, for the high  $Pe$  limit, the orientation

distribution for tumbling particles ( $Pe \gg \phi_T^{-3}$ ) matches the distribution of Leal and Hinch (Leal & Hinch, 1971) and the orientation distribution in the  $\phi$  direction for aligning particles ( $Pe \gg |\phi_s|^{-3}$ ) is matched with Brenner's result (Brenner, 1974) as shown in figures S1 (a) and (b). The moments of  $\mathbf{p}$  obtained from the BD simulations match the asymptotic values with a maximum error of 1% for  $Pe \gtrsim |\phi_s|^{-3}$  or  $Pe \gtrsim 10 \phi_T^{-3}$ .

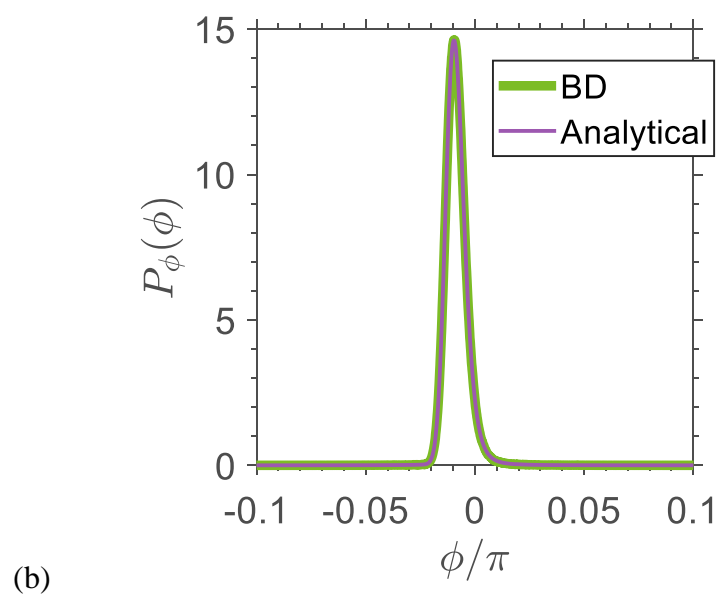
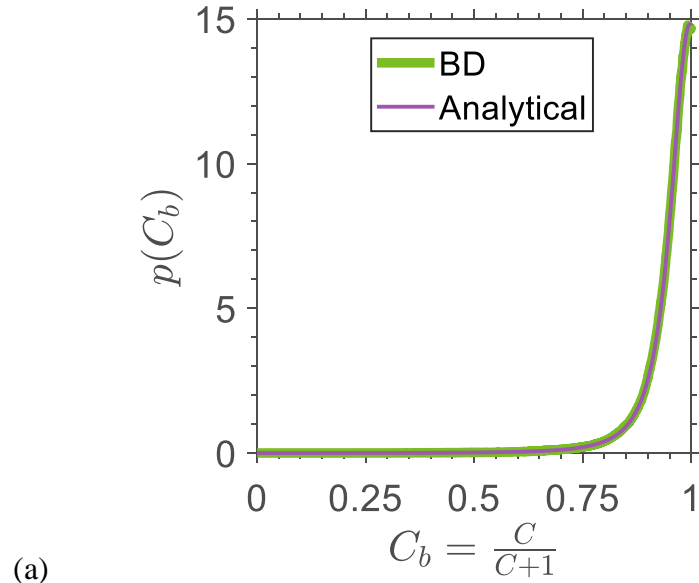
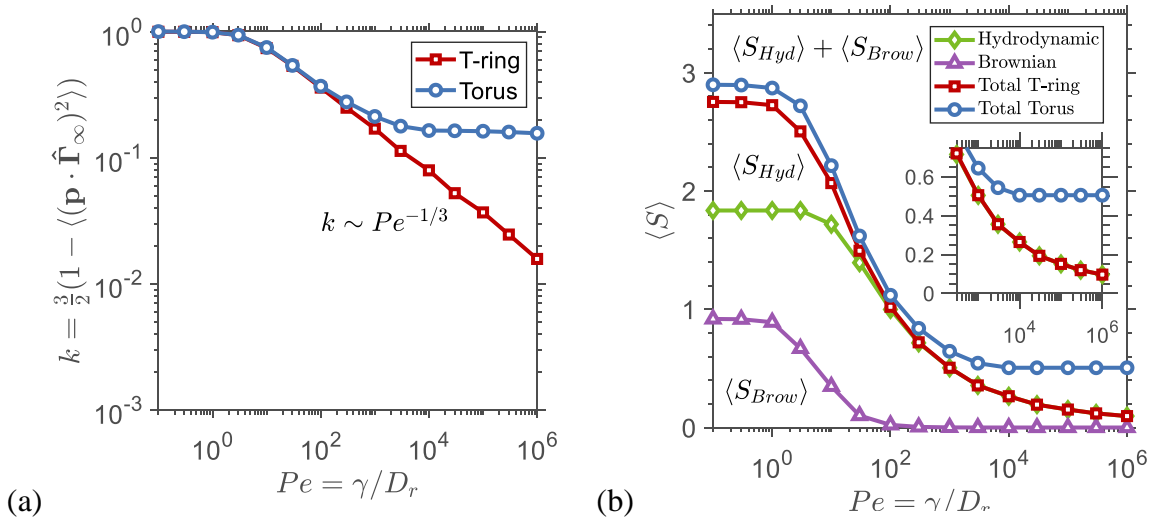
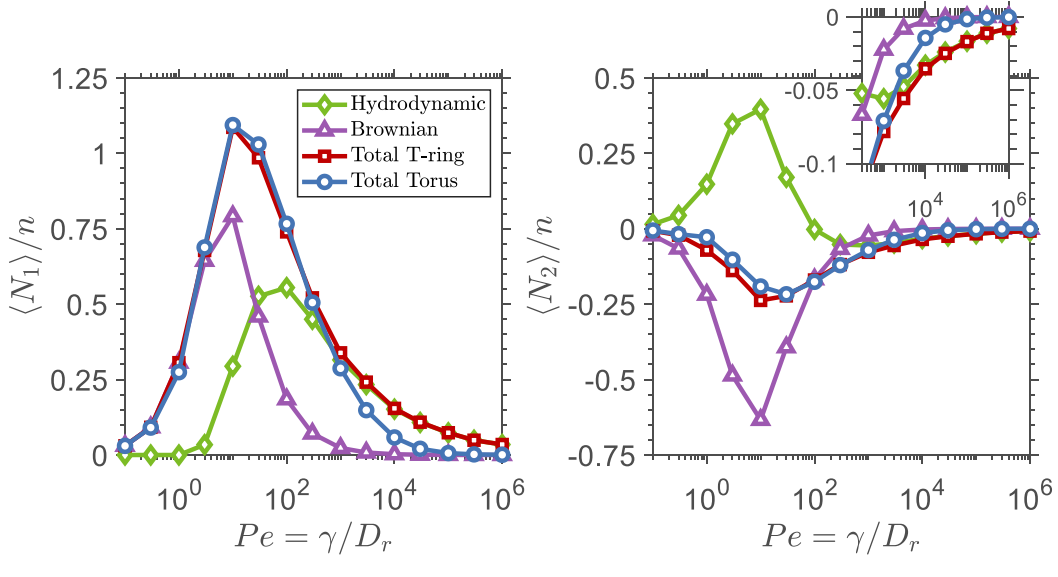


Figure S1 (a) The orbit distribution probability  $p(C_b)$  obtained from BD simulations along with the analytical distribution of (Leal & Hinch, 1971)  $Pe = 10^5$  for an  $A = 55$  torus. (b)  $P_\phi(\phi)$ , the steady state probability distribution of the azimuthal angle for a T-ring with  $A = 55$  at  $Pe = 10^5$  obtained from BD simulations and semi-analytical prediction from the solution of the convection diffusion equation:  $\frac{\partial P_\phi}{\partial t} + \frac{d}{d\phi} \left( \dot{\phi}_J P_\phi - \frac{1}{Pe} \frac{dP_\phi}{d\phi} \right) = 0$ .

Figure S2 (a) shows the variation of the flow-alignment parameter ( $k$ ) as a function of  $Pe$ . The flow alignment parameter  $k$  is proportional to  $Pe^{-\frac{1}{3}}$  for  $Pe \gg 1$  for both a torus and a SAP at  $A = A^* = 26$  as shown by (Brenner, 1974). The  $Pe^{-\frac{1}{3}}$  dependence of  $k$  is retained for the SAP while it attains the value corresponding to the weak Brownian motion limit of (Leal & Hinch, 1971). The Brownian stresslet  $\langle S_{Brow} \rangle$ , hydrodynamic stresslet  $\langle S_{Hyd} \rangle$ ; and the normal stress differences as a function of  $Pe$  are shown in figure S2 (b) and (c) respectively.  $\langle S_{Hyd} \rangle$  converges to its steady state value of  $O(1/A^{*2})$  as  $Pe \rightarrow \infty$  which is still larger than the  $O(\Delta A/A^3) + O(1/A^2)$  value of an  $A = 55$  SAP due to a smaller aspect ratio. At  $Pe = 10^6$   $\langle S_{Hyd} \rangle$  is almost 76% larger than its equilibrium value when  $\mathbf{p} = \mathbf{p}_s$ . The normal stresses differences approach towards a zero value as  $Pe \rightarrow \infty$ , but otherwise have a similar variation to a SAP with non-zero  $|\phi_s|$  for  $Pe \ll |\phi_s|^{-3}$ .





(c)

Figure S2 Variation of the flow-alignment parameter ( $k$ ), the Brownian  $\langle S_{Brow} \rangle$  and hydrodynamic stresslet  $\langle S_{Hyd} \rangle$ , and the normal stress differences( $\langle N_1 \rangle, \langle N_2 \rangle$ ) for a T-ring at the critical aspect ratio  $A = A^* \approx 26$ .

### 1.2 Pairwise interaction simulation strategy

The methodology for simulating pairwise interactions (PIs) between two particles includes modeling of hydrodynamic interactions (HIs) using slender body theory and collisions using a short-range repulsive force (Borker and Koch ring paper). Consider two particles with orientations  $\mathbf{p}_I$  and  $\mathbf{p}_{II}$  and with the position of their centers of mass located at  $\mathbf{r}_{I,COM}$  and  $\mathbf{r}_{II,COM}$  respectively. The leading order effect of the presence of second particle is embedded in the slender body theory formulation through an additional velocity disturbance  $\mathbf{u}'_\infty$  which is given by

$$u'_{\infty,i}(\mathbf{r}) = \int_0^1 2\pi ds f_j(\mathbf{r}') J_{ij}(\mathbf{r}'') , \quad (S 2.1)$$

where  $J_{ij}(\mathbf{r})$  is the Oseen tensor equal to  $(\delta_{ij}/r + r_i r_j/r^3)/(8\pi)$ ,  $s$  is a coordinate measured along the centerline of the ring cross-section,  $\mathbf{r}'' = \mathbf{r} - \mathbf{r}'$ ,  $\mathbf{r}'$  being the position on the centerline of the second ring,  $\mathbf{f}$  is the force per unit length exerted by the particle on the fluid obtained from the

SBT solution of a single force and torque free ring in a simple shear flow ( $\mathbf{f}_{SSF}$ ) (Borker & Koch, in press) and the force per unit length due to collision  $\mathbf{f}_{col}$  discussed later in the text.  $\mathbf{u}'_\infty$  also termed the first reflection accurately describes the rheology of high-aspect ratio fibers which are mainly driven by hydrodynamic interactions rather than collisions (Mackaplow & Shaqfeh, 1996). The velocity disturbance produced by the first reflection is accurate because subsequent reflections are smaller by a factor of  $O(1/\ln(8A))$ , making the influence of each reflection smaller than the previous one.  $\mathbf{u}'_\infty$  induces an angular velocity  $\boldsymbol{\omega}_{HI}$ , a translational velocity  $\mathbf{U}_{HI}$  and a force per unit length  $\mathbf{f}_{HI} = 4\pi\epsilon_R(\mathbf{U}_{HI} + \boldsymbol{\omega}_{HI} \times \mathbf{r}_c - \mathbf{u}'_\infty) \cdot (\mathbf{I} - 0.5 \mathbf{e}_z \mathbf{e}_z)$ , where  $\epsilon_R = 1/\ln(8R_{SBT}/a)$  is the slender parameter in the SBT formulation and is obtained from 2D Stokes flow calculation which determines  $R_{SBT} = 1 + O(1/A)$  as the equivalent radius of the ring through the computation of the apparent hydrodynamic center of resistance, and  $a \sim O(1/A)$  being the equivalent radius of the cross-section. Using  $\epsilon_R$  instead of  $1/\ln(A)$ , where  $A$  is the ratio of the extent of the particle in the plane of the ring and the extent normal to the plane, ensures greater accuracy of the SBT formulation, particularly  $\mathbf{f}_{SSF}$  can be analytically obtained with errors of  $O(1/A^2)$ . We retain the use of  $\epsilon = \epsilon_R + O(\epsilon_R^2/A)$  in scaling arguments because the purely geometric quantity  $A$  is more intuitive to readers than  $R_{SBT}/a$  which comes from a hydrodynamic calculation. The components of  $\mathbf{f}_{HI}$  expressed in the  $(n, b, p)$  coordinate system are

$$\begin{aligned}\frac{f_{HI,I,n}}{8\pi\epsilon_R} &= \frac{U_{HI,n}(3 + \cos(2 \cdot 2\pi s))}{8} + \frac{U_{HI,b} \sin(2 \cdot 2\pi s)}{8} - \frac{\omega_{HI,p} \sin(2\pi s)}{4} - q_n, \\ \frac{f_{HI,I,b}}{8\pi\epsilon_R} &= \frac{U_{HI,n} \sin(2 \cdot 2\pi s)}{8} + \frac{U_{HI,b}(3 - \cos(2 \cdot 2\pi s))}{8} + \frac{\omega_{HI,p} \cos(2\pi s)}{4} - q_b, \\ \frac{f_{HI,I,p}}{8\pi\epsilon_R} &= \frac{U_{HI,p}}{2} + \frac{\omega_n \sin(2\pi s)}{2} - \frac{\omega_b \cos(2\pi s)}{2} - q_p, \quad (S\ 2.2)\end{aligned}$$

where  $\mathbf{q}$  is given by

$$\begin{aligned}q_n &= \frac{(1 + \cos^2(2\pi s))}{4} \mathbf{u}'_\infty(\mathbf{r}_c) \cdot \mathbf{n} + \frac{\sin(2\pi s) \cos(2\pi s)}{4} \mathbf{u}'_\infty(\mathbf{r}_c) \cdot \mathbf{b}, \\ q_b &= \frac{\sin(2\pi s) \cos(2\pi s)}{4} \mathbf{u}'_\infty(\mathbf{r}_c) \cdot \mathbf{n} + \frac{(1 + \sin^2(2\pi s))}{4} \mathbf{u}'_\infty(\mathbf{r}_c) \cdot \mathbf{b}, \\ q_p &= \frac{1}{2} \mathbf{u}'_\infty(\mathbf{r}_c) \cdot \mathbf{p}. \quad (S\ 2.3)\end{aligned}$$

The vector  $\mathbf{n}$  is a unit vector along  $(\mathbf{I} - \mathbf{p}\mathbf{p}) \cdot \hat{\mathbf{U}}_\infty$  and  $\mathbf{b} = \mathbf{p} \times \mathbf{n}$ .  $\mathbf{U}_{HI}$  obtained by applying the force-free condition is given by

$$U_{HI,n} = \frac{4}{3\pi} \int_0^1 2\pi ds q_n, U_{HI,b} = \frac{4}{3\pi} \int_0^1 2\pi ds q_b, U_{HI,p} = \frac{1}{\pi} \int_0^1 2\pi ds q_p, \quad (S 2.4)$$

and  $\omega_{HI}$  obtained by applying the torque-free condition is given by

$$\begin{aligned} \omega_{HI,n} &= \frac{2}{\pi} \int_0^{2\pi} d\phi q_p \sin(\phi), & \omega_{HI,b} &= -\frac{2}{\pi} \int_0^{2\pi} d\phi q_p \cos(\phi), \\ \omega_{HI,p} &= \frac{2}{\pi} \int_0^{2\pi} d\phi (-q_n \sin(\phi) + q_b \cos(\phi)). \end{aligned} \quad (S 2.5)$$

Solid-body collisions and HIs both influence the behavior of high-aspect ratio particles at dilute particle concentrations. The importance of collisions relative to HIs can be quantified by obtaining the order of magnitude scaling of the mean square change in its orientation  $\Delta p^2$  (Rahnama, et al., 1995) which is simply the product of the event frequency and the square of change in the particle orientation due to that event. The frequency of collision is equal to the product of the collision cross-section, the relative velocity and the event probability. The collision frequency is  $O(|\phi_S|^2)$  for a suspension of SAPs and  $O(\phi_T)$  for a suspension of rotating particles. The collision of two-SAPs changes the particles orientation by  $O(|\phi_S|)$ , while the orientation of a rotating ring in its aligned phase changes by  $O(1)$  when it collides with a rotating ring in its tumbling phase. This implies that  $\Delta p^2$  is  $O(|\phi_S|^4)$  for SAPs and  $O(\phi_T)$  for tumbling rings.  $\Delta p^2$  due to purely hydrodynamic interactions, summarized in table S 2, is  $O(|\phi_S|^2)$  for SAPs and  $O(\phi_T)$  for rotating particles. Based on the scaling arguments it can be claimed that the rheology of SAPs is mainly determined by the hydrodynamic interactions while the rheology of rotating rings has a major contribution from collisions.

Type of interactions	Collision cross- × Relative velocity × Event probability	=	Collision Frequency
----------------------	--	---	------------------------

	sectional area
SAP-SAP :	$ \phi_S  \times  \phi_S  \times 1 = O( \phi_S ^2)$
Aligned-Aligned (Tumblers) :	$\phi_T \times \phi_T \times 1 = O(\phi_T^2)$
Aligned-Tumbling (Tumblers) :	$1 \times 1 \times \phi_T = O(\phi_T)$
Tumbling-Tumbling (Tumblers) :	$1 \times 1 \times \phi_T^2 = O(\phi_T^2)$

Table S1. Frequency of collision between two SAPs and between two rotating particles. The latter has three cases: (1) both particles are in the aligned phase, (2) one particle is in the aligned phase and the second one tumbles and (3) both particles are in the tumbling phase.

Type of HIs	Square of the change in $\mathbf{p}$ during the interaction	$\times$	Event probability	=	Mean square change in $\mathbf{p}$
SAP-SAP	$(\epsilon \phi_S )^2$	$\times$	1	=	$O(\epsilon^2 \phi_S ^2)$
Aligned-Aligned (Tumblers)	$(\epsilon\phi_T)^2$	$\times$	1	=	$O(\epsilon^2\phi_T^2)$
Aligned-Tumbling (Tumblers)	$\epsilon^2$	$\times$	$\phi_T$	=	$O(\epsilon^2\phi_T)$
Tumbling-Tumbling (Tumblers)	$\epsilon^2$	$\times$	$\phi_T^2$	=	$O(\epsilon^2\phi_T^2)$

Table S2. Mean squared orientation changed due to interactions between two SAPs and between two rotating particles. The latter has three cases: (1) both particles are in the aligned phase, (2) one particle is in the aligned phase and the second one tumbles and (3) both particles are in the tumbling phase.

Before explaining the modeling strategy for collision, we explain how high-aspect ratio rings can make solid-body contacts. The lubrication force between two high-aspect ratio tori which are almost colliding is  $O(\dot{\delta}/(A^2\delta))$ , similar to the lubrication force between nearly colliding cylinders (Yamane, et al., 1994), where  $\delta$  is the distance of minimum separation between the particles and  $\dot{\delta}$  is the time rate of change of  $\delta$ . In an  $O(1)$  time  $\delta$  changes by a factor of  $\exp(-A^2)$ , leading to sub-atomic separations for any sub-mm sized particle with  $A > 5$ . The details of the cross-sectional shape would not change the order of magnitude of the lubrication force and the argument that lubrication is too weak to prevent collision remains valid for any high-aspect ratio ring.

The collision event near the point of contact is simulated by applying a short-range repulsive force,  $\mathbf{F}_{col}$ , that prevents particles from passing through each other and acts on one or

two points on the rings and depends only on the distance of minimum separation between the rings  $\delta$ . T-rings and L-rings are modeled as tori with the same aspect ratio  $A_{SBT}$  and an equivalent hydrodynamic cross-sectional radius obtained from SBT (Borker & Koch, in press). This approximation only changes the position of the point of contact by  $O(1/A)$  leading to small changes in the overall trajectory of the particle. The rheology of a suspension of discs for which collisions are important was found to be insensitive to the choice of the functional form  $\mathbf{F}_{col}$  on  $\delta$  as long as it increases steeply ( (Yamamoto & Matsuoka, 1997; Meng & Higdon, 2008)).  $\mathbf{F}_{col}$  used in our simulations had a functional form on  $\delta$  similar to  $\mathbf{F}_{col}$  used to simulate collision of two discs by Meng and Higdon (Meng & Higdon, 2008) which is given by

$$\mathbf{F}_{col} = \frac{8\pi}{A^2} C_p \frac{\delta_{min}}{\delta} \left( \eta - \frac{\eta^2}{2} \right)^3 \mathbf{d}, \quad (S 2.6)$$

where  $\eta = 1 - \delta/\delta_{min}$ ,  $\mathbf{d}$  is a unit vector normal to the collision surface pointing towards the surface of each sphere and  $C_p$  is an  $O(1)$  constant chosen to be unity for our simulation (Meng & Higdon, 2008).  $\delta_{min}$  was chosen to be  $10^{-2}/A$  and  $\mathbf{F}_{col}$  is capped to a maximum value corresponding to  $\delta = 10^{-2}\delta_{min}$  for all our simulations to avoid small time steps. Collisions induce linear ( $\mathbf{U}_{col}$ ) and angular ( $\boldsymbol{\omega}_{col}$ ) velocities and a force per unit length  $\mathbf{f}_{col}$ .  $\mathbf{U}_{col}$  and  $\boldsymbol{\omega}_{col}$  obtained by applying the force and torque free condition on the particle are given by

$$\begin{aligned} \mathbf{U}_{col} &= \frac{\mathbf{F}_{col}}{6\pi^2\epsilon_R} \cdot \left( \frac{1 - \frac{17}{6}\epsilon_R}{1 - \frac{5}{2}\epsilon_R - \epsilon_R^2} (\mathbf{I} - \mathbf{p}\mathbf{p}) + \frac{3}{4} \frac{1}{1 + \frac{\epsilon_R}{2}} \mathbf{p}\mathbf{p} \right), \\ \boldsymbol{\omega}_{col} &= \frac{(\mathbf{r}_{c,col} \times \mathbf{F}_{col})}{4\pi^2\epsilon_R} \cdot \left( \frac{\mathbf{n}\mathbf{n} + \mathbf{b}\mathbf{b}}{1 - 1.5\epsilon_R} + \frac{\mathbf{p}\mathbf{p}}{1 - 2\epsilon_R} \right). \end{aligned} \quad (S 2.7)$$

The force per unit length due to collision  $\mathbf{f}_{col}$  is given by

$$\begin{aligned} \frac{f_{col,n}}{8\pi\epsilon_R} &= \frac{U_{col,n}(3 + \cos(2 \cdot 2\pi s))}{8} + \frac{U_{col,b} \sin(2 \cdot 2\pi s)}{8} - \frac{\omega_{col,p} \sin(2\pi s)}{4}, \\ \frac{f_{col,b}}{8\pi\epsilon_R} &= \frac{U_{col,n} \sin(2 \cdot 2\pi s)}{8} + \frac{U_{col,b}(3 - \cos(2 \cdot 2\pi s))}{8} + \frac{\omega_{col,p} \cos(2\pi s)}{4}, \end{aligned}$$

$$\frac{f_{col,p}}{8\pi\epsilon_R} = \frac{U_{col,p}}{2} + \frac{\omega_{col,n} \sin(2\pi s)}{2} - \frac{\omega_{col,b} \cos(2\pi s)}{2}. \quad (S 2.8)$$

$\mathbf{f}_{col}$  is included while computing the velocity disturbance on the particle and is important when the particles collide.

The particle position  $\mathbf{r}_{k,COM}$  and orientation  $\mathbf{p}_k$  are obtained by solving a set of ordinary differential equations given by

$$\begin{aligned} & \frac{d\mathbf{r}_{k,COM}}{dt} \\ &= \mathbf{u}_\infty(\mathbf{r}_{k,COM}) + \eta_1 \mathbf{E}_\infty \cdot \mathbf{p}_k + \eta_2 \mathbf{E}_\infty : \mathbf{p}_k \mathbf{p}_k \mathbf{p}_k + \mathbf{U}_{HI} + \mathbf{U}_{col}, \quad (S 2.9) \end{aligned}$$

$$\frac{d\mathbf{p}_k}{dt} = \mathbf{p}_k \cdot \mathbf{R}_\infty + \lambda(\mathbf{E}_\infty \cdot \mathbf{p}_k - \mathbf{E}_\infty : \mathbf{p}_k \mathbf{p}_k \mathbf{p}_k) + (\boldsymbol{\omega}_{HI} + \boldsymbol{\omega}_{col}) \times \mathbf{p}_k, \quad (S 2.10)$$

where  $k = \{I, II\}$ ,  $\eta_1$  and  $\eta_2$  are translation parameters determining the deviation of the particle's velocity from the fluid velocity at its center of mass in the absence of particle interactions. The Runge-Kutta method with adaptive time-stepping was used to march forward in time. The initial center of mass positions of the two particles were chosen to be  $\mathbf{r}_{I,COM} = 0$  and  $\mathbf{r}_{II,COM} = -\Delta\mathbf{r}_0$  such that  $\Delta\mathbf{r}_0 \cdot \hat{\mathbf{U}}_\infty \gg 1$  simulating an initial large separation between the particles. The choice of  $\Delta\mathbf{r}_0$  is discussed shortly at the end of the paragraph. The only difference between the simulation of SAPs and rotating rings is the specification of the initial orientations. For SAPs the initial orientations of both the particles  $\mathbf{p}_{I,0}$  and  $\mathbf{p}_{II,0}$  are equal to one of the stable equilibrium orientation  $\mathbf{p}_{S,I}$  or  $\mathbf{p}_{S,II}$  shown in figure 1 (c) of the main text. For rotating particles, the  $\mathbf{p}_{I,0}$  and  $\mathbf{p}_{II,0}$  are chosen from the statistical steady state orientation distribution set by pairwise interactions. The initial conditions for the simulation of SAPs involve only two degrees of freedom  $(\Delta\mathbf{r}_0 \cdot \hat{\mathbf{\Gamma}}_\infty, \Delta\mathbf{r}_0 \cdot \hat{\mathbf{\Omega}}_\infty)$  while rotating particles requires an four additional orientational degrees of freedom. The procedure for obtaining this steady state distribution is described in Borker and Koch (ring rheology paper). For rings with  $\phi_T \ll 1$ , the orientation distribution determined by particle interactions is close to the orientation distribution set by weak Brownian motion ( $Pe \gg \phi_T^{-3}$ ).

Monte-Carlo integration is used to compute quantities of interest from such as orientational dispersion, hydrodynamic diffusivity or stresslet. The statistical ensemble average of any quantity

of interest  $\mathbf{X}$  obtained from the flux of particles passing through the flow-vorticity plane is given by

$$\frac{\langle \mathbf{X} \rangle_{PI}}{n} = \sum_j A_j \sum_{k=1}^{N_j} \frac{(\Delta \mathbf{r}_0)_k \cdot \hat{\mathbf{\Gamma}}_\infty}{N_j} \int_{-\infty}^{\infty} dt \left( \mathbf{X}_k(t) - \mathbf{X}_{J,k}(t) \right) = \sum_j A_j \sum_{k=1}^{N_j} \frac{I_k}{N_j}. \quad (S 2.11)$$

where the subscript  $k$  refers to the  $k^{th}$  pairwise interaction between 2 particles,  $\mathbf{X}_{J,k}$  is the value of  $\mathbf{X}$  evaluated in the absence of the second particle,  $(\Delta \mathbf{r}_0)_k \cdot \hat{\mathbf{\Gamma}}_\infty$  specifies velocity of the particles,  $A_j$  is the area of the  $j^{th}$  region in the  $\hat{\mathbf{\Gamma}}_\infty - \hat{\mathbf{\Omega}}_\infty$  plane and  $I_k$  is simply the value of the integral times the probability of the interaction  $(\Delta \mathbf{r}_0)_k \cdot \hat{\mathbf{\Gamma}}_\infty$ . The inner summation in equation (S 2.11) gives the flux per unit area contribution to  $\langle \mathbf{X} \rangle_{PI}/n$ . The values of  $\Delta \mathbf{r}_0 \cdot \hat{\mathbf{\Omega}}_\infty$  and  $\Delta \mathbf{r}_0 \cdot \hat{\mathbf{\Gamma}}_\infty$  are generated with uniform probability in each of the  $j^{th}$  region. The standard deviation of  $I_k$  in the  $j^{th}$  region  $\sigma_{I,j}$  mathematically given by

$$\sigma_{I,j}^2 = \frac{1}{N_j} \sum_{k=1}^{N_j} \left( I_k - \sum_{k=1}^{N_j} \frac{I_k}{N_j} \right)^2, \quad (2.12)$$

is used to express the statistical error. The expression for  $\langle \mathbf{X} \rangle_{PI}$  with the standard error within 95% confidence limits is given by

$$\frac{\langle \mathbf{X} \rangle_{PI}}{n} = \sum_j A_j \left\{ \sum_{k=1}^{N_j} \frac{I_k}{N_j} \pm 1.96 \frac{\sigma_{I,j}}{\sqrt{N_j}} \right\} \quad (2.13)$$

$\sigma_{I,j} \ll 1\%$  for the Monte-Carlo simulations of SAPs while its value was about 2% for tumblers.

The stresslet in a dilute suspension of rings can be expressed as  $\langle \mathbf{S} \rangle = \langle \mathbf{S}_{Hyd} \rangle + n (\langle \mathbf{S}_p \rangle/n + \langle \mathbf{S}_f \rangle/n + \langle \mathbf{S}_{col} \rangle/n)$ , where  $\langle \mathbf{S}_p \rangle$  is the stresslet driven by the transient change in the particles orientation due to PIs,  $\langle \mathbf{S}_f \rangle$  the stresslet induced by  $\mathbf{f}_{HI}$ , and  $\langle \mathbf{S}_{col} \rangle$  is the stresslet imparted from particle collisions ( $\mathbf{F}_{col}$ ).  $\langle \mathbf{S}_p \rangle$  is expressed as

$$\frac{\langle \mathbf{S}_p \rangle}{n} = \sum_j \frac{A_j}{N_j} \sum_{k=1}^{N_j} (\Delta \mathbf{r}_0)_k \cdot \hat{\mathbf{r}}_\infty \int_0^\infty dt [\mathbf{S}_{Hyd}(\mathbf{p}) - \mathbf{S}_{Hyd}(\mathbf{p}_s)]. \quad (S\ 2.14)$$

$\langle \mathbf{S}_f \rangle$  is the ensemble average of  $\mathbf{S}_f = \int ds ((\mathbf{f}_{HI} \mathbf{r}_c + \mathbf{r}_c \mathbf{f}_{HI})/2 - (\mathbf{r}_c \cdot \mathbf{f}_{HI}) \mathbf{I}/3)$ , given by

$$\frac{\langle \mathbf{S}_f \rangle}{n} = \sum_j \frac{A_j}{N_j} \sum_{k=1}^{N_j} (\Delta \mathbf{r}_0)_k \cdot \hat{\mathbf{r}}_\infty \int_{-\infty}^\infty dt \mathbf{S}_f, \quad (S\ 2.15)$$

and  $\langle \mathbf{S}_{col} \rangle$  is given by

$$\frac{\langle \mathbf{S}_{col} \rangle}{n} = \sum_j \frac{A_j}{N_j} \sum_{k=1}^{N_j} (\Delta \mathbf{r}_0)_k \cdot \hat{\mathbf{r}}_\infty \int_{-\infty}^\infty dt \mathbf{S}_{col}. \quad (S\ 2.16)$$

Equations (2.14)-(2.16) face the problem of a non-integrable area integral over the  $\hat{\mathbf{r}}_\infty - \hat{\Omega}_\infty$  plane because  $\mathbf{S}_f$  and  $\mathbf{S}_p$  scale as  $\Delta r^{-3}$ ,  $\Delta r$  being the measure of the distance away from the particle. To prevent this divergent behavior, a renormalization procedure similar to (Batchelor & Green, 1972), is used to compute the contribution of the second particle. In this procedure, the position, orientation and  $\mathbf{f}_{HI}$  are observed as a second SAP particle passes by on a streamline with the same  $\Delta \mathbf{r}_0$  value as the original pairwise interaction calculation. The ensemble average stresslet exerted by particle-I in this new calculation should be exactly equal to  $\mathbf{S}_{Hyd}(\mathbf{p}_s)$ . In this new calculation,  $\mathbf{S}_f^{RN}$  and  $\mathbf{S}_p^{RN}$ , similar to  $\mathbf{S}_f$  and  $\mathbf{S}_p$  for the pairwise calculation respectively, have the same  $\Delta r^{-3}$  decay as  $\mathbf{S}_f$  and  $\mathbf{S}_p$ . The ensemble averages  $\langle \mathbf{S}_f^{RN} \rangle$  and  $\langle \mathbf{S}_p^{RN} \rangle$  should be equal to zero over all possible realizations of the system at  $O(n)$ . This calculation is a way of computing the stress on a test SAP in a sea of other SAPs, which at  $O(n)$  should be identical to  $-n \mathbf{S}_{Hyd}(\mathbf{p}_s)$ . Therefore, the renormalized equation for evaluating  $\langle \mathbf{S}_f \rangle$  is given by

$$\frac{\langle \mathbf{S}_f \rangle}{n} = \sum_j \frac{A_j}{N_j} \sum_{k=1}^{N_j} (\Delta \mathbf{r}_0)_k \cdot \hat{\mathbf{r}}_\infty \int_{-\infty}^\infty dt (\mathbf{S}_f - \mathbf{S}_f^{RN}), \quad (S\ 2.17)$$

and for  $\mathbf{S}_p$  is given by

$$\begin{aligned} \frac{\langle S_p \rangle}{n} = & \sum_j \frac{A_j}{N_j} \sum_{k=1}^{N_j} (\Delta r_0)_k \\ & \cdot \hat{\Gamma}_\infty \int_0^\infty dt \{ [S_{Hyd}(\mathbf{p}) - S_{Hyd}(\mathbf{p}_s)] - [S_{Hyd}(\mathbf{p}^{RN}) - S_{Hyd}(\mathbf{p}_s)] \}, \quad (S 2.18) \end{aligned}$$

where  $\mathbf{p}^{RN}$  is the value of  $\mathbf{p}$  calculated for the additional calculation for the renormalization procedure. The time integral of  $(S_f - S_f^{RN})$  and  $[S_{Hyd}(\mathbf{p}) - S_{Hyd}(\mathbf{p}_s)] - [S_{Hyd}(\mathbf{p}^{RN}) - S_{Hyd}(\mathbf{p}_s)]$  are  $O(|\Delta r_0 \cdot (I - \hat{U}_\infty \hat{U}_\infty)|^{-6})$  as  $\Delta r_0 \cdot (I - \hat{U}_\infty \hat{U}_\infty) \rightarrow \infty$ , leading to a convergent area summation. Evaluating the time integration using equations (S 2.17) –(2.18) isolates the influence of the pairwise interaction for each trajectory, and thereby minimizes the statistical uncertainty of the Monte-Carlo procedure.

The simulations are first performed with uniformly seeded points in region 1 whose extent along  $\hat{\Gamma}_\infty$  is  $L_3 = 2$  and the extent along  $\hat{\Omega}_\infty$  is  $L_2 = 3$  as shown in figure S3 (a). It takes about  $10^3$  simulations for obtaining steady state contribution in this region as shown by the convergence of  $\langle S_p \rangle$  as a function of the number of Monte-Carlo simulations  $N_{sim}$  as shown in figure S3 (b). The statistical error in region-1 has a magnitude of less than about 0.01% of the mean value in that region. A similar pattern is followed by other quantities of interest. This steady state value of  $\langle S_p \rangle$  can be improved by including the contribution from additional regions (2, 3) whose extent along  $\hat{\Gamma}_\infty$  and  $\hat{\Omega}_\infty$  is doubled for each subsequent region- $k$ ,  $k = (2,3)$  as shown in figure S3 (a). The contribution of regions 2-and-3 are insignificant compared to the one of region-1 as shown in figure S3 (c). The simulations were therefore terminated after region (3). For  $A = 30$  particle we performed the simulations in regions 4 and 5 and found their respective contribution to  $\langle S_p \rangle/n$  to progressively get smaller.

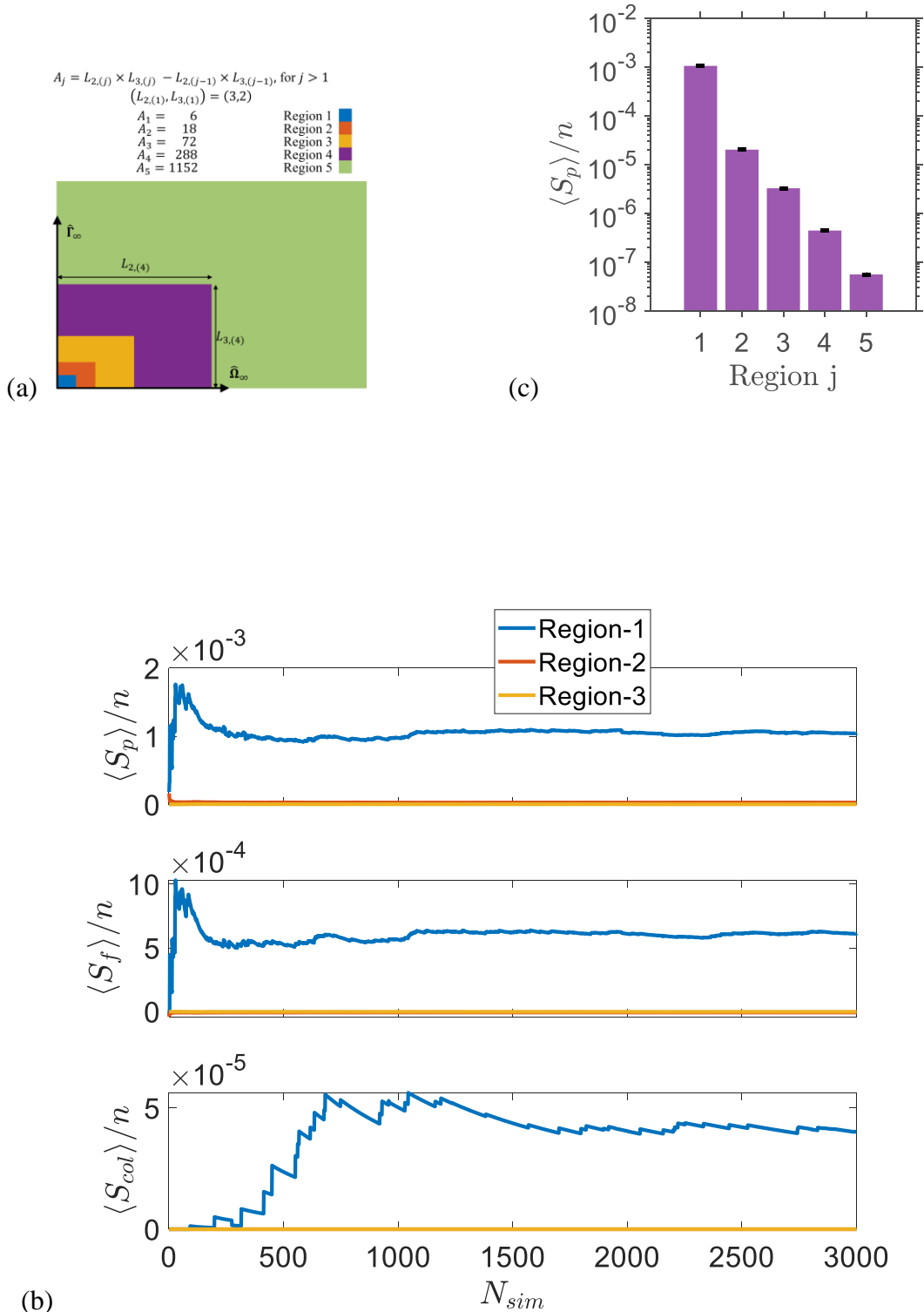


Figure S3 (a) Division of  $\hat{\Gamma}_\infty - \hat{\Omega}_\infty$  plane into five regions, to establish convergence with the domain size. SAPs have a skewed domain because of the alignment near the flow-vorticity plane leads to a stronger interaction in  $\hat{\Omega}_\infty$  direction compared to  $\hat{\Gamma}_\infty$  direction. ( $L_2, L_3$ ) for region  $j$

increases by a factor of 2 compared with  $(L_2, L_3)$  for region  $j - 1$ . (b) Mean value of  $(\langle S_p \rangle, \langle S_f \rangle, \langle S_{col} \rangle)/n$  vs the number of simulations  $N_{sim}$  for different regions. (c) Decreasing  $\langle S_p \rangle/n$  contribution with increasing region index  $j$ . Thus, the inner summation decreases faster than the increase in the area establishing convergence of equation (S 2.11). In general contribution from region-1 is sufficient for the simulations.

### 1.3 Particle attraction towards a wall

The velocity disturbance due to the image singularities can be computed by integrating the velocity disturbance of the image of a stokeslet  $\mathbf{f}_{SSF}$  along the centerline of the image ring obtained using equation (8) of Blake and Chwang (Blake & Chwang, 1974).  $\zeta_w$  can be estimated for  $h \gg 1$  by assuming  $\mathbf{p} = \mathbf{p}_s$  which implies  $\mathbf{f} \cdot \hat{\mathbf{U}}_\infty = f_n$ ,  $\mathbf{f} \cdot \hat{\boldsymbol{\Omega}}_\infty = f_b$  and  $\mathbf{f} \cdot \hat{\mathbf{r}}_\infty \approx f_n |\phi_s|$ . For  $h \gg 1$ , the velocity disturbance in the gradient direction at the center of the ring due to the image ring, obtained analytically using elementary algebra, is given by

$$\begin{aligned} \mathbf{u}_\infty^{wall} \cdot \hat{\mathbf{r}}_\infty &\approx \frac{13\pi}{8h^2} \int_0^{2\pi} d\phi \frac{(f_n \cos(\phi) + f_b \sin(\phi))}{8\pi} \\ &\approx -\left(\frac{1}{h^2}\right) \frac{13\pi |\phi_s| \epsilon}{16 \left(1 - \frac{5}{2}\epsilon\right)} \left(1 - \epsilon \frac{\bar{\alpha}_2 \cos(2\theta_{02})}{2 \left(1 - \frac{5}{2}\epsilon\right)} + \frac{3\bar{\alpha}_3 \cos(3\theta_{03})}{A}\right) = -\frac{\zeta_w}{h^2}. \quad (S 3.1) \end{aligned}$$

Equation (S 3.1) accurately predicts  $\zeta_w$  for rings until  $h \approx 2$  as seen in figure 4 (f) in the main text.

## CHAPTER 6

### Future work

Our work demonstrates a new class of suspensions of self-aligning particles that have a much smaller effective viscosity, hydrodynamic diffusivity and orientation dispersion in comparison to a suspension of tumbling particles of the same aspect ratios. The rheology of can be passively controlled by changing the geometry of individual particles. Discs are known to strongly align near the flow vorticity plane for  $n \sim O(1)$  under shear due to excluded volume interactions (Meng & Higdon, 2008). The excluded volume of a rings is only about 15% smaller than that of a circumscribing disc (Wensink & Avendaño, 2016). Furthermore, rings of are known to transition to a liquid crystal smectic phase at  $n \approx 0.8$  for  $A \approx 17$  (Carlos Avendaño, 2016). These findings suggest that self-aligning rings should retain orientational order for almost all values of  $n$  compared to fiber or disc suspensions offering a unique route to synthesizing materials with tunable properties using existing processing flow technologies. Our work should motivate researchers to experimentally observe this new and exciting regime of flowing suspensions whose properties should be significantly different from their tumbling counterparts. T-rings and L-rings of feature sizes of a few microns could be fabricated using photolithography (Foulds & Parameswaran., 2006). Coutte cell of gap-size of at least 5 particle diameters is sufficient to ignore wall effects and observe alignment for a time that is atleast 10 times the time period of a equivalent torus. Finally, ring suspensions owing to a large hole can have a very small packing fraction and has applications in producing structured porous medium which have applications in storage of hydrogen,  $CO_2$  or metal melts for energy needs.

Simulating rheology at  $n \sim O(1)$  requires calculating the velocity disturbances as well as collisions from multiple particles. Hydrodynamic interactions can be computed using the slender body theory formulation from the analytical force distribution of Borker and Koch (*in press*) similar to the ring simulations carried out in chapter 4. The slender body theory formulation is able to accurately predict the rheology of fibers when  $nL^3 \gg 1$  and  $nL^3 \lesssim \ln(8A)$ . Multiple contacts between rings can be captured using a scheme developed by Vierra (1997). Furthermore, effect of Brownian motion can also be embedded in this calculation by simply prescribing stochastically

varying linear and angular velocities. The center of mass position  $\mathbf{r}_{COM,i}$  and orientation  $\mathbf{p}_i$  of the  $i^{th}$  particle are given by

$$\frac{d(\mathbf{r}_{COM,i})}{dt} = \mathbf{u}_\infty(\mathbf{r}_{COM,i}) + \eta_1 \mathbf{p}_i \cdot \mathbf{E}_\infty + \eta_2 \mathbf{p}_i \mathbf{p}_i \mathbf{p}_i : \mathbf{E}_\infty + \sum_{\substack{k=1 \\ k \neq i}}^N (\mathbf{U}_{HI,k} + \mathbf{U}_{col,k}) + \mathbf{D}_t f_t,$$

$$\frac{d\mathbf{p}_i}{dt} = \mathbf{p}_i \cdot \boldsymbol{\Omega}_\infty + \lambda(\mathbf{p}_i \cdot \mathbf{E}_\infty - \mathbf{p}_i \mathbf{p}_i \mathbf{p}_i : \mathbf{E}_\infty) + \sum_{\substack{k=1 \\ k \neq i}}^N (\boldsymbol{\omega}_{HI,k} + \boldsymbol{\omega}_{col,k}) + \mathbf{D}_r (\mathbf{I} - \mathbf{p}_i \mathbf{p}_i) f_r,$$

where,  $\eta_1, \eta_2$  are the translational parameters and  $\lambda$  is the rotational parameter of the ring;  $\mathbf{D}_t$  and  $\mathbf{D}_r$  are the translational and rotational diffusivities of the particle respectively; and  $(f_t, f_r)$  are random numbers generated using a normal distribution.

This calculation allows for the investigation of a phase transition behavior in ring suspensions under shear. An isotropic to smectic or nematic phase transitions has been observed for Brownian rings with only excluded volume interactions (Carlos Avendaño, 2016). A similar phase transition should also exist in a sheared suspension. Such a calculation can also confirm our predictions of having suspensions with an ordered phase at all particle concentrations for a suspension of T-rings, something that has never been observed before.

One can also study a polydisperse suspension of rings. The velocity disturbance created by a ring is proportional to the cube of its absolute size. Thus, a ring with a larger radius will create velocity disturbances with greater magnitude. Rheology of polydisperse suspension of high-aspect ratio particles other than fibers is again absent. Rings provide a computationally inexpensive route to perform this calculation through the use of slender body theory for modeling the hydrodynamic interactions. Additionally, rings of different sizes can pass through each other, as shown in figure 6.1. This in turn will impact the suspension rheology in non-trivial ways particularly when  $n \sim O(1)$ . Multi-particle simulation strategy suggested above can be used to study such polydisperse ring suspensions.

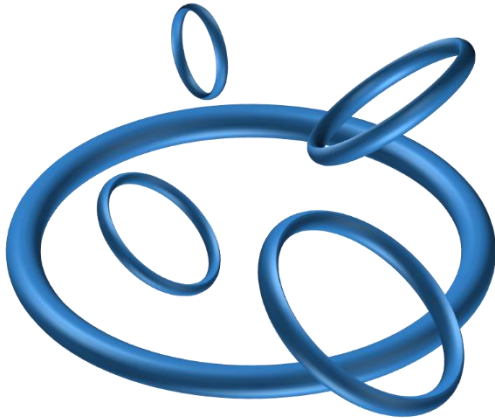


Figure 6.1 Polydisperse suspension of rings can have particle passing through each other interacting hydrodynamically without collisions.

In this work, the focus was mainly on axisymmetric particles, because the simulation and the rheology were more tractable with the computing power available to perform dilute suspension rheology. However, non-axisymmetric particles have a much richer dynamical behavior which can be utilized to passively control suspension rheology. For instance, cylinders with an L-shaped cross-section shown in chapter 3, rotate chaotically unlike the periodic rotation of circular cylinders. This will imply that the steady state orientation distribution would be different thereby affecting the rheology. This effect would also exist for rings or discs which are non-axisymmetric. Such non-axisymmetric particles when rotating near the flow-gradient plane would have a much different effect on the rheology than the ones mentioned in chapter 4. Slender-body theory developed in section-3 allows one to systematically design particle shapes that could have interesting dynamical behavior in shear flows. One example of such geometries is wavy rings. Using slender body theory (Cox 1970) one can easily show that an out of plane perturbation of the ring centerline of the form  $\mathbf{r}_c \cdot \mathbf{p} = \alpha_R \cos(3\phi - 3\phi_0)$  can self-align in a finite amount of time. Here  $\phi$  is the azimuthal angle in a cylindrical coordinate system with the z-axis normal to the plane of the ring. However, such an equilibrium node need not be globally stable. The motion of curved particles with exotic cross-sectional shapes could potentially have hidden dynamical behavior that is yet to be explored.

## REFERENCES

- Abramowitz, M. and Stegun, I. (1964). Handbook of Mathematical Functions: with formulas, graphs and mathematical tables. *Courier Corp.*
- Acrivos, A, Shaqfeh, E. S. G. (1988). The effective thermal conductivity and elongational viscosity of a nondilute suspension of aligned slender rods. *Phys. Fluids* (1958–1988) 31, 1841–1844. (doi:10.1063/1.866681)
- Anczurowski, E. and Mason, S.G. (1967). The kinetics of flowing dispersions, *J. Colloid and Interface Science*, vol. 23, 4, 533-546, [http://doi.org/10.1016/0021-9797\(67\)90200-7](http://doi.org/10.1016/0021-9797(67)90200-7)
- Anczurowski, E., and Mason, S. G., (1968) “Particle motions in sheared suspension. XXIV. Rotations of rigid spheroids and cylinders,” *Trans. Soc. Rheol.* 12, 209–215
- Bao, G., Hutchinson, J.W., McMeeking, R.M. (1991) Particle reinforcement of ductile matrices against plastic flow and creep, *Acta Metallurgica et Materialia*, 39 (8) 1871-1882, [http://doi.org/10.1016/0956-7151\(91\)90156-U](http://doi.org/10.1016/0956-7151(91)90156-U).
- Batchelor, G. K. (1970). Slender-body theory for particles of arbitrary cross-section in Stokes flow. *J. Fluid Mech.*, 44(3), 419-440. <http://doi.org/10.1017/S002211207000191X>
- Batchelor, G. K. (1954). The skin friction on infinite cylinders moving parallel to their length. *The Quarterly Journal of Mechanics and Applied Mathematics*, 7(2), 179-192.
- Beckers, K. F., Koch, D. L., & Tester, J. W. (2015). Slender-body theory for transient heat conduction: theoretical basis, numerical implementation and case studies. *Proc. R. Soc. A* 471, 2184, 20150494.
- Berg H C and Anderson R A 1973 Bacteria swim by rotating their flagellar filaments *Nature* 245 380–2.

Blake, J. R., & Chwang, A. T. (1974). Fundamental singularities of viscous flow. *Journal of Engineering Mathematics*, 8, 23-29. doi:10.1007/BF02353701

Borker, N. S., Stroock, A. D., & Koch, D. L. (2018). Controlling rotation and migration of rings in a simple shear flow through geometric modifications. *Journal of Fluid Mechanics*, 840, 379-407.

Borker, N. S., & Koch, D. L., Slender body theory for particles with non-circular cross-sections with application to particle dynamics in shear flows (*in press*)

Bray, D 2000 Cell Movements (New York: Garland)

Brennen, C and Winet, H 1977 Fluid mechanics of propulsion by cilia and flagella *Annu. Rev. Fluid Mech.* 9 339–98

Brenner, H. (1964). The Stokes resistance of an arbitrary particle—III, *Chemical Engineering Science*, 19 (9), 631-651. [http://dx.doi.org/10.1016/0009-2509\(64\)85052-1](http://dx.doi.org/10.1016/0009-2509(64)85052-1).

Brenner, H. (1974). Rheology of a dilute suspension of axisymmetric Brownian particles,. International Journal of Multiphase Flow, 1(2), 195-341.

Bretherton, F. (1962). The motion of rigid particles in a shear flow at low Reynolds number. *J. Fluid Mech.*, 14(2), 284-304. <http://doi.org/10.1017/S002211206200124X>

Carlos Avendaño, G. J. (2016). Assembly of porous smectic structures formed from interlocking high-symmetry planar nanorings. *Proceedings of the National Academy of Sciences*, 113(35), 9699–9703.

Chen, HS, Acrivos, A. (1976) On the effective thermal conductivity of dilute suspensions containing highly conducting slender inclusions. *Proc. R. Soc. Lond. A* 349, 261–276. (doi:10.1098/rspa.1976.0072)

Chung, D. D. (2001). Thermal interface materials. *Journal of Materials Engineering and Performance*, 10(1), 56-59.

Cox, R. G. (1970). The motion of long slender bodies in a viscous fluid Part 1. General theory. *Journal of Fluid Mechanics*, 44(4), 791-810. doi:10.1017/S002211207000215X

Cox, R. G. (1971). The motion of long slender bodies in a viscous fluid. Part 2. Shear flow. *Journal of Fluid Mechanics*, , 45(4), 625-657.

De, S., Higgins, T.M., Lyons, P.E., Doherty, E.M., Nirmalraj, P.N., Blau, W.J., Boland, J.J., Coleman, J.N. (2009) Silver nanowire networks as flexible, transparent, conducting films: extremely high DC to optical conductivity ratios. *ACS Nano*, 3(7), pp. 1767-1774.

Dubovik, O., Holben, B. N., Lapyonok, T., Sinyuk, A., Mishchenko, M. I., & P. Yang, a. I. (2002). Non-spherical aerosol retrieval method employing light scattering by spheroids. *Geophysical Research Letters*, 29(54).

Einarsson, J., Mihiretie, B. M., Laas A., Ankardal, S., Anglella, J. R., Hanstorp D. & B. Mehlig (2016) Tumbling of asymmetric microrods in a microchannel flow. *Physics of Fluid*, **28**, 013302. (<https://doi.org/10.1063/1.4938239>)

Einstein, A. (1906). Eine neue Bestimmung der Moleküldimensionen. *Annalen der Physik*, 324 (2), 289-306. <http://dx.doi.org/10.1002/andp.19063240204>

Folgar, F., & Tucker III, C. L. (1984). Orientation behavior of fibers in concentrated suspensions. *Journal of reinforced plastics and composites* , 3(2), 98-119.

Foulds, I. G., & Parameswaran, M. (2006). A planar self-sacrificial multilayer SU-8-based MEMS process utilizing a UV-blocking layer for the creation of freely moving parts. *J. Micromech. and Microeng.*, 16 (10), 2109-2115. <http://doi.org/10.1088/0960-1317/16/10/026>

Fredrickson, G. H., Shaqfeh, E. S. G. (1989) Heat and mass transport in composites of aligned slender fibers. *Phys. Fluids A, Fluid Dyn.* (1989–1993) 1, 3–20. (doi:10.1063/1.857546)

Gao, W., & Wang, J. (2014). The environmental impact of micro/nanomachines: a review. *Acs Nano*, 8(4), 3170-3180. (<https://doi.org/10.1021/nn500077a>)

Gabdoulline, R. R., & Wade, R. C. (1998). Brownian dynamics simulation of protein–protein diffusional encounter. *Methods*, 14(3), 329-341.

Guasto, Jeffrey S., Roberto Rusconi, and Roman Stocker (2012) Fluid mechanics of planktonic microorganisms. *Annual Review of Fluid Mechanics* 44, 373-400.

Hansen, J., Sato, M., Ruedy, R., Lacis, A., & Oinas, a. V. (2000). Global warming in the twenty-first century: An alternative scenario. *Proceedings of the National Academy of Sciences* , 97, 9875.

Harlen, O., Sundararajakumar, R. R., & Koch, D. L. (1999). Numerical simulations of a sphere settling through a suspension of neutrally buoyant fibres. *Journal of Fluid Mechanics*, 388, 355-388.

Hassanpour, Mahmoud, Shafiq, Payam , Bin Mahmud, Hilmi (2012) Lightweight aggregate concrete fiber reinforcement – A review

Hinch, E. & Leal, L. (1972). The effect of Brownian motion on the rheological properties of a suspension of non-spherical particles. *Journal of Fluid Mechanics*, 52(4), 683-712. doi:10.1017/S002211207200271X

Isla, A., Brostow, W., Bujard, B., Esteves, M., Rodriguez, J.R., Vargas, S. and Castano, V.M. (2003). Nanohybrid scratch resistant coatings for teeth and bone viscoelasticity manifested in tribology. *Mat. Res. Innovat.*, 7, 110. <http://doi.org/10.1007/s10019-003-0236-4>

Jeffery, G. B. (1922). The motion of ellipsoidal particles immersed in a viscous fluid. *Proc. Roy. Soc. Lond. A*, 102 (715), 161-179. <http://doi.org/10.1098/rspa.1922.0078>

Jeffrey S. Guasto, R. R. (2012). Fluid Mechanics of Planktonic Microorganisms. Annual Review of Fluid Mechanics , 44(1), 373-400 .

Johnson, R. E. (1980). An improved slender-body theory for Stokes flow. *Journal of Fluid Mechanics*, 99(2), 411-431. (<https://doi:10.1017/S0022112080000687>)

Johnson, R. E. & Brokaw, C. J. (1979) Flagellar hydrodynamics. A comparison between resistive-force theory and slender-body theory. *Biophys. J.* 25, 113–127. ([https://doi:10.1016/S0006-3495\(79\)85281-9](https://doi:10.1016/S0006-3495(79)85281-9))

Johnson, R. E., & Wu, T. (1979). Hydromechanics of low-Reynolds-number flow. Part 5. Motion of a slender torus. *J. Fluid Mech.*, 95(2), 263-277. (<https://doi:10.1017/S0022112079001464>)

Jones, R. T. (1946) Properties of low-aspect-ratio pointed wings at speeds below and above the speed of sound. *Report no. 835. Washington, DC: National Advisory Committee for Aeronautics*.

Keller, J., & Rubinow, S. (1976). Slender-body theory for slow viscous flow. *Journal of Fluid Mechanics*, 75(4), 705-714. (<https://doi:10.1017/S0022112076000475>)

Khayat, R.E. and Cox, R.G., 1989. Inertia effects on the motion of long slender bodies. *Journal of Fluid Mechanics*, 209, 435-462.

Kim, S. and Karilla, S. J. (1991). *Microhydrodynamics*. Dover

Kim, Y. J. and Rae, W. J. (1991). Separation of screw-sensed particles in a homogeneous shear field, *Int. J. Multiphase Flow*, 17(6), 717-744. [http://dx.doi.org/10.1016/0301-9322\(91\)90053-6](http://dx.doi.org/10.1016/0301-9322(91)90053-6).

Koens, L., & Lauga, E. (2016). Slender-ribbon theory. *Physics of Fluids*, 28(1), 013101.

Lamb, S. H., (1932). Hydrodynamics University Press.

Leahy, B., Koch, D. L., & Cohen, I. (2015). The effect of shear flow on the rotational diffusion of a single axisymmetric particle. *Journal of Fluid Mechanics*, 772, 42-79., 42-79.

Leal, L., & Hinch, E. (1971). The effect of weak Brownian rotations on particles in shear flow. *J. Fluid Mech.*, 46(4), 685-703. <http://doi.org/10.1017/S0022112071000788>

Lighthill, M. J. 1960 Note on the swimming of slender fish. *J. Fluid Mech.*, 9, 305–317. ([doi:10.1017/S0022112060001110](https://doi:10.1017/S0022112060001110))

Lighthill, M. J. 1971 Large-amplitude elongated-body theory of fish locomotion. *Proc. R. Soc. Lond. B* 179, 125–138. (<https://doi:10.1098/rspb.1971.0085>)

Lin, Neil Y.C., Ness, Christopher, Cates, Michael E.; Sun, Jin, Cohen, Itai 2016 Tunable shear thickening in suspensions. *Proceedings of National Academy of Sciences*, 113 (39) 10774-10778

Lopez, M. & Graham, M. D. 2007 Shear-induced diffusion in dilute suspensions of spherical or non-spherical particles: Effects of irreversibility and symmetry breaking. *Phys. Fluids* 19, 073602.

Mackaplow, M. &. (1996). A numerical study of the rheological properties of suspensions of rigid, non-Brownian fibres. *Journal of Fluid Mechanics*, 329, 155-186., 329, 155-186. doi:[doi:10.1017/S0022112096008889](https://doi:10.1017/S0022112096008889)

Mackaplow, M. B, Shaqfeh, ESG. 1998 A numerical study of the sedimentation of fibre suspensions. *J. Fluid Mech.*, 376, 149–182. (<https://doi:10.1017/S0022112098002663>)

Mackaplow, M. B, Shaqfeh, E. S. G., Schiek, R. L. 1994 A numerical study of heat and mass transport in fibre suspensions. Proc. R. Soc. Lond. A 447, 77–110. (<https://doi:10.1098/rspa.1994.0130>)

Meng, Q., & Higdon, J. J. (2008). Large scale dynamic simulation of plate-like particle suspensions. Part I: Non-Brownian simulation. *Journal of Rheology*, 52(1), 1-36. doi:doi:10.1122/1.2798236

Meng, Q., & Higdon, J. J. (2008). Large scale dynamic simulation of plate-like particle suspensions. Part II: Brownian simulation. *Journal of Rheology*, 52(1), 37-65.

Mueller, S., Llewellyn, E. W., & Mader, H. M. (2009). The rheology of suspensions of solid particles. *Proceedings of the Royal Society A: Mathematical, Physical and Engineering Sciences*, 466, 1201-1228.

Munk, M. M. 1924 The aerodynamic forces on airship hulls. Report no. 184. Washington, DC: *National Advisory Committee for Aeronautics*.

Newman, J. N. (1964) A slender-body theory for ship oscillations in waves. *J. Fluid Mech.* 18, 602–618. (<https://doi:10.1017/S0022112064000441>)

Newman, J. N. (1970) Applications of slender-body theory in ship hydrodynamics. *Annu. Rev. Fluid Mech.* 2, 67–94. (<https://doi:10.1146/annurev.fl.02.010170.000435>)

N. Ibarra-Avalos, A. G.-V. (2007). Excluded volume of hard cylinders of variable aspect ratio,. Molecular Simulation, 33:6, 505-515,, 33(6), 505-515. doi:10.1080/08927020701191349

Nir, A., & Acrivos, A. (1973). On the creeping motion of two arbitrary-sized touching spheres in a linear shear field. *J. Fluid Mech.*, 59(2), 209-223. <http://doi.org/10.1017/S0022112073001527>

Paulsen, K. S., Di Carlo, D. and Chung, A. J. (2015). Optofluidic fabrication for 3D-shaped particles. *Nature. Communications* 6, 6976. <http://doi.org/10.1038/ncomms7976>

Pozrikidis, C. 2002 A Practical Guide to Boundary Element Methods With the Software Library BEMLIB. Chapman and Hall/CRC

Rahnama, M., Koch, D. L., Iso, Y., & Cohen, C. (1993). Hydrodynamic, translational diffusion in fiber suspensions subject to simple shear flow. *Physics of Fluids A: Fluid Dynamics*, 5(4), 849-862. Retrieved from <https://doi.org/10.1063/1.858890>

Rahnama, M., Koch, D. L. and Shaqfeh, E. S. G., (1995). The effect of hydrodynamic interactions on the orientation distribution in a fiber suspension subject to simple shear flow. *Physics of Fluids*, 7(3), pp.487-506. <http://dx.doi.org/10.1063/1.868647>

Raney, J.R. and Lewis, J.A. (2015). Printing mesoscale architectures, *MRS Bulletin*, 40 (11), 943–950. <http://doi.org/10.1557/mrs.2015.235>

Rocha, A, Acrivos, A. (1973 a) On the effective thermal conductivity of dilute dispersions: general theory for inclusions of arbitrary shape. *Q. J. Mech. Appl. Math.*, **26**, 217–233. (<https://doi:10.1093/qjimam/26.2.217>)

Rocha, A, Acrivos, A. (1973 b) On the effective thermal conductivity of dilute dispersions: highly conducting inclusions of arbitrary shape. *Q. J. Mech. Appl. Math.* **26**, 441–455. (<https://doi:10.1093/qjimam/26.4.441>)

Sacanna, S, Korpics, M, Rodriguez, K, Colón-Meléndez, L, Kim, S-H, Pine, D. J., Yi, Gi-Ra, Shaping colloids for self-assembly (2013) *Nature Communications*, 4, 1688.

Shaqfeh, E. S. G. (1988) A nonlocal theory for the heat transport in composites containing highly conducting fibrous inclusions. *Phys. Fluids* (1958–1988) **31**, 2405–2425. (<https://doi:10.1063/1.866594>)

Singh, V., Koch, D. L., & Stroock, A. D. (2013). Rigid ring-shaped particles that align in simple shear flow. *J. Fluid Mech*, 722, 121-158. <http://doi.org/10.1017/jfm.2013.53>

Singh, V., Koch, D. L., Subramanian, G., & Stroock, A. D. (2014). Rotational motion of a thin axisymmetric disk in a low Reynolds number linear flow. *Physics of Fluids*, 26(3), 033303.

Soler, L., & Sánchez, S. (2014). Catalytic nanomotors for environmental monitoring and water remediation. *Nanoscale*, 6(13), 7175-7182.

Stover, C. A., & Cohen, C. (1990). The motion of rodlike particles in the pressure-driven flow between two flat plates. *Rheologica Acta*, 29 (3), 192-203. <http://doi.org/10.1007/BF01331355>

Suarez, S. S., & Pacey, A. A. (2006). Sperm transport in the female reproductive tract. *Human reproduction update*, 12(1), 23-37

Subramanian, G., & Koch, D. (2005). Inertial effects on fibre motion in simple shear flow. *Journal of Fluid Mechanics*, 535, 383-414. doi:doi:10.1017/S0022112005004829

Tekce, H. S., Kumlutas, D., & Tavman, I. H. (2007). Effect of Particle Shape on Thermal Conductivity of Copper Reinforced Polymer Composites. *Journal of Reinforced Plastics and Composites*, 26(1), 113–121. (<https://doi.org/10.1177/0731684407072522>)

Thorp, I., & Lister, J. (2019). Motion of a non-axisymmetric particle in viscous shear flow. *Journal of Fluid Mechanics*, 872, 532-559. doi:10.1017/jfm.2019.367

Trevelyan, B. J., and Mason, S. G., (1951). "Particle motions in sheared suspensions. I. Rotations." *Journal of Colloid Science*, 6 (4), 354-367. [http://dx.doi.org/10.1016/0095-8522\(51\)90005-0](http://dx.doi.org/10.1016/0095-8522(51)90005-0)

van der Kooij, F. M. (2000). Rheology of dilute suspensions of hard platelike colloids. *Journal of Colloid Interface Science* , 235, 344–349.

Viera, M. N. (2002). Large scale simulation of Brownian suspensions. Ph.D. thesis, University of Illinois at Urbana-Champaign.

Wang, J., Graham, M. D., Klingenberg, D. J. 2014 Shear-induced diffusion in dilute curved fiber suspensions in simple shear flow *Physics of Fluids* 26(3), 033301. (<https://doi.org/10.1063/1.4867171>)

Wang, J., Tozzi, E. J., Graham, M. D., and Klingenber, D. J. (2012). Flipping, scooping, and spinning: Drift of rigid curved nonchiral fibers in simple shear flow. *Phys. Fluid*, 24 (12), 123304.  
<http://dx.doi.org/%2010.1063/1.4769980>

Wensink, H. H., & Avendaño, C. (2016). Empty smectic liquid crystals of hard nanorings: Insights from a second-virial theory. *Physical Review E*, 94(6), 062704.

Yarin, A. L., Gottlieb, O., & Roisman, I. V. (1997). Chaotic rotation of triaxial ellipsoids in simple shear flow. *J. Fluid Mech.*, 340, 83-100. (<https://doi.org/10.1017/S0022112097005260>)

Yamamoto, S., & Matsuoka, T. (1997). Dynamic simulation of a plate-like particle dispersed system. *Journal of Chemical Physics*, 107, 3300–3308.

Yamane, Y., Kaneda, Y. & Dio, M., (1994) Numerical simulation of semi-dilute suspensions of rodlike particles in shear flow. *Journal of Non-Newtonian Fluid Mechanics*, 54, 405-421.

Yang, S.-M., & Leal, L. G. (1984). Particle motion in Stokes flow near a plane fluid–fluid interface. Part 2. Linear shear and axisymmetric straining flows. *Journal of Fluid Mechanics*, 149, 275-304.

Yasuda, Kazunori, Mori, Noriyasu & Nakamura, Kiyoji (2002) A new visualization technique for short fibers in a slit flow of fiber suspensions, *International Journal of Engineering Science*, 40 (9), 1037-1052.

Youngren, G. K., and Acrivos, A. (1975). Stokes flow past a particle of arbitrary shape: A numerical method of solution, *J. Fluid Mech.*, 69 (02), 377-403.  
<http://doi.org/10.1017/S0022112075001486>

Yu, A., Ramesh, P., Itkis, M. E., Bekyarova, E., & Haddon, R. C. (2007). Graphite Nanoplatelet–Epoxy Composite Thermal Interface Materials. *The Journal of Physical Chemistry C*, 7565-7569. doi:doi: 10.1021/jp071761s